



# Mechanisms of context-dependent translation inhibition by ribosome-targeting antibiotics

Élodie Leroy

## ► To cite this version:

Élodie Leroy. Mechanisms of context-dependent translation inhibition by ribosome-targeting antibiotics. Immunology. Université de Bordeaux, 2021. English. NNT : 2021BORD0275 . tel-03520733

**HAL Id: tel-03520733**

**<https://theses.hal.science/tel-03520733>**

Submitted on 11 Jan 2022

**HAL** is a multi-disciplinary open access archive for the deposit and dissemination of scientific research documents, whether they are published or not. The documents may come from teaching and research institutions in France or abroad, or from public or private research centers.

L'archive ouverte pluridisciplinaire **HAL**, est destinée au dépôt et à la diffusion de documents scientifiques de niveau recherche, publiés ou non, émanant des établissements d'enseignement et de recherche français ou étrangers, des laboratoires publics ou privés.

THÈSE PRÉSENTÉE  
POUR OBTENIR LE GRADE DE

**DOCTEUR DE**  
**L'UNIVERSITÉ DE BORDEAUX**

ÉCOLE DOCTORALE SCIENCES DE LA VIE ET DE LA SANTÉ  
SPÉCIALITÉ IMMUNOLOGIE ET MICROBIOLOGIE

Par Elodie LEROY

**MECHANISMS OF CONTEXT-DEPENDENT TRANSLATION  
INHIBITION BY RIBOSOME-TARGETING ANTIBIOTICS**

Sous la direction de : Dr. C. Axel INNIS

Soutenue le 22 novembre 2021

Membres du jury :

Prof BLANCHARD, Scott	Professeur, St. Jude Children's Research Hospital	Rapporteur
Dr ENNIFAR, Eric	Directeur de recherche, IBMC, Université de Strasbourg	Rapporteur
Prof SANYAL, Suparna	Professeur, Department of Cell and Molecular Biology, Uppsala RNA Research Centre – URR	Examineur
Dr DARFEUILLE, Fabien	ARNA laboratory INSERM U1212 CNRS 5320 Université de Bordeaux	Examineur



*To my mom,*



## ACKNOWLEDGEMENTS

I would like to thank all the members of the jury, **Prof. Scott Blanchard**, **Dr. Eric Ennifar**, **Prof. Suparna Sanyal** and **Dr. Fabien Darfeuille**, for taking the time to read and evaluate my work. My research was funded by the European Research Council (ERC) under the European Union's Horizon 2020 research and innovation program (Grant Agreement No. 724040).

Moving from Paris to Bordeaux was probably one of the best decisions of my life. My PhD was tough in several aspects, but I'm glad now, and even a little bit proud, of my journey. However, I would have given up everything without the help and the joy offered by the many incredible people I met during this adventure.

First of all, I would like to thank my supervisor **Axel Innis**, for accepting me in the lab as a PhD student. Thank you for believing in me from the very start. I learnt so many things under your supervision, and I developed my scientific skills and improved my english. You always let me manage my projects and test my ideas, even if sometimes you were not 100% confident about the purposes. You gave me access to wonderful scientific meetings and always encouraged me to talk to others and start collaborations. During the tough times, you were always present and supportive. I will never forget that you were here the 13-11-2018. Thank you for your kindness and your rigor. You always valued my work and my efforts, without stopping pushing me beyond my limits. It made me grow up as a scientist, but also as a person. I also would like to thank you for the huge time you spent on my thesis during your vacations, I feel very lucky for having been supervised by you. I need to admit it and to say it now: "Je sers la science, et c'est ma joie".

I would like next to thank **Mélanie Gillard** for her teachings in biology, her help and her kindness. En arrivant au labo, je n'aurais sincèrement jamais cru que je nouerai une telle amitié avec quelqu'un. Je te dois énormément. Tu fais partie des personnes qui ont influencé le cours de ma thèse, et sans qui tout aurait été plus difficile encore. Je te remercie pour ton écoute, pour tes câlins dans les moments difficiles, tes mots d'encouragement et tes conseils. Nos fous rires dans le bureau, nos pétages de câbles et notre amour des plantes (sauf Calimero pour ma part) seront les choses qui me manqueront le plus une fois partie. Tu es une personne merveilleuse, et je te remercie de tout mon cœur pour tout ce que tu m'as donné.

I also need to thank **Alba Herrero del Valle** for sharing incredible moments of PhD life. I missed you so much these last two years. I really want to thank you for your support, our laughs, our happy hours and coffee breaks. You are an example to me, I deeply admire you and wish you the best for the future.

I have a special thought for **Pauline Cossard**. Je ne pensais pas à ton arrivée qu'un petit bout de femme comme toi me ferait vivre autant d'ascenseurs émotionnels en si peu de temps. Tu as fait preuve à tes débuts d'un superbe sens de l'adaptation, où après t'avoir expliqué brièvement 2/3 bases de biologie moléculaire, tu as pu faire ton bonhomme de chemin en seulement quelques semaines, et ce de manière autonome. Tu m'as ensuite rappelé que rien n'était acquis,

et tu nous as tous donné la définition des mots « force » et « courage ». Pour cela, je pense que nous devons tous te remercier. Le vent tournera pour toi j'en suis certaine et je te souhaite le meilleur pour la suite.

I would like now to thank **Thibaud Renault**, for his help concerning the inverse toeprinting data analysis and his daily support. Avant ton arrivée dans l'équipe, j'appréciais déjà beaucoup ta compagnie lors de nos déjeuners à la fameuse cantine du CNRS. Ensuite, lorsque tu es monté au deuxième étage, tu t'es tout de suite intéressé et impliqué dans mes projets, et j'ai été plutôt surprise de tant d'engouement. Mais lorsque j'ai vu ton implication quotidienne et la rigueur que tu mettais dans les analyses de mes résultats, sans jamais t'imposer ni m'oublier, j'ai compris que j'avais énormément de chance. Tu as ensuite accepté de travailler sur les manuscrits, et de relire ma thèse et pour tout ce temps et ces efforts, je te dis mille mercis.

I need to thank now the previous members of the lab, and particularly **Guénaël Sacheau**, (Maurice pour les intimes), for having such fun times together. You also taught me how to make perfect toeprinting gels, and after maybe, approximatively 1595203 more or less successful gels, I guess I should thank you for this. I would also like to thank **Aitor Manteca**, for your support and your kindness, particularly during our trip in Merida. I needed a friend at that time, and you were here. Thank you for everything. I would like to thank my previous colleagues, **Anne-Xander van der Stel**, **Mecit Gökçe**, **Britta Seip**, **Carolin Seefeldt** and **Natacha Perebaskine** for their wise advices and their active and helpful participation.

I would like now to thank **Fanny Boissier** and **Anne Bourdoncle** for their sympathy and daily support. You just arrived in the team, but I shared already very pleasant times with you. I wish you the best for the future. Merci beaucoup Fanny pour ton aide à ton arrivée concernant cette fichue HPLC. Par la même occasion, je voudrais aussi remercier **Laure Bataille**, qui a aussi passé beaucoup de temps avec moi à tenter de dompter cette machine ! Je te remercie aussi Laure pour ton soutien, pour cette capacité d'écoute et d'empathie dont tu as toujours fait preuve à mon égard. Tu as été d'une grande aide, surtout en cette fin de thèse, merci beaucoup.

I need also to thank our collaborators, and particularly prof. **Daniel Wilson** for his help during my mid-thesis and for his enthusiasm concerning my work on several common projects. I also thank **Nora Vazquez-Laslop** and **Alexander Shura Mankin** for the great scientific talks, but also **Lars Bock**, **Gregory Boël** and **Yaser Hashem** for the same reasons.

I have also a thought for the different technicians and engineers of IECB. I would like to thank **Delphine Dargere**, **Myriam Mederic**, **Stéphanie Durrieu** and **Sonia San Jose** for their help, their listening and our chattering. I thank the **Fronzes** team, for welcoming me at the beginning of my PhD. A special thanks to **Ester Marza** for her help with my teachings, and her advices during my mid-thesis.

But what would be a thesis without friends? I feel so lucky to have met such incredible friends. **Camila Parrot**, **Heddy Soufari**, **Florent Waltz**, **Chiara Rapisarda**, **Florian Bernard** and also **Pauline Pony**, **Robin Anger** and **Pierre Nottelet**: guys, you made me laugh so hard so

many times. I think the most beautiful times of this PhD were shared with you, and I missed you so much these last few years/months. I think I lost several years of life because of you, as my liver still remembers our times together, but all of it was worth it.

I would like to thank also my **family** and my other **friends** for their support. This includes **Leonardo Talachia-Rosa** and his wife **Ana**. Thank you for having taken the time to read and correct my thesis. Your feedback was super helpful. I thank life for letting our paths meet. You are a model of honesty, kindness and modesty. I really admire you, your words touched my soul so many times, thank you.

I also have two soul mates, **Chloé Heilles** and **Cécile Brunerie**. Je ne vous remercierai jamais assez les filles d'être aussi extraordinaires. Vous avez toujours été d'un soutien à toute épreuve, sans limite. Sans vous les filles, ma vie serait bien maussade. Vous m'avez aidé à tenir bon ces quatre dernières années, et malgré les tempêtes, vous m'avez fait rire aux éclats tout du long (sauf aux mille bornes, mais ça c'est un sujet sensible).

The last word is obviously for my husband, **Thomas Perry**. Travailler et vivre avec toi est un combo dont je n'avais jamais espéré rêver auparavant. Tu as ce don d'éclaircir au quotidien les couleurs de la vie. Sans cette force, ma thèse se serait arrêtée il y a déjà bien longtemps. Merci d'être toi, merci pour tout.

PS: I also need to thank the **coffee machine** and all the **coffee trees** that contributed to the writing of this thesis.



## RÉSUMÉ COURT

### **Titre : Mécanismes d'inhibition de la traduction contexte-dépendants par des antibiotiques ciblant le ribosome bactérien**

#### **Résumé :**

Au cours des dernières décennies, le nombre d'agents pathogènes multi-résistants aux antibiotiques a augmenté tandis que le nombre de nouvelles molécules entrant sur le marché a régulièrement diminué, faisant de la résistance aux antibiotiques une grave menace pour la santé publique. De nombreux antibiotiques bloquent la synthèse des protéines en ciblant le ribosome bactérien, la machinerie cellulaire qui traduit en protéines l'information génétique codée dans l'ARN messager. Jusqu'à présent, la plupart de ces antibiotiques étaient considérés comme des inhibiteurs universels de la traduction, empêchant la synthèse de toute protéine avec une efficacité comparable. Cependant, une grande variété d'acides aminés, d'ARNs de transfert et de codons traverse le ribosome pendant la traduction, ayant chacun leurs propre structure et propriétés chimiques, et il a été démontré que plusieurs antibiotiques, tels que les macrolides ou le chloramphénicol, arrêtent la synthèse des protéines d'une manière dépendante du contexte ou des substrats spécifiques. Cette propriété est exploitée par des bactéries pathogènes, qui utilisent de courts peptides, dits "leader", pour détecter les antibiotiques dans leur environnement et induire l'expression de leurs gènes de résistance. Comprendre les déterminants de séquence sous-jacents à ce phénomène pourrait donc aider à développer des médicaments qui empêchent une telle activation de se produire. Plus important encore, l'inhibition dépendante du contexte pourrait être une propriété générale des antibiotiques ciblant les ribosomes, et la détermination du mode d'action précis de nombreux médicaments largement utilisés en médecine humaine ou vétérinaire pourrait fournir des pistes d'optimisation de ces molécules pour faire face à la menace mondiale de résistance aux antimicrobiens. Par conséquent, mon travail de thèse s'est concentré sur le réexamen des modes d'action des antibiotiques ciblant le ribosome, afin d'apporter de nouvelles solutions dans la lutte contre les agents pathogènes multi-résistants.

Pour y parvenir, j'ai d'abord choisi d'étudier la dépendance de séquence de peptides leader courts qui contrôlent l'expression de différentes méthylases de résistance à l'érythromycine (Erm) en réponse aux antibiotiques macrolides. Pour ce faire, j'ai utilisé l'*inverse toeprinting*, une technique de profilage *in vitro* développée dans notre groupe pour étudier les transcrits

codant pour des peptides qui induisent l'arrêt des ribosomes. En modifiant systématiquement la séquence de trois peptides leader Erm différents, j'ai obtenu de nouvelles informations sur leur mode d'action et révélé le principal mécanisme par lequel les antibiotiques macrolides inhibent le ribosome. Ensuite, j'ai cherché à découvrir la dépendance de contexte de divers antibiotiques ciblant le ribosome et connus pour inhiber des étapes spécifiques du processus d'élongation de la traduction. En combinant la méthode d'*inverse toeprinting* avec une bibliothèque d'ARNm codant pour  $\sim 10^{12}$  peptides aléatoires, j'ai pu obtenir une vue globale du blocage des ribosomes d'*Escherichia coli* exposés aux différents antibiotiques d'intérêt, ainsi qu'une liste complète de motifs de séquences qui arrêtent la traduction en présence de certains antibiotiques. Puis en utilisant des techniques de biochimie et la cryo-microscopie électronique, j'ai pu caractériser les mécanismes par lesquels deux classes d'antibiotiques, les tuberactinomycines capréomycine et viomycine, ainsi qu'un antibiotique moins caractérisé, la tétracénomycine X, inhibent la traduction d'une manière dépendante de la nature des ARN de transfert et du peptide naissant, respectivement. Cette étude m'a permis ainsi de révéler de nouveaux modes d'inhibition des ribosomes par ces antibiotiques, ouvrant la possibilité de les optimiser.

Mots clés : Ribosome, Antibiotiques, Traduction, Antibio-résistance, Bactéries pathogènes

---

**ARNA INSERM U1212, CNRS UMR 5320**

146 rue Léo Saignat, 33076 Bordeaux

## SHORT SUMMARY

### **Title: Mechanisms of context-dependent translation inhibition by ribosome-targeting antibiotics**

#### **Abstract:**

Over the past few decades, the number of multidrug-resistant pathogens has increased while the number of new antibiotics entering the market has steadily decreased, making antibiotic resistance a severe threat to public health. Many antibiotics block protein synthesis by targeting the bacterial ribosome, the cellular machinery that translates the genetic information encoded in messenger RNA into proteins. Until recently, most of these antibiotics were thought to be universal translation inhibitors that prevent the synthesis of all proteins with comparable efficiency. However, during translation, a variety of amino acids, transfer RNAs and codons pass through the ribosome during translation, each with its own structure and chemical properties. In this sense, several antibiotics, such as the macrolides or chloramphenicol, have been shown to arrest protein synthesis in a context-dependent manner, only when specific substrates are present in the ribosome. This property is exploited by pathogenic bacteria, which use short leader sequences to detect antibiotics in their surroundings and induce the expression of their resistance genes in a drug-dependent manner. Understanding the sequence determinants underlying this phenomenon could therefore help develop drugs that prevent such activation from taking place. Perhaps more importantly, context-dependent inhibition may be a general feature of ribosome-targeting antibiotics, and determining the precise mode of action of many drugs widely used in human or veterinary medicine may provide clues on how to optimize them to address the global threat of antimicrobial resistance. In this context, my PhD work focused on reexamining the modes of action of ribosomal antibiotics in order to provide new solutions in the fight against multidrug resistant pathogens.

To achieve this, I first chose to study the sequence dependence of short leader peptides that control the expression of different erythromycin resistance methylases (Erm) in response to macrolide antibiotics. To do so, I used inverse toeprinting, an *in vitro* profiling technique developed in our group to study transcripts encoding peptides that induce ribosome stalling. By systematically modifying the sequence of three different Erm leader peptides, I obtained new insights into their mode of action and revealed the main mechanism by which macrolide antibiotics inactivate the ribosome. Next, I sought to uncover the context dependency of various

ribosomal antibiotics known to inhibit specific steps of the translation elongation process. Using inverse toeprinting in combination with a library of mRNAs encoding  $\sim 10^{12}$  random peptides, I determined the stalling landscapes of *Escherichia coli* ribosomes exposed to a variety of different antibiotics and obtained a comprehensive list of sequence motifs that arrest translation in the presence of some of these drugs. Using biochemistry and cryo-electron microscopy, I was then able to characterize the mechanisms by which two classes of antibiotics, the tuberactinomycins capreomycin and viomycin, and the less characterized antibiotic tetracenomycin X, inhibit translation in a manner dependent on the nature of the transfer RNAs and the nascent peptide, respectively. Thus, I could reveal new modes of ribosome inhibition by these antibiotics, opening up the possibility of optimizing them through rational design.

Keywords: Ribosome, Antibiotics, Translation, Antibiotic Resistance, Bacterial pathogens

---

**ARNA INSERM U1212, CNRS UMR 5320**

146 rue Léo Saignat, 33076 Bordeaux



## Résumé en français

Les bactéries sont présentes partout dans notre environnement et sont indispensables à notre physiologie. Malheureusement, certaines d'entre elles provoquent également des maladies infectieuses, que nous traitons avec des antibiotiques. Dans certains cas, ces bactéries pathogènes sont capables de survivre à ces antibiotiques, grâce à une série de phénomènes connus sous le nom de résistance aux antibiotiques, et l'utilisation excessive des antibiotiques a accéléré ce processus. En effet, au cours des dernières décennies, le nombre de pathogènes multi-résistants a augmenté tandis que le nombre de nouveaux antibiotiques entrant sur le marché a régulièrement diminué, faisant de la résistance aux antibiotiques une grave menace de santé publique. De nombreux antibiotiques bloquent la synthèse des protéines en ciblant le ribosome bactérien, la machinerie cellulaire qui traduit l'information génétique codée dans l'ARN messager (ARNm) en protéines. Les ribosomes se composent d'une grande sous-unité 50S et d'une petite sous-unité 30S. La formation d'une liaison peptidique a lieu au cœur du ribosome dans le PTC (*Peptidyl Transferase Center*). Une cavité, appelée tunnel de sortie, allant du PTC vers l'extérieur du ribosome, permet au peptide d'atteindre le cytoplasme. Les ARN de transfert (ARNt) chargés par la protéine naissante et les nouveaux acides aminés circulent au sein du ribosome au sein de trois sites, nommés site A (*Aminoacyl-tRNA*), site P (*Peptidyl-tRNA*) et site E (*Exit*). Au sein du ribosome, le processus de traduction se déroule en trois étapes principales :

- 1 L'étape d'**initiation**, où les deux sous-unités du ribosome sont assemblées sur un codon d'initiation de l'ARNm.
- 2 Le processus d'**élongation**, où le ribosome traduit l'ARNm pour former la liaison peptidique entre la protéine naissante attaché à un ARNt situé dans le site P du ribosome, et l'ARNt amino-acylé entrant dans le site A. Du PTC, la chaîne peptidique naissante traverse le tunnel de sortie pour atteindre le cytoplasme. Une fois que la formation de la liaison peptidique s'est produite, l'ARNt déacylé dans le site P et le l'ARNt peptidylé dans le site A se déplacent avec l'ARNm d'un codon par rapport à la position du ribosome vers les sites E et P du ribosome respectivement, par un processus appelé translocation.
- 3 Les étapes de **terminaison** et de **recyclage** ; une fois que le ribosome atteint le codon stop, le complexe est désassemblé et recyclé, afin de pouvoir réengager un nouveau cycle de traduction.

La majorité des antibiotiques ciblent en fait l'étape d'élongation de la traduction. Jusqu'à présent, la plupart de ces antibiotiques étaient considérés comme des inhibiteurs universels de la traduction, empêchant ainsi la synthèse de toutes les protéines avec une efficacité comparable. Cependant, une grande variété de substrats sont utilisés par le ribosome pendant la traduction. Il a été démontré que plusieurs antibiotiques, tels que les macrolides ou le chloramphénicol, arrêtent la synthèse des protéines d'une manière dépendante du contexte et de ces substrats. Cette propriété est exploitée par des bactéries pathogènes, qui utilisent de courtes séquences leader pour détecter les antibiotiques dans leur environnement et induire l'expression de leurs gènes de résistance. Comprendre les déterminants de séquence sous-jacents à ce phénomène pourrait donc aider à développer des médicaments qui empêcheraient une telle activation de se produire. Plus important encore, l'inhibition dépendante du contexte pourrait être une propriété générale des antibiotiques ciblant les ribosomes, et la détermination du mode d'action précis de nombreux médicaments largement utilisés en médecine humaine ou vétérinaire pourrait fournir des indices sur la façon de les optimiser pour faire face à la menace mondiale de résistance aux antibiotiques. Par conséquent, mon travail de thèse s'est concentré sur le réexamen des mécanismes d'action des antibiotiques ciblant le ribosome, afin d'apporter de nouvelles solutions dans la lutte contre les agents pathogènes multi-résistants.

Mes travaux ont donc porté sur la compréhension de la manière dont les antibiotiques peuvent inhiber la traduction bactérienne de manière contextuelle. Plus précisément, j'ai cherché (i) à comprendre le mécanisme par lequel les bactéries deviennent résistantes aux antibiotiques largement utilisés comme les macrolides et les cétolides, qui interagissent avec le peptide naissant produit pendant la phase d'élongation pour inhiber la PTC, et (ii) à déterminer le mode d'action moléculaire de plusieurs antibiotiques, dont les antituberculeux de seconde ligne capréomycine et viomycine, et l'antibiotique tétracénomycine X, plus récent mais très prometteur. Une meilleure compréhension de ces processus pourrait à terme apporter des solutions pour ralentir la propagation de la résistance aux antibiotiques.

Dans un premier temps, j'ai d'abord choisi d'étudier la dépendance de séquence de peptides leader courts qui contrôlent l'expression de différentes méthylases de résistance à l'érythromycine (Erm) en réponse aux antibiotiques macrolides. Pour ce faire, j'ai utilisé l'*inverse toeprinting*, une technique de profilage *in vitro* développée dans notre groupe pour étudier les transcrits codant pour des peptides qui induisent l'arrêt des ribosomes. En modifiant systématiquement la séquence de trois peptides leader Erm différents, j'ai obtenu de nouvelles informations sur leur mode d'action et révélé le principal mécanisme par lequel les antibiotiques macrolides inhibent le ribosome. Grâce à un travail collaboratif combinant plusieurs approches

techniques, j'ai prouvé en utilisant l'*inverse toeprinting* que le peptide ErmDL présente un double mécanisme pour détecter le macrolide érythromycine ou le cétolide télithromycine pour inhiber le ribosome. De la même manière, j'ai pu expliquer pourquoi l'érythromycine affiche un mécanisme peptide-dépendant moins strict en comparaison à la télithromycine. J'ai également expliqué plus généralement comment certains peptides contenant un motif +X+ (+ représente un acide aminé chargé positivement, et X n'importe quel résidu) inhibent le PTC en présence de ces antibiotiques. Parallèlement, en utilisant la même approche basée sur l'*inverse toeprinting*, j'ai démontré que les peptides ErmCL et ErmAL1 inhibent le ribosome par un mode d'action identique, basé sur deux positions clés de résidus au sein de ces peptides, où leurs mutations peuvent, soit complètement abolir, soit restreindre ou permettre leur traduction en présence de macrolides liés au ribosome. Ces nouvelles connaissances ont soulevé de nombreuses questions concernant le rôle de telles variations au sein des séquences leader des gènes *erm*. Ces différences en termes de sélectivité de traduction sont probablement cruciales *in vivo* pour réguler étroitement l'expression du gène de résistance, et réduire le coût de valeur sélective (*fitness*) induit par une telle expression. Répondre à ces problématiques aiderait à comprendre l'expression inductible par *erm*, et aiderait au développement d'antibiotiques macrolides et cétolides moins spécifiques afin de limiter l'apparition de souches multi-résistantes.

Dans la deuxième partie de mon travail, j'ai étudié comment d'autres catégories d'antibiotiques ciblant le processus d'élongation pouvaient inhiber ou non le ribosome de manière contextuelle lors de la traduction. J'ai pour cela choisi divers antibiotiques connus pour inhiber des étapes spécifiques du processus d'élongation. En combinant la méthode d'*inverse toeprinting* et en utilisant une bibliothèque d'ARNm codant pour  $\sim 10^{12}$  peptides aléatoires, j'ai pu obtenir une vue globale du blocage des ribosomes d'*Escherichia coli* exposés à ces différents antibiotiques, ainsi qu'une liste complète de motifs de séquences qui arrêtent la traduction en leur présence. Certains antibiotiques présentaient un mode d'action spécifique dépendant du contexte de traduction, jusqu'alors inconnu. En utilisant des techniques de biochimie et la cryo-microscopie électronique, j'ai premièrement montré que l'inhibition induite par la capréomycine, un antibiotique de seconde ligne utilisé en cas de résistance contre la tuberculose, dépend de la nature de l'ARNt du site A. D'après la littérature, c'est la première fois que le mode d'action d'un antibiotique repose sur la nature d'un ARNt. Par ailleurs, les travaux réalisés sur la capréomycine ont posé la question du choix des conditions expérimentales dans l'étude du mode d'action des antibiotiques. En effet, j'ai démontré en utilisant différentes concentrations d'antibiotiques ou différentes conditions de tampons, que le mode d'action de la capréomycine pouvait fortement varier en fonction des conditions utilisées pour l'expérience. Ces observations

ont rappelé l'importance de limiter autant que possible l'utilisation de conditions très artificielles (fortes concentrations de sels ou d'antibiotiques par exemple) pour étudier le mode d'action des antibiotiques. Parmi les autres antibiotiques identifiés par *inverse toeprinting* et présentant un mode d'action dépendant du contexte, la tétracénomycine X, un nouvel antibiotique récemment décrit ciblant le tunnel de sortie des ribosomes procaryotes, mais également eucaryotes, n'a pu seulement inhiber la traduction de quelques peptides présentant des motifs de séquence particuliers, de la même manière que ce qui étaient déjà décrits pour les macrolides et les cétolides. Ces nouveaux résultats ont fourni de nouvelles informations sur la façon dont le tunnel de sortie du ribosome, le peptide naissant et l'antibiotique interagissent avec le PTC et les ARNt pour inhiber la formation de liaisons peptidiques. En effet, le mode d'action de la tétracénomycine X correspond à un mécanisme inédit, où l'extrémité 3' de l'ARNt du site P est non seulement déformée, mais aussi tirée à l'intérieur du tunnel de sortie du ribosome, ce qui a pour conséquence d'augmenter la distance entre les l'ARNt peptidylé et l'ARNt aminoacylé, empêchant ainsi la formation de la liaison peptidique.

L'étude du mode d'action précis de notre arsenal actuel d'antibiotiques est d'une grande importance pour lutter contre la menace grandissante du développement de souches bactériennes multi-résistantes, car elle fournit des pistes prometteuses pour améliorer et optimiser l'activité de nos antibiotiques actuels afin de (i) Réduire leur spécificité traduction pour avoir de meilleurs médicaments, (ii) Augmenter cette spécificité pour utiliser ces antibiotiques non pas contre les bactéries, mais contre des cellules humaines, afin d'en obtenir des anticancéreux intéressants et/ou d'inhiber la traduction de protéines spécifiques en cas de maladies génétiques par exemple et (iii) Améliorer leurs propriétés pharmaceutiques, pour réduire au maximum l'apparition de la résistance. Les informations fournies par mon travail et par de telles études ouvriront la voie au développement d'approches fondées sur les connaissances du fonctionnement de ces antibiotiques, afin de lutter contre la résistance et de relancer en profondeur le processus de découverte d'antibiotiques.

## Table of content

<b>ACKNOWLEDGEMENTS .....</b>	<b>3</b>
<b>RÉSUMÉ COURT .....</b>	<b>7</b>
<b>SHORT SUMMMARY.....</b>	<b>9</b>
<b>RÉSUMÉ EN FRANÇAIS.....</b>	<b>11</b>
<b>TABLE OF CONTENT .....</b>	<b>15</b>
<b>LIST OF FIGURES.....</b>	<b>17</b>
<b>LIST OF TABLES .....</b>	<b>19</b>
<b>ABBREVIATIONS.....</b>	<b>20</b>
<b>PART I: GENERAL INTRODUCTION .....</b>	<b>23</b>
1.1. ANTIBIOTICS AND THE GLOBAL EMERGENCE OF DRUG RESISTANCE.....	24
1.2. BACTERIAL PROTEIN SYNTHESIS AS A MAJOR ANTIBIOTIC TARGET .....	30
1.2.1. <i>The bacterial ribosome .....</i>	<i>30</i>
1.2.2. <i>The bacterial translation cycle .....</i>	<i>32</i>
1.2.2.1. Initiation.....	33
1.2.2.2. Elongation .....	36
Peptide bond formation.....	38
The six- and eight-membered proton shuttle models.....	40
The proton wire model.....	41
tRNA-mRNA translocation .....	42
1.2.2.3. Termination and recycling .....	45
1.2.3. <i>Ribosome-targeting antibiotics.....</i>	<i>46</i>
1.2.3.1. Overview of ribosome-targeting antibiotics.....	46
1.2.3.2. Context-specific action of ribosome-targeting antibiotics.....	48
Macrolides and ketolides .....	48
Chloramphenicol and oxazolidinones.....	50
Kasugamycin.....	51
1.3. AIMS AND OBJECTIVES.....	52
<b>PART II: METHODOLOGICAL OVERVIEW.....</b>	<b>55</b>
2.1. DETERMINING RIBOSOMAL STALLING LANDSCAPES WITH INVERSE TOEPRINTING.....	56
<i>Classical versus Inverse toeprinting .....</i>	<i>56</i>
2.2. VISUALIZING FUNCTIONAL RIBOSOMAL COMPLEXES BY CRYO-EM.....	60
<b>PART III: UNDERSTANDING THE SEQUENCE DETERMINANTS UNDERLYING MACROLIDE CONTEXT-DEPENDENT INHIBITION .....</b>	<b>63</b>
3. INTRODUCTION .....	64
3.1.1. <i>Natural and synthetic macrolides discovery and development .....</i>	<i>64</i>
3.1.2. <i>Mode of action of macrolides.....</i>	<i>66</i>
3.1.3. <i>Macrolide resistance and erythromycin resistance methyltransferase genes (erm) .....</i>	<i>67</i>
3.2. METHODOLOGICAL OVERVIEW .....	75
3.3. RESULTS.....	76
3.3.1. <i>Structural and mechanistic basis for translation inhibition by macrolide and ketolide antibiotics .....</i>	<i>76</i>
3.3.2. <i>ErmCL and ErmAL1 arrest peptides affect the A-site properties of the PTC in presence of cladinose-containing macrolide antibiotics using the same mechanism of inhibition.....</i>	<i>77</i>
3.3.2.1. MATERIALS AND METHODS.....	77
3.3.2.2. RESULTS.....	83
3.3.2.3. Discussion.....	90
3.4. CONCLUSIONS AND DISCUSSION OF PART III.....	95
<b>PART IV: REVEALING THE SEQUENCE DEPENDENCE OF RIBOSOMAL ANTIBIOTICS .....</b>	<b>98</b>
4.1. INTRODUCTION .....	101

4.2.	RESULTS.....	102
4.2.1.	<i>Ribosomal stalling landscapes altered by antibiotics.....</i>	102
4.2.2.	<i>The tuberactinomycins capreomycin and viomycin.....</i>	110
4.2.3.	<i>The aromatic polyketide tetracenomycin X.....</i>	112
4.2.4.	<i>The five-membered ring aminocyclitol antibiotic pactamycin.....</i>	116
4.3.	PERSPECTIVES AND DISCUSSION.....	121
4.4.	MATERIALS AND METHODS.....	123
4.4.1.	<i>Inverse toeprinting to characterize in vitro the stalling landscapes of drug-bound E. coli ribosomes.....</i>	123
4.4.2.	<i>Toeprinting technique for the study of the effect of mutations on ribosomal stalling.....</i>	124
4.4.3.	<i>Structural characterization of 70S ribosomal complexes blocked in the presence of the drug of interest.....</i>	128
	<b>PART V: GENERAL CONCLUSIONS AND PERSPECTIVES.....</b>	<b>129</b>
	<b>REFERENCES.....</b>	<b>133</b>
	<b>SUPPLEMENTARY DATA.....</b>	<b>153</b>

## List of Figures

<b>Figure 1 : Timeline showing the decade new classes of antibiotic reached the clinic .....</b>	<b>25</b>
<b>Figure 2 : Schematic overview of the bacterial 70S ribosome.....</b>	<b>30</b>
<b>Figure 3 : Schematic and three-dimensional tRNA representations.....</b>	<b>31</b>
<b>Figure 4 : Schematic overview of the prokaryotic translation cycle .....</b>	<b>33</b>
<b>Figure 5 : Overview of the initiation step on an SD-containing mRNA.....</b>	<b>35</b>
<b>Figure 6 : Schematic overview of the prokaryotic elongation cycle .....</b>	<b>37</b>
<b>Figure 7 : tRNAs and 30S movements during translocation.....</b>	<b>43</b>
<b>Figure 8 : Antibiotics target sites during bacterial protein synthesis.....</b>	<b>47</b>
<b>Figure 9 : Toeprinting, Inverse toeprinting and ribosome profiling overviews .....</b>	<b>57</b>
<b>Figure 10 : Overview of the inverse toeprinting procedure .....</b>	<b>59</b>
<b>Figure 11 : Overview of the cryoEM procedure.....</b>	<b>61</b>
<b>Figure 12 : Structures of erythromycin, clarithromycin and telithromycin .....</b>	<b>64</b>
<b>Figure 13 : Schematic representation of the binding site of erythromycin or telithromycin within the exit tunnel of the ribosome .....</b>	<b>66</b>
<b>Figure 14 : Antibiotic targets and antibiotic resistance mechanisms.....</b>	<b>69</b>
<b>Figure 15 : Macrolide-inducible resistance mechanism of erm genes.....</b>	<b>70</b>
<b>Figure 16 : Single-codon and 7/10 double codons mutants ermCL libraries. Single codon and 6/9 double codons mutants ermAL1 libraries .....</b>	<b>78</b>
<b>Figure 17 : Inverse toeprints repartition for ermCL and ermAL1 mutant libraries translated in presence of erythromycin.....</b>	<b>84</b>
<b>Figure 18 : Histograms of score distribution furnished by Enrich2 for both ermCL and ermAL1 mutant variant libraries translated in presence of erythromycin.....</b>	<b>85</b>
<b>Figure 19 : Sequence-function map of the ErmCL and ErmAL1 peptides translated in the presence of erythromycin .....</b>	<b>86</b>
<b>Figure 20 : Sequence-function map furnished by Enrich2.....</b>	<b>87</b>
<b>Figure 21 : Double mutants score correlation plot.....</b>	<b>88</b>
<b>Figure 22 : Histograms of score distribution furnished by Enrich2 corresponding to ErmAL1 stalling on codon 9.....</b>	<b>89</b>
<b>Figure 23 : Sequence-function analysis of the ErmAL1 erythromycin-dependent arrest on codon 9.....</b>	<b>91</b>
<b>Figure 24 : Organization of the ermA operon and structure of the ermA regulatory region .....</b>	<b>94</b>

<b>Figure 25 : Antibiotics tested by inverse toeprinting .....</b>	<b>103</b>
<b>Figure 26 : DNA template used for inverse toeprinting .....</b>	<b>105</b>
<b>Figure 27 : Examples of inverse toeprinting data using the results of the NNN15 library translated in presence of capreomycin .....</b>	<b>106</b>
<b>Figure 28 : Chemical structures of Elloramycin, Tetracenomycin C and Tetracenomycin X. ....</b>	<b>115</b>
<b>Figure 29 : Pactamycin binding site .....</b>	<b>117</b>
<b>Figure 30 : Structure of pactamycin and size distribution of inverse toeprints .....</b>	<b>118</b>
<b>Figure 31 : Nucleotides enrichments scores obtained in presence of pactamycin.....</b>	<b>119</b>
<b>Figure 32 : Toeprinting analysis of E. coli ribosomes translating an mRNA template encoding for the “CAP” motif in presence of pactamycin. ....</b>	<b>120</b>



## List of Tables

<b>Table 1 : The WHO list of most threatening pathogens for human health (2017).....</b>	<b>26</b>
<b>Table 2 : Leader peptides of macrolide resistance operons .....</b>	<b>72</b>
<b>Table 3 : Antibiotics tested by inverse toeprinting, their binding site and the molecular mechanism they target .....</b>	<b>104</b>
<b>Table 4 : Three generations of tetracycline antibiotics, their structure and clinical use .....</b>	<b>113</b>
<b>Table 5: Summary of reads processing .....</b>	<b>118</b>
<b>Table 6 : Reaction mixture of toeprinting reactions .....</b>	<b>126</b>
<b>Table 7 : Program for sequencing reaction .....</b>	<b>127</b>
<b>Table 8 : Gel mix for sequencing PAGE .....</b>	<b>128</b>
<b>Supplementary Table 1 : List of oligos, section 3.3.2 .....</b>	<b>153</b>
<b>Supplementary Table 2 : List of oligos, section 4.2.4 .....</b>	<b>156</b>

## Abbreviations

**Δ** - Deletion

**(-)** - Negatively charged amino acid

**(+)** - Positively charged amino acid

**2D** - Two dimensional

**3D** - Three dimensional

**A** - Adenine

**Ala/A** -Alanine

**Arg/R** - Arginine

**A-site** - Aminoacyl-tRNA binding site

**ASF** – A-Site Finger

**Asp/D** - Aspartic acid

**Asp/N** - Asparagine

**ATP** - Adenosine triphosphate

**bp** - Base pair

**C** – Cytosine

**Cap** – capreomycin

**cDNA** – Complementary DNA

**CryoEM** - Cryo-electron microscopy

**CTP** - Cytidine triphosphate

**Cys/C** - Cysteine

**DNA** - Deoxyribonucleic acid

***E. coli*** - *Escherichia coli*

**EF-G** – Elongation Factor G

**EF-Tu** - Elongation Factor Thermo-unstable

**EM** - Electron microscopy

***erm*** - *erythromycin resistance methylase*

**Ery** - Erythromycin

**E-site** – Exit, deaminoacyl tRNA binding site

**fMet-tRNA<sub>i</sub><sup>Met</sup>** - formyl-methionyl-initiator tRNA

**G** – Guanine

**GAC** - GTPase Activating Center  
**GDP** - Guanosine diphosphate  
**Gln/Q** - Glutamine  
**Glu/E** - Glutamic acid  
**Gly/G** - Glycine  
**GTP** - Guanosine triphosphate  
**GTPase** - Guanosine triphosphatase  
**HEPES** - 4-(2-hydroxyethyl)-1- piperazineethanesulfonic acid  
**His/H** - Histidine  
**IF** - Initiation Factor  
**Ile/I** - Isoleucine  
**Kd** - Equilibrium dissociation constant  
**kobs** - Observed association rate  
**koff** - Dissociation rate constant  
**KOH** - Potassium hydroxyde  
**kon** – Association rate constant  
**Leu/L** - Leucine  
**Lys/K** - Lysine  
**MDa** - Mega Dalton  
**Met/M** - Methionine  
**mRNA** - Messenger RNA  
**NGS** - Next Generation Sequencing  
**Nt** - Nucleotide  
**OD600** - Optical density at 600 nm  
**OH** - hydroxyl  
**ORF** - Open reading frame  
**Pac** – Pactamycin  
**PDB** - Protein Data Bank  
**Phe/F** - Phenylalanine  
**PHENIX** - Python-based Hierarchical ENvironment for Integrated Xtallography  
**Pro/P** - Proline  
**P-site** - Peptidyl-tRNA binding site  
**PTC** - Peptidyl transferase center

**RBS** - Ribosome binding site  
**RELION** - REgularised LIkelihood Optimisation  
**RF** - Release Factor  
**RNA**- Ribonucleic acid  
**RNase** - Ribonuclease  
**RRF** - Ribosome recycling factor  
**rRNA** - Ribosomal RNA  
**S** - Svedberg  
**SD** - Shine Dalgarno  
**Ser/S** - Serine  
**SRL** - Sarcin-ricin loop  
**T** - Thymine  
***T. thermophilus*** - *Thermus thermophilus*  
**Tel** – Telithromycin  
**TcmX** – Tetracenomycin X  
**Thr/T** – Threonine  
**tRNA** – Transfer RNA  
**Trp/W** - Tryptophan  
**Tyr/Y** - Tyrosine  
**U** - Uracil  
**uORF** - upstream ORF  
**UTP** - Uridine triphosphate  
**UTR**- Untranslated region  
**Val/V** - Valine  
**Vio** – Viomycin  
**WHO** – World Health Organization  
**WT** - Wild-type  
**X** - Any amino acid  
**X-gal** - 5-bromo-4-chloro-3-indolyl- $\beta$ -D- galactopyranoside

## Part I: General introduction

### 1.1. Antibiotics and the global emergence of drug resistance

The discovery of antibiotics was a major advance in the medical field which allowed to save millions of lives from bacterial diseases (tuberculosis, pneumoniae, the plague, septicemia...), as reviewed by (Aminov, 2010; Durand et al., 2019; Hutchings et al., 2019). Antibiotics are natural or synthetic compounds which specifically target bacteria by impeding their growth or killing them. They can be found in plant or mold extracts which have been used since the earliest civilizations to treat infections (Haas, 1999). Until the 20<sup>th</sup> century, infections that we now consider easy to treat (diarrhea, bacterial skin infections etc.) were the leading cause of human death. For example, during the 14<sup>th</sup> century, the black plague decimated 25% to 50% of the European population and claimed seven million victims in France alone, out of a population of 17 million. Today, thanks to antibiotics, the pathogen responsible for the black plague (*Yersinia pestis*) has been nearly eradicated.

#### The Golden Era of antibiotics discovery

In the 1930's, the Ukrainian-American biochemist Selman Waksman studied the process of degradation of the tuberculosis' bacillus in soils, in order to find a cure. Tuberculosis, also defined as the “white plague”, was at the time one of the most dangerous diseases, responsible for the death of a quarter of the adult population in Europe during the 19<sup>th</sup> century. By studying the micro-organisms present in soils, he discovered a bacterium able to fight tuberculosis, namely *Streptomyces griseus*. With his colleague Albert Schatz, they extracted the first antibiotic used to treat tuberculosis from *Streptomyces griseus*; streptomycin (**Figure 1**). Selman Waksman received the Nobel Prize in 1952 for his work on streptomycin, which became the first specific marketed agent effective in the treatment of tuberculosis (Waters and Tadi, 2021). Waksman was also the first to employ the word “antibiotic” and during his lifetime, he and his team discovered about 20 effective antibiotics, including neomycin, used to fight intestinal bacterial overgrowth (Waksman and Lechevalier, 1949). The discovery of streptomycin illustrates the beginning of the period we call “the Golden Age” of antibiotic discovery (**Figure 1**) (Aminov, 2010; Hutchings et al., 2019).

Among the major discoveries made during the Golden Age, tetracycline antibiotics were discovered by Benjamin Minge Duggar in 1945 and reported in the scientific literature in 1948 as broad-spectrum natural antibiotics produced from actinomycetes soil bacteria. They were commercialized with clinical success in the late 1940s to the early 1950s (Grossman, 2016;

Nguyen et al., 2014). (Fun fact: Nubian mummies studied in the 1990s were found to contain significant levels of tetracycline coming from the beer brewed at the time (Bassett et al., 1980). Who said beer wasn't healthy?). The 1950s and the 1960s offered a diversity of antibiotic compounds

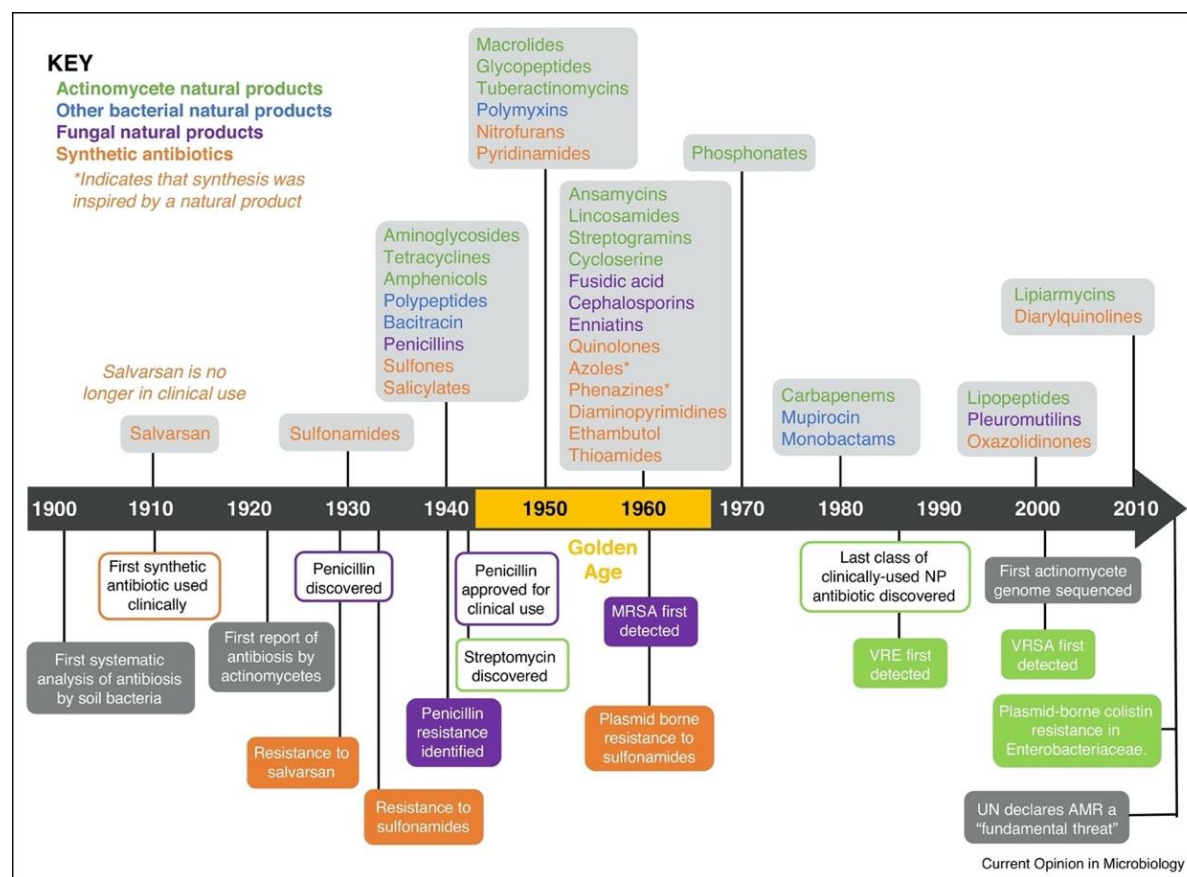


**Figure 1 : Timeline showing the decade new classes of antibiotic reached the clinic**

The antibiotics are colored per their source: green = actinomycetes, blue = other bacteria, purple = fungi and orange = synthetic. At the bottom of the timeline are key dates relating to antibiotic discovery and antimicrobial resistance, including the first reports of drug resistant strains methicillin-resistant *Staphylococcus aureus* (MRSA), vancomycin-resistant enterococci (VRE), vancomycin-resistant *Staphylococcus aureus* (VRSA) and plasmid-borne colistin resistance in Enterobacteriaceae. From (Hutchings et al., 2019).

which were then chemically optimized for pharmaceutical purposes and conducted to the marketing of numerous derivatives of these compounds. A famous example is erythromycin, first isolated in 1952 by J.M. McGuire from the bacteria *Saccharopolyspora erythraea* (McGUIRE et al., 1952), which became the first macrolide ever marketed (Dinos, 2017; Vázquez-Laslop and Mankin, 2018a). Erythromycin rapidly substituted penicillin in cases where the latter caused allergy or resistance, and led to the development of semi- or fully-synthetic classes of macrolides antibiotics, some of which are still used in human medicine (see

1.2.3.2). A second example is the discovery of nalidixic acid, a quinolone antibiotic isolated in 1962 by George Leshner, first used to treat urinary tract infections (Emmerson and Jones, 2003). Since the introduction of nalidixic acid, four generations of quinolones derivatives, including fluoroquinolones in the 1980s were developed and largely used to treat tuberculosis, including resistant-strains (Jia and Zhao, 2021).

The Golden Age of antibiotic discovery provided molecules that are still in clinical use today but whose effectiveness is increasingly threatened by multidrug-resistant pathogens (**Figure 1**). The rapid discovery of multiple classes of antibiotics during a relatively short period led to the excessive use of these drugs (Levy and Marshall, 2004). Additionally, the dramatic slowdown in antibiotic discovery since the 1970s strongly favored the appearance of new resistant strains (**Figure 1**).

PRIORITY		
MEDIUM	HIGH	CRITICAL
<i>Streptococcus pneumoniae</i>	<i>Enterococcus faecium</i>	<i>Mycobacteria (Mycobacterium tuberculosis)</i>
<i>Haemophilus influenzae</i>	<i>Staphylococcus aureus</i>	<i>Acinetobacter baumannii</i>
<i>Shigella spp.</i>	<i>Helicobacter pylori</i>	<i>Pseudomonas aeruginosa</i>
	<i>Campylobacter spp.</i>	<i>Enterobacteriaceae, (Klebsiella pneumonia,</i>
	<i>Salmonellae</i>	<i>Escherichia coli, Enterobacter spp., Serratia</i>
	<i>Neisseria gonorrhoeae</i>	<i>spp., Proteus spp., and Providencia spp,</i>
		<i>Morganella spp.)</i>

**Table 1 : The WHO list of most threatening pathogens for human health (2017)**

Pathogens are classified in a list of antibiotic-resistant “priority pathogens”, a catalogue of 12 families of bacteria that pose the greatest threat to human health. The list was drawn up to guide and promote research and development of new antibiotics, as part of WHO’s efforts to address growing global resistance to antimicrobial medicines. The WHO list is divided into three categories according to the urgency of need for new antibiotics: critical, high and medium priority. The most critical group of all includes multidrug resistant bacteria that pose a particular threat in hospitals, nursing homes, and among patients whose care requires devices such as ventilators and blood catheters. These bacteria have become resistant to a large number of antibiotics, including carbapenems and third generation cephalosporins – the best available antibiotics for treating multi-drug resistant bacteria. The second and third tiers in the list – the high and medium priority categories – contain other increasingly drug-resistant bacteria that cause more common diseases. The bacteria colored in red represent the six members of the ESKAPE pathogens group. WHO, <https://www.who.int/news-room/detail/27-02-2017-who-publishes-list-of-bacteria-for-which-new-antibiotics-are-urgently-needed>



By definition, bacterial resistance is the capacity of bacteria to survive the effects of antibiotic molecules that are designed to kill or hinder their ability to grow and replicate. To address this developing threat and guide the discovery and development of new antibiotics, the WHO classified resistant pathogens according to the level of threat they pose to human health (**Table 1**). They describe three categories of pathogens namely critical, high and medium priority, according to the urgency of need for new antibiotics. The list includes the six members of the ESKAPE group, namely *Enterococcus faecium*, *Staphylococcus aureus*, *Klebsiella pneumoniae*, *Acinetobacter baumannii*, *Pseudomonas aeruginosa*, and *Enterobacter spp.* ESKAPE pathogens are responsible for a majority of nosocomial infections and are capable of escaping the action of antibiotics (Mulani et al., 2019; Navidinia, 2016; Rice, 2008).

### Antibiotics decline

At the beginning of the 1970s, research on antibiotics slowed down sharply, as the therapeutic arsenal of the time made it possible to effectively treat most bacterial infections (Gould, 2016; Hutchings et al., 2019). Globally, in half a century and in combination with the development of vaccination, antibiotics have been largely responsible for eliminating major epidemic diseases in developed countries, as vaccination also reduces the propagation of antibiotic resistance strains (Klugman and Black, 2018). There are, however, additional reasons leading to the decrease in the development of new antibiotics.

First, it is scientifically very difficult to develop an antibiotic for medicinal purposes (Levy and Marshall, 2004); indeed, once in the body, the drug needs to be highly specific for its target, but also stable in the human body, and active at a concentration which is not toxic for the patient (Hughes and Karlén, 2014). Besides, bacteria have selected multiple resistance mechanisms to survive, and can degrade the antibiotic molecules or expel them from the cytoplasm using efflux pumps (Levy and Marshall, 2004; Wilson, 2014).

Secondly, most antibiotics are natural molecules found in soil microbes, already evolutionary developed and optimized to act as communication metabolites or antimicrobials (Embley and Stackebrandt, 1994; Klassen, 2014; Seipke et al., 2012; Traxler and Kolter, 2015). Unfortunately, many soil microbes are difficult to grow in a laboratory (Chaudhary et al., 2019), reducing the number and the diversity of organisms from which natural antibiotics can be isolated (Nichols et al., 2010). These limitations lead to the persistent rediscovery of already known compounds and hinder the detection of new natural antimicrobial molecules.

Finally, there are also economic reasons that explain the decrease in number of drugs entering the antibiotic market (Wouters et al., 2020): developing an antibiotic is an expensive process that can span approximately a decade. Each new formulation needs to go through rigorous testing for activity and patient safety, and only a minority of tested compounds will actually make it through the whole drug-development process (Dijksteel et al., 2021). Resistance development, on the other hand can be fast (**Figure 1**), rendering the drug quickly inefficient, and resulting in low profits for the developing company (Hutchings et al., 2019; Miethke et al., 2021). In addition, novel antibiotics would have to be used with parsimony to avoid resistance development. Poor financial incentives and technical difficulties accompanied by an unsuccessful investment in numerous high-throughput screening programs, have led many pharmaceutical companies to scale-down or abandon their antibiotic development programs (Miethke et al., 2021).

Despite the difficulties underlying the antibiotic marketing process, the emergence of greater resistance against the Golden Era compounds stimulated the resumption of antibiotic discovery process (**Figure 1**). In 2000, the antibiotic linezolid from the oxazolidinone family of compounds, was approved by the FDA in 2000 and was commercialized in the United States (**Figure 1**) (Zhao et al., 2021). It was the first time in 20 years that a new class of antibiotic compounds had been introduced into the market. In December 2018, around 45 new antibiotics were candidates in clinical trials for the US market, illustrating the restart of antibiotic research (Hutchings et al., 2019). Among them, 28 belonged to known natural product classes and 17 to synthetic compounds. Most of the natural products were variants of beta-lactams, tetracyclines, aminoglycosides, or macrolides. Only two of the molecules accepted in Phase III clinical trials were synthetic compounds displaying a novel type of antimicrobial activity: the first one, ridinilazole, specifically blocks cell division in *Clostridium difficile* through a mechanism that has not been identified yet (Collins et al., 2021); and the second one, murepavedin, has a novel mechanism of action and inhibits the LPS-assembly protein precursor LptD, thereby blocking the lipopolysaccharide transport to the bacterial outer membrane (Srinivas et al., 2010). More interestingly, murepavidin is effective against the antibiotic-resistant pathogen *Pseudomonas aeruginosa* (Srinivas et al., 2010). It is therefore encouraging to observe that new categories of molecules have been discovered and are currently being tested under clinical trials conditions. However, considering the effective rate of molecules accepted after these trials for clinical purposes, and the increasing number of multidrug-resistant pathogens, this is still insufficient

to face the most threatening pathogens; therefore, new antimicrobial technologies are needed and/or our current arsenal of antibiotics needs to be redesigned.

A possible solution is to look at the arsenal of natural molecules already at our disposal in order to (i) develop improved versions of existing drugs by better understanding their mechanisms of action, or (ii) characterize whether less studied molecules have the potential to become useful antibiotics. Our antibiotics target a variety of biological processes inside bacterial cells, which can broadly be classified as follows (as reviewed in (Kohanski et al., 2010)):

- **The cell wall or membranes surrounding the bacterial cell.** Penicillin targets the synthesis of peptidoglycans of the cell wall
- **The machineries responsible for the production/folding of nucleic acids (DNA and RNA).** Quinolones target DNA gyrase and topoisomerases II and IV, preventing bacterial DNA replication.
- **The machinery responsible of protein production (the ribosome and associated proteins).** Streptomycin binds to the bacterial ribosome and inhibits protein production.

These targets are either absent or different in eukaryotic cells, making antibiotics theoretically harmless for the host. Currently, more than half of the antibiotics of our arsenal (streptomycin, tetracycline, erythromycin, linezolid ...) target protein synthesis by binding to the bacterial ribosome, as reviewed by (Wilson, 2014). Protein synthesis is consequently a large platform for the development of antibiotics resistance by bacteria. Therefore, I focused my PhD work on antibiotics which bind and inhibit the functioning of the bacterial ribosome, the machinery responsible of protein synthesis within the cell, and worked on the mechanism of resistance of few of them. In order to understand the mechanistic aspects of antibiotics action, it is necessary to be familiar with the function of the ribosome. Thus, in the next section, I will describe how bacterial translation occurs under physiological conditions.

## 1.2. Bacterial protein synthesis as a major antibiotic target

### 1.2.1. The bacterial ribosome

Ribosomes are large macromolecular complexes of 2.5 MDa composed of RNA and proteins, responsible for translation of messenger RNA (mRNA) into proteins helped by the presence of transfer RNAs (tRNAs) that are adaptor molecules ensuring the proper connection between the mRNA codon and the amino acid of proteins. In bacteria, ribosomes are referred as 70S particles, which corresponds to the sedimentation velocity of ribosomes. The ribosome is composed of two individual subunits, commonly referred to as 30S and 50S subunits and is composed of approximately 35% protein and 65% rRNA. The small, 30S, subunit contains a single ribosomal RNA (rRNA) molecule of approximately 1,500 nucleotides (16S rRNA) and 21 proteins. The large, 50S, subunit contains two rRNA molecules totaling approximately 3,000 nucleotides (120 for the 5S rRNA and 2,900 for the 23S rRNA) as well as approximately 36 proteins. Most of the reactions are performed by the rRNAs, but additional ribosomal proteins and protein factors are needed to increase the processivity of the translational cycle (Schmeing and Ramakrishnan, 2009a).

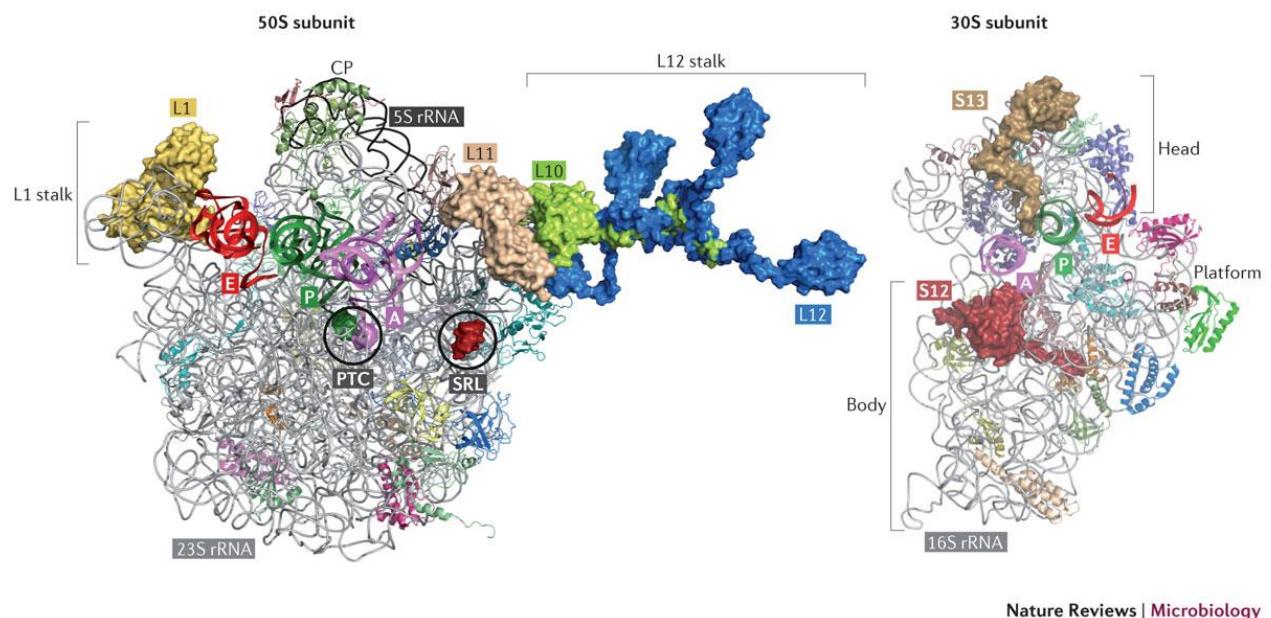


**Figure 2 : Schematic overview of the bacterial 70S ribosome**

Both subunits are shown from the interface side. The large 50S subunit contains the 23S ribosomal RNA (rRNA) and 5S rRNA (light grey and dark grey, respectively), and the small 30S subunit is composed of the 16S rRNA (light grey). Ribosomal proteins are represented as colored ribbons, and those that have specific roles in translocation, as well as the sarcin-ricin loop (SRL) of the 23S rRNA and the acceptor ends of A- and P-site tRNAs within the peptidyl-transferase center (PTC), are highlighted by surface representation. The A-site, P-site and E-site tRNAs are also shown. For clarity, only the

anticodon stem-loops of the tRNAs are shown on the 30S subunit. CP, central protuberance. From (Yamamoto et al., 2014).

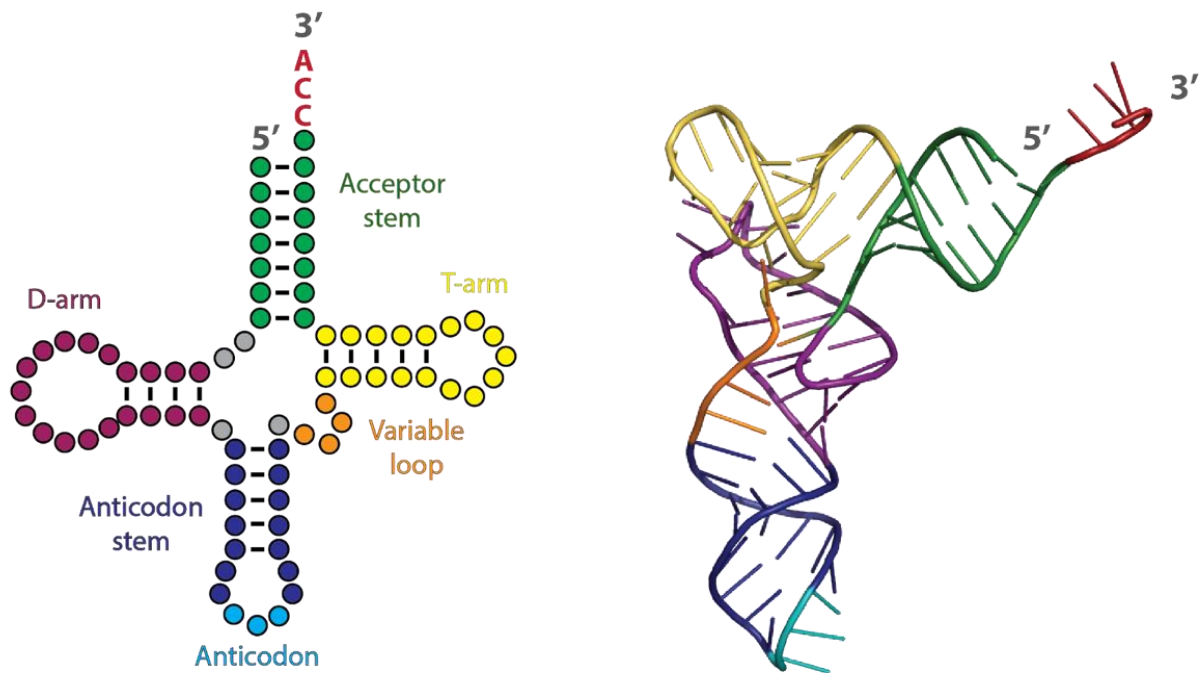


**Figure 3 : Schematic and three-dimensional tRNA representations**

Two-dimensional representation of the tRNA structure (left) and three-dimensional representation in cartoon (right) following same the color-code.

The small 30S subunit (**Figure 2**) is mainly responsible for decoding the mRNA template and therefore manages the interactions with the anticodon stem-loop regions of ribosome-associated transfer RNA molecules within a site called the decoding center (Ogle et al., 2003; Wimberly et al., 2000). The ribosome has three distinct binding positions for tRNAs: the aminoacyl-site (A site) is the binding site for the aminoacylated tRNA; the peptidyl-site (P site) is the position in which the tRNA is connected to the nascent chain; and the exit site (E site) is the position from which the deacylated tRNA is released (Agrawal and Burma, 1996).

The large 50S ribosomal subunit (**Figure 2**) is responsible for the catalysis of peptide bond formation, an enzymatic activity that covalently links amino acids carried by adjacently bound tRNA substrates into a polypeptide chain. Peptide bond formation on the large subunit occurs within the peptidyl-transferase center (PTC) (Maden et al., 1968; Monro, 1967; Traut and Monro, 1964). This site contains highly conserved rRNA bases which form base-pairing interactions with the universally conserved 3'-CCA ends located at the acceptor stem region of

tRNA substrates (**Figure 3**). The large subunit also contains the GTPase activating center that triggers GTP hydrolysis within the ribosome-associated translation factors including elongation factors (EF)-Tu and (EF)-G, initiation factor (IF)-2, as well as release factor (RF)-3 in *E. coli* (Schmeing and Ramakrishnan, 2009a). Another key element of the 50S subunit is the nascent polypeptide exit tunnel, through which nascent proteins must travel on their way out of the ribosomal complex. In some cases, the exit tunnel can interact with nascent peptides, resulting in translational arrest. Peptide-induced ribosome stalling is a natural phenomenon involved in the regulation of the cellular metabolism, but can also occur in the presence of antibiotics bound within the exit tunnel of the ribosome (Ito and Chiba, 2013; Seip and Innis, 2016; Wilson, 2014).

### **1.2.2. The bacterial translation cycle**

Protein synthesis can be divided into four phases (**Figure 4**) (Rodnina, 2018; Schmeing and Ramakrishnan, 2009a):

1. The initiation step, where the ribosomal complex is assembled on a start codon of the mRNA. This is the rate-limiting step of the translation cycle.
2. The elongation process, where the ribosome translates the mRNA to form the peptide bond between the nascent protein and the incoming amino-acyl tRNA. From the PTC, the nascent peptide chain passes through the exit tunnel to reach the cytoplasm. Once peptide bond formation occurred, the deacyl- and peptidyl- tRNAs move with the mRNA from one mRNA codon relative to the ribosome position through a process called translocation, and allowed by successive movements of the ribosome and the GTPase activity of Elongation Factor-G.
3. The termination and recycling steps; once the ribosome reaches the stop codon, the complex is disassembled and recycled

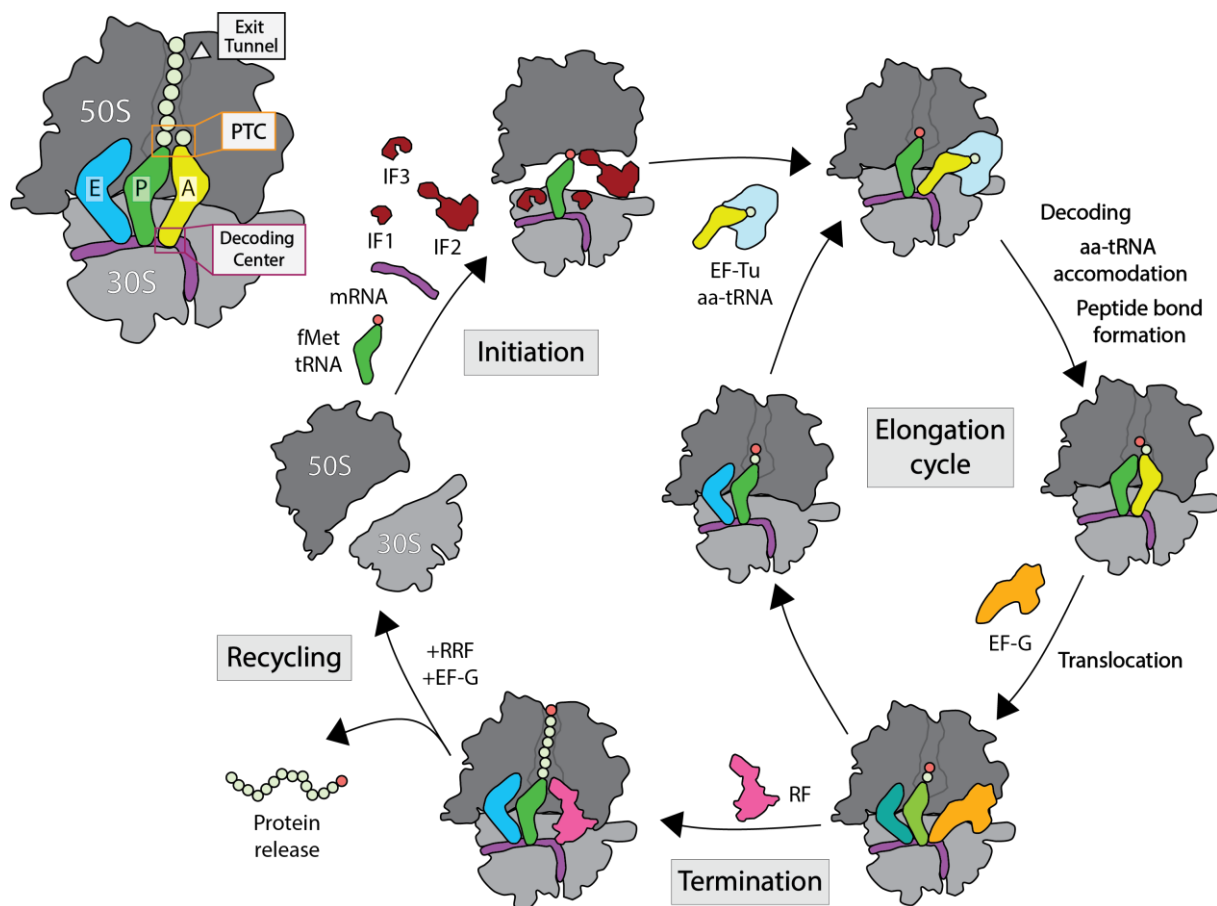


**Figure 4 : Schematic overview of the prokaryotic translation cycle**

The bacterial translation cycle can be divided into four phases: initiation, elongation, termination and recycling. The 30S subunit is represented in light grey and the 50S subunit in grey. The transfer RNAs (tRNAs) can be located in the E- (cyan), P- (green) and A- (yellow) sites of the ribosome. PTC = Peptidyl Transferase Center; IF = Initiation Factor; fMet tRNA = formyl methionine tRNA; mRNA = messenger RNA; EF-Tu = Elongation Factor – Thermo unstable; aa-tRNA = aminoacyl tRNA; EF-G = Elongation Factor-G; RF = Release Factor; RRF = Ribosome Recycling Factor.

#### 1.2.2.1. Initiation

The initiation step of translation allows the recruitment and assembly of the two ribosomal subunits and the initiator transfer RNA (tRNA) on a start codon of the mRNA (Laursen et al., 2005). The start codon corresponds to the methionine codon AUG. In the case of prokaryotic initiation, the initiator tRNA (tRNA<sub>i</sub>) is slightly different from the other tRNAs and is the only one responsible for initiation; indeed, the tRNA<sub>i</sub> is specific to the formyl-methionine group. Therefore, the tRNA<sub>i</sub> is referred as tRNA-fMet for tRNA formyl-methionine. To be used during the initiation step of translation, the methionine first needs to be attached to the CCA 3' end of the tRNA-fMet by methionyl-tRNA synthetase and formylated on its  $\alpha$ -amine by methionyl-

tRNA formyltransferase (fMet-tRNA<sup>Met</sup><sub>i</sub>). Co-translationally on the ribosome, the formyl-methionine residue will be eliminated from most of proteins by peptide deformylase which removes the formyl group and methionine aminopeptidase which cleaves the N-terminal methionine residue from the protein (Sherman et al., 1985). Importantly, formylation of elongator Met-tRNA<sup>Met</sup> does not take place because initiator tRNA<sup>Met</sup><sub>i</sub> has a sequence different from that of the elongator tRNA-Met (Barraud et al., 2008; Mayer et al., 2001; Schmitt et al., 1998), which results in a mismatch between nucleotides C1 and A72 that are critical for efficient formylation. This formylation is also a positive determinant for the binding of the initiation factor protein IF2, whereas it is a negative one for the binding of Elongation Factor – Thermo-unstable (EF-Tu), therefore limiting fMet-tRNA<sup>Met</sup><sub>i</sub> to the initiation step. The anticodon stem loop of tRNA<sup>Met</sup><sub>i</sub> also contains a series of G-C base pairs, providing a higher rigidity and affinity for the P-site, resulting in an efficient initiation of translation in the cell.

### *Initiation on mRNAs containing a Shine Dalgarno leader sequence*

At the 5' end of the open reading frame (ORF), upstream from the start codon, some mRNAs contain a six to seven nucleotides-long ribosomal binding site (RBS) known as the Shine-Dalgarno (SD) sequence (Ringquist et al., 1992; Shine and Dalgarno, 1974). The 3' end of the 16S rRNA in the small ribosomal subunit contains an anti-SD sequence that can base pair with this region, allowing the correct positioning of the small subunit on the mRNA (Shine and Dalgarno, 1974). During initiation, three initiation factors (IF1, 2, 3) ensure the correct assembly of the ribosome on the mRNA (Laursen et al., 2005). Initiation factor 3 (IF3) binds then to the E-site of the ribosome and prevents premature binding of the 50S subunit (Dallas and Noller, 2001; Karimi et al., 1999; Shine and Dalgarno, 1974). IF3 also ensures the fidelity of fMet-tRNA<sup>Met</sup><sub>i</sub> selection over the elongator aminoacyl-tRNAs (aa-tRNAs), and helps to discriminate against mRNAs with unfavorable translation initiation regions (Duval et al., 2015; Gualerzi and Pon, 2015; Milón and Rodnina, 2012). Similarly, IF1 binds to the A site and prevents premature association of aminoacyl tRNA (Antoun et al., 2006a, 2006b). IF2 is a GTPase that binds on IF1 in the A site and which recognizes the initiator fMet-tRNA<sup>Met</sup><sub>i</sub> to place it into the P-site (Antoun et al., 2003). Within the P site of the ribosome, the tRNA-fMet anticodon stem loop forms three Watson–Crick base pairs with the mRNA codon within the small subunit-decoding region to form the pre-initiation complex. The correct annealing of the initiator tRNA establishes the reading frame of protein synthesis and is therefore a key determinant of the overall fidelity of translation. After proper binding of the initiator tRNA, IF1



and IF3 are released from the 30S subunit after GTP hydrolysis on IF2, allowing the recruitment of the 50S subunit and the release of IF2 to start the elongation process (**Figure 5**) (Simonetti et al., 2013).

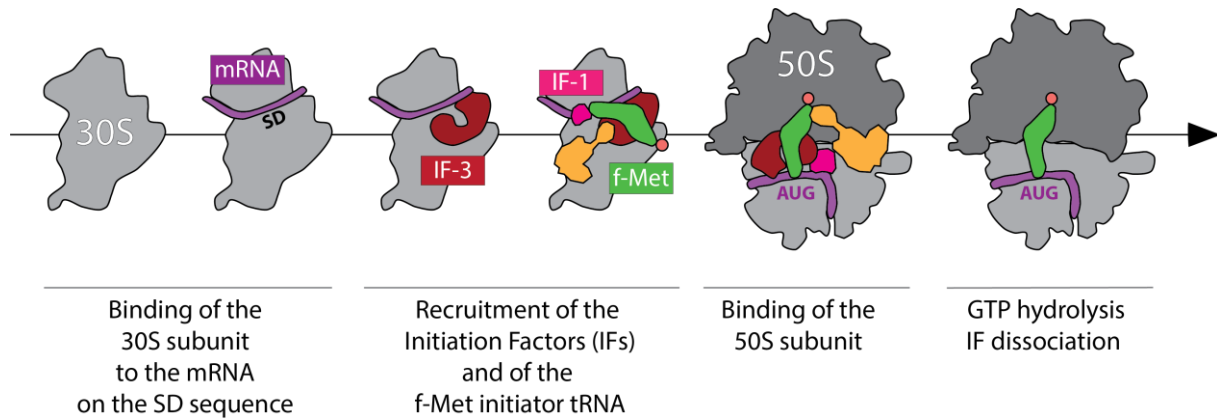


### Figure 5 : Overview of the initiation step on an SD-containing mRNA

The annealing of the 30S subunit on the SD sequence of the mRNA allows the recruitment of the initiation factors to properly position the initiator tRNA and ends with the assembly through GTP hydrolysis of the 50S subunit and the departure of the initiation factors.

### *Initiation on non-Shine Dalgarno or leaderless mRNAs*

Among the different types of mRNAs found in prokaryotes, mRNAs containing SD-leader (SD-led) sequence are particularly well studied. However, in bacteria and archaea, not all mRNAs contain an SD sequence (Chang et al., 2006; Tolstrup et al., 2000; Weiner et al., 2000). Among fully-sequenced prokaryotic genomes, the number of SD-led genes varies from ~12% to 90%, suggesting a significant number of non-SD-led or leaderless mRNAs (Chang et al., 2006). Very little is known about initiation on non-SD-led mRNAs except that the 5' UTR is usually unfolded and the AUG start codon resides in a single-stranded mRNA region close to the 5' end of the mRNA (Krishnan et al., 2010; Scharff et al., 2011). Additionally, recent data have shown that the context of the start codon is important, and that the SD sequence only affects the level of expression (Saito et al., 2020). The other group of non-SD-led mRNAs comprises leaderless mRNAs that lack a 5' UTR. Such mRNAs are widespread in a variety of bacteria and may play an important role in regulating the stress response (Grill et al., 2000; Vesper et al., 2011). These leaderless mRNAs can bind to 70S ribosomes directly and the recruitment of fMet-tRNA<sub>i</sub><sup>Met</sup> is facilitated by IF2 and IF3 (Grill et al., 2000; Sprink et al., 2016). While IF2 can bind to either the 30S subunit or 70S ribosome (Goyal et al., 2015), IF3 must move from

its binding site on the 30S subunit to allow formation of the 70S ribosome, thus promoting the dissociation into subunits, which allows translation initiation to occur.

#### *1.2.2.2. Elongation*

Elongation corresponds to the protein synthesis phase of translation (**Figure 6**) (Rodnina, 2018; Schmeing and Ramakrishnan, 2009a). The incorporation of one amino acid to the nascent protein can be described as an independent cycle, involving three major steps. First, an aminoacylated-tRNA is delivered to the A site of the ribosome by elongation factor Tu (EF-Tu) in complex with GTP. During the process of decoding, the ribosome monitors the base-pairing interaction between the mRNA codon and the tRNA anticodon in the A site, ensuring that only tRNAs bearing the correct amino acid are accommodated. Secondly, once the cognate tRNA is bound, peptide bond formation occurs between the aminoacyl moiety of the A-site tRNA and the peptidyl tRNA in the P site, resulting in transfer of the nascent peptide from the P-site tRNA to the A-site one. Finally, to allow the ribosome to proceed to the next amino acid incorporation, a directional translocation of the two bound tRNAs and the mRNA from the A and P sites to the P and E sites occurs with the help of Elongation Factor G (EF-G) to liberate the A-site and start a new cycle of elongation (**Figure 6**).

#### *Aminoacyl-tRNA accommodation and mRNA decoding*

The ribosome lacks a proofreading capacity rendering the mechanism of tRNA selection critical in maintaining the corresponding fidelity between the mRNA ORF and the protein sequence. As for initiation, the process of aa-tRNA selection is driven by Watson–Crick base-pairing interactions between the tRNA anticodon and the mRNA codon and is a key determinant of translational fidelity. The genetic code contains 64 possible codon combinations for only 20 amino acids and two type I release factors. Consequently, multiple codons can encode the same amino acid. To reduce the number of tRNAs within the cell, only the first two bases of the codon form Watson-Crick base pairs with the mRNA while the third base can form in some cases wobble base pairs instead of standard Watson-Crick pairs (Giegé et al., 1973). The presence of modified bases within the tRNA sequences influences the ability of the cognate tRNA to decode the mRNA codon (Agris, 2004, 2008). Other modifications at key positions of the tRNA facilitate the translocation process and ensure the maintenance of the correct reading frame by reducing the internal dynamics of the tRNA molecule, notably those presenting important A-U contents in their anticodon stem loop (Agris, 2004, 2008). Aminoacylated-

tRNAs are recognized through their acceptor stem by the Elongation Factor Thermo-unstable (EF-Tu) in its GTP bound form (**Figure 6**) (Lipmann, 1969; Nissen et al., 1995). The aminoacylated-tRNA in complex with EF-Tu is then recruited through the bL12 stalk of the ribosome to position the tRNA in the A-site, thus allowing the formation of the codon-anticodon interactions with the mRNA (Girshovich et al., 1986). During its accommodation, the A-site tRNA has to go through large conformational changes rendering it the rate-limiting step of peptide bond formation (Pape et al., 1998; Valle et al., 2002).

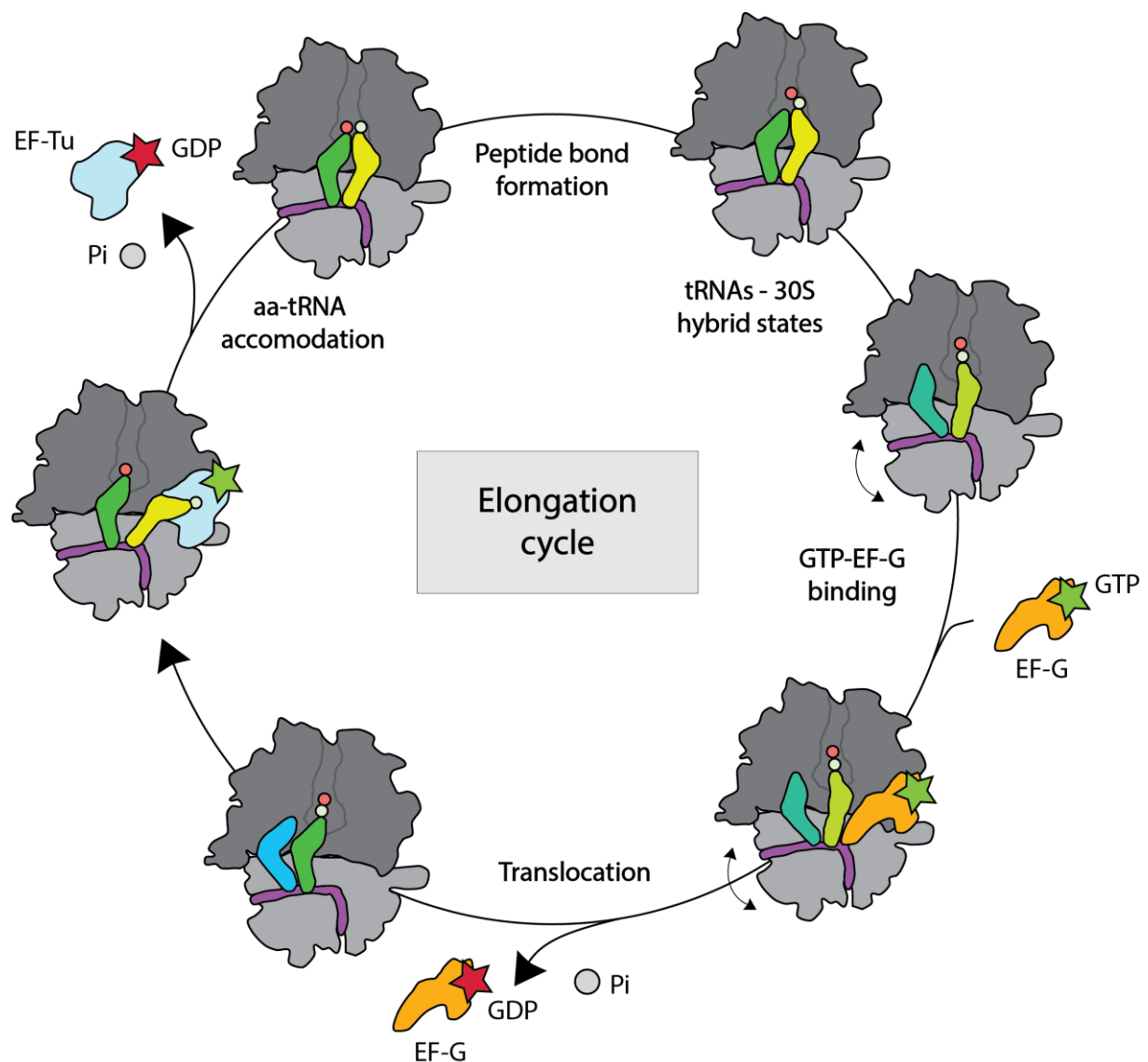


**Figure 6 : Schematic overview of the prokaryotic elongation cycle**

The bacterial elongation cycle can be divided into several phases: first the aminoacyl tRNA is brought to the ribosomal A site by EF-Tu to allow the decoding and the accommodation of the cognate tRNA. Peptide bond formation then occurs within the PTC between the aminoacyl tRNA and the peptidyl tRNA located in the P site. The attachment of the peptide to the A-site tRNA leads to a destabilization of the tRNAs thus adopting hybrid conformations. These hybrid states coupled to movements of the 30S

subunit favor the binding of EF-G which promotes tRNA translocation through GTP hydrolysis, thereby liberating the A site to restart the elongation cycle. The 30S subunit is represented in light grey and the 50S subunit in grey. The transfer RNAs (tRNAs) can be located in the E (cyan), P (green) and A- (yellow) sites of the ribosome. EF-Tu = Elongation Factor – Thermo unstable; aa-tRNA = aminoacyl tRNA; EF-G = Elongation Factor-G; GDP/GTP = guanosine di- or tri- phosphates; Pi = inorganic phosphate.

The correct match between the anticodon of the tRNA and the codon of the mRNA is ensured by the right positioning of the key nucleobases A1493 and A1492 of helix 44 and G530 of the 16S rRNA, which form the decoding center of the ribosome (Ogle et al., 2001). The accommodation of the proper cognate anticodon triggers a conformational change of bases A1493 and A1492 of helix 44 and G530, thereby adopting a flipped-out conformation to interact with and stabilize the first two base pairs of the mRNA-tRNA duplex in the A-site. These conformational changes cause movements within the L7/12 stalk and the GTPase activating centre (GAC) (Ogle et al., 2002). They also cause distortions of the tRNA (Valle et al., 2002) which in turn cause rearrangements of EF-Tu to avoid clashing with the sarcin-ricin loop (Diaconu et al., 2005; Ogle et al., 2003). The rearrangements of EF-Tu activate its GTPase activity to weaken its interactions with tRNA and the ribosome, thus allowing the release of EF-Tu (Voorhees and Ramakrishnan, 2013; Voorhees et al., 2010). GTP hydrolysis by EF-Tu occurs on the ribosome during the selection process, through a mechanism that is allosterically regulated by the nature of the codon–anticodon interaction. Rapid and efficient GTP hydrolysis selectively occurs when the cognate tRNA is recognized through shape-selective elements of the small subunit of the ribosome, that allow the catalytic histidine of EF-Tu to attack the gamma-phosphate of GTP through a water molecule. Subsequent release of inorganic phosphate and dissociation of GDP-bound EF-Tu from the ribosome allows the 3'-CCA end of the aminoacyl-tRNA to enter the Peptidyl Transferase Center.

### Peptide bond formation

Peptide bond formation between the C-terminal amino acid of peptidyl-tRNA and the incoming amino acid takes place within the Peptidyl Transferase Center (PTC), the catalytic site of the ribosome composed primarily of 23S rRNA residues (Ban et al., 2000; Nissen et al., 2000; Noller, 1993; Polikanov et al., 2014a). Within the PTC, the amino acid attached to the 3'-CCA end of the A-site tRNA needs to be well positioned in a particular pocket called the A-site crevice to undergo peptide bond formation. In fact, the correct positioning of the aminoacyl A-site tRNA induces conformational changes within the ribosome, where the PTC switches from

the uninduced state to the induced-state (Schmeing et al., 2005a). In the uninduced state, the ester bond between residue A76 of the P-site tRNA and the last amino acid of the peptide needs to be protected from premature hydrolysis, and is thus shielded by the bases of 23S rRNA residues U2585, A2451, and C2063 (Schmeing et al., 2005b). The accommodation of the aminoacyl-tRNA into the A site triggers conformational changes in the PTC to reach the induced state (Schmeing et al., 2005a). These changes include the pairing of residue C75 from the aminoacyl tRNA with residue G2553 of the 23S rRNA, of residue A76 of the A-site tRNA with residue U2585 of 23S rRNA, stacking of A2602 between the CCA ends of the P-site tRNA and the A-site tRNA, and the shifting of 23S RNA bases U2583, G2584 and A2451 (Kim and Green, 1999; Nissen et al., 2000). These movements favor the nucleophilic attack of the  $\alpha$ -amino group of the aminoacyl-tRNA onto the ester carbonyl carbon of the P-site tRNA by deprotecting the peptidyl-tRNA ester function. In solution, this reaction would occur much slower, but the ribosome acts as a catalyst by enhancing the rate of peptide bond formation by  $10^7$ -fold (Sievers et al., 2004). The reaction of peptide bond formation reaction generates an oxyanion-containing tetrahedral carbon transition state, and its resolution yields the final products, namely a deacylated tRNA within the P site, and a peptidyl-tRNA with a peptide chain elongated by one amino acid within the A site (Rodnina, 2018; Schmeing and Ramakrishnan, 2009a). Prior to this reaction, the nucleophilicity of the aminoacyl-tRNA is enhanced by the deprotonation of the  $\alpha$ -amino group of the A-site amino acid to yield an uncharged amine (Rodnina, 2018; Schmeing and Ramakrishnan, 2009a).

A first attempt to explain how peptide bond occurs on the ribosome was the acid-base reaction model (Nissen et al., 2000). This model was based on a crystal structure of the archaeon *Haloarcula martismortui* 50S subunit in complex with an analog of the tetrahedral intermediate (Nissen et al., 2000). This analog was formed by coupling the 3' OH of the CCdA oligonucleotide to the amino group of the O-methyl tyrosine residue of puromycin via a phosphate group meant to mimic the transition state of peptide bond formation (Welch et al., 1995). This analog binds tightly to the ribosome, and inhibits its peptidyl transferase activity (Welch et al., 1995). According to the proposed model, the protonated third nitrogen atom (N3) of the base of 23S rRNA residue A2451 in *E. coli* (A2486 in the archaeon) would stabilize the carbonyl oxyanion formed during the tetrahedral transition state (Nissen et al., 2000). A2451 is one of the five universally conserved bases located in the PTC (Gregory et al., 2001; Youngman et al., 2004). It was also hypothesized that the base of G2447 lowers the pK<sub>a</sub> of A2451 due to

hydrogen bonding increasing the basicity of the N3 atom, thus facilitating the deprotonation of the  $\alpha$ -amino group (Nissen et al., 2000). However, several observations argue against this model. First, mutation of A2451 and G2447 result in growth defects, but mutant ribosomes are still capable of peptide bond formation (Beringer et al., 2003, 2005; Gregory et al., 2001; Polacek and Mankin, 2005). Second, the acid dissociation constant (pKa) of N3 needed to deprotonate the  $\alpha$ -amino group of the aminoacyl tRNA would have had to be altered by several pH units for this model to be correct, while biochemical analyses showed that this was not the case (Parnell et al., 2002). The pH independence of the peptide bond formation was demonstrated by replacing  $\alpha$ -amino acids by  $\alpha$ -hydroxy acids and by performing the reaction at different pH (Bieling et al., 2006), making an acid-base catalyzed mechanism unlikely, and these results were further supported by molecular dynamics studies (Bieling et al., 2006; Trobro and Aqvist, 2005). Furthermore, the substrate analog used in the archaeon 50S complex structure lacked the functionally important 2' hydroxyl (OH) of the P-site A76 nucleobase and was thus a poor mimic of its natural substrate (Nissen et al., 2000). Subsequent X-ray crystallography structures of the 50S ribosomal subunit showed that N3 is not positioned correctly and that no  $Mg^{2+}$  or other cation could be localized within the PTC, rendering a metal-catalyzed mechanism also unlikely (Schmeing et al., 2005b). Instead, well-ordered water molecules were observed and proposed to stabilize the oxyanion intermediate (Hansen et al., 2002; Schmeing et al., 2005a).

There are currently three main models involving water molecules that could explain the movement of protons around the PTC, initiated by the deprotonation of the  $\alpha$ -amino group of the A-site amino acid during peptide bond formation: the six- (Dorner et al., 2002) and eight-membered (Schmeing et al., 2005a; Wallin and Aqvist, 2010) proton shuttle models and the proton wire model (Polikanov et al., 2014a).

#### The six- and eight-membered proton shuttle models

The two proton shuttle models are concerted models in which proton transfer occurs in a single-step from the attacking amine to the 2' hydroxyl of the P-site tRNA A76 ribose. Biochemical and molecular dynamics studies have shown that the 2' hydroxyl group of A76 is necessary for peptide bond formation when the tRNA is located in the P site (Dorner et al., 2002, 2003; Trobro and Aqvist, 2005; Weinger et al., 2004). In the six-membered proton shuttle model, the proton from the  $\alpha$ -amino group of the aminoacyl-tRNA is transferred to the 2' hydroxyl of P-tRNA

residue A76, which in turn gives a proton to the neighboring 3' hydroxyl to break down the tetrahedral intermediate. The eight-membered proton shuttle model (Schmeing et al., 2005b), is similar to the six-membered model but incorporates a water molecule interacting with the 2' hydroxyl of A76 of the P-site tRNA to facilitate proton transfer (Schmeing et al., 2005a). It suggests that the attack of the  $\alpha$ -amino group on the ester carbonyl carbon results in an eight-membered transition state in which a proton from the  $\alpha$ -amino group is received by the 2' hydroxyl of A76, which at the same time donates its proton to the carbonyl oxygen by way of an adjacent water molecule (Kuhlenkoetter et al., 2011). The well-ordered water molecule in close proximity to the 2' hydroxyl of A76 of the P-site tRNA could possibly form an eight-membered proton shuttle with a second water molecule stabilizing the oxyanion transition state (Schmeing et al., 2005b). Molecular dynamics suggest that the eight-membered proton shuttle is preferred over the six-membered proton shuttle (Wallin and Aqvist, 2010).

#### The proton wire model

While A2451 was not implicated in the proton shuttle model, the lack of the 2' hydroxyl group of A2451 leads to a 1000-fold factor reduction in peptide bond formation (Erlacher et al., 2005, 2006; Lang et al., 2008; Trobro and Aqvist, 2005). Structural studies involving high-resolution X-ray structures of the pre-attack and post-catalysis states of the 70S *Thermus thermophilus* ribosome with full-length aminoacyl-tRNA and peptidyl-tRNA mimics, revealed three trapped water molecules within the PTC. Based on these observations, the authors formulated the proton wire model, where in contrast to the two previous models, the three water molecules and the 2' hydroxyl group of A2451 are considered (Polikanov et al., 2014a).

Indeed, while the two proton shuttle models present a proton transfer occurring simultaneously with the nucleophilic attack, the proton wire model occurs in two stages. The first step corresponds to a rate-limiting transition state, where a network of hydrogen bonding between the 2' hydroxyl of A76 of the P-site tRNA and the 2' hydroxyl of A2451 allow, through three water molecules, the transfer of three protons. The first proton is liberated from the attacking amino group of the aminoacyl tRNA and transferred through the hydrogen bonds network until it reaches a water molecule coordinated by the N-terminus of protein bL27, the 2' hydroxyl of A2451, the base of 23S rRNA residue A2602 and the A76 phosphate group of the A-site tRNA. This transfer of protons allows the deprotonation of the attacking amine and the formation of the tetrahedral intermediate. The second step proposed by the model corresponds to a partial



reversal of this proton-transfer event and results in intermediate breakdown yielding the final products, namely peptidyl-tRNA in the A site and the deacylated tRNA in the P site.

The eight-membered and proton wire models agree on the concerted movement of three protons thus forming the rate-limiting transition state of peptide bond formation, but disagree on the exact pathway followed by the protons. One argument against the proton wire model (Polikanov et al., 2014a) is that deletion of bL27 has no apparent effect on peptide bond formation (Maracci et al., 2015). On the other hand, the two proton shuttle models are not based on an entire and substrate-containing ribosome, but only on a 50S subunit structure lacking in full-length peptidyl- and aminoacyl-tRNA substrates; therefore, this complex is limited and probably poorly mimics a biologically-relevant complex. Finally, the proton shuttle model has a less optimal stereochemistry than the proton wire model (Polikanov et al., 2014a).

#### tRNA-mRNA translocation

Once peptide bond formation has taken place, the deacyl-tRNA needs to move from the P site to the E site, and the newly formed peptidyl-tRNA from the A site to the P site in order for the ribosome to take part in another round of elongation (**Figure 6**) (Rodnina, 2018; Schmeing and Ramakrishnan, 2009a). To preserve the reading frame, the ribosome needs to be translocated exactly one codon further towards the 3' end of the mRNA, and, thereby base pairing between the codon of the mRNA and the anticodon of the tRNA moving from the A site to the P site must be strictly maintained during this process.

Due to steric clashes with the ribosome, the P-site tRNA cannot move to the E site until the peptide bond is formed and it becomes deacylated (Rheinberger et al., 1981; Schmeing et al., 2003). Following peptide bond formation, the binding affinities of the tRNAs for their current positions are decreased, resulting in the movement of the tRNAs between several pre-translocation states: the deacyl- and peptidyl-tRNAs can rapidly and spontaneously unlock from their classical P/P and A/A positions respectively adopted during peptide bond formation, to achieve multiple “hybrid” states, where the tRNA anticodon stem loops (ASLs) remain bound to the mRNA codons in the A and P sites on the small subunit, while the acceptor arms of tRNAs are shifted into the P and E sites of the large subunit, leading the tRNAs to adopt P/E and A/P hybrid states (**Figure 7**) (Carbone et al., 2021; Rundlet et al., 2021). Numerous hybrid conformations actually exist, because the ribosome possesses multiple conformational degrees of freedom, and the tRNA molecule itself is flexible. The tRNA positions correlate with the



degree of 30S subunit rotation and particularly with the movement of the head domain of the small subunit (**Figure 7**) (Adio et al., 2015; Ramrath et al., 2013; Wasserman et al., 2016). Indeed, the pre-translocation ribosome can adopt various different conformations, ranging from the non-rotated to the fully rotated conformations which interconvert spontaneously, where the last can display rotation angles of the small subunit relative to the large by up to 10 degrees or more (Carbone et al., 2021; Rundlet et al., 2021). These movements lower the energetic barrier of translocation and thus facilitate the movement of the mRNA-(tRNA)<sub>2</sub> complex (Blanchard et al., 2004; Cornish et al., 2008; Dorner et al., 2006; Frank and Agrawal, 2000; Moazed and Noller, 1989; Valle et al., 2003). Therefore, because of these oscillations, the translocation process can occur very slowly and spontaneously *in vitro* but rapid and effective translocation *in vivo* requires the GTP-dependent action of Elongation Factor-G (EF-G) (Munro et al., 2010).

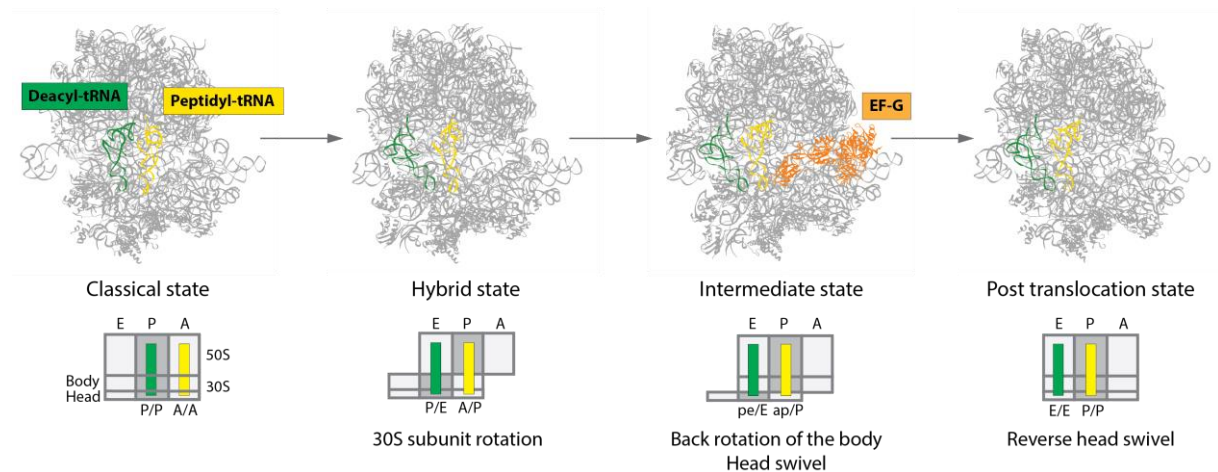


**Figure 7 : tRNAs and 30S movements during translocation**

After peptide bond formation, the deacyl- (green) and the peptidyl-tRNAs (yellow) are destabilized and can adopt hybrid states (P/E and A/P respectively) where the acceptor arm of each tRNA move from its initial position. These movements coupled to rotations of the 30S subunit (rotated state of the ribosome) allows EF-G to bind the complex and catalyze GTP hydrolysis stabilizing the tRNA P/E and A/P hybrid states, thus forming the intermediate states of translocation. The Pi release coupled to the back rotation of the body domain of the 30S subunit induce conformational changes in EF-G triggering the movements of the deacyl- and the peptidyl tRNAs to the E- and P-sites respectively through head swivel. Finally, after reverse swiveling of the head domain, the ribosome adopts again a post-translocation non-rotated conformation where EF-G can leave the complex.

EF-G binds specifically to the pre-translocation ribosome and couples the translocation of tRNAs to GTP hydrolysis (**Figure 7**) (Munro et al., 2010). A certain number of pre-translocation ribosomal conformational changes are necessary for EF-G to act. First, the pre-translocation ribosome engages a spontaneous reverse rotation of the small subunit head and

body domains in the same counterclockwise direction relative to the large subunit. In this conformation, the relative position of the small subunit and the 50S SRL are complementary to the GTP-bound conformation of EF-G's GTPase domain (Carbone et al., 2021; Petrychenko et al., 2021). Second, the deacyl-tRNA must adopt the P/E hybrid state and the peptidyl tRNA the A/P\* state, where “\*” represents a tRNA conformation where the tRNA elbow is slightly translocated in comparison to the A/P state; G19-C56 base pair of the peptidyl tRNA elbow is at first fixed to the ASF of the 50S subunit (A/P state) and then moves towards the E-site (A/P\* state). EF-G is sterically incompatible with A/A and A/P tRNAs conformations, as EF-G translocase domain 4 (amino acids 490 to 610; *E. coli* numbering) needs to bind within the A-site where domain 4 sterically hinders the A/P\* tRNA from returning to the canonical A/A state. Indeed, EF-G loop 1 of domain 4 (amino acids 507 to 514) is inserted between the peptidyl-tRNA, the 30S shoulder and the 30S head domains and reaches toward the 16S nucleotide conserved decoding base G530 on the 30S shoulder, responsible for decoding and “locking” of the cognate A-site-tRNA. The loop 2 of domain 4 (amino acids 582 to 588) fits into the helix 34 of 16S rRNA to bind the ribosome when the 30S head domain adopts a pre-swiveled conformation. Thus, domain 4 is positioned to “unlock” the codon-anticodon helix from the decoding center and follow the head during translocation. Once the ribosome is in the appropriate pre-translocation conformation, EF-G•GTP spontaneously engages the GTPase Activating Center (GAC) of the large subunit (Savelsbergh et al., 2003, 2005) to enter the A-site of the small subunit aided by the bL12 stalk stabilizing the ribosome in the rotated conformation (Carbone et al., 2021; Ermolenko et al., 2007a). Once EF-G bound, GTP is rapidly hydrolyzed on the pre-translocation ribosome. After GTP hydrolysis, the switch loops of the GTPase center remain well ordered because they are stabilized by the rotated 30S conformation (Carbone et al., 2021; Petrychenko et al., 2021).

Then, the small subunit body begins moving backward in the clockwise direction, whereas the head remains in the previous state (Belardinelli et al., 2016a; Carbone et al., 2021; Guo and Noller, 2012; Petrychenko et al., 2021; Rundlet et al., 2021; Wasserman et al., 2016). This movement of the body domain coincides with the Pi release and with conformational changes of switch loop 1 of EF-G GTPase domain (Carbone et al., 2021; Petrychenko et al., 2021). These EF-G and ribosome conformational changes open the decoding region sufficiently to dissociate the tRNAs from the interactions with the ribosomal elements that hold the mRNA and the tRNA anticodons in the A and P sites, thus forming the tRNA intermediate states of the translocation process (Rundlet et al., 2021). The backward swivel of the head domain moves

EF-G into the A site, thus completing translocation relative to the 30S body (Carbone et al., 2021; Petrychenko et al., 2021; Rundlet et al., 2021). At this step, the tRNAs adopt their canonical E/E- and P/P post-positions in the E and P sites respectively and EF-G leaves the ribosome. Within the E site, while the head domain moves further backward, the deacetylated tRNA loses its E-site codon–anticodon interactions leading to its dissociation from the ribosome (Adio et al., 2015; Belardinelli et al., 2016b). Wasserman et al. NSMB 2016 and Alejo et al. 2019 argue that E-site tRNA dissociation is a stochastic process that often occurs during the process of translocation. Finally, the remaining peptidyl-tRNA locates within the P site with a classical P/P position, thereby letting a new cognate aminoacyl-tRNA accommodate into the A site (**Figure 7**).

#### 1.2.2.3. Termination and recycling

From the PTC, the nascent peptide chain passes through the exit tunnel to reach the cytoplasm and leave from the protein translocation machinery (**Figure 4**). The elongation cycle proceeds until the ribosome reaches an mRNA stop codon (UAA, UGA, UAG). Release factors 1 and 2 are class I termination enzymes able to recognize stop codons at the decoding center in the A-site of the ribosome (Klaholz, 2011). RF1 recognizes the stop codon UAG while RF2 recognizes UGA. The last UAA stop codon is recognized by both RF1 and RF2 (Scolnick et al., 1968; Wilson et al., 2000). The binding of release factors enables water to enter the PTC and be correctly positioned in order to hydrolyze and release the nascent peptide from the P-site tRNA (**Figure 4**). Release factors display specific tripeptide anticodon motifs able to interact with and recognize the mRNA stop codon within the A site (Schmeing and Ramakrishnan, 2009b). Once the stop codon is recognized, nucleobases A1492 and A1493 of the 16S rRNA and A1913 of the 23S rRNA in the decoding center move to allow the proper accommodation of RF-1 or RF-2 for the docking of a conserved GGQ motif into the PTC (Schmeing and Ramakrishnan, 2009b). This GGQ motif, by means of a water molecule, catalyzes the deacylation of the tRNA and the release of the peptide (Korostelev et al., 2008; Laurberg et al., 2008). In *E. coli*, a third factor, RF-3, binds to the A site and uses GTP hydrolysis to generate a rotation of the 30S subunit. This rotation destabilizes the binding of RF-1/2 (Frank et al., 2007; Freistroffer et al., 1997; Goldstein and Caskey, 1970; Klaholz et al., 2004).

After dissociation of the release factors, the two ribosomal subunits need to dissociate to liberate the mRNA and the tRNAs from the ribosome and recycle them. In order to do so, the recycling factor (RRF) bind to the ribosomal P site, stabilizing the ribosome in a ratcheted state and the deacylated tRNA in a hybrid P/E state (**Figure 4**). The dissociation of the two subunits is then produced by the binding and the GTP hydrolysis of EF-G within the A site of the ribosome (Hirashima & Kaji, 1973; Peske, Rodnina, & Wintermeyer, 2005). The tRNA and the mRNA are then removed from the small subunit by the rebinding of IF-3 to the E site, thereby allowing the beginning of a new round of translation (Antoun et al., 2006b; Karimi et al., 1999; Peske et al., 2005).

### **1.2.3. Ribosome-targeting antibiotics**

#### *1.2.3.1. Overview of ribosome-targeting antibiotics*

Being essential to microbial life while differing from their eukaryotic equivalents, the bacterial ribosome is a major antibiotic target. (Wilson, 2014) provides a comprehensive review of the modes of action of different antibiotic classes. Most of the antibiotics targeting the ribosome inhibit the elongation process (**Figure 8**), including a large part of the widely used antibiotics, such as aminoglycosides, chloramphenicols, fusidic acids, lincosamides, macrolides, oxazolidinones, streptogramins or tetracyclines. Considering the size of the ribosome and the number of factors and substrates involved in bacterial translation, it is surprising that our current arsenal of antibiotics targets only a small number of key sites within the translational complex.

On the 30S subunit, most of the antibiotic binding sites are located on the path of the mRNA and tRNAs. Pactamycin, edeine and kasugamycin inhibit translation initiation by preventing the stabilization of the initiator tRNA on the start codon at the ribosomal P-site. In other cases, 30S-targeting antibiotics interfere with either the delivery of tRNAs into the A-site (such as tetracyclines and streptomycin) or with the translocation of the mRNA–tRNA complex through the ribosome (such as aminoglycosides like hygromycin B, neomycin, pactamycin and spectinomycin; and as tuberactinomycins, viomycin and capreomycin) (Wilson, 2014).

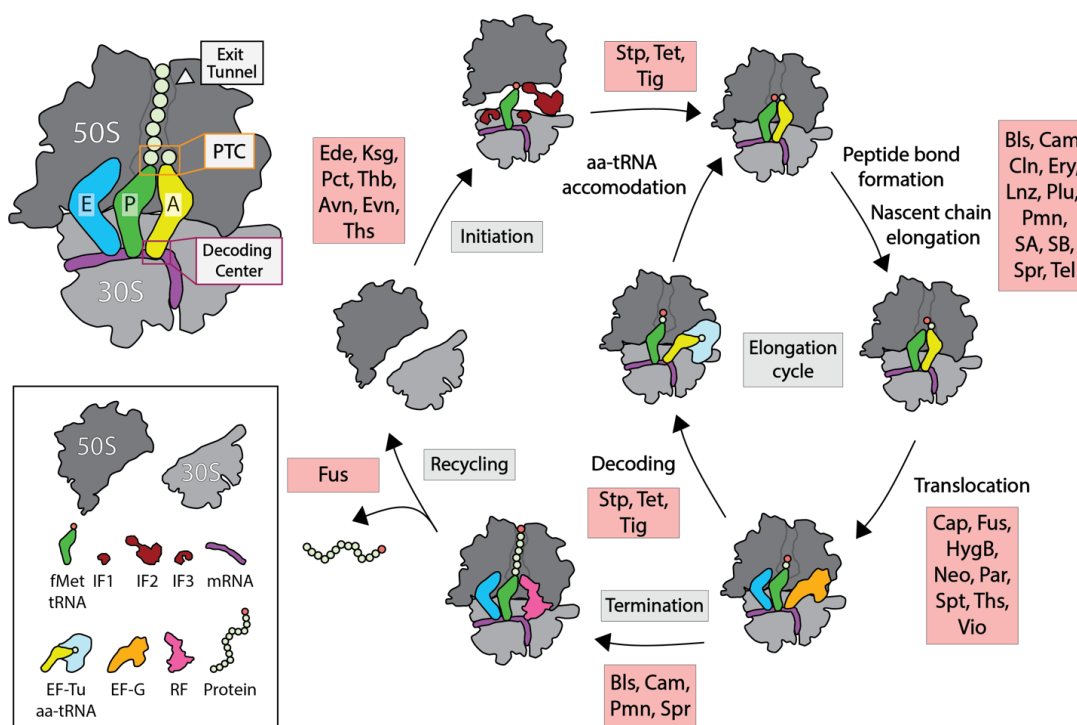


**Figure 8 : Antibiotics target sites during bacterial protein synthesis**

Initiation of protein synthesis involves the formation of a 70S ribosome with the initiator tRNA and start codon of the mRNA positioned at the P-site. This process is inhibited by the antibiotics edeine (Ede), kasugamycin (Ksg), pactamycin (Pct) and thermorubin (Thb) on the 30S subunit, and by the orthosomycins avilamycin (Avn) and evernimicin (Evn), as well as thiostrepton (Ths) on the 50S subunit. The elongation cycle involves the delivery of the aminoacyl-tRNA (aa-tRNA) to the A-site of the ribosome by EF-Tu, which is inhibited by streptomycin (Stp), tetracyclines (Tet) and glycylcyclines (tigecycline (Tig)). Peptide-bond formation between the A- and P-site tRNAs is inhibited by blasticidin S (Blis), chloramphenicol (Cam), lincosamides (clindamycin (Cln)), oxazolidinones (linezolid (Lnz)), pleuromutilins (Plu), puromycin (Pmn), streptogramin A (SA) and sparsomycin (Spr). Translocation of the tRNAs is catalyzed by EF-G and inhibited by the tuberactinomycins capreomycin (Cap) and viomycin (Vio), the aminoglycosides hygromycin B (HygB), neomycin (Neo) and paromomycin (Par), as well as fusidic acid (Fus), spectinomycin (Spt) and Ths. Elongation of the nascent chain is inhibited by the macrolides (erythromycin (Ery)), streptogramin B (SB) and ketolides (telithromycin (Tel)). The final phases of termination and recycling lead to release of the polypeptide chain and subsequent dissociation of the 70S ribosome, followed by recycling of the components for the next round of initiation. Termination is inhibited by peptidyl-transferase inhibitors, such as Blis, Cam, Pmn and Spr, whereas recycling is inhibited by translocation inhibitors, especially Fus. Adapted from (Wilson, 2014).

Antibiotics can also bind to the 50S subunit and inhibit translation by interfering with the binding and movements of essential translation factors or tRNAs; as reviewed by (Wilson, 2014). The orthosomycins (evernimicin and avilamycin) interact with helices H89 and H91 of the 23S rRNA and prevent efficient tRNA accommodation. Finally, thiostrepton-like thiopeptides interact with H43 and H44 of the 23S rRNA and interfere with the binding of EF-G, EF-Tu and IF2. A host of other antibiotics targeting the 50S subunit bind closer to the PTC.

These antibiotics inhibit peptide bond formation by perturbing or preventing the correct positioning of the aminoacylated ends of tRNAs within the PTC, often overlapping with the A-site tRNA (for example, chloramphenicol, oxazolidinones (linezolid) lincosamides (clindamycin), oxazolidinones (linezolid), hygromycin A, puromycin and sparsomycin) or the P-site tRNA (blasticidin S), or spanning both the A and P sites (for example, the pleuromutilin and streptogramin A classes). Several antibiotics are able to bind within the exit tunnel of the ribosome, adjacent to the PTC, such as macrolides, ketolides, streptogramins and tetracenomycin X. These antibiotics can interplay with the nucleobases of either the PTC and/or either the tunnel, and sometimes with residues of the nascent peptide, to inhibit peptide-bond formation or prevent the progression of the peptide through the tunnel. These interactions often lead to a drop off of the peptidyl-tRNA and to the abortion of translation. A last interesting example is puromycin, an antibiotic that reacts covalently with the nascent chain and results in premature termination (Darken, 1964). Puromycin and its derivatives are widely used as tools in several biochemical, kinetic and structural studies to study peptide bond formation and nascent chain-mediated translational arrest (Muto et al., 2006; Schmeing et al., 2002; Traut and Monro, 1964).

#### *1.2.3.2. Context-specific action of ribosome-targeting antibiotics*

Most antibiotics targeting the bacterial ribosome are thought to be universal translation inhibitors, blocking the ribosome irrespective of the nature of their different substrates, which vary with each round of elongation. However, in some cases the nature of the translation complex is critical for efficient drug-dependent inhibition. In fact, many ribosomal antibiotics are thought to impact protein synthesis in a context-specific manner, where their inhibition relies on the nature of the substrates being translated (Vázquez-Laslop and Mankin, 2018b). I will present throughout the next sections the few documented examples of context-dependent antibiotics, in order to illustrate the need to re-evaluate the mechanism of action of our antibiotic arsenal; optimizing existing drugs by deeply understanding their mode of action and reexamining the potential of less studied and/or old compounds to become useful antibiotics would be of high interest in the research of innovative solutions against antibiotic resistance.

#### *Macrolides and ketolides*

Macrolides represent a large family of antibiotics that are of important clinical interest for human therapy. They were discovered in 1950, where the majority of the natural macrolides

came from *Streptomyces* strains. They are composed of a 12 to 16 carbon long macrocyclic lactone ring connected to an amino-sugar or deoxy-sugar via a glycosylic bond, and are mainly active against Gram-positive bacteria (as reviewed in Dinos, 2017). Macrolides and ketolides bind in a similar way to the nascent polypeptide exit tunnel of the large (50S) ribosomal subunit, occupying a site close to the PTC (Bulkley et al., 2010; Dunkle et al., 2010; Tu et al., 2005). Until recently, macrolides and ketolides were thought to act by simply blocking the exit tunnel, thus forcing peptidyl-tRNAs longer than 3-10 amino acids to drop off the ribosome (Contreras and Vazquez, 1977; Odom et al., 1991; Schlünzen et al., 2001; Tenson et al., 2003). However, it has since been shown that their mechanism is more complex because certain nascent peptides can bypass the antibiotic inside the tunnel, leading to the synthesis of long polypeptides and to the interruption of protein synthesis at a later stage, after the nascent chain has moved past the antibiotic binding site (Kannan et al., 2012, 2014; Sothiselvam et al., 2016). In fact, bacterial protein synthesis is not completely inhibited in the presence of macrolides. For example, addition of erythromycin at concentrations exceeding the minimal inhibitory concentrations (MICs) by 100-fold on *E. coli* cultures fails to inhibit the production of 5 to 7% of proteins that are normally synthesized, whereas an equivalent amount of telithromycin leads to the production of almost 25% of all proteins (Almutairi et al., 2017; Kannan et al., 2012).

Moreover, X-ray structures of macrolide-bound ribosomes show that the exit tunnel is wide enough to let a peptide pass through (Tu et al., 2005). The recent expansion of the ribosome profiling method (Ingolia et al., 2009) to bacterial samples has increased our understanding of the effects of macrolides on the elongation step of translation. This technique provides a quantitative distribution of ribosomes on the translated mRNAs: the slower the translation, the greater the density of ribosomes that can be detected at a particular location. Therefore, ribosome profiling is a suitable technique to analyze at a genome-scale level the distribution of macrolide-dependent ribosome stalling by comparing cells treated with antibiotics to untreated cells (Davis et al., 2014; Ingolia et al., 2009; Kannan et al., 2014). Translation of nearly 80% of genes in macrolide-treated cells is blocked at early codons (Davis et al., 2014; Kannan et al., 2014). However, many ribosomes are arrested at specific sites along the mRNAs, revealing amino acid sequence-specific arrest motifs (Davis et al., 2014; Kannan et al., 2014). The most predominant motif corresponds to the +X+ pattern (+ for the positively charged amino acids arginine and lysine, and X for any amino acid). Interestingly, the most common arrest motif for ketolides such as telithromycin is this +X+ motif, whereas cladinose-containing macrolides like erythromycin or azithromycin present a wider and more diverse range of patterns (Davis et al.,



2014; Kannan et al., 2014). This observation can explain the difference in global protein production between erythromycin and telithromycin, where telithromycin appears to be a more selective inhibitor due to its high selectivity for +X+ motifs. This implies that the chemical structure of these antibiotics can change their mechanism of action.

The ability of macrolides and ketolides to inhibit the bacterial translation of specific arrest motifs has been used by bacteria to regulate expression of their antibiotic resistance genes (Weisblum, 1995). These genes are activated only when the cells are exposed to the respective drug, which then acts as an inducer. In the absence of the inducer, the gene remains silent and cells remain susceptible to the drug (Gupta et al., 2013; Sutcliffe and Leclercq, 2002). This ON/OFF induction mechanism reduces the fitness cost generated by a constitutive expression of the resistance gene, which can impair translation within the bacterial cell. A small leader ORF constitutively translated by the ribosome and located upstream of the resistance gene contains one of these arrest motifs. In the presence of the drug, ribosomes translating this leader sequence stall on the motif. This destabilizes the mRNA conformation and frees the RBS of the resistance gene which was previously sequestered in a secondary structure to result in its activation and the survival of the bacteria (Dar and Sorek, 2017; Depardieu et al., 2007; Weisblum, 1995). Therefore, many of these small leader sequences carry the +X+ motif or others known to be inhibitors of ribosomal translation in the presence of macrolides or ketolides. Understanding the mechanism of induction of such resistance genes and highlighting the differences between the modes of action of macrolides and ketolides could lead to the development of antibiotics that do not trigger the expression of the resistance genes.

### Chloramphenicol and oxazolidinones

The PTC is a major target for antibiotics, including chloramphenicol and oxazolidinones (Polacek and Mankin, 2005; Wilson, 2014). Chloramphenicol is a broad-spectrum antibiotic, naturally produced by several *Streptomyces* species (Vázquez, 1979), which binds to the 50S subunit within the PTC, occupying the space normally dedicated to the acceptor amino-acid in the A-site crevice (Bulkley et al., 2010; Dunkle et al., 2010; Schlünzen et al., 2001). A more recent antibiotic used in clinics from the family of the oxazolidinones, linezolid, binds in a similar way to the PTC (Moellering, 2003). Both chloramphenicol and linezolid were thought to act as universal inhibitors of peptide-bond formation because they displace and prevent the proper accommodation of the amino-acyl tRNA within the A-site of the PTC.



Yet, these PTC-binding drugs interfere with translation in a context-specific manner, that is, by preferentially inhibiting peptide bond formation of specific amino acids. Ribosome profiling data of *E. coli* cells exposed to high concentrations of chloramphenicol or linezolid presented ribosomes arrested at preferential mRNA sites (Marks et al., 2016; Nakahigashi et al., 2014). Inhibition of translation by chloramphenicol or linezolid relies on the nature of the nascent peptide, where inhibition of protein synthesis induced by these drugs is most efficient when the nascent peptide carries an alanine, a serine or a threonine residue in its penultimate position. Likewise, the inhibitory action of chloramphenicol and linezolid is strongly reduced when a glycine residue occupies the P- or A-sites. These results were confirmed by toeprinting (Marks et al., 2016). To understand this phenomenon, the mechanism of action of chloramphenicol and linezolid was assessed by single-molecule fluorescence resonance energy transfer spectroscopy, in order to monitor translation arrest induced by antibiotics (Choi et al., 2020). The presence of chloramphenicol or linezolid does not alter protein synthesis until the ribosome encounters the peptide arrest motif. The inhibition of peptide bond formation induced by the presence of a problematic residue forces the fully accommodated A-site tRNA to undergo repeated rounds of dissociation and nonproductive rebinding (Choi et al., 2020). Two recent preprints provided high resolution structures of ribosomal complexes translating various specific peptide motifs, able to inhibit translation in presence of chloramphenicol (Syroegin et al., 2021), linezolid or a new type of oxazolidinone, namely radezolid (Tsai et al., 2021). The comparison of the different structures explained how the nature of the penultimate residue of the nascent peptide directly defines the ability of the drug to stably bind or not upon the PTC to inhibit protein synthesis.

Similarly to *erm* genes, inducible chloramphenicol resistance genes exploit the specificity of chloramphenicol action. The *cmlA* gene is regulated by an upstream ORF which contains a programmed translation arrest site defined by the presence of an alanine. The configuration is the same for the *cat86A* chloramphenicol resistance-gene presenting a leader ORF containing a threonine codon (Marks et al., 2016). The context-specific action of chloramphenicol and linezolid and the presence of such resistance mechanisms provide new arguments in favor of the reexamination of the precise mode of action of our current arsenal of antibiotics.

### Kasugamycin

Kasugamycin is an aminoglycoside antibiotic originally isolated in 1965 from *Streptomyces kasugaensis*, a streptomycete found in soils near the Kasuga shrine in Nara, Japan. A high-

resolution crystallographic structure of the kasugamycin-70S ribosome complex from *E. coli* revealed that the drug binds to the 30S subunit of the ribosome between the universally conserved G926 and A794 nucleotides of the 16S rRNA (Schuwirth et al., 2006). Kasugamycin occupies a site overlapping with the E-site and P-site codons of the mRNA, thus blocking the mRNA path of the ribosome and inhibiting the binding of the initiator tRNA to the P site. Consequently, kasugamycin was thought to be a universal inhibitor of initiation by acting as a competition inhibitor for the binding of initiator tRNA.

However, recent studies showed kasugamycin specifically inhibits translation initiation of canonical but not of leaderless mRNA. While SD-led initiation is driven by the 30S subunit (see 1.2.2.1), translation of leaderless mRNAs is initiated by the 70S ribosome (Moll et al., 2004; Udagawa et al., 2004). For initiation on leaderless mRNA, the binding of the initiator tRNA is stabilized by the presence of the 50S subunit, which reduces the overlap between the mRNA and the kasugamycin binding site. In this configuration, kasugamycin does not affect the binding of the ribosome to the start codon, nor the initiation of translation (Chin et al., 1993; Moll and Bläsi, 2002). Consistent with these observations, kasugamycin differentially inhibits the synthesis of cytoplasmic and envelope proteins in *E. coli* (Hirashima et al., 1973). Additionally, previous studies showed that kasugamycin could inhibit the initiation of a reporter gene containing an SD sequence, whereas the insertion of two nucleotides before the start codon within the same sequence completely reduced this ability (Schuwirth et al., 2006). Kasugamycin therefore stands out as it is the first example of mRNA sequence-dependent inhibition induced by an antibiotic, although its precise mode of action and the mRNA preferences of kasugamycin are still very unclear.

### 1.3. Aims and objectives

The rise of bacterial multiple-drug resistance is an alarming threat and new therapeutic strategies need to be identified. A possible solution is to develop improved versions of existing drugs by better understanding their mechanisms of action. This is made possible by the fact that the tools at our disposal nowadays, such as cryoEM or ribosome profiling, are more powerful than they were before and therefore provide us with more insights into the mechanisms of antibiotic action. Consistently, the very recent notion of the context-specific action of certain ribosome-targeting antibiotics comes indeed from studies performed in the last decade and represents a nice example of how we are still lacking specific molecular details on the mode of

action of our current arsenal of antibiotics. In particular, why particular substrate combinations are problematic for the antibiotic-bound ribosome and how changes in drug structures affect the specificity of their action remain to be understood. The aim of my PhD work was to reexamine the modes of action of ribosomal antibiotics in order to provide new solutions for the fight against multidrug resistant pathogens.

The first objective of my thesis was to study the sequence dependence of short leader peptides that control the expression of different erythromycin resistance methylases (Erm) in response to macrolide or ketolide antibiotics. Understanding the principles of context specificity in *erm*s induction and the differential mode of action of macrolides and ketolides could lead to the development of antibiotics that would not trigger these sensing systems and prevent induction of resistance. To do so, I used inverse toeprinting, an *in vitro* profiling technique developed in our group to study transcripts encoding peptides that stall the ribosome during their own translation. By systematically mutating the sequence of three different Erm leader peptides, I obtained new insights into their mode of action and revealed the main mechanism by which macrolide antibiotics inactivate the ribosome. A deep mutational scan of the ErmDL macrolide- or ketolide-dependent arrest peptide, combined with biochemical, structural and molecular dynamics techniques, in collaboration, we could not only shed light onto the mechanism by which +X+ motifs lead to stalling in the presence of macrolides and ketolides, but could also explain the drug-dependent stalling on *ermDL* leading to the induction mechanism of *ermD*. In addition, I gained new insights into the mode of action of the erythromycin-dependent arrest peptides ErmCL and ErmAL1, which actually display a similar mechanism. Indeed, the erythromycin-dependent stalling of ErmCL and the stalling of ErmAL1 rely on the same mechanism, involving the P-site tRNA and the -2 residue, where the combination formed by the nature of the residues located at these two key positions render the A-site of the PTC either restrictive, selective or permissive.

In the introduction, I presented categories of antibiotics, other than macrolides, that stall the ribosome in a context-dependent manner (see 1.2.3.2). Most clinically used antibiotics were discovered through large-scale screening approaches relying on measures of antimicrobial activity and cellular toxicity. Thus, in most cases, the precise mode of action of these antibiotics remains unclear, and we could assume that few of them might display a context-specific activity similarly to macrolide or chloramphenicol antibiotics (Vázquez-Laslop and Mankin, 2018b). Therefore, the second objective of my work was to assess the sequence dependence of a large

panel of ribosomal antibiotics. In particular, I focused on molecules affecting the decoding or translocation processes, as the close proximity to variable substrates make them potential candidates for inducing context-dependent inhibition of translation. Using inverse toeprinting in combination with a library of mRNAs encoding  $\sim 10^{12}$  random peptides, I determined the stalling landscapes of *E. coli* ribosomes exposed to a variety of different antibiotics and obtained a comprehensive list of sequence motifs that arrest translation in the presence of some of these drugs. Using biochemistry and cryo-electron microscopy, I was then able to get new insights into the mechanisms of action of several classes of antibiotics preferentially inhibit the translation of certain codon or amino acid combinations, including the tuberactinomycins capreomycin and viomycin, and the less characterized antibiotic tetracenomycin X. By doing so, I could observe that capreomycin and viomycin inhibit translation in a manner dependent on the nature of the transfer RNAs. In parallel, tetracenomycin X could only inhibit translation of specific nascent amino acid motifs, revealing a novel mechanism of inhibition of the ribosome. Collectively, the insights gained through this work could help the development of improved antibiotics that either bypass existing resistance mechanisms or have improved activity against the ribosomes of resistant bacteria.

## Part II: Methodological overview

The major advances in our understanding of how ribosomal antibiotics work have been brought by a combination of several recently developed, powerful *in vivo* and *in vitro* techniques. In the following sections, I will introduce the main techniques I used for my PhD work in order to uncover and characterize the context-specific action of few ribosome-targeting antibiotics.

## 2.1. Determining ribosomal stalling landscapes with inverse toeprinting

### Classical versus Inverse toeprinting

To examine the influence of the translational context on drug-induced ribosomal inhibition, two types of “toeprinting” techniques have been reported, both of which I used for my thesis work.

The earlier toeprinting technique will be referred here as “classical” toeprinting. It is a reverse-transcription based *in vitro* assay, also known as primer extension inhibition assay, which allows the position of ribosomes stalled during translation of a single mRNA template to be determined with codon resolution (Hartz et al., 1988). The annealing of a 5'-fluorescently-labeled DNA oligonucleotide to an *in vitro*-transcribed mRNA template acts as primer for a reverse transcriptase to produce a fluorescent complementary DNA (cDNA). If this mRNA is translated *in vitro*, the reverse transcriptase synthesizes cDNA until it encounters a ribosome arrested on the mRNA template, then falls off (**Figure 9**). Sanger sequencing of the template sequence is performed and used to locate precisely the mRNA codon on which the ribosome has stalled in a given condition of translation. The application of toeprinting to study ribosome progression along an mRNA has been facilitated by the development of the PURE system, where each of the proteins required for translation, tRNAs, and ribosomes are individually purified and then combined together (Hartz et al., 1988; Shimizu et al., 2001). The toeprinting technique has been successfully applied to studies of intrinsic and drug-induced translation arrest (Orelle et al., 2013; Vazquez-Laslop et al., 2008). However, this method requires to test each variant of interest in a separate reaction, and this low-throughput aspect does not allow the use of sequence libraries.

To increase throughput and study how ribosome-targeting antibiotics affect the translational landscape of a cell, a different approach was needed. Ribosome profiling or Ribo-Seq relies on deep sequencing of ribosome footprints — the short fragments of mRNA that are protected by the ribosome upon digestion by an RNA nuclease. These footprints are converted into a library

of DNA fragments and analyzed by next-generation sequencing (**Figure 9**) (Ingolia et al., 2009; McGlincy and Ingolia, 2017).

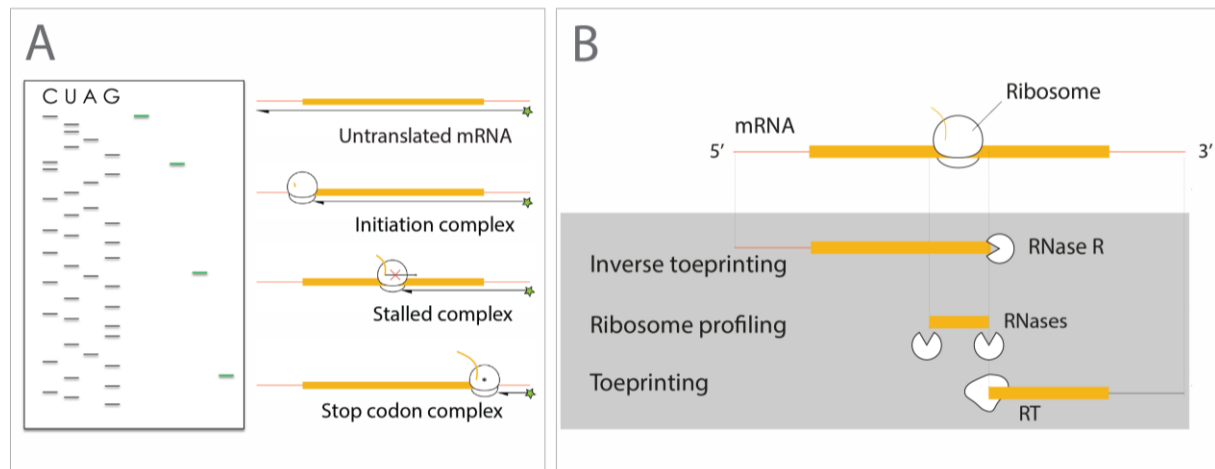


**Figure 9 : Toeprinting, Inverse toeprinting and ribosome profiling overviews**

(A) Overview of the toeprinting technique. A fluorescent primer, annealed to the 3' end of the mRNA, is extended using a reverse transcriptase (RT). The enzyme stops the synthesis of the cDNA when it encounters the ribosome, thus the length of the fluorescent cDNA relies on the position of the ribosome on the mRNA. The 3' end of the cDNA product is separated by 16 to 17 nucleotides from the first nucleotide of the mRNA codon in the ribosomal P-site. (B) Comparison between inverse toeprinting, ribosome profiling, and classical toeprinting (adapted from (Seip et al., 2018))

Deep-sequencing technologies provide high sequencing yields, by furnishing hundreds of millions reads per single experiment, each read corresponding to a single ribosomal footprint and reporting the position of one ribosome among a single mRNA (Ingolia et al., 2009; Oh et al., 2011). Therefore, ribosome profiling provides a snapshot of the mRNA coding sequences being translated at the moment when the cells are harvested and frozen, allowing the precise positioning and distribution of translating ribosomes in the cell to reveal the average ribosome occupancy of every codon of each gene. However, ribosome-protected mRNA footprints obtained by ribosome profiling are short and only provide the sequence of a few amino acids from the translated peptide upstream of the stalling site (Mohammad et al., 2016; Woolstenhulme et al., 2015). To access the full nucleotide sequence that was translated, the reads need to be mapped to a reference genome. Consequently, ribosome profiling cannot be used on a complex library featuring random or uncharacterized coding sequences, or on organisms for which the sequence of the genome is poorly characterized. Moreover, ribosome profiling requires medium to large bacterial culture volumes and large depth of sequencing, which are cost prohibitive with analyzing dozens or hundreds of different conditions per

experiment. Therefore, to uncover the context-dependent action of various categories of antibiotics, another *in vitro* method was necessary to provide complementary advantages and reduce the cost of such experiments.

To overcome the limitations of toeprinting and ribosome profiling, our group developed an “inverse” toeprinting approach, and this method was freshly available when I joined the laboratory to pursue my doctoral work in 2017. Inverse toeprinting is a highly scalable *in vitro* method used in my case to investigate ribosomal stalling by nascent peptides encoded within transcript libraries of any given complexity (Seip et al., 2018). Inverse toeprinting is a versatile selection strategy that relies on a highly processive 3' to 5' RNA exonuclease, RNase R (Vincent and Deutscher, 2006), which degrades the mRNA downstream of the leading ribosome on a transcript. This makes it possible to determine the position of stalled ribosomes on the mRNA with codon resolution, while protecting the entire upstream peptide-encoding region. Unlike classical toeprinting, inverse toeprinting is a high-throughput technique and, like ribosome profiling, relies on next-generation sequencing to generate millions of DNA reads corresponding to the ribosome-protected mRNA fragments (**Figure 10**).

For all of the projects described in this manuscript, I used inverse toeprinting to explore context-specific translation inhibition by a variety of ribosome-targeting antibiotics. As will become apparent in the coming chapters, I could detect, for some antibiotics, sequence motifs that were problematic for the drug-bound ribosome. In order to better characterize these motifs, I used classical toeprinting to measure the effect of these antibiotics on the translation of sequences containing variants of such arrest motifs. The combined use of these two *in vitro* techniques provided new insights into the inhibition mechanism of several antibiotics. However, in order to highlight their precise modes of action, structural information was required. By reproducing the *in vitro* translational conditions used during toeprinting, I made functional complexes of ribosomes stalled in the presence of antibiotic and studied them using cryo-electron microscopy.



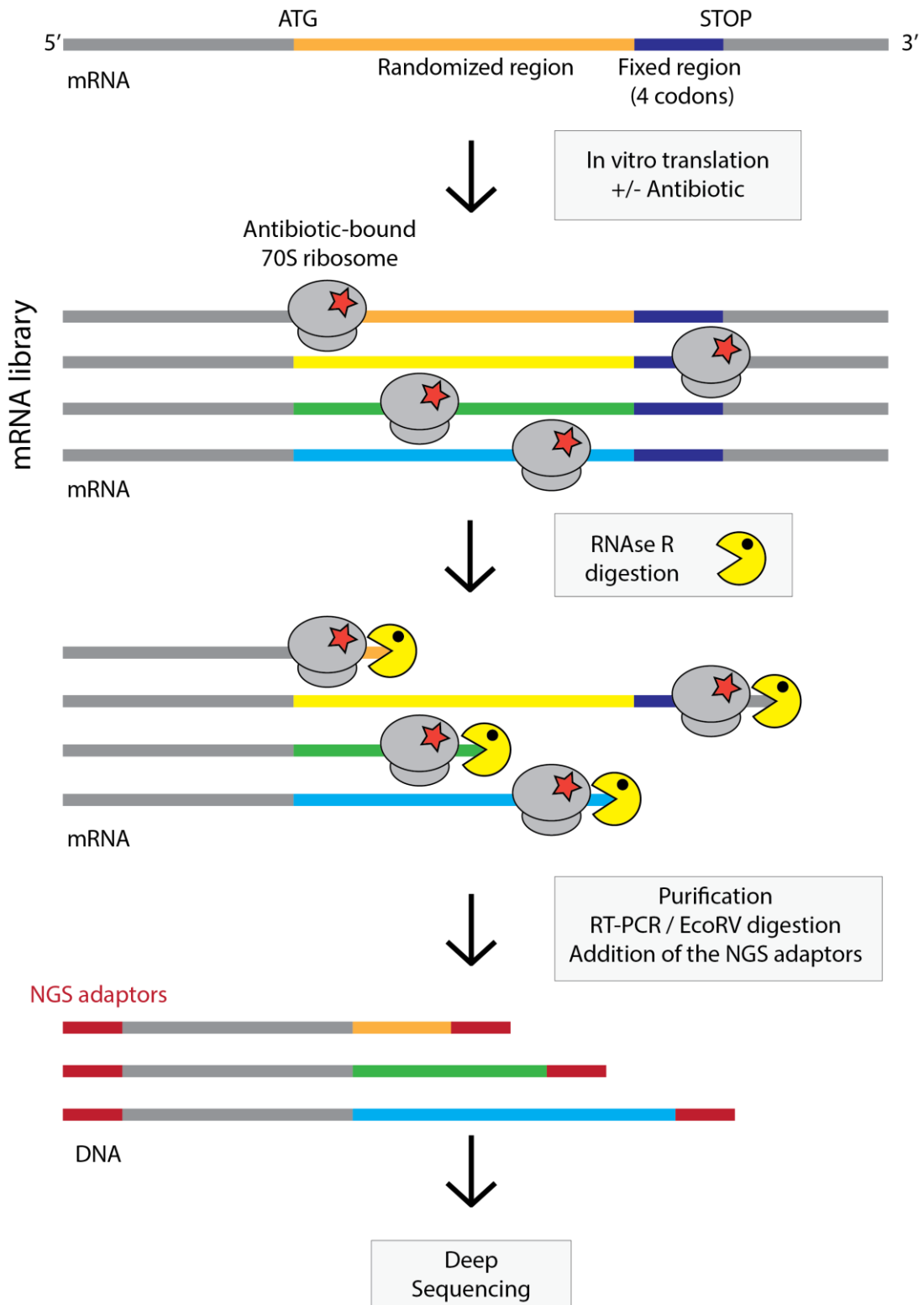


**Figure 10 : Overview of the inverse toeprinting procedure**

A designed library containing a random region is translated in presence of customized in vitro conditions, namely w/wo antibiotics in this case. The RNaseR digests the mRNA from its 3' end until it encounters a stalled ribosome. The mRNA is then purified, reverse transcribed and the corresponding cDNA is amplified by PCR where NGS adaptors are added at each extremity to send the sample for sequencing.

## 2.2. Visualizing functional ribosomal complexes by cryo-EM

Understanding the mode of action of antibiotics on the ribosome requires three-dimensional structural information to identify the drug binding site(s) and understand the interactions between the drug and its target. Until recently, structural studies concerning ribosome-targeting antibiotics mostly relied on X-ray crystallography (Tsegaye et al., 2021). The main advantages of this technique are the high resolution that it can provide and the relatively easy and fast throughput for ribosome samples. However, the molecular size of the antibiotic-ribosome complex, its complexity and flexibility, and sometimes the difficulties in producing or purifying sufficient quantities of the complex for structural determination, strongly limit the efficiency of this technique for the study of antibiotics mode of action. Indeed, the formation of crystals requires static samples that allow the resolution of high-resolution structures of antibiotics-bound ribosomes. However, the use of crystals strongly limits our ability to obtain structures of functional complexes, such as those of ribosomes engaged in translation in the presence of a given antibiotic. Indeed, the process of crystallization forces the ribosome to adopt a non-rotated state, thus impeding in some cases the understanding of the precise molecular mode of inhibition of ribosome-targeting antibiotics. The recent improvements of the high-resolution single-particle cryo-EM technique has been largely used to study the structure of large biomolecules and has proven to be a valuable tool for studying the mechanism of translation and the mode of action of small molecules targeting the ribosome, including antibiotics (Herrero del Valle and Innis, 2020; Razi et al., 2017; Tsegaye et al., 2021).

Cryo-EM is an imaging technique in which an electron beam is transmitted through a frozen sample to form a projected image captured by a detector. By averaging the projections of numerous identical biomolecules trapped in the vitreous ice in different orientations, single particle analysis allows their three-dimensional structure to be reconstructed at high resolution (Cheng, 2015). Advantages of the cryo-EM single particle technique for the study of ribosomal complexes includes (1) the low amounts of sample required and the lower number of screening parameters necessary to get optimal freezing conditions compared to crystallography, (2) the ability of the technique to image molecules ranging from less than 100 kDa to several MDa including large dynamic macromolecular assemblies that are otherwise difficult to produce, purify and/or crystallize and (3) the visualization of molecules in solution, allowing the observations of various conformations of the same sample, as reviewed by (Benjin and Ling, 2020; D'Imprima and Kühlbrandt, 2021; Herrero del Valle and Innis, 2020; Lyumkis, 2019;

Murata and Wolf, 2018). Limitations of this technique include the difficulty of obtaining informative structural data for molecules smaller than 100 kDa, long data collection time per data set and the computational power needed for processing thousands of micrographs, compared to X-ray crystallography.

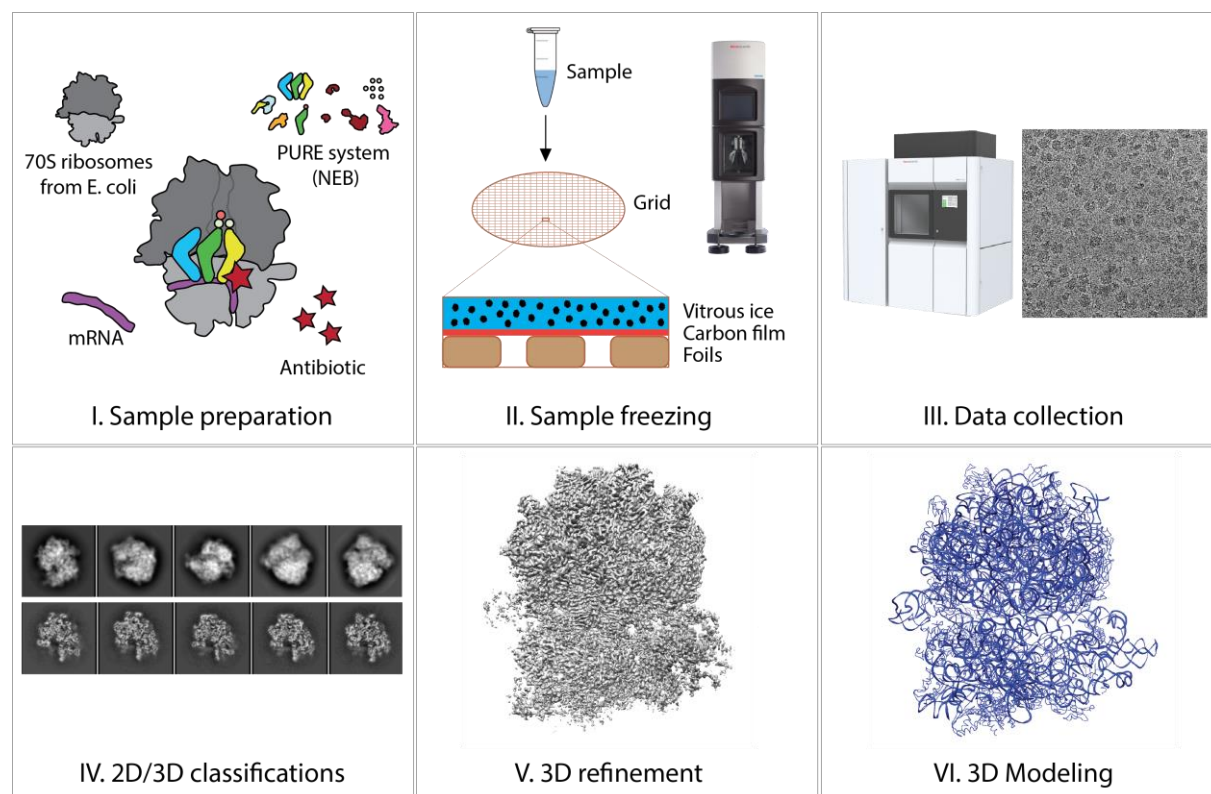


**Figure 11 : Overview of the cryoEM procedure**

The sample corresponds to an *in vitro* translation reaction using the PureSystem kit (NEB) where the ribosomes translate in presence of antibiotic an mRNA containing the antibiotic-dependent arrest motif of interest. After a simple dilution, the sample is frozen on glow-discharged carbon-coated grids using the Vitrobot (ThermoFischer). After screening of the grids, the images are collected on the Talos Arctica (ThermoFischer) and then processed using RELION 3.1 to generate 2D and 3D classes of the 70S ribosomes bound to tRNAs and/or elongation factors. After 3D refinement of the map, a model is manually built on Coot and refined on PHENIX to generate the structure of the complex.

The first application of cryo-EM to the study of the ribosome provided structures with an average resolution of 25 Å (Agrawal et al., 1999; Frank et al., 1995). Thus, X-ray crystallography was until recently the method of choice to obtain structural insights into the mode of action of antibiotics targeting the ribosome. The development of better microscopes comprises the improvement of specimen stage stability, the reduction of temperature variations and vibrations in order to realize parallel illumination and to ensure the high stability of

imaging. In addition, the introduction in 2012–2013 of direct electron detectors that allow movie collection mode reducing beam-induced motion and stage drift (Kühlbrandt, 2014), the improvement of the 3D classification schemes used to separate heterogenous particles within the same sample (Sigworth, 1998; Sigworth et al., 2010) and the development of user-friendly processing software (Grigorieff, 2016; Moriya et al., 2017; Punjani et al., 2017; de la Rosa-Trevín et al., 2013; Scheres, 2012) rendering the technique more accessible, led to the determination of cryo-EM structures with near-atomic resolutions. Together with improved sample preparation techniques, these technological developments provided structural details that could previously only be attained with X-ray crystallography. This phenomenon was described as the “resolution revolution” of the cryoEM technique and led to the Nobel prize of the scientists Jacques Dubochet, Joachim Frank and Richard Henderson for the development of the technique in 2017 (Cheng, 2015; Kühlbrandt, 2014; Nogales, 2016).

In my PhD work, I used cryoEM to solve the structures of *E. coli* 70S ribosomes translating an mRNA encoding for an arresting motif, in presence of the antibiotic of interest (**Figure 11**). Combined with the use of the *in vitro* translation Pure System kit (Shimizu et al., 2001), I could capture by direct freezing functional translating complexes stalled by antibiotics during translation of specific mRNAs. In combination with the functional data obtained by inverse toeprinting, toeprinting and *in vivo* reporter assays, the structural data derived from such complexes yielded new insights into the inhibition mechanism of these antibiotics, and highlighted new modes of action for several categories of antibiotics of high interest for human medicine.

## Part III: Understanding the sequence determinants underlying macrolide context-dependent inhibition

### 3. Introduction

#### 3.1.1. Natural and synthetic macrolides discovery and development

Macrolides are ribosome-targeting antibiotics commonly used in human medicine that display excellent antimicrobial activity against Gram-positive bacteria and various *Mycoplasmas* (Béb  ar et al., 1997; Doucet-Populaire et al., 1998; Morozumi et al., 2008). Macrolides are classified according to their macrocyclic lactone ring size (12-, 14-, 15-, or 16-membered ring) and may contain several chemical modifications, primarily sugar moieties connected by a glycosidic bond (as reviewed in Dinos, 2017). The first generation of macrolides comprises naturally occurring molecules discovered in the 1950s that have excellent antimicrobial activity, but poor activity against eukaryotes due to their low affinity for eukaryotic ribosomes (Dao Duc et al., 2019; V  zquez-Laslop and Mankin, 2011). Erythromycin is the best known member of the first generation (14-membered group) and was isolated from *Streptomyces erythraeus*, a soil-dwelling bacterium, in 1949 (**Figure 12**) (McGUIRE et al., 1952). Erythromycin is currently used against several pathogens involved in skin or upper respiratory tract infections.

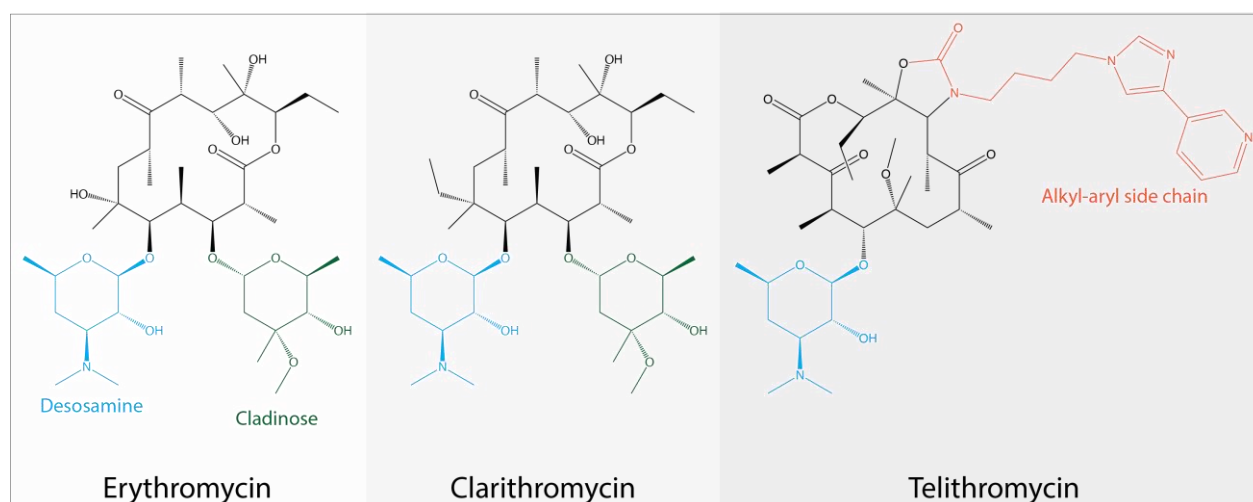


**Figure 12 : Structures of erythromycin, clarithromycin and telithromycin**

Despite these important advantages, the first generation of macrolides did not have good stability, especially at low pH, and furthermore suffered from poor bioavailability. These pharmaceutical problems therefore spurred the development of second-generation semi-synthetic macrolide derivatives, which are still in clinical use today (Counter et al., 1991; Girard et al., 1987; Omura et al., 1992). Several derivatives of erythromycin were developed and marketed, such as clarithromycin or azithromycin, which are highly consumed worldwide

(Figure 11) (Bahal and Nahata, 1992). These derivatives have better bioavailability due to their higher lipophilicity, which increases their ability to penetrate human tissue, and are less sensitive to low stomach pH (Bahal and Nahata, 1992; Foulds et al., 1990; Girard et al., 1987; Hardy et al., 1992; Piscitelli et al., 1992; Rodvold, 1999; Wise, 1989).

However, the widespread use of these derivatives subsequently led to the development of a large number of macrolide-resistant bacteria. To address this dangerous situation, a third generation of macrolides was developed, called ketolides where the cladinose ring of the first two generations macrolides was replaced by a keto group (as reviewed in Katz and Ashley, 2005). In addition, nearly all ketolides feature the addition of a 11,12-cyclic carbamate as well as a variable alkyl–aryl side chain tethered to different positions of the lactone ring. A detailed review covers all chemical efforts to improve the activity of ketolides (Liang and Han, 2013).

Ketolides show improved bactericidal activity, even against macrolide-resistant strains, and unlike azithromycin and clarithromycin. One of the most famous elements of the ketolide group corresponds to telithromycin. Telithromycin is not a substrate for efflux pumps and does not induce the ribosomal methylation associated with inducible macrolide–lincosamine–streptogramin B (MLSB) resistance in streptococci and staphylococci (Bryskier, 2000; Farrell et al., 2015; Shortridge et al., 2002). Unlike macrolides, which are considered time-dependent bactericides, ketolides show concentration-dependent killing (Woosley et al., 2010; Zhanel et al., 2002). However, ketolides sometimes exhibit significant and irreversible cytotoxicity, notably in the case of telithromycin (Denis et al., 1999), which was marketed as “Ketek” by Aventis and subsequently withdrawn due to its dangerous side effects. Telithromycin’s alkyl–aryl side chain contains a pyridine ring that blocks nicotinic acetylcholine receptors, resulting in severe hepatotoxicity known as “Ketek effects” (Fernandes et al., 2016). Lastly, solithromycin (Pereira and Fernandes, 2011) is currently in Phase III clinical trials (Farrell et al., 2015) and appears to be the most promising ketolide. Nevertheless, new ketolide-resistant strains have recently been discovered worldwide (Doern, 2006; Felmingham et al., 2007), making it a priority to understand the complete modes of action of these antibiotics and the different mechanisms by which resistance against them arises.

### 3.1.2. Mode of action of macrolides

All three generations of macrolides/ketolides bind to the large subunit of the bacterial ribosome, within the nascent polypeptide exit tunnel near the peptidyl transferase center (PTC) (Tu et al., 2005). The macrolactone ring is always similarly oriented on ribosome, irrespective of the drug or the bacterial species because the bases U2611, A2058, and A2059 of the tunnel provide a hydrophobic surface upon which the macrolactone ring rests (Bulkley et al., 2010; Dunkle et al., 2010). Macrolides and ketolides interact with adenosine 2058 of the 23S rRNA, via a hydrogen bond formed between the hydroxyl group of the drugs' desosamine ring and the N1 atom of A2058. While the interactions anchoring the macrolactone ring are identical between erythromycin and telithromycin, the main differences correspond therefore to the nature and positioning of the drug chemical modifications within the tunnel (the sugar moieties of macrolides, the alkyl-aryl side chain of ketolides etc.).

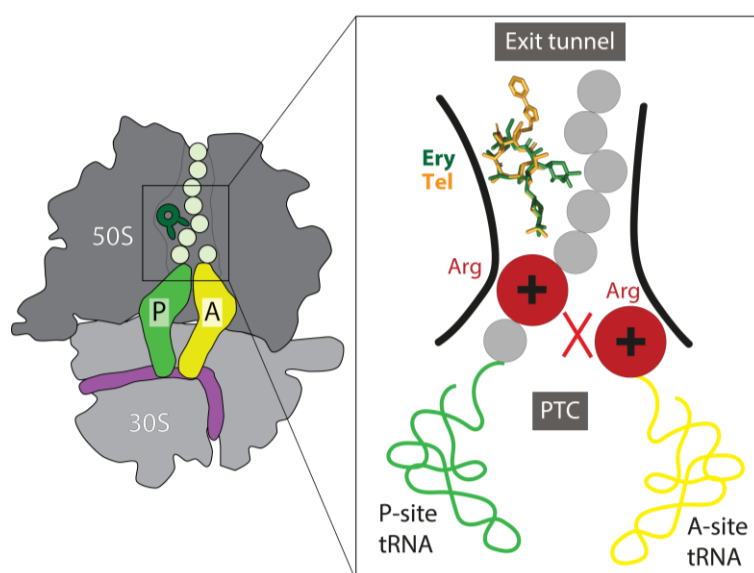


**Figure 13 : Schematic representation of the binding site of erythromycin or telithromycin within the exit tunnel of the ribosome**

Erythromycin and telithromycin inhibit the peptide bond formation between the two arginines of the RXR motif within the PTC.

Until recently, macrolides and ketolides were thought to be universal inhibitors of translation that blocked nascent peptide synthesis and progression within the ribosomal exit tunnel equally for all proteins. In this scenario, the drugs allow the synthesis of small nascent peptides reaching 5-12 amino acids until the prolongation is blocked leading to the dissociation from the ribosome of the peptidyl-tRNA by drop-off (Contreras and Vazquez, 1977; Lovmar et al., 2004; Odom



et al., 1991; Schlünzen et al., 2001; Tenson et al., 2003). Contrary to this view, a subset of specific peptides can actually stall translation in the presence of the drug by interacting with the exit tunnel of the ribosome. In this case, the peptidyl-tRNA remains bound to the ribosome, but peptide bond formation with an incoming aminoacyl-tRNA is prevented. Moreover, as presented in the introduction, recent ribosome profiling data have shown that macrolides and ketolides inhibit the prokaryotic ribosome in a sequence-dependent manner, as ribosomes stall on specific mRNA sequence motifs (Kannan et al., 2012, 2014; Sothiselvam et al., 2014, 2016). Therefore, macrolides and ketolides allow proteins which do not contain certain macrolide-dependent arrest motifs to be translated, while selectively blocking the synthesis of others. Among these, the “+X+” motif accounts for 80% of ketolide-specific arrest motifs and is largely responsible for macrolide-dependent translation inhibition as well. Here, the ribosome stalls when the codon encoding the middle X amino acid of the motif is in the ribosomal P site and the second + amino acid (Arg or Lys) is in the A site (**Figure 13**). Macrolides like erythromycin or azithromycin, which contain a cladinose moiety, block the synthesis of a wider array of amino acid motifs compared to ketolides, which explains their ability to inhibit the synthesis of a greater number of proteins (Almutairi et al., 2017; Kannan et al., 2012, 2014; Sothiselvam et al., 2016).

In addition to the inhibition activity differences observed between macrolides and ketolides, macrolides and ketolides also exhibit very different kinetic parameters for ribosome binding. While both macrolides and ketolides are slow-binding inhibitors and display similar association constants (*kon*), ketolides present a very low dissociation constant (*koff*); indeed, the alkyl-aryl side chain of ketolides is able for example to make several additional contacts with the ribosomal nucleobases of the exit tunnel, which strongly increase the binding stability of the drug (Svetlov et al., 2017). As a consequence, ketolides are able to bind almost irreversibly to the ribosome, which explain their bactericidal activity. Therefore, considering not only the affinity of macrolides/ketolides for the ribosome, but also the dynamics of their interaction with the target, should guide future efforts for drug development.

### **3.1.3. Macrolide resistance and erythromycin resistance methyltransferase genes (*erm*)**

Before going into specific details about macrolide resistance mechanisms, the phenomenon of antibiotic resistance spreading and the resistance mechanisms need to be shortly introduced. Bacteria are evolutionary optimized to survive to antibiotics, as it is a natural event. Indeed,

naturally produced antibiotics are estimated to have originated >40 million years ago, suggesting that antibiotic resistance should be similarly old and spread relatively easily (Levy and Marshall, 2004). Two criteria result in the circulation of resistance: first the antibiotic, which inhibits susceptible organisms and selects the resistant ones; and second the genetic resistance determinant in microorganisms selected by the antibiotic (Levy and Marshall, 2004). Antibiotic resistance emerges only when the two criteria come together in an environment or host. Selected resistance genes and their hosts spread under continued antibiotic selection to amplify and extend the problem to other hosts and other geographic locations. Therefore, the close proximity of antibiotics and resistant pathogens within hospitals strongly favors the propagation of resistance, thus leading to the apparition of nosocomial diseases. The spreading of resistance genes is possible because of their mobility; they can be transferred among different bacteria by means of mobile genetic elements such as plasmids, linear naked DNA fragments, transductor bacterial phages or transposons (Levy and Marshall, 2004). In the absence of these mobile genetic elements (which generally mediate high-level resistance), a step-wise progression from low-level to high-level resistance occurs in bacteria through sequential mutations within the bacterial chromosome (Levy and Marshall, 2004).

This wide variety of cellular mechanisms blocked by antibiotics is also reflected in the number of resistance mechanisms identified in bacteria in an attempt to survive them (**Figure 14**) (Levy and Marshall, 2004; Wilson, 2014, 2016). There are mostly four main modes of resistance employed by the bacteria to fight antibiotics:

- ***Membrane permeability:*** Resistance to all major classes of ribosome-targeting antibiotics is also conferred to some extent by efflux in all bacteria. In bacteria, antibiotics usually permeate the cell via outer membrane porins, such as TolC. This porin uses different adaptor proteins to recruit the inner membrane pumps for efflux. For example, the adaptor AcrA recruits the AcrB pump. The ArcAB–TolC complex has a broad substrate profile, including antibiotics such as chloramphenicol, fusidic acid and tetracycline (Weston et al., 2018). Additionally, Gram-negative bacteria have an outer layer (membrane) that protects them from their environment. These bacteria can use this membrane to selectively keep antibiotic drugs from entering.

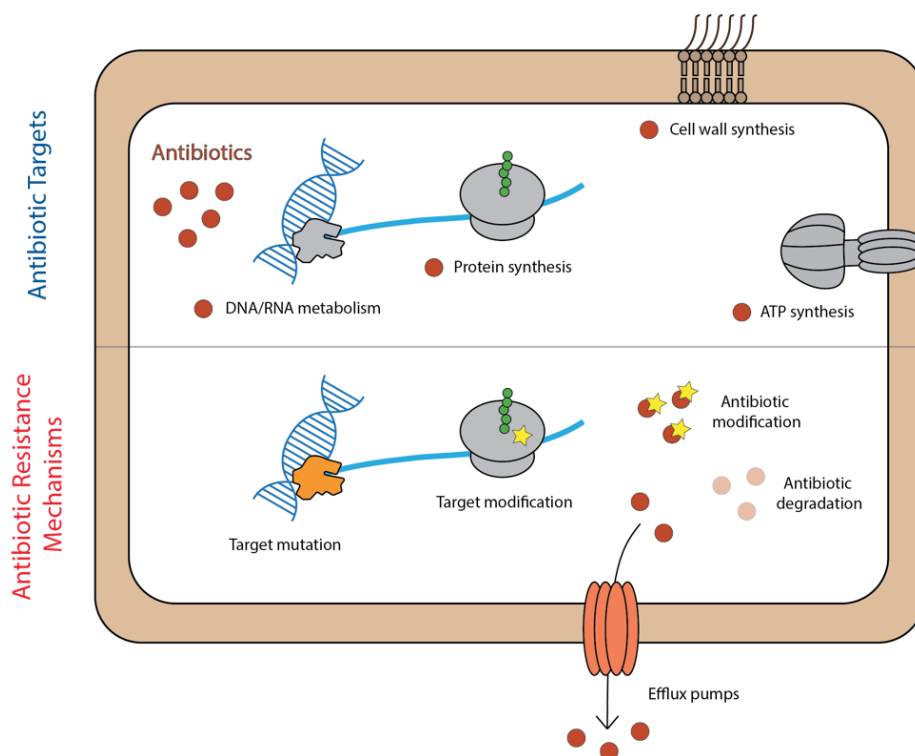


**Figure 14 : Antibiotic targets and antibiotic resistance mechanisms**

Schematic representation of the main targets of antibiotic in the bacterial cell (upper part) and the primary mechanisms of bacterial resistance to antibiotics (lower part).

- **Mutation and modification of the target:** Many antibiotic drugs are designed to bind and inhibit specifically a single cellular target. To avoid this inhibition, bacteria can mutate or modify the antibiotic's target. *Escherichia coli* bacteria with the *mcr-1* gene can add a compound to the outside of the cell wall so that the drug colistin cannot latch onto it (Hussein et al., 2021). The Erm methyltransferases mono- or di-methylate 23S rRNA nucleotide A2058 within the exit tunnel of the bacterial ribosome, preventing the binding of macrolides, ketolides, lincosamides and streptogramins antibiotics (Dinos, 2017; Vázquez-Laslop and Mankin, 2018a).
- **Drug modification and degradation.** Bacteria can modify or degrade the antibiotics with specific enzymes. Enterobacteria such as *Klebsiella pneumoniae*, produce enzymes called carbapenemases, which hydrolysis carbapenem drugs and most other beta-lactam drugs (Reyes et al., 2019).
- **Overexpression and protection of the target.** Resistance to some antibiotics arises as a result of increased expression of the target or of a mimic of the target because the mimic or target sequesters the drug, leaving some target molecules uninhibited. For example,

overexpression of an rRNA fragment resembling h34 of the 16S rRNA confers resistance to the antibiotic spectinomycin (Thom and Prescott, 1997). Another mechanism of resistance to ribosomal antibiotics involves factor-assisted protection of the drug target, like the TetM and TetO proteins, which confer resistance to tetracycline (Grossman, 2016; Nguyen et al., 2014). TetO and TetM are paralogues of the elongation factor-G protein (EF-G) and bind to tetracycline-stalled ribosomes to sterically dislodge the drug from its binding site (Arenz et al., 2015; Dönhöfer et al., 2012; Li et al., 2013).

In the context of macrolide antibiotics, one of the most important resistance mechanisms against macrolides involves modifications of the 23S rRNA. This type of resistance is mediated by erythromycin resistance methyltransferase (*erm*) genes, which encode various methyltransferases that prevent macrolides from binding to the ribosome by methylating 23S rRNA nucleotide A2058 (Kelemen et al., 1994; Kwak et al., 1991; Min et al., 2008; Sutcliffe and Leclercq, 2002; Tu et al., 2005; Weisblum, 1995). *Erm* genes are often found in plasmids or transposons in association with other resistance genes. Their expression can be constitutive and does not require the presence of macrolides, but this mode of resistance comes with a fitness cost for the bacteria because it affects the cellular proteome by impairing the translation of the host proteins. To avoid this problem, certain *erm* genes are inducible and ribosomal methylation only occurs after cells are exposed to macrolide antibiotics.

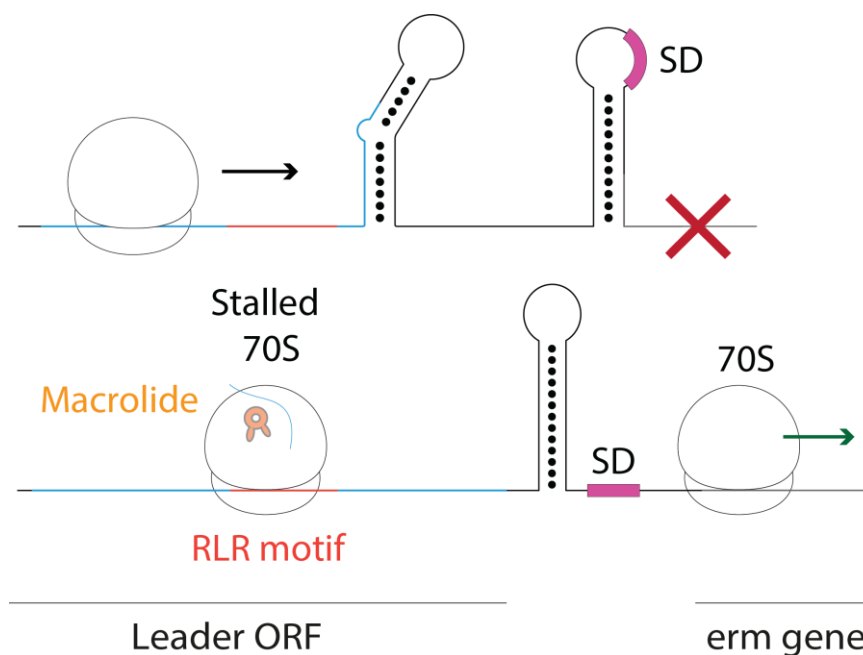


**Figure 15 : Macrolide-inducible resistance mechanism of *erm* genes**

An elegant regulatory mechanism based on antibiotic-dependent arrest motifs has been revealed for the induction of macrolide resistance (Dar and Sorek, 2017; Depardieu et al., 2007; Gryczan et al., 1980; Horinouchi and Weisblum, 1980). This mechanism relies on the presence of a short leader sequence located upstream of the resistance gene on the mRNA, which encodes a peptide containing a macrolide-dependent arrest motif. This arrest motif does not affect the progression of the ribosome on the mRNA in the absence of drug. However, the antibiotic-dependent stalling of the ribosome translating this leader sequence results in a conformational change within the intergenic region of the mRNA that frees the ribosome binding site of the downstream *erm* gene. The leader peptide and the ribosome that translates it therefore act as drug sensors capable of turning on the expression of the resistance gene in the presence of antibiotics (

**Figure 15).**

Although at first glance the general mechanism by which all inducible *erm* genes are regulated appears to be more or less the same, with antibiotic-dependent ribosome stalling occurring within the first ten codons of the *erm* leader, the sequence of individual leader peptides and their ability to sense macrolides and/or ketolides differ from system to system (**Table 2**) (Almutairi et al., 2015; Ramu et al., 2009; Sothiselvam et al., 2014). Yet, common signatures composed of three or four critical residues within a C-terminal “arrest domain” allow the classification of these leader peptides into several classes (Ramu et al., 2009):

- The “+X+” motif “RLR” is highly represented in several leader ORFs, most notably in the ErmDL peptide, which induces the expression of the *ermD* gene in the presence of both macrolide or ketolides. The “RLR” motif is also found in ErmQL, ErmDL, ErmXL and others, and in the leader ORFs of several *msr* genes encoding for ABC-F proteins able to remove the antibiotic from its binding site.
- The “IFVI” motif found originally in the ErmCL peptide regulates the expression of the *ermC* gene, and can stall the ribosome only in the presence of a macrolide such as erythromycin but not in presence of a ketolide such as telithromycin (Schmitz et al., 2002). This “IFVI” sequence is also found in the leader ORFs of several other *erm* genes: *ermAL2*, *ermGL*, *ermTL*, *ermYL* or *erm33L*.

- The “IAV” motif, relatively close to the first “IFVI” motif, regulates the expression of other *erm* genes, and is found in the ErmAL1 or Erm36L leader peptides. Like the “IFVI” motif, the “IAV” motif can stall the ribosome only in presence of cladinose-containing macrolides like erythromycin. A recent comparison between ErmCL and ErmAL1 modes of action showed that the identity of the residue at position -2 relative to the C-terminus of ErmAL1 and ErmCL nascent peptides is the key element that influences the properties of the A-site, which can become either restrictive in the case of ErmCL (F at position -2), or either selective in the case of ErmAL1 (A at position -2) (Ramu et al., 2011).

Name	Sequence	Accession No
IFVI		
<b>ErmAL2</b>	MGMFS <u>IFV</u> IERFHYQPNQK	X03216
<b>ErmCL</b>	MGIFS <u>IFV</u> ISTVHYQPNKK	V01278
<b>ErmGL2</b>	MGLYS <u>IFV</u> IETVHYQPNEK	M15332
<b>ErmTL</b>	MGIFS <u>IFV</u> INTVHYQPNKK	M64090
<b>ErmYL</b>	MGNCS <u>LFV</u> INTVHYQPNEK	AB014481
<b>Erm33L</b>	MGIFS <u>IFV</u> INTVHYQPNKK	AJ313523
SIAV		
<b>ErmAL1</b>	MCT <u>SIAV</u> VEITLSHS	X03216
<b>Erm36L</b>	MGSP <u>SIAV</u> TRFRRF	AF462611
RLR		
<b>ErmDL</b>	MTHSM <u>RLR</u> FPTLNQ	M29832
<b>ErmQL</b>	MIMNGGIAS <u>IRL</u> RR	L22689
<b>ErmXL</b>	MLISGTAFL <u>RLR</u> TNR	U21300
<b>Erm34L</b>	MHF <u>IRL</u> RFLVLNK	AY234334
Others		
<b>ErmBL</b>	MLVFQMRNVDKTSTVLKQTKNSDYADK	M11180
<b>ErmGL1</b>	MRIDDYCS	L42817
<b>ErmGL2</b>	MNHEYVLFSKNINIRKEMQ	L42817
<b>ErmVL</b>	MAANNAITNSGLGRGCAHSVRMRRGPGALTGPGSHTAR	U59450

**Table 2 : Leader peptides of macrolide resistance operons**

The arrest motif of each leader peptide is underlined, and the accession numbers furnished in the last column correspond to the GenBank code accession numbers. Adapted from (Ramu et al., 2009).

- Other motifs not matching the three above can also be found. For example, the 27 amino acid-long ErmBL peptide induces the expression of the *ermB* gene when the macrolide-bound or the ketolide-bound ribosome stalls on the 10<sup>th</sup> codon of *ermBL*, where the C-terminal “RNVDK” motif appears to be essential for stalling (Arenz et al., 2016).

CryoEM structure of 70S ribosomes translating the ErmBL peptide in presence of erythromycin showed that the antibiotic restricts the placement of the peptide within the exit tunnel and causes the reorientation and displacement of the C-terminus end of the nascent peptide, thus impeding peptide bond formation by increasing the distance between the attacking amide of the A-site lysine and the carbonyl carbon of the aspartate located in the P-site (Arenz et al., 2016).

I will now provide some background on two sets of Erm peptides, which constitute the focus of the work described in this part of my thesis.

### ErmDL

Ribosome inhibition by macrolides is a complex affair, as illustrated by ErmDL, an arrest peptide found in *Bacillus* strains (Kwak et al., 1991). The *ermDL* ORF encodes the 14 amino acid-long ErmDL peptide MTHSMRLRFPTLNQ. Mutation of codons 4–7 of *ermDL* negatively affect *ermD* induction, indicating that the sequence of this stretch of amino acids is critical for ribosome stalling on codon 8. Moreover, translation of the short truncated ErmDL leader peptide MRLR is sufficient to arrest the erythromycin-bound ribosome even though the nascent peptide is too short to establish a direct contact with the drug (Sutcliffe and Leclercq, 2002; Weisblum, 1995). Therefore, it appears that protein synthesis stops because the macrolide prevents peptide bond formation rather than physically blocking the progression of the peptide inside the exit tunnel. This suggests that the binding of the antibiotic modifies the PTC such that it is unable to catalyze peptide bond formation when certain combinations of aminoacyl- and peptidyl-tRNAs occupy the A and P sites (Kannan et al., 2014; Sothiselvam et al., 2014, 2016). The size and the chemical properties of the amino acid side chains at the PTC ultimately seem to matter more than the overall size of the peptide in the tunnel, showing that the old “plug in the bottle” model for macrolide inhibition is incomplete (Sothiselvam et al., 2016). But if the “RLR” motif is sufficient to induce arrest, then what role does the N-terminal part of ErmDL, which is located in the exit tunnel and can therefore interact directly with the drug, play in drug-induced ribosomal arrest?

## ErmCL and ErmAL1

Another example of the complexity of macrolide-dependent translation inhibition is the mechanism by which the nascent ErmCL and ErmAL1 peptides interact with cladinose-containing macrolides and the ribosome to render the A-site highly selective (ErmAL1) and even restrictive (ErmCL) for certain amino acids, thereby arresting translation (Ramu et al., 2011). As described earlier, the “IFVI” motif is responsible for the arrest of ErmCL translation in the presence of macrolide, when the 9th codon of *ermCL* (I9) is located in the P-site of the ribosome and the conformation of the PTC prevents peptide bond formation from taking place between I9 and the incoming S10 (Gryczan et al., 1980; Horinouchi and Weisblum, 1980; Vazquez-Laslop et al., 2008). Mutating 23S rRNA nucleotides A2062 of the ribosomal tunnel to uridine or cytosine, or the absence of the cladinose sugar of erythromycin both abolish ErmCL stalling (Vazquez-Laslop et al., 2008). Collectively, these data suggest a complex network of interactions between the ErmCL peptide, the cladinose moiety of macrolide, and the exit tunnel, which forces the PTC to adopt a restrictive conformation to inhibit peptide bond formation. The cryoEM structure of *E. coli* ribosomes translating the ErmCL peptide in presence of erythromycin provided strong insights into the mechanism by which the nascent peptide promotes translational arrest (Arenz et al., 2014a). In fact, the binding of erythromycin to the ribosomal exit tunnel promotes various rearrangements of the ErmCL peptide conformation but also of 23S rRNA nucleotides A2062, A2602 and U2585 (Arenz et al., 2014a). In this situation, ErmCL forces U2585 to adopt an alternative flipped conformation, which also displaces A2062 and the 3'CCA end of the P-site tRNA from their canonical positions. These conformational changes are not favorable for the stable accommodation of the Ser-tRNA within the A-site of the PTC and thus inhibit peptide bond formation (Arenz et al., 2014a). These observations contrast with the case of the ErmBL arrest peptide. Indeed, contrary to ErmBL, ErmCL is able to directly interact with erythromycin within the exit tunnel, because the peptide adopts a different path, which in the case of the ErmBL nascent chain stabilizes the position of U2585 in the unaccommodated state; U2585 in this case does not impede the binding of the A-site tRNA, but hinders the proper accommodation of the A-site tRNA and thus inhibits peptide bond formation.

To understand how the PTC is inactivated by the nature of the ErmCL residues located within the exit tunnel of the ribosome in presence of macrolides, a comparison was done with the case of the ErmAL1 arrest peptide (Ramu et al., 2011). The *ermA* gene is regulated by two distinct



upstream ORFs: the first one encodes the ErmAL1 leader peptide, containing an “IAVV” arrest motif, and the second one codes for the ErmAL2 peptide which contains the same “IFVI” arrest motif found in ErmCL (Min et al., 2008; Murphy, 1985a; Ramu et al., 2011; Sandler and Weisblum, 1988). The *ermA* transcript has the potential to fold into a secondary structure that sequesters the ribosome binding site of *ermAL2* and *ermA*. By analogy with *ermC*, it was suggested that drug-dependent ribosome stalling at the *ermAL1* ORF triggers translation of *ermAL2* and that subsequent drug-dependent stalling by the “IFVI” motif encoded by *ermAL2* allows for activation of *ermA* expression. In the case of ErmAL1, the ribosome stalls when the eighth codon (V8) is located in the P-site; however, unlike ErmCL/ErmAL2 stalling, the identity of the A site (ninth) amino acid of ErmAL1 dramatically affects the efficiency of stalling (Ramu et al., 2011). As the sequence of the 15 amino acid ErmAL1 peptide is different from both ErmCL and ErmAL2, but shares a common hydrophobic core, it makes it an attractive model for gaining new insights into the molecular mechanisms of drug- and nascent peptide-dependent ribosome stalling. For nomenclature purposes, the P-site position of the ribosome, representing actually the last C-terminus residue of the nascent peptide will be designed as the “0” position, the amino acid attached to the A-site tRNA will be named as the “+1” position and the E-site corresponding actually to the penultimate residue of the nascent peptide will correspond the “-1” position. The other residues of the nascent peptide will follow this nomenclature and will be designed as the “-2” or “-3” etc. positions, where the most negative positions correspond to the N-terminus part of the nascent peptide. In addition, the selectivity of the PTC is strongly influenced by the nature of the amino acid incorporated at the position -2 of the nascent peptide attached to the peptidyl tRNA located within the P-site (F7 in ErmCL or A6 in ErmAL1), which can render the A-site of the PTC either selective as in ErmAL1 or either restrictive as in ErmCL (Ramu et al., 2011). Moreover, a single mutation F7 to A at the position -2 in the ErmCL nascent peptide, is sufficient to alter the properties of the A-site from restrictive (as in the wild-type ErmCL stalled complex) to selective (as in the ErmAL1 complex) (Ramu et al., 2011).

### 3.2. Methodological overview

In the third part of this thesis, I will focus on understanding the molecular mechanisms by which the ErmDL and ErmCL/ErmAL1 peptides block their own translation. On one hand, ErmDL is a perfect example to illustrate and understand the general mode of action of macrolide antibiotics, and the strong specificity of ketolides for the “+X+” motifs. On the other hand, the

comparison of the ErmCL and ErmAL1 mechanisms illustrates how the sequence of the nascent peptide within a drug-bound ribosome can modulate PTC activity to fine-tune the expression of resistance genes. Moreover, ErmCL and ErmAL1 can only undergo translational arrest in the presence of cladinose-containing macrolides like erythromycin, making them ideal models for studying how the structure of the antibiotic affects the stalling process. In addition, an in-depth analysis of both systems will shed light on the process of activation of inducible resistance genes. Understanding how the Erm leader peptides sense antibiotics to regulate the expression of resistance genes may ultimately help develop drugs that prevent such activation from taking place.

To understand the contribution of each residue within the macrolide-dependent arrest motifs of *erm* leader sequences, but also to assess the role of the evolutionary preserved N-terminal segment, I employed inverse toeprinting and performed a deep mutational scan of *ermDL*, *ermCL* and *ermAL1* sequences. To assay the *erm*-specific translation inhibition of free and macrolide- or ketolide-bound ribosomes engaged, I designed focused libraries encoding for single- or double- mutant *ermDL*, *ermAL1* or *ermCL* transcripts. The protocol was done as described in the “materials and methods” paragraph of the *ermDL* manuscript (section 3.3.1) or in section 3.3.2 for the work done on *ermAL1* and *ermCL*.

### 3.3. RESULTS

#### 3.3.1. Structural and mechanistic basis for translation inhibition by macrolide and ketolide antibiotics

To understand the role of codons 4-7 of *ermDL* in the macrolide-dependent induction mechanism of *ermD*, but also understand how the short MRLR peptide is sufficient to arrest the ribosome, I used inverse toeprinting, by systematically mutating the sequence of the macrolide- or ketolide-dependent arrest ErmDL peptide. I obtained new insights into its mode of action and revealed the main mechanism by which macrolide antibiotics inactivate the ribosome in this case. A collaborative combination of biochemical, structural and molecular dynamics techniques, shed light onto the mechanism by which +X+ motifs lead to stalling in the presence of macrolides and ketolides, but could also explain the drug-dependent stalling on *ermDL* leading to the induction mechanism of *ermD*. This work was published in 2021 and is presented in the following manuscript.









ARTICLE



<https://doi.org/10.1038/s41467-021-24674-9>

OPEN

# Structural and mechanistic basis for translation inhibition by macrolide and ketolide antibiotics

Bertrand Beckert<sup>1,5</sup>, Elodie C. Leroy <sup>2,5</sup>, Shanmugapriya Sothiselvam<sup>3,5</sup>, Lars V. Bock <sup>4,5</sup>✉, Maxim S. Svetlov<sup>3</sup>, Michael Graf<sup>1</sup>, Stefan Arenz<sup>1</sup>, Maha Abdelshahid<sup>1</sup>, Britta Seip <sup>2</sup>, Helmut Grubmüller <sup>4</sup>, Alexander S. Mankin <sup>3</sup>, C. Axel Innis <sup>2</sup>✉, Nora Vázquez-Laslop <sup>3</sup>✉ & Daniel N. Wilson <sup>1</sup>✉

Macrolides and ketolides comprise a family of clinically important antibiotics that inhibit protein synthesis by binding within the exit tunnel of the bacterial ribosome. While these antibiotics are known to interrupt translation at specific sequence motifs, with ketolides predominantly stalling at Arg/Lys-X-Arg/Lys motifs and macrolides displaying a broader specificity, a structural basis for their context-specific action has been lacking. Here, we present structures of ribosomes arrested during the synthesis of an Arg-Leu-Arg sequence by the macrolide erythromycin (ERY) and the ketolide telithromycin (TEL). Together with deep mutagenesis and molecular dynamics simulations, the structures reveal how ERY and TEL interplay with the Arg-Leu-Arg motif to induce translational arrest and illuminate the basis for the less stringent sequence-specific action of ERY over TEL. Because programmed stalling at the Arg/Lys-X-Arg/Lys motifs is used to activate expression of antibiotic resistance genes, our study also provides important insights for future development of improved macrolide antibiotics.

<sup>1</sup>Institute for Biochemistry and Molecular Biology, University of Hamburg, Hamburg, Germany. <sup>2</sup>Univ. Bordeaux, Centre National de la Recherche Scientifique, Institut National de la Santé et de la Recherche Médicale, ARNA, UMR 5320, U1212, Institut Européen de Chimie et Biologie, Pessac, France. <sup>3</sup>Center for Biomolecular Sciences, University of Illinois at Chicago, Chicago, IL, USA. <sup>4</sup>Theoretical and Computational Biophysics Department, Max Planck Institute for Biophysical Chemistry, Göttingen, Germany. <sup>5</sup>These authors contributed equally: Bertrand Beckert, Elodie C. Leroy, Shanmugapriya Sothiselvam, Lars V. Bock. ✉email: [lbock@mpibpc.mpg.de](mailto:lbock@mpibpc.mpg.de); [axel.innis@inserm.fr](mailto:axel.innis@inserm.fr); [nvazquez@uic.edu](mailto:nvazquez@uic.edu); [daniel.wilson@chemie.uni-hamburg.de](mailto:daniel.wilson@chemie.uni-hamburg.de)

The ribosome and protein synthesis represent one of the major targets in the bacterial cell for clinically-relevant antibiotics<sup>1,2</sup>. One important family of ribosome-targeting antibiotics are the macrolides, which display broad-spectrum activity against many Gram-positive bacteria, and have been in clinical usage since the discovery of the founding member erythromycin (ERY) in the 1950s<sup>3,4</sup>. ERY contains a 14-membered macrolactone ring and is decorated with cladinose and desosamine sugars at the C3 and C5 positions, respectively (Fig. 1a). The emergence of antibiotic resistance to ERY and other macrolide antibiotics prompted the development of semi-synthetic derivatives, including the third generation ketolides, such as telithromycin (TEL)<sup>3,4</sup>. Like ERY, TEL contains a 14-membered macrolactone ring and the C5-desosamine, but lacks the C3-cladinose, which is replaced with a keto group (hence the name ketolide) (Fig. 1b). Additionally, TEL contains an extended alkyl-aryl side chain (Fig. 1c) linked via a carbamate to the C11 and C12 of the macrolactone, which is important for its bactericidal activity<sup>5,6</sup>. Structures of macrolides and ketolides in complex with the ribosome revealed that these compounds bind in a similar fashion within the nascent polypeptide exit tunnel (NPET)<sup>7–10</sup>. The presence of the macrolides narrows the diameter of the NPET, which reinforced the prevailing model that these drugs act as plugs for the tunnel and thereby inhibit translation of every protein indiscriminately (reviewed by ref. 11). However, this oversimplified view of macrolide action has been challenged in the past years with the finding that macrolides and ketolides are not global inhibitors of translation, but rather selectively interfere with the translation of a specific subset of proteins<sup>12,13</sup>.

Ribosome profiling analysis indicates that macrolides and ketolides can arrest translation at specific sequence signatures within the nascent polypeptide chain<sup>14,15</sup>. Interestingly, the specificity of action was shown to depend on the chemical structure of the macrolide, such that Arg/Lys-X-Arg/Lys, or so called “+X+” motifs (where + represent amino acids with positive charges and X is any amino acid) account for almost 80% of the strongest arrest sites in the presence of the ketolide TEL<sup>14</sup>. While macrolides, like ERY, also arrest translation at +X+ motifs, a more diverse range of arrest motifs, such as X+P, XDK, and XPW is observed<sup>14–16</sup>. In the

macrolide-stalled ribosome, the arrest motif is located at the peptidyl-transferase center (PTC) and thus the macrolides inhibit translation by preventing the ribosome from catalyzing peptide bond formation<sup>4,13,14</sup>. For an Arg-Leu-Arg (+X+) motif, the ribosome stalls because the peptidyl-Arg-Leu-tRNA located at the P-site cannot undergo peptide bond formation with the incoming Arg-tRNA at the A-site<sup>4,13,14,17,18</sup>. For the +X+ motif, it appears that in addition to the positive charge of the Arg and Lys, the length of the side chain may play a role<sup>18</sup>, which may explain why Arg-X-Arg motifs induce an overall stronger arrest than Lys-X-Lys<sup>14</sup>. Importantly, because the arrest motif is located at the PTC, it is perceived as unable to establish direct contact with the macrolide bound deeper within the NPET, suggesting that macrolides exert their inhibitory action via the nascent chain and/or allosterically via nucleotides of the 23S rRNA<sup>4,13,17</sup>.

Importantly, arrest motifs, such as the +X+ motif, are found in many regulatory short upstream open reading frames (leader uORFs) that play a critical role in regulating the expression of macrolide-resistance genes, including rRNA methyltransferases (Erms)<sup>17,19,20</sup>. Erms methylate the N6 of A2058 (*E. coli* numbering used throughout) of the 23S rRNA<sup>21</sup>, which reduces the affinity of macrolides for their binding site by precluding water-mediated interactions between the desosamine sugar of the macrolide and A2058<sup>10</sup>. While Erms represent one of the most important mechanisms of resistance to macrolide antibiotics, the methylation of A2058 also confers a fitness cost to the bacteria<sup>22</sup>, therefore, Erm expression is tightly regulated via macrolide-dependent translation arrest<sup>19,21</sup>. One well-characterized example is the ErmDL leader uORF that regulates expression of the ErmD methyltransferase<sup>23–25</sup>. In the absence of ERY, ribosomes translate ErmDL, but the expression of the downstream ErmD methyltransferase is disfavored, presumably because of the unfavorable mRNA secondary structure (Fig. 1c). By contrast, in the presence of ERY, ribosomes become stalled at the Arg-Leu-Arg (+X+) arrest motif located between residues 6–8 of ErmDL, which in turn triggers mRNA refolding thereby favoring expression of the ErmD methyltransferase (Fig. 1d).

Despite the importance of the +X+ motif for general macrolide and ketolide inhibition, as well as the critical role of the +X+

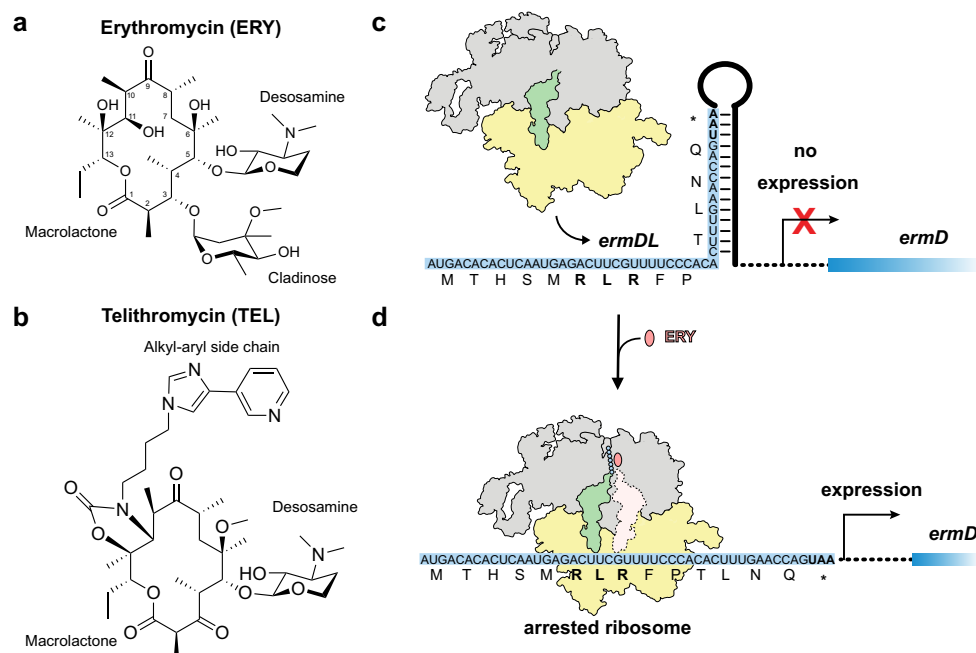


**Fig. 1** Macrolide-dependent regulation of *ermD* expression. **a, b** Chemical structures of **a** erythromycin (ERY) and **b** telithromycin (TEL). **c, d** Schematic of the *ermDL*-mediated regulation of the expression of *ermD* in the **c** absence and **d** presence of macrolide antibiotic.

motif for inducible Erm expression, a structural and molecular basis for how the drug, the ribosome and the +X+ motif interplay to mediate translational arrest has been lacking. Here, we employ the ErmDL leader uORF as a model system to study translational arrest at +X+ motifs in the presence of the macrolide ERY and the ketolide TEL. Using a combination of toeprinting and inverse toeprinting assays, we demonstrate that an intact +X+ motif is critical for ErmDL stalling in the presence of TEL, whereas it is dispensable for ERY-mediated programmed translation arrest. A molecular basis for these findings is revealed by cryo-EM structures of translating ribosomes stalled on the Arg6-Leu7-Arg8 sequence of ErmDL in the presence of ERY or TEL. In these structures, the drugs promote a conformation of the ErmDL nascent chain such that the side chain of Arg6 extends directly into the A-site pocket, where it would sterically clash with an incoming Arg-tRNA. In comparison to TEL, the conformation of ErmDL is further compacted by the presence of cladinose of ERY, to such an extent that the PTC of the ribosome cannot adopt the induced conformation necessary for accommodation of the A-site tRNA, thus explaining why the +X+ motif is dispensable for translational arrest in the presence of ERY. Collectively, our findings provide not only structural insights into the mechanism by which macrolides and ketolides interplay with the nascent chain to promote translation arrest, but also illustrate how specific chemical features of these antibiotics contribute to differentially modulate the conformation of the nascent chain and dramatically alter the mechanism of inhibition.

## Results

**The +X+ arrest motif is critical for ErmDL stalling in the presence of TEL.** Induction of *ermD* by ERY had been demonstrated previously<sup>23–25</sup>, but it has remained unknown whether the ketolide TEL also serves as an inducer. To address this, we constructed a reporter plasmid containing the intact *ermDL* gene, the entire 276-nucleotide *ermDL-ermD* intergenic region as well as the first six codons of *ermD* fused in frame with the *lacZα* reporter (Fig. 2a) and introduced it into *E. coli* cells. The blue halo observed in a drug-diffusion assay<sup>26</sup> suggests that not only ERY, but also TEL can readily activate the expression of the inducible *ermD* (Fig. 2a), possibly due to its ability to mediate programmed translation arrest within the *ermDL*-coding sequence, as reported previously for ERY<sup>17,23–25</sup>. Indeed, toeprinting analysis (Fig. 2b) showed that in a cell-free translation system, TEL directs ribosome arrest during translation of the Arg6-Leu7-Arg8 motif of ErmDL, when the Leu7 and Arg8 codons of the *ermDL* ORF are positioned at the P- and A-sites, respectively, of the stalled ribosome (Fig. 2c, d). By contrast, TEL was unable to stall the ribosome when the Arg6 and Arg8 codons of the *ermDL* ORF were mutagenized individually or simultaneously to Ala codons, or when all codons of the Arg-Leu-Arg sequence were changed to Ala (Fig. 2c, d). These results demonstrate the critical importance of the integrity of the Arg6-Leu7-Arg8 motif for TEL-mediated ribosome stalling on *ermDL*.

To evaluate more precisely the impact of the +X+ motif on TEL-dependent stalling and to also explore the possible role of the preceding N-terminal segment of the nascent ErmDL peptide, we employed inverse toeprinting<sup>16</sup> to perform a deep mutational scan of *ermDL*. Like ribosome profiling<sup>27</sup>, inverse toeprinting can determine, with codon resolution, the position of paused ribosomes on a library of mRNA transcripts. This in vitro technique exploits a highly processive 3' to 5' RNA exonuclease (RNase R), such that the leading ribosome on each transcript protects the entire mRNA upstream of the pause site from degradation (Fig. 2e and Supplementary Fig. 1a). Therefore, a priori knowledge of the transcript sequences is not required and

custom libraries of any complexity can be used. Here, we translated an mRNA library encoding all possible single amino acid substitutions at each of the positions 2–8 of ErmDL in the absence or presence of TEL, and produced ribosome-protected inverse toeprints. We then computed the change in each variant's frequency observed by deep sequencing upon addition of TEL, yielding scores for 132 of the 134 possible ErmDL variants (Supplementary Fig. 1b), which reflect their effect on ribosome stalling. These scores followed a bimodal distribution (Supplementary Fig. 1c), with all tested mutations either having a neutral ( $> -1.5$ ) or detrimental ( $< -1.5$ ) effect on TEL-dependent stalling (Fig. 2f and Supplementary Fig. 1b). As expected, the mutation of Arg at positions 6 or 8 of ErmDL to residues other than Lys dramatically reduced TEL-dependent stalling (Fig. 2f and Supplementary Fig. 1b). We also noted that the mutation of Met5 to Pro, to a negatively charged (Asp, Glu), or to small polar amino acids (Ser, Thr) also negatively impacted stalling (Fig. 2f and Supplementary Fig. 1b). Thus, the results of inverse toeprinting confirm that TEL-dependent stalling is entirely dependent on the +X+ motif, in accordance with the general trends of ketolide-dependent arrest observed in vivo<sup>14</sup>.

## Cryo-EM structure of ErmDL-TEL-stalled ribosome complex.

To ascertain how TEL induces stalling at +X+ motifs, we determined a cryo-EM structure of an ErmDL-TEL-stalled ribosomal complex (SRC). To achieve this, an *E. coli* in vitro translation system was employed to translate a bicistronic *2XermDL* mRNA template in the presence of 20  $\mu$ M TEL, similar to the approach described previously for generating ErmBL-SRCs and ErmCL-SRCs<sup>28–30</sup>. The resulting disomes of the ErmDL-TEL-SRC were isolated by sucrose gradient ultracentrifugation, converted to monosomes, and analyzed using single-particle cryo-EM (see “Methods” section). In silico sorting of the cryo-EM data revealed that the majority (76.4%) of ribosomes contained a P-site tRNA, but were heterogeneous with respect to presence or absence of A-site and/or E-site tRNAs (Supplementary Fig. 2a). We refined two subclasses, one containing only P-site tRNA (26.2%), and a second with stoichiometric A-site and P-site tRNAs (21.7%), yielding final reconstructions of the ErmDL-TEL-SRCs (Fig. 3) with average resolutions of 3.1 Å (Supplementary Fig. 2b) and local resolution extending towards 2.8 Å in the core of the large 50S subunit (Supplementary Fig. 2c, d). The density for the P-site tRNA was consistent with the presence of tRNA<sup>Leu(GAG)</sup> base-pairing with the 7th codon (Leu CUU) of the *ermDL* mRNA (Supplementary Fig. 2e, f). Additional density was also observed for the variable region of tRNA<sup>Leu(GAG)</sup> comprising a four G-C base pair stem and a four nucleotide (AAUA) loop (Supplementary Fig. 2e, f), which is shorter or absent in many other tRNAs, such as tRNA<sup>fMet</sup> and tRNA<sup>Phe</sup>. Particularly well-resolved was the density for the CCA-end of the P-site tRNA, as well as for the ketolide TEL, the latter bound in an identical position to that observed previously in vacant ribosomes<sup>7,9,10</sup> (Supplementary Fig. 2g, h). The density for the majority of the ErmDL nascent polypeptide chain was also well-resolved enabling Thr2 to Leu7 to be modeled de novo, except for Met1 that was apparently flexible precluding the N-terminal amino acid from being visualized (Fig. 3b and Supplementary Fig. 2g, h). The density for the side chain of Arg6 of ErmDL suggests that it adopts two alternative conformations, a minor one oriented back towards the A76 of the tRNA and a major one that stacks upon the U2504-C2452 base pair within the 23S rRNA (Fig. 3b, c and Supplementary Fig. 2h). The latter conformation of Arg6 of ErmDL is additionally stabilized by potential hydrogen bond interactions with the nucleobase of G2061 (Fig. 3c). We note that the density of the P-site tRNA, ErmDL, TEL and PTC nucleotides are identical (within the limits of the resolution) in the absence or presence of A-site tRNA. In the structure of the A-site tRNA-containing complex, the



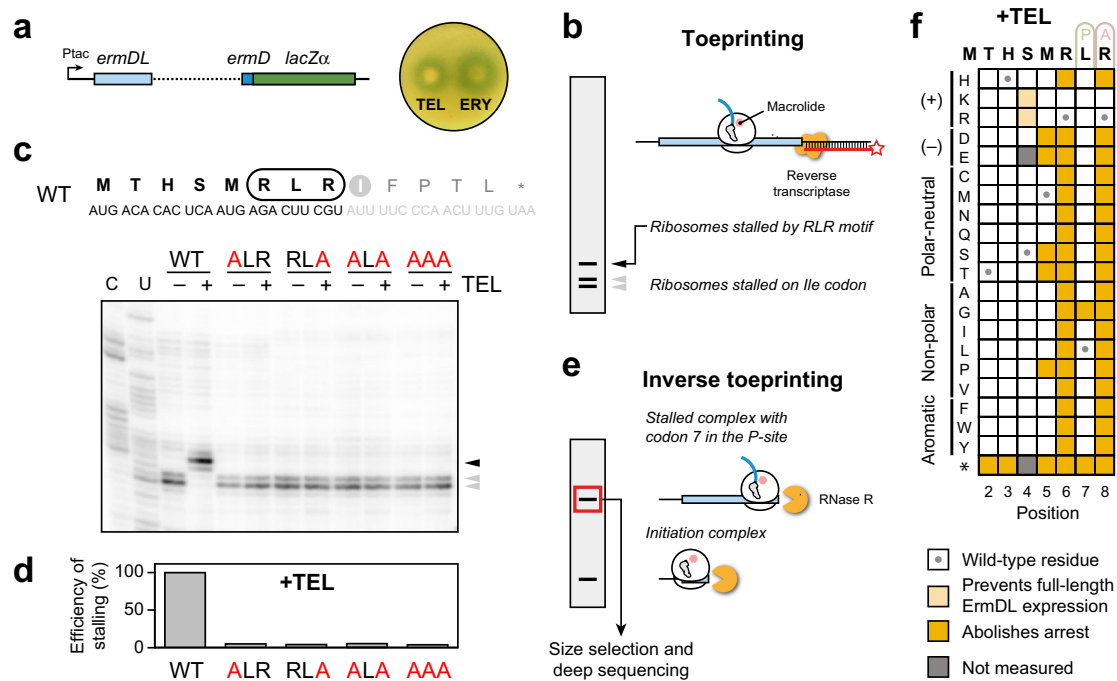


**Fig. 2** Sequence dependence of translation arrest at *ermDL* in response to TEL. **a** Induction of expression of the *ermDL* reporter by macrolides. Left: schematic of the *ermDL-ermD1-6-lacZα* reporter construct. Right: Expression of the reporter, visualized as blue halos, is induced by diffusion of telithromycin (TEL) or erythromycin (ERY) on a lawn of *Escherichia coli* cells grown on LB agar reporter plates. **b** Overview of the toeprinting approach. Ribosomes that stall at a macrolide arrest motif (such as RLR) due to the presence of a macrolide antibiotic in a cell-free translation reaction produce a long cDNA band. Ribosomes that fail to stall at the arrest sequence are trapped at a downstream “hungry” codon (the trap codon) and produce a shorter cDNA band. **c** Top: The sequence of the *ermDL* ORF used for in vitro toeprinting assays. The RLR (Arg<sub>6</sub>-Leu<sub>7</sub>-Arg<sub>8</sub>) motif encoded in the ORF is highlighted. The original *ermDL* ORF was modified to contain the trap codon Ile-AUU (circled in gray) at position 9. Bottom: Toeprinting assay testing TEL-induced translation arrest at *ermDL* sequences, where the RLR motif is intact (wt) or contains the indicated Ala mutations. The toeprint band produced by TEL stalled ribosomes with the Leu<sub>7</sub> codon at the P site is indicated by a black arrow. The toeprint bands of ribosomes stalled at codon 8 due to the lack of Ile-tRNA (due to the presence of the Ile-tRNA synthetase inhibitor mupirocin in the reactions), are shown with gray arrows. C-specific and U-specific sequencing reactions are shown. **d** Efficiency of TEL-mediated ribosome stalling estimated by quantifying the relative intensities of the toeprint bands of codons 7 and 8 in the mutant templates relative to those in the wt template. Stalling efficiency at the wt template was set to 100%. Circles indicate the values of two independent experiments, whereas the bar represents the mean. **e** Overview of the inverse toeprinting methodology. **f** Sequence-function map for seven positions of the ErmDL peptide translated in the presence of TEL, where mutations that abolish arrest (score < -1.5) are shown in yellow, as described in Supplementary Fig. 1. The ribosomal P (green) and A (pink) sites are indicated above the wild-type ErmDL sequence. Variants in gray were not measured and cells marked with a circle correspond to the wild-type amino acid. Mutations S4K and S4R lead to the appearance of a (K/R)MR arrest motif at position 4 that prevents the synthesis of the full peptide and leads to spuriously low scores for these two variants.

acceptor arm of the A-site tRNA was well-resolved and had accommodated on the 50S subunit, however, the CCA-end (and attached Arg residue) appeared to be flexible and no density was observed within the A-site pocket at the PTC.

Overall, the path of ErmDL in the presence of TEL is very different from that observed for other nascent polypeptide chains (Supplementary Fig. 3a–h), including the macrolide-dependent stallers ErmBL and ErmCL (Supplementary Fig. 3a–d)<sup>28–30</sup>. Rather than extending directly into the NPET as other nascent polypeptide chains (Supplementary Fig. 3a–h), ErmDL is oriented in a way that the C-terminal residues reach towards the A-site region then curl back past the desosamine sugar of TEL, such that the N-terminal residues can then extend into the lumen of the NPET (Fig. 3b). As a consequence of this conformation, in its predominant orientation (see above) the side chain for Arg<sub>6</sub> extends directly into the A-site pocket at the PTC, where it would be predicted to clash with the arginyl (or lysinyl) moiety of an aminoacyl-tRNA (aa-tRNA) accommodated at the A-site (Fig. 3d and Supplementary Fig. 4a). By contrast, computationally substituting the Arg<sub>8</sub> of the A-site tRNA with Ala (Fig. 3e) or mutating Arg<sub>6</sub> to Ala (Fig. 3f) relieves the steric clash consistent with our functional assays demonstrating that, substitutions of Arg<sub>6</sub> or Arg<sub>8</sub> to Ala dramatically reduces the

efficiency of ErmDL-mediated stalling in the presence of TEL (Fig. 2c, d, f). However, steric interference is apparently not sufficient to mediate stalling since superimposing an accommodated Phe-tRNA in the A-site from the pre-attack state<sup>31</sup> also leads to clashes with Arg<sub>6</sub> (Supplementary Fig. 4b), yet inverse toeprinting indicates that substitutions of Arg<sub>8</sub> to bulky amino acids, including Phe, reduces the efficiency of stalling (Fig. 2f). Similarly, while substitutions of Arg<sub>6</sub> of ErmDL to Lys would be predicted to produce clashes with Arg<sub>8</sub>-tRNA in the A-site (Supplementary Fig. 4c), consistent with the stalling observed by inverse toeprinting (Fig. 2f), we also note that Arg<sub>6</sub> to Phe substitutions would also produce clashes with Arg<sub>8</sub>-tRNA in the A-site (Supplementary Fig. 4d), yet the inverse toeprinting results show that substitutions of Arg<sub>8</sub> to bulky amino acids, including Phe, also reduces the efficiency of stalling (Fig. 2f). Thus, in addition to the size, it appears that the charge of the residue in the 6th and 8th positions of ErmDL may be important for stalling in the presence of TEL, as proposed in a previous study examining the macrolide-dependent stalling mechanism of a short MRLR peptide<sup>18</sup> (see also Supplementary Notes and Supplementary Fig. 4e–h).

Our finding that the Arg-Leu-Arg (+X+) motif within ErmDL is critical for stalling in the presence of TEL is likely a manifestation of

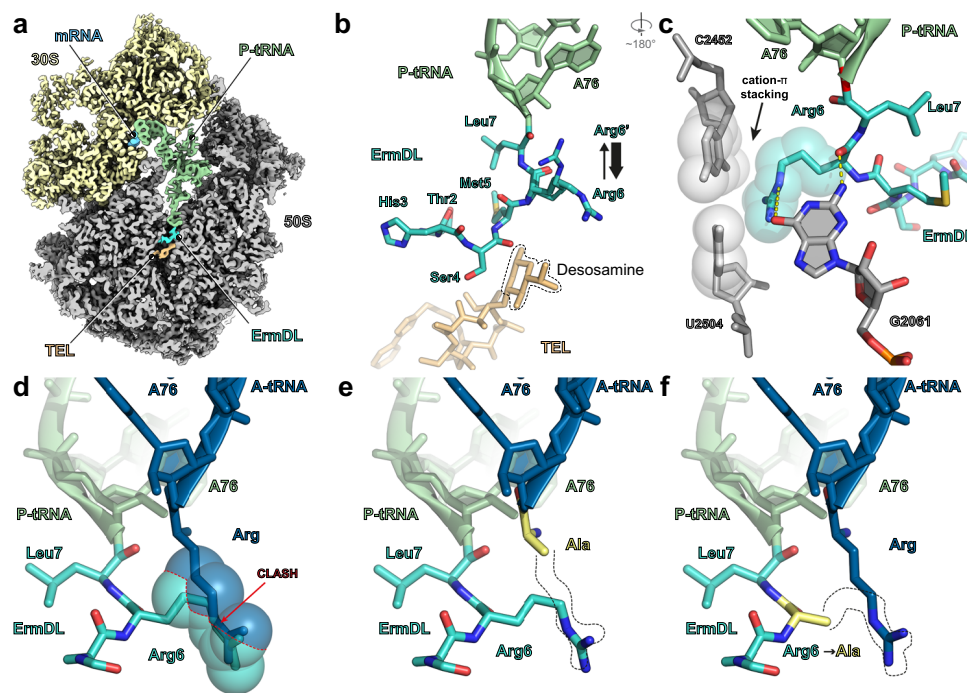


**Fig. 3 Cryo-EM structure of ErmDL-TEL-SRC.** **a** Transverse section of the cryo-EM map of the ErmDL-TEL-SRC with isolated densities highlighting the 30S (yellow) and the 50S (gray) subunits, P-site tRNA (green), mRNA (gray), ErmDL nascent chain (cyan) and telithromycin (TEL, orange). **b** Molecular model of the ErmDL nascent chain (cyan), P-site tRNA (green) and telithromycin (TEL, orange) from the ErmDL-TEL-SRC. The desosamine sugar of TEL is highlighted with dashed line and the alternative conformations of Arg6 are shown with weighted arrows indicating relative stoichiometries based on density. **c** Interactions of Arg6 of ErmDL with 23S rRNA, including stacking interaction with the U2504-C2452 base pair (arrowed). Dashed lines to G2061 indicate potential hydrogen bonding with Arg6. **d** Superimposition of the ErmDL-TEL-SRC with an A-site Arg-tRNA in silico mutated from the ErmBL A-site Lys-tRNA (blue, PDB 5JTE)<sup>28</sup>, illustrating that Arg6 of ErmDL nascent chain clashes (indicated by spheres) with the Arg side chain of the accommodated A-site tRNA. **e, f** In silico mutations of **e** A-site tRNA to Ala (based on Phe-tRNA from pre-attack state PDB ID 1VY7)<sup>31</sup>, and **f** Arg6 to Ala mutation in ErmDL nascent chain.

a more general phenomenon revealed by Ribo-seq data showing that ribosomes stall most often at Arg-X-Arg (+X+) motifs in the presence of TEL<sup>14</sup>. By contrast, while Ribo-seq data indicate that ribosome stalling also occurs at +X+ motifs in the presence of ERY<sup>14,15</sup>, the prevalence of stalling at +X+ motifs was much lower than for TEL and other sequence motifs were associated with the sites of ERY-induced arrest. These observations prompted us to assess the importance of the Arg-Leu-Arg (+X+) motif in ErmDL for ribosome stalling in the presence of ERY.

**The RLR motif is dispensable for ErmDL stalling in the presence of ERY.** Similar to TEL and consistent with previous reports<sup>23–25</sup>, ERY readily activates the expression of the *ermDL-ermD<sub>1–6</sub>-lacZa* reporter in *E. coli* cells (Fig. 2a). Also in line with previously published data<sup>17</sup>, ERY stalls the ribosome at the Arg6-Leu7-Arg8 motif of *ermDL* during in vitro translation (Fig. 4a, b). However, in stark contrast with the TEL-induced translation arrest (Fig. 2c, d, f and Supplementary Fig. 1b), the integrity of the +X+ motif is less critical for ERY-dependent ribosome stalling, since Ala mutations of either Arg6 or Arg8 of *ermDL* only minimally affected stalling (Fig. 4a, b). Even the simultaneous Ala mutations of both Arg6 and 8 resulted in a fairly efficient arrest (nearly 50% of the stalling efficiency observed with *ermDL* encoding the original Arg6-Leu7-Arg8 motif), and only the consecutive mutation of the Arg6-Leu7-Arg8 triplet to Ala residues abolished ribosome stalling at *ermDL* with ERY (Fig. 4a, b). These results suggest that, in contrast with the requirements for TEL-dependent stalling, where the presence of the Arg6-Leu7-Arg8 motif plays a dominant role, the N-terminus of the ErmDL nascent chain also contributes to ERY-mediated programmed translation arrest within the *ermDL* ORF.

To expand upon this surprising finding, we employed inverse toeprinting and performed a deep mutational scan of *ermDL*, monitoring its translation in the absence or presence of ERY (Fig. 4c and Supplementary Fig. 1d). The inverse toeprinting data show that, in striking contrast to the critical role of the Arg residues at position 6 or 8 for TEL-dependent stalling, these same positions can be mutated to almost any other amino acid without compromising the ability of ErmDL to undergo ERY-dependent arrest (compare Figs. 2f and 4c). Notable exceptions are replacements of Arg6 with Asp, Glu, or Pro, as well as Arg8 with Cys, which reduce the efficiency of ERY-mediated arrest. Inverse toeprinting revealed that many single amino acid substitutions at positions 4 and 5 dramatically reduce ERY-dependent stalling, especially at position 4, where all substitutions of the Ser4 residue led to reduced stalling with the exception of Ala or Gly (Fig. 4c). Altogether, our inverse toeprinting data show that the N-terminal segment of ErmDL preceding the Arg6-Leu7-Arg8 sequence is sufficient to direct ERY-dependent stalling, and that ribosome arrest induced by ERY at the *ermDL* ORF does not rely exclusively on the +X+ motif. Thus, two closely related but distinct antibiotic molecules direct ribosome stalling with ErmDL by what appears to be two principally different mechanisms.

**Cryo-EM structure of ErmDL-ERY-SRC.** To understand why stalling of ErmDL by ERY is distinct from that by TEL, we set out to determine a structure of an ErmDL-ERY-SRC. To do this, ErmDL-ERY-SRCs were generated as for the ErmDL-TEL-SRCs, except that TEL was substituted with ERY (see “Methods” section). In silico sorting of the cryo-EM data revealed that the majority of ribosomes contained a P-site tRNA (72%), with

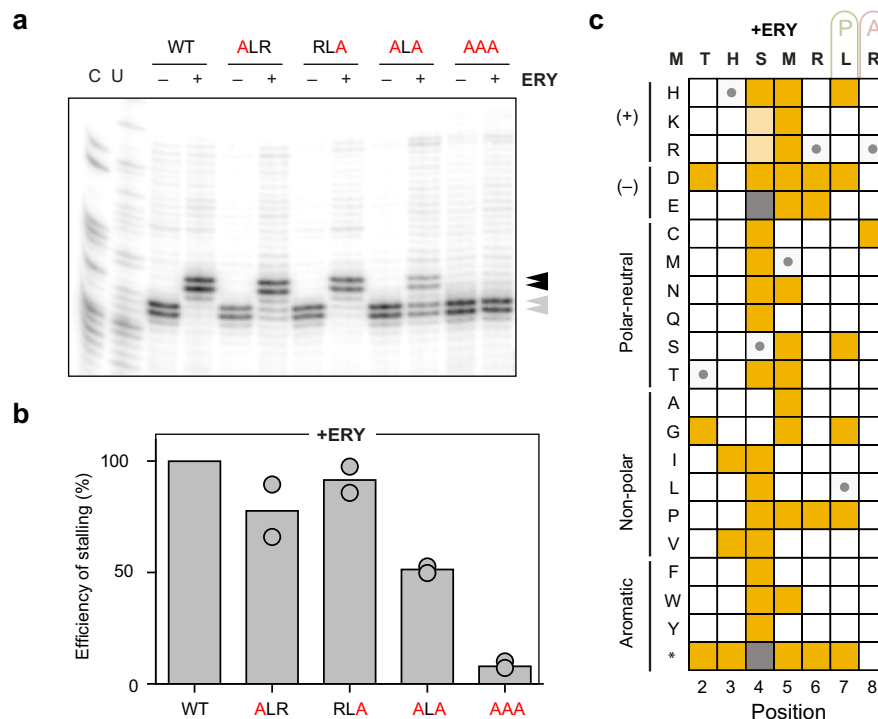


**Fig. 4 Sequence dependence of ErmDL arrest in the response to ERY.** **a** The RLR motif of *ermDL* is not critical for ribosomes stalling with ERY. Toeprinting assay to assess translation arrest at *ermDL* sequences, with the original RLR motif (wt) or containing Ala mutations, in the presence of ERY. The toeprinting bands of ERY stalled ribosomes at codon 7 (Leu or Ala) is indicated by a black arrow; the bands from ribosomes arrested at codon 8 because of the presence of mupirocin (see legend of Fig. 1d) are shown with gray arrows. Sequencing reaction lanes are labeled with C and U. **b** Efficiency of ribosome stalling with ERY estimated as described in the legend of Fig. 1d. Circles represent the values from two independent experiments, whereas the bar represents the mean value. **c** Sequence-function map for seven positions of the ErmDL peptide translated in the presence of ERY, where mutations that abolish arrest (score < -1.5) are shown in yellow, as described in Supplementary Fig. 1. The ribosomal P (green) and A (pink) sites are indicated above the wild-type ErmDL sequence. Variants in gray were not measured and cells marked with a circle correspond to the wild-type amino acid. Mutations S4K and S4R lead to the appearance of a (K/R)MR arrest motif at position 4 that prevents the synthesis of the full peptide and leads to spuriously low scores for these two variants.

approximately half of the particles bearing an additional E-site tRNA (Supplementary Fig. 5a). Refinement of all the P-site tRNA containing particles yielded a final reconstruction of the ErmDL-ERY-SRC (Fig. 5a) with an average resolution of 2.9 Å (Supplementary Fig. 5b), and local resolution extending towards 2.5 Å in the core of the large 50S subunit (Supplementary Fig. 5c, d). As for the ErmDL-TEL-SRC, the density for the P-site tRNA was consistent with stalling occurring with tRNA<sup>Leu(GAG)</sup> base-pairing with the 7th codon (Leu CUU) of the ErmDL mRNA (Supplementary Fig. 5e, f). Both the CCA-end of the P-site tRNA as well as the attached ErmDL nascent polypeptide chain were well-resolved, enabling all seven residues of ErmDL to be modeled unambiguously (Fig. 5b and Supplementary Fig. 5g, h). As expected, density was also observed for ERY bound in an identical position to that observed previously in vacant ribosomes<sup>7,8</sup> as well as in ErmBL-SRCs and ErmCL-SRCs<sup>28–30</sup>. The density for the cladinose and desosamine sugars as well as the associated region of the macrolactone ring (C1–C6) of ERY was very well-resolved (Supplementary Fig. 5g, h), whereas the rest of the lactone ring appeared flexible and was observable only at lower thresholds, as observed previously for ErmBL-stalled and ErmCL-stalled ribosomes in the presence of ERY<sup>28–30</sup>. By contrast, this region of TEL in the ErmDL-TEL-SRC was well-ordered (Supplementary Fig. 5g, h), as observed previously for TEL<sup>9,10</sup>, possibly due to interaction of the heterocyclic sidechain of TEL with U2609-A752 basepair. We could also refine a minor (11.4%) subpopulation of ribosomes that contained A-site and P-site tRNAs, yielding a final reconstruction with an average resolution of 3.6 Å

(Supplementary Fig. 5a). The position and conformation of the P-site tRNA, ErmDL, ERY and PTC nucleotides were indistinguishable (within the limits of the resolution) with or without A-site tRNA. As we observed for the A-site tRNA in the ErmDL-TEL-SRC, the acceptor stem of the A-site tRNA was also accommodated in the presence of ERY, yet no density for the CCA-end or the attached amino acid (Arg8) was observed within the A-site pocket at the PTC. Instead, the CCA-end appeared to adopt an alternative conformation where A76 stacked upon A2602 of the 23S rRNA (Supplementary Fig. 6a–c), analogous to that observed previously when the A-site pocket at the PTC was occupied by the antibiotic hygromycin A (Supplementary Fig. 6d–g)<sup>32</sup>.

Overall, the conformation of ErmDL in the presence of ERY is reminiscent of that observed in the presence of TEL with Arg6 also extending into the A-site pocket of the PTC (Fig. 5b, c), where it sterically clashes with the arginyl-moiety of an A-site Arg-tRNA (Fig. 5d). This is consistent with Ribo-seq data showing that, like with TEL, Arg/Lys-X-Arg/Lys (+X+) motifs are enriched at the sites of ERY-induced ribosome stalling<sup>14,15</sup>. But how then to rationalize our observations that ErmDL stalling in the presence of TEL is strictly dependent on an intact +X+ motif, but not in the presence of ERY? One obvious difference between the ErmDL-TEL-SRC and ErmDL-ERY-SRC structures is that the presence of the cladinose in ERY forces the ErmDL nascent chain to shift slightly towards the PTC when compared with TEL (Fig. 5c). Inversely, the absence of the cladinose sugar in TEL enables the ErmDL peptide to adopt a somewhat more



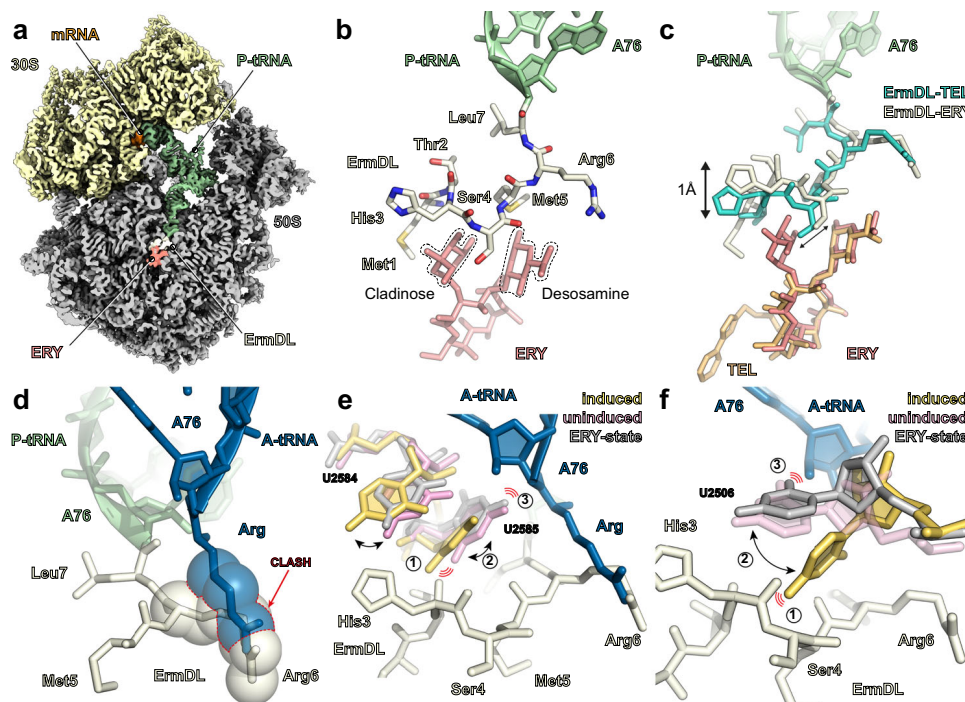


**Fig. 5 Cryo-EM structure of ErmDL-ERY-SRC.** **a** Transverse section of the cryo-EM map of the ErmDL-ERY-SRC with isolated densities highlighting the 30S (yellow) and 50S (gray) subunits, P-site tRNA (green), mRNA (orange), ErmDL nascent chain (beige) and erythromycin (ERY, salmon). **b** Molecular model of the ErmDL nascent chain (beige), P-site tRNA (green) and erythromycin (ERY, salmon). The cladinose and desosamine sugars of ERY are highlighted with dashed line. **c** Superimposition of ErmDL nascent chains from the ErmDL-ERY-SRC (beige) and ErmDL-TEL-SRC (turquoise). Erythromycin (ERY) and telithromycin (TEL) from the respective structures are shown in salmon and orange. **d** Superimposition of the ErmDL-ERY-SRC with an A-site Arg-tRNA in silico mutated from the ErmBL A-site Lys-tRNA (blue, PDB 5JTE)<sup>28</sup>, illustrating that Arg6 of ErmDL nascent chain clashes with the Arg8 side chain of the accommodated A-site tRNA. **e, f** ErmDL stabilizes the uninduced state of the PTC to inhibit A-tRNA accommodation, as evident by comparison of the conformation of **e** U2584 and U2585 and **f** U2506 in ErmDL-ERY-SRC (gray) with the uninduced (pink, PDB 1VQN) and induced states (yellow, PDB 1VQ6)<sup>34</sup>.

relaxed conformation occupying this vacant space, and thereby extending slightly deeper into the NPET (Fig. 5c). Although this shift of the nascent chain is relatively modest, i.e., in the order of 1 Å, it is enough to cause a number of critical conformational changes of 23S rRNA nucleotides within the NPET and PTC. Firstly, A2062 of the 23S rRNA undergoes a rotation of approximately 90° compared to its position in the ErmDL-TEL-SRC structure, which appears to be the consequence of the altered position and conformation of the side chain of Met5 of ErmDL-ERY-SRC (Supplementary Fig. 7a–d). A second, and seemingly more relevant, consequence of the more compacted conformation of ErmDL in the presence of ERY is the inability of U2506 and U2585 to adopt the induced state conformation required for proper accommodation of the aa-tRNAs at the A-site<sup>31,33,34</sup>. In the conformation of these residues observed in the ErmDL-ERY-SRC, they impede placement of the acceptor substrate at the PTC by sterically clashing with the ribose of the 3' terminal A76 of the A-site tRNA (Fig. 5e, f). In the induced conformation of these residues required for peptide bond formation they would clash with the backbone of the ErmDL peptide between His3 and Ser4 (Fig. 5e, f). By contrast, in the ErmDL-TEL-SRC structure, the shift in position of the ErmDL peptide deeper into the NPET is sufficient to allow an unhindered transition of U2585 and U2506 into the induced conformation (Supplementary Fig. 7e, f), which nevertheless does not lead to peptide bond formation due to the invasion of the A-site by the Arg6 side chain. The ErmDL-ERY-SRC structure also provides a possible explanation for the importance of Ser4 of ErmDL observed by the inverse toeprinting assay (Fig. 4c). In the structure, the side chain of Ser4 is tucked within a small cleft between the cladinose and desosamine sugars of ERY (Fig. 5b), which would be compatible with side chains of

amino acids smaller than Ser, such as Ala or Gly, but incompatible with almost all other amino acids bearing large side chains. Therefore, larger side chains presumably perturb the conformation of ErmDL required for the arrest, or alternatively promote peptidyl-tRNA drop-off even before the ribosome reaches the site of the programmed translation arrest within the *ermDL* ORF (Fig. 4c).

Taken together, our findings rationalize the dramatic effect of the cladinose arm of the macrolide antibiotic on ErmDL stalling, such that in the presence of ERY, the cladinose sugar causes compaction of the ErmDL nascent chain that in turn prevents the PTC from adopting the induced conformation required for A-site tRNA accommodation. Thus, ribosome stalling still occurs in the presence of ERY despite those substitutions within the +X+ motif that remove steric clashes between the ErmDL peptide and the A-site tRNA. By contrast, in the presence of TEL, the ErmDL nascent chain is positioned slightly deeper in the NPET due to the absence of the cladinose sugar, providing the necessary space to allow the transition of the PTC into the induced state. This makes TEL-dependent stalling strictly dependent on the Arg6-Leu7-Arg8 (+X+) motif, which operates via invasion of the A site by the Arg6 side chain and thus prevents accommodation of the acceptor substrate (the Arg moiety of the Arg8-tRNA) into the A-site.

**Molecular dynamics simulations of ErmDL-SRCs.** To capture the effect of the antibiotics on the dynamics of the ErmDL nascent peptide, we performed all-atom explicit-solvent molecular dynamics (MD) simulations of ribosome-bound ErmDL in the presence or absence of ERY or TEL. The simulations involving TEL or ERY were started from the respective cryo-EM structures,

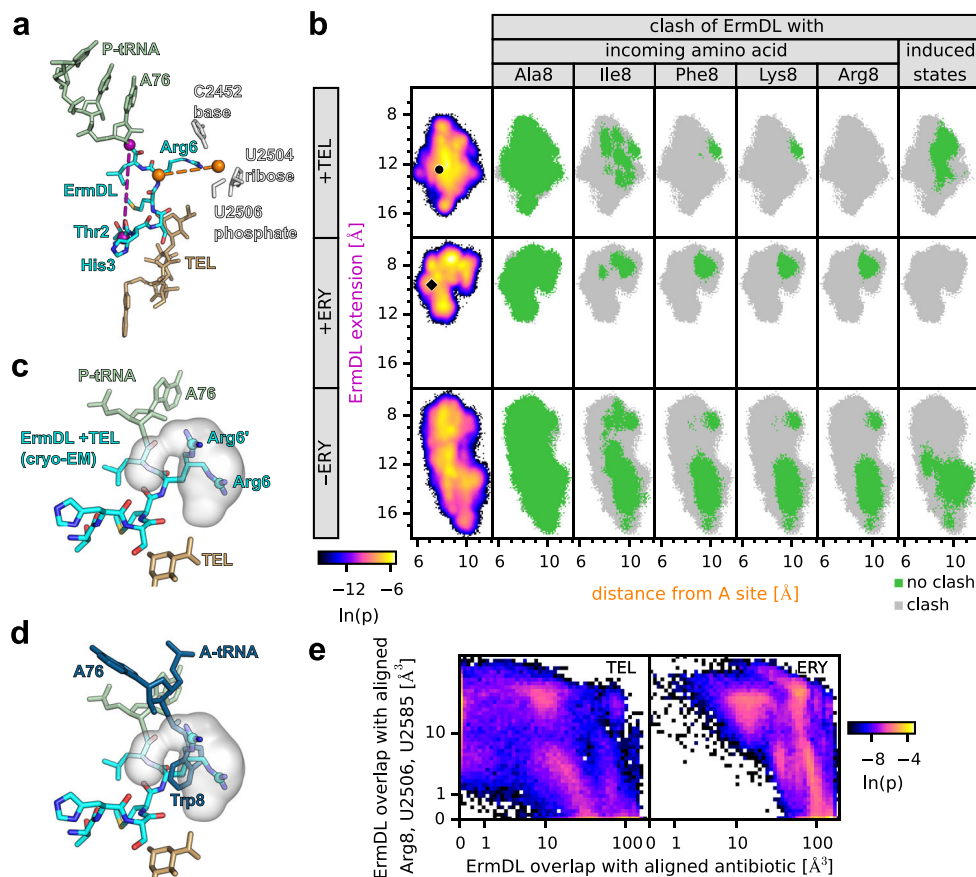


**Fig. 6 Dynamics of ErmDL obtained from MD simulations.** **a** Molecular model of the ErmDL nascent chain, P-site tRNA, and telithromycin (TEL) from the ErmDL-TEL-SRC. The ErmDL extension (purple dashed line) is defined as the distance between O3' atom of A76 (P-site tRNA) and C $\alpha$  atom of Thr2. The position of the A site (right orange sphere) is defined as the center of geometry of the base-atoms, ribose-atoms, and phosphate-atoms of C2452, U2504, and U2506, respectively. The ErmDL distance from the A site (orange dashed line) is the distance between the C $\alpha$  atom of Arg6 and the position of the A site. **b** Distance densities and clashes characterizing ErmDL fluctuations. The first column displays the logarithm (color coded) of the probability density  $p$  along the two distances indicated in **a**. The distances found in the cryo-EM structures with TEL and ERY (circle and diamond) are also shown. In columns 2–6, gray areas indicate distances where all conformations clash with the aligned Ala8, Ile8, Lys8, Arg8, and the induced states of 23S rRNA nucleotides (U2506, U2585), respectively. Green denotes regions with conformations that do not clash. **c, d** For the C $\zeta$  atom of Arg6, the probability density of its positions sampled in the +TEL simulations is shown (gray isosurface at  $p = \exp(-10)$ ) in comparison with the two Arg6 conformations (C $\zeta$  atoms shown as spheres) of the ErmDL-TEL-SRC cryo-EM structure (cyan). Comparison with rotamer conformation of Trp8 (**d**) that clashes with all conformations obtained from the +TEL MD simulations. **e** For simulations after the removal of ERY, the probability density of the van der Waals-overlap of ErmDL with the aligned antibiotic (TEL, left panel; ERY right panel) as well as with aligned A-site Arg8 and the induced nucleotides is shown.

whereas the simulations in the absence of antibiotic were initiated from the ERY-bound structure after computational removal of the drug. For each scenario (+TEL, +ERY, –ERY), we performed twenty 2- $\mu$ s simulations encompassing all residues within a 35 Å distance of the P-tRNA CCA-end, the ErmDL peptide and ERY/TEL. To monitor the conformational dynamics of the ErmDL peptide, we measured two distances for each frame of each simulation, namely, the extension of the peptide (purple line in Fig. 6a) and the distance from the ErmDL Arg6 residue to the A site (orange line in Fig. 6a). Figure 6b (first column) shows the probability of each pair of distances calculated from all the simulations. In the presence of TEL, ErmDL explores conformations around that observed by cryo-EM (circle in Fig. 6b), extending between 8–16 Å and deviating by 6–11 Å from the A-site. By contrast, in the presence of ERY, the ErmDL peptide is more compact (7–13 Å) (Fig. 6b), reflecting the additional spatial restriction imposed by the cladinose sugar on ERY. Removing the drug (–ERY) promotes extension (7–18 Å) of the ErmDL peptide further down the NPET (Fig. 6b), where it occupies the space that has become available due to the absence of the drug (Supplementary Fig. 8a).

Arg6 of ErmDL in the presence of TEL is not restricted to a single conformation as indicated by the two conformations resolved by cryo-EM (Fig. 3b), which are also observed in the simulations (Fig. 6c). Therefore, we analyzed whether any of the explored Arg6 conformations alleviated the clash between Arg6 and different aa-tRNAs accommodated in the A-site of the PTC (Fig. 6b, columns 2–5 and Supplementary Fig. 8b). To that aim, we used the only available structures of ribosomal complexes containing A-site tRNAs, namely with Lys-tRNA<sup>28</sup> and Phe-tRNA<sup>31</sup>, aligned all possible rotamers of the amino acids (Ala, Val, Ile, Phe, Met, Lys, Tyr, Trp, and Arg) to the Lys-tRNA and Phe-tRNA and subsequently selected the rotamers that did not overlap with rRNA nucleotides. For each frame of the simulation, we calculated van-der-Waals clashes of ErmDL with each of the selected rotamers. Most ErmDL conformations did not clash when the A-site tRNA was bearing small amino acids, such as Ala (Fig. 6b) and Val (Supplementary Fig. 8b), suggesting that these tRNAs can accommodate at the PTC and undergo peptide bond formation despite the presence of the side chain of Arg6 of ErmDL extending into the A-site. This is consistent with the inverse toeprinting analysis showing that mutation of Arg8 to

small amino acids such as Ala or Val also relieved the translational stalling in the presence of TEL (Fig. 2f). As expected, we found that with increasing side chain length of the A-site amino acid, there was also an increase in the clashes observed with Arg6. While Ile displayed intermediate levels (Fig. 6b), for longer amino acids, such as Phe, Met, Tyr, all rotamers clashed with almost all Arg6 conformations (Fig. 6b and Supplementary Fig. 8b). This was particularly striking for Trp, where the single rotamer of Trp that is compatible with the A-site clashed with all conformations of Arg6 (Fig. 6d and Supplementary Fig. 8b). Since mutation of Arg8 to Trp relieved ErmDL stalling in the presence of TEL (Fig. 2f), this observation suggests that Trp (and most likely also Phe, Met, and Tyr) may displace Arg6 of ErmDL during A-site accommodation to undergo peptide bond formation. Despite the similarity in clashing profiles of Lys and Arg compared to other long amino acids, such as Phe, Met, Tyr, and Trp, the strong stalling indicates that these amino acids cannot displace Arg6 of ErmDL during accommodation and that another characteristic of the A-site amino acid, such as charge, contributes to stalling efficiency.

In the presence of ERY, we always observed a few conformations of ErmDL that did not produce a clash between Arg6 and the aminoacyl moiety of the A-site tRNA, regardless of whether it was Ala, Ile, Lys or Arg (Fig. 6b). This is consistent with our findings that for ErmDL-mediated translational stalling in the presence of ERY, an intact +X+ motif is dispensable (Fig. 4a–c). To understand why Arg6 can move out of the A-site in the presence of ERY, but not in the presence of TEL, we aligned the non-clashing Arg6 conformations from the +ERY simulations with the backbone of Arg6 in the TEL simulations. This revealed that all of the aligned Arg6 side-chain conformations from the +ERY simulations clash with either G2505 or U2506 in the ErmDL-TEL-SRC, indicating that these non-clashing conformations of Arg6 are incompatible with the backbone conformation of ErmDL in the presence of TEL. The structure of the ErmDL-ERY-SRC indicated that the ErmDL peptide adopts a compacted conformation in the presence of ERY that precludes the PTC from transitioning to the induced state. Therefore, we also analyzed whether any of the conformations explored by ErmDL could alleviate the clash between the ErmDL peptide and the induced conformation of U2506 and U2585 at the PTC<sup>31,33,34</sup>. In the simulations performed in the presence of TEL, we observed a subset of conformations that allowed U2506 and U2585 to adopt the induced state, whereas no conformations of ErmDL were observed in the presence of ERY that were compatible with the induced state (Fig. 6b, sixth column). An explanation for this finding is that in the presence of TEL, the ErmDL peptide extends deeper into the NPET, thereby providing the space required at the PTC for U2506 and U2585 to adopt the induced state (Supplementary Fig. 8c). By contrast, in the presence of ERY, the cladinose sugar of ERY prevents ErmDL from extending deeper into the NPET with the consequence that ErmDL is compacted at the PTC in a manner that precludes U2506 and U2585 from reaching the induced state (Supplementary Fig. 8d). This is corroborated by the simulations performed in the absence of drug (–ERY), where upon computational removal of ERY, the ErmDL peptide becomes much more flexible and extends deeper into the NPET, which by vacating the PTC provides multiple opportunities for U2506 and U2585 to attain the induced state (Fig. 6b and Supplementary Fig. 8a).

Crucially, this result also indicates that the timescales of the simulations are sufficient to observe conformational changes of ErmDL into non-stalling conformations in the absence of antibiotics, suggesting that it is indeed the antibiotics that hinder these conformational changes. To further explore whether the non-stalling conformations are sterically prevented by TEL and

ERY for the simulations after removal of ERY, we first calculated the van-der-Waals overlap of the peptide with the region that would be occupied by Arg8 and the induced nucleotides. Second, to identify which conformations would be possible with TEL or ERY bound, we calculated the overlap with the region that would be occupied by either antibiotic. The probability density of these volumes shows that a large number of the ErmDL conformations would overlap with TEL and ERY (Fig. 6e). In particular, the conformations that we expect to alleviate stalling (no overlap with A-site Arg8 and induced nucleotides) only occur when the peptide has marked overlap with the antibiotic binding sites. These results underscore that the non-stalling conformations are generally inaccessible to ErmDL in the presence of ERY or TEL.

## Discussion

Here we have employed the ErmDL leader uORF that bears an internal Arg6-Leu7-Arg8 (+X+) motif as a model to investigate the molecular basis of translation arrest at these sequences by the macrolide ERY and the ketolide TEL. We have demonstrated that in the presence of TEL, an intact +X+ motif is critical since substitution of Arg6 or Arg8 to any other amino acid, except Lys, abolished the translational arrest (Fig. 2b, c, f). A structure of the ErmDL-TEL-SRC revealed that, in the presence of TEL, the ErmDL nascent chain adopts a defined conformation in which Arg6 of ErmDL is directed into the A-site of the PTC active site, where it would clash with the incoming Arg8, thus providing a simple explanation for how TEL and ErmDL interplay to arrest translation. Consistently, mutation of Arg8 to Ala alleviates the steric clash (Fig. 3e) and accordingly relieves the translational arrest (Fig. 2b, c, f). The extent of clashing between the penultimate residue of the ErmDL nascent chain and the incoming amino acid plays an important role; indeed, Arg and Lys are the residues with the longest side chains among the proteinogenic amino acids. However, our biochemical data and MD simulations suggest that length of the side chains at these positions is not the only factor for stalling because replacement of Arg6 or Arg8 with comparably bulky amino acids, is not predicted to resolve the clash, but nevertheless prevents TEL-induced translation arrest (Fig. 2f). This is highlighted by the mutation of Arg8 to Trp, which alleviates the stalling (Fig. 2f), yet is not predicted to resolve the clash with Arg6 (Supplementary Fig. 8b). Since the relief of stalling requires the accommodation of the Trp-tRNA at the A-site so that peptide bond formation can ensue, we assume that in the case of amino acids with large side chains (other than Lys or Arg), the incoming acceptor substrate can displace Arg6 of ErmDL from the A-site of the PTC. This raises the question as to why other amino acids can achieve this displacement, whereas Lys and Arg cannot? A likely answer is that in addition to carrying the longest side chains, Lys and Arg are also unique in that they are both positively charged so that electrostatic repulsion helps to prevent the Lys8-tRNA or Arg8-tRNA accommodation (Fig. 7a), as previously proposed for macrolide-dependent stalling of short MRLR sequences<sup>18</sup>. Furthermore, the positive charge at the end of the ErmDL's penultimate amino acid could be a prerequisite for the A site invasion due to its stacking interaction with the U2504-C2452 base pair (Fig. 3c). We note that in the ErmDL-TEL-SRC, we observed two alternative conformations for Arg6 (Fig. 3b) and multiple conformations in the simulations that may contribute to the repulsion of the incoming positively charged aminoacyl-tRNA (Fig. 6c). Finally, the mutation of Arg6 to any other amino acid except for the positively charged Lys, also removes the repulsion effect, thus allowing accommodation and peptide bond formation and thereby relieving the translational stalling, re-emphasizing the critical role of the +X+ motif in the TEL-induced translation arrest of ErmDL. Because we observed a



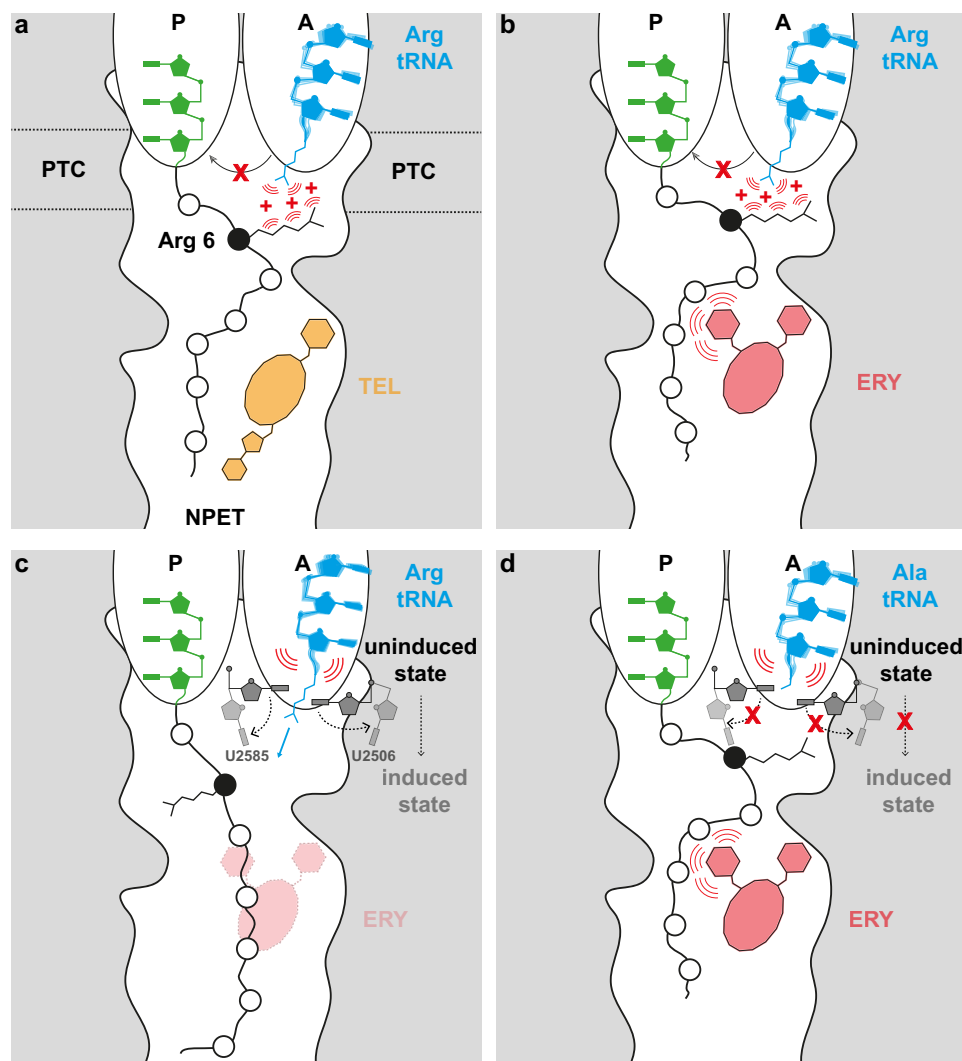


**Fig. 7 Model for the ErmDL-mediated translation arrest in presence of TEL or ERY.** **a** The presence of TEL in the tunnel restricts the space available for the ErmDL nascent chain, constraining the ErmDL Arg6 side chain to extend into the A-site and thereby preventing accommodation of the incoming Arg-tRNA via charge repulsion. **b** The presence of ERY with its cladinose ring further restricts the space available for the ErmDL nascent chain constraining the ErmDL Arg6 side chain to extend into the A-site preventing via a charge repulsion mechanism the incoming Arg-tRNA in the A-site to adopt a stable conformation. **c** In the absence of ERY, the ErmDL nascent chain freely explores the NPET and adopts an extended conformation. During the accommodation of an incoming A-tRNA, 23S residues U2506 and U2585 shift from their uninduced state to their induced state. **d** In the presence of ERY, the compacted conformation of ErmDL prevents the PTC from adopting the induced conformation necessary for accommodation of the A-site Ala-tRNA independently of the charge repulsion mechanism from **c**.

similar conformation of ErmDL in the presence of ERY, where the side chain of Arg6 extends into the A-site, it is likely that in most cases, stalling at +X+ motifs in the presence of ERY may also utilize a charge repulsion mechanism, analogous to that outlined above for TEL (Fig. 7b). In our MD simulations, removal of the antibiotic enabled the nascent chain to extend deeper into the ribosomal tunnel, leading to the retraction of the side chain of Arg6 from the A-site pocket at the PTC (Fig. 7c). This explains why translational stalling at +X+ motifs is not observed in the absence of the drugs<sup>14,15</sup>.

It is noteworthy that in the presence of TEL or ERY, ribosomes do not stall at every +X+ motif present within proteins<sup>14,15</sup>, indicating that the context of the +X+ motif also plays an important role (Supplementary Fig. 9a). In keeping with this notion, changing the ErmDL N-terminal sequence from MTHSMRLR to MDTLNRLR by compensatory frame-shifting mutations alleviates translation arrest at the Arg6-Leu7-Arg8 (+X+) sequence of the modified ORF with either ERY or TEL

(Supplementary Fig. 9b). In light of our ErmDL-SRC structures, one can envisage that some amino acid sequences N-terminal to the +X+ motif, juxtaposed against the drug molecule in the NPET, could alter the conformation of the nascent chain such that, even in the presence of the macrolide/ketolide, the side chain of the first positively charged Lys/Arg residues of the +X+ motif does not extend into the A-site, thereby allowing accommodation of the second Lys/Arg-tRNA at the A-site leading to productive peptide bond formation.

Our study has revealed that both TEL and ERY arrest the ribosome, when it reaches the 7th codon of the *ermDL* uORF. Given the overall structural similarity of the two related drugs, it is striking that they utilize seemingly principally different mechanisms for ribosome stalling. Given the conservation of +X+ motifs in the regulatory uORFs of macrolide resistance genes (Sothiselvam et al.<sup>17</sup>), it was counterintuitive that the +X+ motif of ErmDL plays little role in the arrest of the ribosome prompted by the presence of ERY (Fig. 4a–c). Instead, the residues more

proximal to the ErmDL N-terminus and more remote from the site of arrest at Leu7, such as Ser4 and Met5, were found to be critical for ERY-dependent stalling (Fig. 4c). The structure of the ERY-ErmDL-SRC provides a likely explanation of why ERY-dependent stalling does not rely on the presence of the +X+ motif. During processive translation, aminoacyl-tRNAs accommodate at the A-site of the PTC through an induced fit mechanism requiring the shift of nucleotides U2506 and U2585 from uninduced to induced conformations (Fig. 7c). By contrast, the presence of ERY in the NPET causes compaction of the N-terminal segment of the ErmDL peptide, such that the PTC cannot adopt the conformation necessary for productive accommodation of the A-site tRNA (Fig. 7d). A comparison of the ErmDL-TEL-SRC and ErmDL-ERY-SRC structures shows that it is the C5 cladinose present in ERY, but absent in TEL, that is responsible for the ErmDL compaction. Such compaction depends on the structure of the nascent chain N-terminal to the site of arrest, as revealed both by the results of deep single amino acid mutagenesis (Fig. 4c), and by frameshifting of the *ermDL* N-terminal coding sequence (Supplementary Fig. 9c). The dependence of ERY-dependent translation arrest on other determinants also explains, why ribosome stalling in the presence of TEL most commonly calls for the presence of the +X+ motif, whereas more diverse motifs are observed at the sites of the ERY-induced arrest in the bacterial genomes as well as the sites of arrest induced by a 15-membered macrolide azithromycin that also bears a C5 cladinose<sup>14,15</sup>.

Our finding that TEL- and ERY-dependent ribosome stalling at the regulatory ORF of the *ermD* resistance gene operates through different mechanisms begs the question of the origin of such dichotomy. The resistance genes are often found in the producers of natural antibiotics or in organisms that are exposed to such antibiotics in their natural environment. Noteworthy, the resistance in the producer of the natural ketolide pikromycin is activated exclusively by ketolides<sup>20</sup>, whereas some macrolide resistance genes are selectively induced by C3 cladinose-containing macrolides<sup>35</sup>. While the origin of the *ermD* gene and its regulatory circuit is unknown, it is possible that it first evolved in the producer of a macrolide antibiotic, and that its induction relied on the compaction of the N-terminal segment of the leader peptide in the macrolide-obstructed NPET. Subsequent acquisition of the ketolide biosynthesis gene cluster could then select for the RLR sequence that would allow induction of the resistance by both types of antibiotics. Alternatively, exposure of bacteria to cladinose-containing macrolides in the environment could lead to selection or acquisition of a macrolide-inducible resistance gene, with subsequent exposure to natural ketolides forcing selection of the +X+ motif in the leader peptide. Importantly, the latter scenario illustrates how the resistance to ketolides could easily evolve in the clinic in pathogens that carry inducible resistance genes originally responding exclusively to macrolides.

Finally, we note that the mechanisms identified here for ErmDL are quite distinct from those observed previously for other macrolide-dependent stalling peptides, for example, ErmBL<sup>28,30</sup> and ErmCL<sup>29</sup>. In the ErmBL-ERY-SRC, accommodation of the A-site tRNA is observed at the PTC, however, peptide bond formation cannot occur because the interplay between ERY and ErmBL creates a suboptimal geometry of the P-site tRNA<sup>28,30</sup>. By contrast, in the ErmCL-ERY-SRC, the drug and ErmCL peptide induce conformational changes within the PTC, in particular rotation of U2585, such that accommodation of the A-site tRNA is prohibited. It will be interesting in the future to investigate whether distinct mechanisms are utilized by other drug-dependent nascent polypeptide chain stalling systems to inactivate the PTC of the ribosome and induce translational arrest.

## Methods

**Reagents.** Mupirocin and ERY were from Sigma Aldrich, telithromycin was from Cempira, Inc. All other reagents were from ThermoFisher. DNA oligonucleotides were synthesized by Integrated DNA Technologies.

**Construction of the inducible *ermD* reporter and antibiotic diffusion test.** A segment of the *ermDL-ermD* operon (encompassing the *ermDL* coding region, the intergenic segment and the first six codons of the *ermD* gene) was amplified from plasmid pBD244 found in the *Bacillus subtilis* strain BG28<sup>24</sup> and kindly provided by Dr. Bechhofer (Mount Sinai School of Medicine, NY). The PCR reaction was carried out using the primers *ermDL*-NdeI-forward and *ermD*-AflII-reverse (Supplementary Table 1). The resulting PCR fragment was used to substitute the *ermCL-ermC* portion of pErmZ101t<sup>36</sup> to yield the plasmid pErmZ101t-*ermD*. *E. coli* strain JM109 cells were transformed with the pErmZ101t-*ermD* plasmid and the induction of the *ermD*<sub>1-6</sub>-lacZa reporter by antibiotics was tested by the diffusion assay as previously described<sup>26</sup>, with minor modifications. Specifically, cells were grown to an A<sub>600</sub> of 1.0 and then 0.5 mL of the culture were mixed with 3.5 mL of soft agar [0.6% (wt/vol) LB agar] at 50 °C and overlaid on agar plates containing 10 µg/mL tetracycline, 0.5 mM IPTG, 80 µg/mL X-Gal, and 0.25 mM of the β-galactosidase inhibitor phenylethyl-b-d-thiogalactopyranoside (PETG). A 1 µL drop of a solution containing 25 µg of ERY or 10 µg of TEL were placed on top of the solidified soft agar. Plates were incubated at 37 °C for 18–24 h and photographed.

**Toeprinting assay.** Linear DNA templates encoding modified versions of the *ermDL* ORF, preceded by the T7 promoter sequence and including the toeprinting primer (NV1) annealing region, were prepared by PCR. Primers T7-MTHSM-fwd and NV1-IFPTL-rev (Supplementary Table 1) at 0.4 µM were mixed with 0.04 µM of forward and reverse primers (Supplementary Table 1) encoding the *ermDL*-derived ORFs with the original Arg<sub>6</sub>-Leu<sub>7</sub>-Arg<sub>8</sub> stalling site (RLR-IFPTL fwd and RLR-IFPTL rev) or its mutant versions. An Ile codon (ATT) was introduced as codon 9 of the templates and codons Asn<sub>13</sub> (ACC) and Gln<sub>14</sub> (CAG) of the original *ermDL* were omitted. The template with no Ala-mutations of the Arg<sub>6</sub>-Leu<sub>7</sub>-Arg<sub>8</sub> stalling motif is referred to as wt-*ermDL*. Templates for the WT *ermDL* and its frame-shifted (FS) mutant version were prepared by PCR combining primers WT-MTHSM-fwd or M3-MDTLN-fwd, respectively, with reverse primer *ermD*-58 nt-rev (Supplementary Table 1). AccuPrime DNA polymerase was used for all PCR reactions. Coupled transcription-translation reactions were carried out in 5 µL of the PURExpress system (New England Biolabs) containing additional 3 mM of MgCl<sub>2</sub> followed by reverse transcriptase-mediated extension of the NV1 primer (Supplementary Table 1), as described previously<sup>37</sup>. Reactions were also supplemented with the Ile-RS inhibitor mupirocin (50 µM) and, where indicated, with erythromycin (50 µM) or telithromycin (100 µM). The cDNA extension products, along with sequencing reactions of the wt-*ermDL* template, were separated in 6% sequencing gels, dried, exposed, and visualized in a Typhoon scanner (GE Healthcare). Intensity of the toeprint bands was quantified using ImageJ<sup>38</sup>. Relative efficiency of antibiotic-mediated stalling was calculated using formula  $E_{\text{stalling}} = I_7 / (I_7 + I_8)$ , where  $I_7$  is the intensity of the toeprint band corresponding to the ribosome stalled with the 7th codon of the *ermDL* template in the P site, representing macrolide-dependent translation arrest, and  $I_8$  is the intensity of the toeprint band at the 8th codon, representing macrolide-independent translation arrest.

## Deep mutational scan of ErmDL

**Single-codon *ermDL* variant library generation.** A library of single-codon *ermDL* variants was generated by mixing equimolar amounts of linear double stranded DNA expression cassettes in which codons 2–8 of *ermDL* had individually been replaced with an “NNS” codon (aNy aNy Strong (G/C)). These expression cassettes were first obtained by polymerase chain reaction (PCR) with Phusion DNA polymerase (20 cycles [98 °C, 10 s; 60 °C, 5 s; and 72 °C, 10 s]), using one of seven degenerate oligonucleotides encoding *ermDL* (*ermDL*-NNS2 to 8) in combination with oligonucleotides T7\_RBS\_ATG\_f and Stop\_EcoRV\_r as templates (1 pmol of each oligonucleotide per 50 µL reaction), and oligonucleotides T7\_f and EcoRV\_r for amplification (10 pmol of each oligonucleotide per 50 µL reaction). The sequence of the expression cassette for wild-type *ermDL* is CGATCGAATCTCT AATACGACTCACTATAGGGCTTAAGTATAAGGAGGAAAAAATATGACAC ACTCAATGAGACTTCGTCGATCTCGGTGTGATGAGATATCAATATCAA AAAGGATCCATATA (the T7 promoter is underlined, the mutated *ermDL* region is in bold; the EcoRV site is in italics). This linear expression cassette was purified using a PCR purification kit (Qiagen) according to the manufacturer's instructions and quantified using a 2100 Agilent Bioanalyzer.

**Inverse toeprinting.** In vitro transcription was performed at 20 °C for 3 h, using T7 RNA polymerase in a buffer containing 80 mM Tris-HCl, 24 mM MgCl<sub>2</sub>, 2 mM spermidine, and 40 mM DTT, pH 7.6, in the presence of 7.5 mM ATP (Sigma Aldrich), CTP and UTP, 0.3 mM GTP (CTP, UTP, and GTP from Jena Bioscience), and 4.5 mM Thio-Phosphate-GMP (Genaxxon Bioscience). Eight picomoles of DNA template were used in a 200 µL reaction volume. Transcripts were purified using the “RNA Clean & Concentrator™-5” purification kit (ZymoClean

Research) according to the manufacturer's instructions. The resulting mRNA library was biotinylated and polyadenylated as described previously<sup>16</sup>.

In vitro translation reactions (5 µL) were carried out with a PURExpress ΔRF-123 ΔRibosome kit (NEB), using ~5 pmol of 5'-biotinylated and 3'-polyadenylated mRNA as a template. Antibiotics (ERY, TEL) were added to a final concentration of 50 µM. Release factors 1 and 3 were added to the translation reaction according to the manufacturer's instructions. Translation was performed at 37 °C for 30 min, after which the samples were placed on ice and 5 µL ice-cold Mg<sup>2+</sup> buffer (50 mM Hepes-KOH pH 7.5, 100 mM K-glutamate, 87 mM Mg-acetate, 1 mM DTT) was added to the reactions, thereby increasing the Mg<sup>2+</sup> concentration to 50 mM. One microliter of RNase R (1 mg/mL) was added, followed by additional incubation for 30 min at 37 °C to ensure complete degradation of the mRNA. One hundred and thirty-nine microliter of 1× BWT buffer was added to stop the reaction (5 mM Tris-HCl, 0.5 mM EDTA, 1 M NaCl, and 0.05% [vol/vol] Tween-20, pH 7.5).

For each sample, 5 µL of M-280 streptavidin Dynabeads (Thermo Fisher Scientific) washed and then diluted in 50 µL of 1× BWT buffer were added to all of the digested RNA, and the mixture was incubated for 15 min at room temperature. After incubation, beads were washed once with 1× BWT buffer to remove unbound RNA, followed by two washes with water to remove the 1× BWT buffer. Beads were resuspended in 9.5 µL of linker ligation reaction mixture containing 4 µL of water, 1 µL of T4 RNA ligase2 truncated buffer (10×-NEB), 3 µL of PEG 8000 (50%-NEB), 1 µL of 3'-linker\_ApoI (10 µM) and 0.5 µL of ligase (T4 RNA ligase 2, truncated—200,000 U/mL—NEB) per reaction. Linker ligation was allowed to proceed for 2.5 h at room temperature. Beads were washed once with water to remove unincorporated linker oligonucleotide and resuspended in 18.5 µL of reverse transcription reaction mixture containing 11.5 µL of water, 1 µL of dNTPs (10 mM of each -NEB), 1 µL of Linker\_r oligonucleotide (2 µM), 4 µL of first strand synthesis buffer (5×—Thermo Fisher Scientific) and 1 µL of DTT (0.1 M—Thermo Fisher Scientific) per reaction. Samples were incubated for 5 min at 65 °C before adding 1 µL of reverse transcriptase (Superscript III—200,000 U/mL—Thermo Fisher Scientific) to each tube and incubating for 30 min at 55 °C.

To generate double stranded DNA for restriction digestion, a fill-up reaction was performed using 10 pmol of cDNA\_f oligonucleotide and all of the reverse transcribed cDNA (10 s denaturation, 10 s annealing at 42 °C, and 30 s elongation at 72 °C). The resulting double stranded DNA was combined with 1 µL of EcoRV restriction enzyme and the sample was incubated at 37 °C for 1 h. Undigested DNA was mixed with 10 pmol of Linker\_r oligonucleotide and amplified by 10–16 cycles of PCR [98 °C, 10 s; 60 °C, 10 s; and 72 °C, 10 s]. The number of PCR cycles was adjusted to give a visible band on the gel while minimizing non-specific byproducts. Bands containing inverse toeprints corresponding to stalled ribosomes with codon 7 of *ermDL* in P-site were excised from the gel with a clean scalpel. Gel pieces were crushed through a 5 mL syringe into tubes containing 5 mL of gel elution buffer (10 mM Tris-HCl, pH 8.0, 500 mM Na-acetate, and 0.5 mM Na-EDTA), and DNA was extracted overnight at room temperature. After removal of the gel debris, each sample was concentrated to ~1 mL using a SpeedVac. DNA was precipitated with 1 mL of isopropanol in the presence of 3.7 µL GlycoBlue (Thermo Fisher Scientific), recovered by centrifugation at 20,000×g for 30 min at 4 °C and resuspended in 20 µL water.

**Next generation sequencing of inverse toeprints.** Long NGS adapter oligonucleotides (NGS\_adaptor\_f and the reverse oligonucleotides NGS\_adaptor\_23 through NGS\_adaptor\_23 + 3) contain Illumina TruSeq adapter sequences followed by 18 nucleotides complementary to the 5' or 3' region of the cDNA. The reverse oligonucleotides also contain barcode sequences for multiplexing according to the TruSeq v1/v2/LT protocol (Illumina). Processed inverse toeprints were amplified by 12–16 cycles of PCR, using 0.02 µM long NGS adapter oligonucleotides (forward and reverse) and 0.2 µM short amplification oligonucleotides (NGS\_f and NGS\_r). The resulting NGS libraries were purified using a Qiagen PCR purification kit. The size and concentration of the fragments thus obtained were determined using a 2100 Agilent Bioanalyzer with the DNA 1000 kit. Next generation sequencing was performed by the BGI Facility in Hong-Kong, on an Illumina HiSeqXten system in rapid run mode with 150 PE reads.

**Analysis of ErmDL deep mutational scanning data.** Unless it is indicated otherwise, data analysis was carried out using a series of custom scripts written in-house in Python, which relied on the use of the Biopython package<sup>39</sup>. Read pairs were assembled using PEAR v0.9.10<sup>40</sup> on a Mac Book Pro with a 2.7 GHz Intel Core i7 processor and 16 GB 1600 MHz DDR3 memory with the maximal proportion of uncalled bases in a read set to 0 (–u option), and the upper bound for the resulting quality score set to 126 (–c option). Regions immediately upstream of the start codon and downstream of the point of cleavage by RNase R were removed using a modified version of the *adaptor\_trim.py* script written by Brad Chapman ([https://github.com/chapmanb/bcb/bblob/master/align/adaptor\\_trim.py](https://github.com/chapmanb/bcb/bblob/master/align/adaptor_trim.py)). The 5' flanking region was defined as GTATAAGGAGGAAAAAAT, whereas the 3' flanking region was GGTATCTCGGTGTGACTG. A maximum of two mismatches within each of these flanking regions was tolerated, whereas all other reads were discarded. Trimming of the retained reads resulted in sequences with a start codon directly at the 5' end and the site of RNase R cleavage at the 3' end. Trimmed reads were analyzed in Enrich2 v1.0.0<sup>41</sup> in a single run with two separate experimental conditions (ERY, TEL), each consisting of 6 replicates (2 biological × 3 technical) of the libraries obtained following selection in the absence or presence of drug. Reads

were required to have a minimum quality score of 30 at all positions and contain no Ns.

**Sample and grid preparation.** The ErmDL construct and ribosome complexes were generated following the same procedure as previously described<sup>28–30</sup>. Briefly, under the control of the T7 promoter, two consecutive ErmDL ORFs with strong ribosome-binding site upstream of the ATG start codon were synthesized (Eurofins, Germany). Both ErmDL ORFs were separated by 22 nt linker enabling an independent initiation of both ORFs and later on the hybridization of complementary DNA oligonucleotide required for RNase H cleavage. In vitro coupled transcription and translation of the 2× ErmDL construct was performed using the Rapid Translation System RTS 100 *E. coli* HY Kit (biotech rabbit GmbH, Berlin) in presence of 10 µM ERY or 10 µM of TEL for 1 h at 37 °C. The ErmDL-stalled disomes were isolated on 10–40% sucrose gradients in buffer A, containing 25 mM HEPES-KOH pH 7.5, 150 mM KOAc, 15 mM Mg(OAc)<sub>2</sub>, 1 mM DTT, 0.01% N-dodecyl β-D-Maltoside, 50 µM erythromycin or tetracycline, by centrifugation at 34,380 × g (SW-40 Ti, Beckman Coulter) overnight at 4 °C. The disome fraction was then pelleted by centrifugation at 109,760 × g (Ti70.1, Beckman Coulter) overnight at 4 °C and re-suspended in buffer B, containing 25 mM HEPES-KOH pH 7.5, 100 mM KOAc, 25 mM Mg(OAc)<sub>2</sub>. Conversion into monosomes was performed first by annealing of a complementary DNA oligonucleotide (5'-TT CCTCCTTATAAACT-3') for 5 min at 30 °C, directly followed by a cleavage of the RNA-DNA hybrid by RNase H (Thermo Fisher Scientific) at 25 °C for 1 h. The reaction was layered on 10–40% sucrose gradient in buffer A and the monosomes were fractionated by centrifugation at 34,380 × g (SW-40 Ti, Beckman Coulter), directly followed by a pelleting centrifugation step at 109,760 × g (Ti70.1, Beckman Coulter) overnight at 4 °C. The stalled monosomes were re-suspended in buffer B to a final concentration of 150 A<sub>260nm</sub>/mL ErmDL-TEL-SRC and 100 A<sub>260nm</sub>/mL ErmDL-ERY-SRC. For grid preparation, 4 µL (5 A<sub>260</sub>/mL) of the freshly prepared ErmDL-TEL-SRC or ErmDL-ERY-SRC complex was applied to 2 nm pre-coated Quantifoil R3/3 holey carbon supported grids and vitrified using a Vitrobot Mark IV (FEI, Netherlands).

**Cryo-electron microscopy and single-particle reconstruction.** Data collection of both ErmDL-TEL-SRC and ErmDL-ERY-SRC was performed on a FEI Titan Krios transmission electron microscope (TEM) (Thermo Fisher) equipped with a Falcon II direct electron detector (FEI). Data were collected at 300 kV with a total dose of 25 e<sup>−</sup>/Å<sup>2</sup> fractionated over 10 frames with a pixel size of 1.084 Å/pixel and a target defocus range of −0.7 to −3 µm using the EPU software (Thermo Fisher). The raw movie frames were summed and corrected for drift and beam-induced motion at the micrograph level using RELION-3.0<sup>42</sup>. The resolution range of each micrograph and the contrast transfer function (CTF) were estimated with Gctf<sup>43</sup>. For ErmDL-TEL-SRC, a total of 5850 micrographs were collected. After manual inspection, 5430 micrographs were used for automated particle picking with Gautomatch (<http://www.mrc-lmb.cam.ac.uk/kzhang/>) resulting in 433,827 initial particles, of which 384,895 were selected for further processing upon 2D classification in RELION-3.0<sup>42</sup>. After initial alignment with a vacant 70S reference, the 384,895 particles (defined as 100%) were 3D classified into eight classes (Supplementary Fig. 2a). Class 4 (83,696 particles, 21.7%) and class 8 (100,679 particles, 26.2%) were further selected for 3D and CTF refinement using RELION-3.0<sup>42</sup>. The final reconstructions were corrected for the modulation transfer function of the Falcon 2 detector and sharpened by applying a negative B-factor estimated by RELION-3.0<sup>42</sup>. The resolution for the class 4 and 8 ErmDL-TEL-SRC were estimated using the “gold standard” criterion (FSC = 0.143)<sup>44</sup> resulting in a final reconstruction of 3.1 Å (Supplementary Fig. 2b). Local-resolution estimation and local filtering of the final volumes were done using Relion-3.0 (Supplementary Fig. 2c–e). For ErmDL-ERY-SRC, a total of 3850 micrographs were collected. After manual inspection, 3170 micrographs were used for automated particle picking with Gautomatch (<http://www.mrc-lmb.cam.ac.uk/kzhang/>) resulting in 288,013 initial particles, of which 240,530 were selected for further processing upon 2D classification in RELION-3.0<sup>42</sup>. After initial alignment with a vacant 70S reference, the 240,530 particles (defined as 100%) were 3D classified into eight classes (Supplementary Fig. 5a). Class 2 (27,397 particles, 11.4%) and class 3, 4, 7, and 8 (172,175 particles, 71.6%) were further selected for 3D and CTF refinement using RELION-3.0<sup>42</sup>. The final reconstructions were corrected for the modulation transfer function of the Falcon 2 detector, and sharpened by applying a negative B-factor estimated by RELION-3.0<sup>42</sup>. The resolution for the ErmDL-TEL-SRC was estimated using the “gold standard” criterion (FSC = 0.143)<sup>44</sup> resulting in a final reconstruction of 2.9 Å (Supplementary Fig. 5b). Local-resolution estimation and local filtering of the final volumes were done using RELION-3.0<sup>42</sup> (Supplementary Fig. 5c–e).

**Molecular modeling.** The model of the *E. coli* 70S ribosome was derived from PDB ID 6TVB<sup>45</sup>. Domain-wise the proteins of the 30S and 50S and the rRNA were fitted separately into locally-filtered electron density maps using UCSF Chimera<sup>46</sup> and Coot<sup>47</sup>. Afterwards manual adjustments were applied to all fitted molecular models using Coot. The ErmDL nascent chain was de novo modeled into the corresponding density. The final combined molecular models were then refined using the real space refinement procedure in Phenix version 1.14 together with



restraints<sup>48</sup>. Statistics for the models were obtained using MolProbity<sup>49</sup> and are represented in Supplementary Table 2.

**Figure preparation.** Figures showing biochemical experiments are fitted and plotted with GraphPad Prism 8.0. Figures showing ribosome profiling data are created using R 3.3.1. Figures showing atomic models and electron densities were generated using either UCSF Chimera<sup>46</sup> or Chimera X<sup>50</sup> and assembled with Inkscape or Illustrator.

**Molecular dynamics (MD) simulations.** To obtain the dynamics of ribosome-bound ErmDL in the presence and absence of the antibiotics ERY and TEL, we carried out all-atom explicit-solvent MD simulations of the region surrounding the peptide. For the simulation systems, all residues within 35 Å of the P-site tRNA CCA-end, the ErmDL peptide and the antibiotic were extracted. The residues of the system bound to residues not included were treated as described earlier<sup>51</sup>. The residues within a 25 Å radius were not restrained, while the outer-shell residues were subjected to position restraints with force constants obtained from their fluctuations in full-ribosome simulations as described earlier<sup>51</sup>. Three systems were simulated: one started from the cryo-EM structure with ERY (without A-site tRNA), one started from the cryo-EM structure with TEL (with A-site tRNA), and one from the ERY-structure after removal of ERY. For ion placement, Mg<sup>2+</sup> ions with 5 Å of each simulation system were extracted from an aligned cryo-EM structure of the ribosome<sup>52</sup>. Histidine protonation states were determined using WHAT IF<sup>53</sup>. Next, each simulation system was first placed in a dodecahedron box with a minimum distance of 15 Å between the atoms and the box boundaries. Water molecules were added using the program solvate<sup>54</sup>.

The charge of the system was neutralized by iteratively replacing the water molecule with lowest Coulomb potential by a K<sup>+</sup> ion. Subsequently, 7 mM MgCl<sub>2</sub> and 150 mM KCl were added using the program GENION<sup>54</sup>. All simulations were carried out with GROMACS 2018<sup>54</sup>, the amber12 forcefield<sup>55</sup>, the SPC/E water model<sup>56</sup>, as well as K<sup>+</sup> and Cl<sup>−</sup> parameters from Joung and Cheatham<sup>57</sup>. Forcefield parameters for ERY were taken from Arenz et al.<sup>28</sup> and parameters for TEL were obtained as described for ERY<sup>28</sup>. During the simulations, Lennard-Jones and short-range Coulomb interactions were calculated within a distance of 1 nm; long-range electrostatics were calculated using particle-mesh Ewald summation<sup>58</sup>. Bond lengths were constrained using the LINCS algorithm<sup>59</sup> and virtual site constraints<sup>60</sup> were used for hydrogen atoms, allowing an integration time step of 4 fs. Solute and solvent atoms were independently coupled to a heat bath at 300 K using velocity rescaling<sup>61</sup> with a coupling constant of 0.1 ps. Initially, each system was energy-minimized (steepest decent) with harmonic position restraints applied to solute heavy atoms ( $k = 1000 \text{ kJ mol}^{-1} \text{ nm}^{-1}$ ). For each system, 20 sets of simulations were carried, each set consisting of three steps. First, the pressure was coupled to a Berendsen thermostat (coupling time 1 ps) and heavy-atom position restraints were applied for 50 ns. Second, during 20 ns, the position-restraints were linearly decreased to the force constant obtained from the full-ribosome simulations<sup>51</sup> for the outer-shell and to zero for all other atoms. Finally, for 2-μs production simulations, the Parinello-Rahman barostat was used<sup>62</sup>. The 20 simulations for each of the three systems result in a total production simulation time of 120 μs. Coordinates were recorded every 5 ps.

#### Assessing conformational changes, fluctuations and van-der-Waals clashes.

At first, all trajectories were rigid-body fitted to the cryo-EM structure (+ERY) using the P atoms of 23S PTC nucleotides (746–748, 751–752, 789–790, 1614, 1781–1782, 2057–2059, 2061–2064, 2251–2253, 2439, 2450–2453, 2503–2508, 2553–2555, 2573, 2576, 2581, 2583–2586, 2601–2602, 2608–2612). Further, an X-ray structure of a *T. thermophilus* ribosome with a pre-attack A-site Phe-tRNA<sup>Phe31</sup>, a cryo-EM structure of an *E. coli* ribosome with an A-site Lys-tRNA<sup>Lys28</sup>, as well as two *H. marismortui* X-ray structures with the PTC in the uninduced and induced conformations<sup>33,34</sup> were fitted to the cryo-EM structure in the same way. To compare the dynamics of Arg6 in the simulations with the two conformations resolved by cryo-EM in the presence of TEL, we calculated the probability density of the Arg6 C $\alpha$  atom using the GROmaps toolset with a  $\sigma$  of 0.5 Å and a spacing of 0.2 Å<sup>63</sup>. To investigate how the presence or absence of the antibiotics affects the accessible conformations of ErmDL, the extension of the peptide and its distance from the critical 23S rRNA nucleotide U2506 were monitored for all simulations. To monitor the peptide extension, the distance between the C3' of the 3' nucleotide of the P-site tRNA and the Ca atom of Thr2 were calculated. The distance from the A site was calculated between the Ca atom of Arg6 and the center of geometry of the centers of U2504 ribose atoms, U2506 phosphate atoms and the C2452 base atoms. For each set of simulations, the distances were sorted into 2-d bins and the logarithm of the probability  $p = c_{ij}/c_{\text{total}}$  for each bin  $i, j$ , where  $c_{ij}$  is the number of frames in the bin and  $c_{\text{total}}$  is the total number of frames was calculated.

To address the question to what extent the conformations of ErmDL interfere with the accommodation of an A-site tRNA, which entails nucleotides U2505 and U2585 adopting their induced conformations, we identified van-der-Waals clashes of the ErmDL peptide with residues from aligned structures. In particular, we identified clashes of Arg6 (ErmDL) with the Lys or Phe attached to the A-site tRNA<sup>28,31</sup>.

Further, we identified clashes of Arg6 with an A-site Ala, obtained from the A-site Phe structure after removing side-chain atoms. Clashes with U2506 and U2585 were identified with ErmDL residues Arg6-His3 and His3-Thr2, respectively. To identify clashes, for each trajectory, we first extracted heavy-atom coordinates of the ErmDL residues at intervals of 50 ps. To find out if the ErmDL residues (set A with  $N_A$  atoms) clash with the aligned residues (set B with  $N_B$  atoms), for each of these snapshots, we constructed a rectangular box which contains the van-der-Waals spheres of all potentially overlapping atoms. To determine the box boundaries, we calculated the two minima, one,  $x_{\text{min},A} = \min(\{x_i - r_i, i \in \{1, \dots, N_A\}\})$ , where  $x_i$  is the x-coordinate of atom  $i$  from set A and  $r_i$  is its van-der-Waals radius, and, two,  $x_{\text{min},B} = \min(\{x_j - r_j, j \in \{1, \dots, N_B\}\})$  for atoms  $j$  in set B. The maximum of the two minima is then used as the lower border of the box along the x-axis. The minimum of the two maxima along the x-axis determines the upper border of the box. For y-directions and z-directions, the borders were determined analogously. Next, a random coordinate within the box was drawn from a uniform distribution. If this coordinate was within the van-der-Waals radius of one atom in set A and of one atom in set B, the snapshot was considered clashing. Otherwise, iteratively, a new random coordinate was drawn until either a clash was found, or 50,000 coordinates were drawn. Only 250 ps intervals in which all five snapshots had an overlap of 0 were considered as non-overlapping conformations. To check which ErmDL conformations can resolve clashes, for each 2-d bin along the two distances (see above), we checked if there is a conformation that does not lead to a clash with A-site amino acids Lys, Phe, and Ala and the induced conformations of U2506 and U2585. To see for a larger set of A-site amino acids and amino acid conformations, in addition to the conformations obtained from structures (described above), if they clash with Arg6 conformations, we constructed all possible rotamer conformations of Val8, Ile8, Phe8, Met8, Lys8, Tyr8, Trp8, and Arg8. To that aim, we took all rotamer conformations from a rotamer library<sup>64</sup>, aligned them to the Lys or Phe attached to the A-site tRNA<sup>28,31</sup> using the N-atoms, Ca-atoms, C $\beta$ -atoms, and C-atoms. Next, we excluded the rotamer conformations which produced a van-der-Waals clash of heavy atoms with rRNA nucleotides. For the remaining conformations, we calculated van-der-Waals clashes with the Arg6 conformations observed in the simulations as described above.

In the simulations after removal of ERY, we observe conformations which do not overlap with the A-site Arg and the induced nucleotides. To check if resolving clashes is correlated with the ErmDL peptide moving into the space which would be occupied by ERY, for each frame of the –ERY simulations, two van-der-Waals overlap volumes were calculated. First, the overlap of the peptide with aligned ERY coordinates and, second, the overlap of the peptide with the A-site Lys and the induced nucleotides. Volumes were calculated as described for the clashes, except that all 50,000 coordinates were drawn. Volumes were estimated by multiplying the volume of the box with number of coordinates that are within van-der-Waals radii of one atom from set A and one atom from set B divided by 50,000.

**Reporting summary.** Further information on research design is available in the Nature Research Reporting Summary linked to this article.

#### Data availability

The data that support this study are available from the corresponding authors upon reasonable request. The cryo-EM maps of the ErmDL-ERY-P-tRNA-SRC, ErmDL-ERY-A-P-tRNA-SRC and ErmDL-TEL-A-P-tRNA-SRC and the associated molecular models have been deposited in the Protein Data Bank and Electron Microscopy Data Bank with the accession codes EMD-12573, EMD-12574, EMD-12575, and PDB 7NSO, 7NSP, 7NSQ respectively. Sequencing data from the inverse toeprinting analysis have been deposited in the National Center for Biotechnology Information Short Read Archive with the accession code PRJNA623725. Source data are provided with this paper.

Received: 26 May 2021; Accepted: 30 June 2021;

Published online: 22 July 2021

#### References

- Wilson, D. N. Ribosome-targeting antibiotics and bacterial resistance mechanisms. *Nat. Rev. Microbiol.* **12**, 35–48 (2014).
- Lin, J., Zhou, D., Steitz, T. A., Polikanov, Y. S. & Gagnon, M. G. Ribosome-targeting antibiotics: modes of action, mechanisms of resistance, and implications for drug design. *Annu. Rev. Biochem.* <https://doi.org/10.1146/annurev-biochem-062917-011942> (2018).
- Dinos, G. P. The macrolide antibiotic renaissance. *Br. J. Pharm.* **174**, 2967–2983 (2017).
- Vazquez-Laslop, N. & Mankin, A. S. How macrolide antibiotics work. *Trends Biochem. Sci.* **43**, 668–684 (2018).
- Svetlov, M. S., Vazquez-Laslop, N. & Mankin, A. S. Kinetics of drug-ribosome interactions defines the fidelity of macrolide antibiotics. *Proc. Natl Acad. Sci. USA* **114**, 13673–13678 (2017).

6. Svetlov, M. S., Cohen, S., Alsuhebany, N., Vazquez-Laslop, N. & Mankin, A. S. A long-distance rRNA base pair impacts the ability of macrolide antibiotics to kill bacteria. *Proc. Natl Acad. Sci. USA* **117**, 1971–1975 (2020).
7. Dunkle, J. A., Xiong, L., Mankin, A. S. & Cate, J. H. Structures of the *Escherichia coli* ribosome with antibiotics bound near the peptidyl transferase center explain spectra of drug action. *Proc. Natl Acad. Sci. USA* **107**, 17152–17157 (2010).
8. Bulkley, D., Innis, C. A., Blaha, G. & Steitz, T. A. Revisiting the structures of several antibiotics bound to the bacterial ribosome. *Proc. Natl Acad. Sci. USA* **107**, 17158–17163 (2010).
9. Svetlov, M. S. et al. Context-specific action of macrolide antibiotics on the eukaryotic ribosome. *Nat. Commun.* <https://doi.org/10.1038/s41467-021-23068-1> (2021).
10. Svetlov, M. S. et al. Structure of Erm-modified 70S ribosome reveals the mechanism of macrolide resistance. *Nat. Chem. Biol.* <https://doi.org/10.1038/s41589-020-00715-0> (2021).
11. Mankin, A. S. Macrolide myths. *Curr. Opin. Microbiol.* **11**, 414–421 (2008).
12. Kannan, K., Vazquez-Laslop, N. & Mankin, A. S. Selective protein synthesis by ribosomes with a drug-obstructed exit tunnel. *Cell* **151**, 508–520 (2012).
13. Vazquez-Laslop, N. & Mankin, A. S. Context-specific action of ribosomal antibiotics. *Annu. Rev. Microbiol.* **72**, 185–207 (2018).
14. Kannan, K. et al. The general mode of translation inhibition by macrolide antibiotics. *Proc. Natl Acad. Sci. USA* **111**, 15958–15963 (2014).
15. Davis, A. R., Gohara, D. W. & Yap, M. N. Sequence selectivity of macrolide-induced translational attenuation. *Proc. Natl Acad. Sci. USA* **111**, 15379–15384 (2014).
16. Seip, B., Sacheau, G., Dupuy, D. & Innis, C. A. Ribosomal stalling landscapes revealed by high-throughput inverse toeprinting of mRNA libraries. *Life Sci. Alliance* **1**, e201800148 (2018).
17. Sothivelvam, S. et al. Macrolide antibiotics allosterically predispose the ribosome for translation arrest. *Proc. Natl Acad. Sci. USA* **111**, 9804–9809 (2014).
18. Sothivelvam, S. et al. Binding of macrolide antibiotics leads to ribosomal selection against specific substrates based on their charge and size. *Cell Rep.* **16**, 1789–1799 (2016).
19. Ramu, H., Mankin, A. & Vazquez-Laslop, N. Programmed drug-dependent ribosome stalling. *Mol. Microbiol.* **71**, 811–824 (2009).
20. Almutairi, M. M. et al. Resistance to ketolide antibiotics by coordinated expression of rRNA methyltransferases in a bacterial producer of natural ketolides. *Proc. Natl Acad. Sci. USA* **112**, 12956–12961 (2015).
21. Weisblum, B. Erythromycin resistance by ribosome modification. *Antimicrob. Agents Chemother.* **39**, 577–585 (1995).
22. Gupta, P., Sothivelvam, S., Vazquez-Laslop, N. & Mankin, A. S. Dereglulation of translation due to post-transcriptional modification of rRNA explains why erm genes are inducible. *Nat. Commun.* **4**, 1984 (2013).
23. Kwak, J. H., Choi, E. C. & Weisblum, B. Transcriptional attenuation control of ermK, a macrolide-lincosamide-streptogramin B resistance determinant from *Bacillus licheniformis*. *J. Bacteriol.* **173**, 4725–4735 (1991).
24. Hue, K. K. & Bechhofer, D. H. Regulation of the macrolide-lincosamide-streptogramin B resistance gene ermD. *J. Bacteriol.* **174**, 5860–5868 (1992).
25. Kwon, A. R. et al. ErmK leader peptide: amino acid sequence critical for induction by erythromycin. *Arch. Pharm. Res.* **29**, 1154–1157 (2006).
26. Bailey, M., Chettiath, T. & Mankin, A. S. Induction of erm(C) expression by noninducing antibiotics. *Antimicrob. Agents Chemother.* **52**, 866–874 (2008).
27. Ingolia, N. T., Ghaemmaghami, S., Newman, J. R. & Weissman, J. S. Genome-wide analysis in vivo of translation with nucleotide resolution using ribosome profiling. *Science* **324**, 218–223 (2009).
28. Arenz, S. et al. A combined cryo-EM and molecular dynamics approach reveals the mechanism of ErmBL-mediated translation arrest. *Nat. Commun.* **7**, 12026 (2016).
29. Arenz, S. et al. Drug sensing by the ribosome induces translational arrest via active site perturbation. *Mol. Cell* **56**, 446–452 (2014).
30. Arenz, S. et al. Molecular basis for erythromycin-dependent ribosome stalling during translation of the ErmBL leader peptide. *Nat. Commun.* **5**, 3501 (2014).
31. Polikanov, Y. S., Steitz, T. & Innis, C. A. A proton wire to couple aminoacyl-tRNA accommodation and peptide-bond formation on the ribosome. *Nat. Struct. Mol. Biol.* **21**, 787–793 (2014).
32. Polikanov, Y. S. et al. Distinct tRNA accommodation intermediates observed on the ribosome with the antibiotics hygromycin A and A201A. *Mol. Cell* **58**, 832–844 (2015).
33. Schmeing, T. M., Huang, K. S., Kitchen, D. E., Strobel, S. A. & Steitz, T. A. Structural insights into the roles of water and the 2' hydroxyl of the P site tRNA in the peptidyl transferase reaction. *Mol. Cell* **20**, 437–448 (2005).
34. Schmeing, T. M., Huang, K. S., Strobel, S. A. & Steitz, T. A. An induced-fit mechanism to promote peptide bond formation and exclude hydrolysis of peptidyl-tRNA. *Nature* **438**, 520–524 (2005).
35. Douthwaite, S. Structure-activity relationships of ketolides vs. macrolides. *Clin. Microbiol. Infect.* **7**, 11–17 (2001).
36. Vazquez-Laslop, N., Ramu, H., Klepacki, D., Kannan, K. & Mankin, A. S. The key function of a conserved and modified rRNA residue in the ribosomal response to the nascent peptide. *EMBO J.* **29**, 3108–3117 (2010).
37. Orelle, C. et al. Tools for characterizing bacterial protein synthesis inhibitors. *Antimicrob. Agents Chemother.* **57**, 5994–6004 (2013).
38. Schneider, C. A., Rasband, W. S. & Eliceiri, K. W. NIH Image to ImageJ: 25 years of image analysis. *Nat. Methods* **9**, 671–675 (2012).
39. Cock, P. J. et al. Biopython: freely available Python tools for computational molecular biology and bioinformatics. *Bioinformatics* **25**, 1422–1423 (2009).
40. Zhang, J., Kobert, K., Flouri, T. & Stamatakis, A. PEAR: a fast and accurate Illumina Paired-End reAd mergeR. *Bioinformatics* **30**, 614–620 (2014).
41. Rubin, A. F. et al. A statistical framework for analyzing deep mutational scanning data. *Genome Biol.* **18**, 150 (2017).
42. Zivanov, J. et al. New tools for automated high-resolution cryo-EM structure determination in RELION-3. *eLife* <https://doi.org/10.7554/eLife.42166> (2018).
43. Zhang, K. Gctf: Real-time CTF determination and correction. *J. Struct. Biol.* **193**, 1–12 (2016).
44. Scheres, S. H. RELION: implementation of a Bayesian approach to cryo-EM structure determination. *J. Struct. Biol.* **180**, 519–530 (2012).
45. Herrero Del Valle, A. et al. Ornithine capture by a translating ribosome controls bacterial polyamine synthesis. *Nat. Microbiol.* **5**, 554–561 (2020).
46. Pettersen, E. F. et al. UCSF chimera—a visualization system for exploratory research and analysis. *J. Comput. Chem.* **25**, 1605–1612 (2004).
47. Emsley, P. & Cowtan, K. Coot: model-building tools for molecular graphics. *Acta Crystallogr. Sect. D* **60**, 2126–2132 (2004).
48. Adams, P. D. et al. PHENIX: a comprehensive Python-based system for macromolecular structure solution. *Acta Crystallogr. D* **66**, 213–221 (2010).
49. Chen, V. B. et al. MolProbity: all-atom structure validation for macromolecular crystallography. *Acta Crystallogr. D* **66**, 12–21 (2010).
50. Goddard, T. D. et al. UCSF ChimeraX: meeting modern challenges in visualization and analysis. *Protein Sci.* **27**, 14–25 (2018).
51. Huter, P. et al. Structural basis for polyproline-mediated ribosome stalling and rescue by the translation elongation factor EF-P. *Mol. Cell* **68**, 515–527 (2017).
52. Fischer, N. et al. Structure of the *E. coli* ribosome-EF-Tu complex at <3 Å resolution by C-corrected cryo-EM. *Nature* **520**, 567–570 (2015).
53. Vriend, G. WHAT IF: a molecular modeling and drug design program. *J. Mol. Graph* **8**, 52–56 (1990).
54. Abraham, M. J. et al. GROMACS: high performance molecular simulations through multi-level parallelism from laptops to supercomputers. *SoftwareX* **1–2**, 19–25 (2015).
55. Case, D. A. et al. The Amber biomolecular simulation programs. *J. Comput. Chem.* **26**, 1668–1688 (2005).
56. Berendsen, H. J. C., Grigera, J. R. & Straatsma, T. P. The missing term in effective pair potentials. *J. Phys. Chem.* **91**, 6269–6271 (1987).
57. Joung, I. S. & T., E. C. III Determination of alkali and halide monovalent ion parameters for use in explicitly solvated biomolecular simulations. *J. Phys. Chem. B* **112**, 9020–9041 (2008).
58. Essmann, U. et al. A smooth particle mesh Ewald method. *J. Chem. Phys.* **103**, 8577 (1995).
59. Hess, B. P-LINCS: a parallel linear constraint solver for molecular simulation. *J. Chem. Theory Comput.* **4**, 116–122 (2008).
60. Feenstra, K. A., Hess, B. & Berendsen, H. J. C. Improving efficiency of large time-scale molecular dynamics simulations of hydrogen-rich systems. *J. Comput. Chem.* **20**, 786–798 (1999).
61. Bussi, G., Donadio, D. & Parrinello, M. Canonical sampling through velocity rescaling. *J. Chem. Phys.* **126**, 014101 (2007).
62. Parrinello, M. & Rahman, A. Polymorphic transitions in single crystals: a new molecular dynamics method. *J. Appl. Phys.* <https://doi.org/10.1063/1.328693> (1981).
63. Briones, R., Blau, C., Kutzner, C., de Groot, B. L. & Aponte-Santamaria, C. GROMaps: a GROMACS-based toolset to analyze density maps derived from molecular dynamics simulations. *Biophys. J.* **116**, 4–11 (2019).
64. Lovell, S. C., Word, J. M., Richardson, J. S. & Richardson, D. C. The penultimate rotamer library. *Proteins* **40**, 389–408 (2000).

## Acknowledgements

We thank Dorota Klepacki for her help with toeprinting experiments and Haripriya Ramu for the construction of the inducible *ermD* reporter. This work has been supported by grants of the National Institutes of Health (R35 GM127134 to A.S.M.), the Deutsche Forschungsgemeinschaft (WI3285/3-1 to D.N.W. and EXC 2067/1-390729940 to L.V.B. and H.G.), the Deutsche Zentrum für Luft- und Raumfahrt (DLR01KI1820 to D.N.W.) and the ANR (ANR-18-JAM2-0005 to C.A.I.) within the “RIBOTARGET” consortium under the frame of JPIAMR (to D.N.W. and C.A.I.). E.L., B.S., and C.A.I. have received funding for this project from the European Research Council (ERC) under the European Union’s Horizon 2020 research and innovation program (Grant Agreement No. 724040). C.A.I. is an EMBO YIP and has received funding from the Fondation Bettencourt-Schueller. Open Access funding enabled and organized by Project DEAL.



## Author contributions

S.A. and M.A. generated complexes for cryo-EM analysis. B.B. and M.G. performed cryo-EM analysis. E.L. performed the complete deep mutational scans, while B.S. performed preliminary inverse toeprinting experiments. S.S. and M.S.S. performed toeprinting analysis. L.V.B. and H.G. performed the MD simulations. N.V.-L., C.A.I., A.S.M., and D. N.W. conceived the project. All authors analyzed and interpreted the results and helped D.N.W. write the paper.

## Funding

Open Access funding enabled and organized by Projekt DEAL.

## Competing interests

The authors declare no competing interests.

## Additional information

**Supplementary information** The online version contains supplementary material available at <https://doi.org/10.1038/s41467-021-24674-9>.

**Correspondence** and requests for materials should be addressed to L.V.B., C.A.I., N.V.-L. or D.N.W.

**Peer review information** *Nature Communications* thanks Jonas Barandun, Jack A.

Dunkle and the other, anonymous, reviewer(s) for their contribution to the peer review of this work.

**Reprints and permission information** is available at <http://www.nature.com/reprints>

**Publisher's note** Springer Nature remains neutral with regard to jurisdictional claims in published maps and institutional affiliations.



**Open Access** This article is licensed under a Creative Commons Attribution 4.0 International License, which permits use, sharing, adaptation, distribution and reproduction in any medium or format, as long as you give appropriate credit to the original author(s) and the source, provide a link to the Creative Commons license, and indicate if changes were made. The images or other third party material in this article are included in the article's Creative Commons license, unless indicated otherwise in a credit line to the material. If material is not included in the article's Creative Commons license and your intended use is not permitted by statutory regulation or exceeds the permitted use, you will need to obtain permission directly from the copyright holder. To view a copy of this license, visit <http://creativecommons.org/licenses/by/4.0/>.

© The Author(s) 2021

### 3.3.2. ErmCL and ErmAL1 arrest peptides affect the A-site properties of the PTC in presence of cladinose-containing macrolide antibiotics using the same mechanism of inhibition.

In order to understand the different properties of the A-site in the PTC observed between ErmCL and ErmAL1 depending of the nature of the residue located at position -2 in the presence of a cladinose-containing macrolide like erythromycin, I performed 3 biological replicates of inverse toeprinting using two types of libraries: a first library containing a single-codon mutagenesis plus an additional double codon mutagenesis of codons F7 and S10 of the full-length ErmCL peptide, and a second library containing a single-codon mutagenesis plus a double codon mutagenesis of codons A6 and E9 of the full-length ErmAL1 peptide. The positions chosen for the double codon mutagenesis, corresponds to the positions -2 and the A site respectively.

#### 3.3.2.1. MATERIALS AND METHODS

DNA and RNA products at various points in the inverse toeprinting protocol were analyzed on 9% acrylamide (19:1) TBE (90 mM Tris, 90 mM boric acid, and 2 mM EDTA) gels and stained with SyBR Gold (Invitrogen). Inverse toeprints were excised from 12% acrylamide TBE gels using a clean scalpel. RNA gel electrophoresis was performed under denaturing conditions (8 M urea in the gel). All reactions were performed using molecular biology grade H<sub>2</sub>O (Millipore). Oligonucleotides used in this study are listed in **Supplementary Table 1**.

#### *Single and double mutants ermCL/ermAL1 variant library generation:*

Using the Opool technology from IDT, I generated expression cassettes for codon 2 to 19 of *ermCL* and for codon 2 to 15 for *ermAL1*, with the addition of one expression cassette containing two “NNN” codons for the codons 7 and 10 of *ermCL* and one expression cassette containing “NNN” codons for the codons 6 and 9 of *ermAL1* (

**Figure 16**). All of the expression cassettes were equally generated by IDT and furnished as a single ready-to-use oligo library.

The sequence of the expression cassette for wild-type *ermCL* is:

CGATCGAATTCTAATACGACTCACTATAGGGCTTAAGTATAAGGAGGAAAAAAT  
ATGTGCATTTTTAGTATTTTTGTAATCAGCACAGTTCATTATCAACCAAACAA  
AAAAGCGATCTCGGTGTGATGAGATATCAATATCAAAAAGGATCCATATA

(the T7 promoter is underlined, the mutated *ermCL* region is in **bold**; the EcoRV site is in *italics*).

The sequence of the expression cassette for wild-type *ermAL1* is:

CGATCGAATTCTAATACGACTCACTATAGGGCTTAAGTATAAGGAGGAAAAAAT  
ATGTGCACCAGTATCGCAGTAGTAGAAATTACTTTATCTCATTTCAGCGATCTC  
GGTGTGATGAGATATCAATATC AAAAAGGATCCATATA.

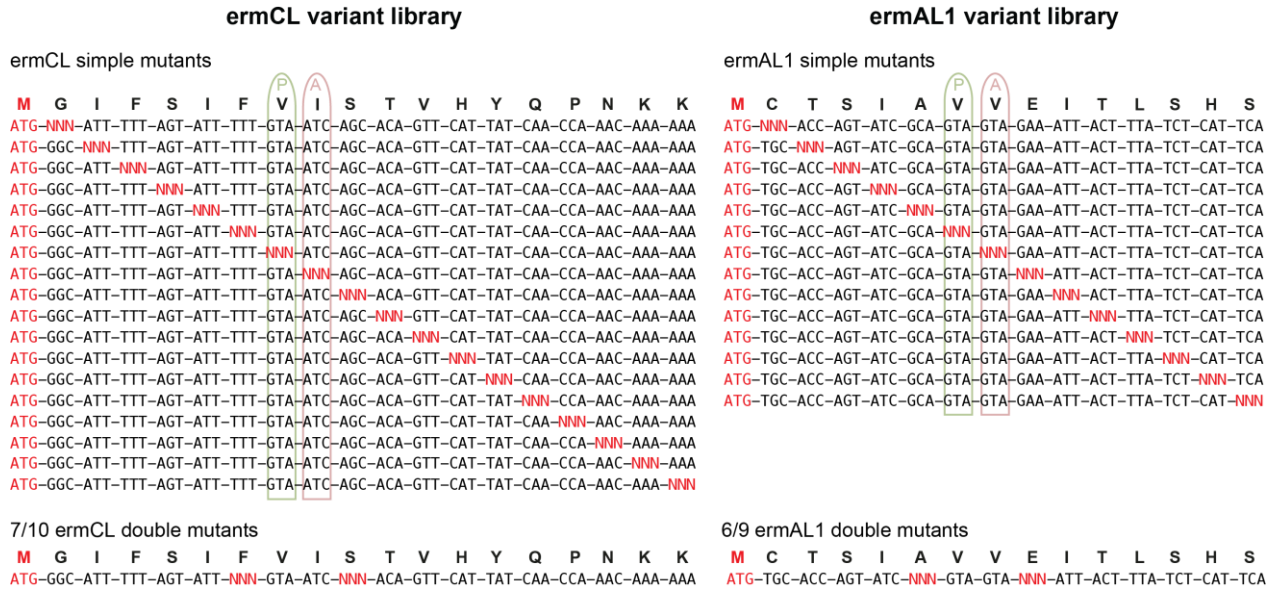


**Figure 16 : Single-codon and 7/10 double codons mutants *ermCL* libraries. Single codon and 6/9 double codons mutants *ermAL1* libraries**

5' and 3' extremities containing for example the T7 promoter, the RBS, and the EcoRV site that are required for inverse toeprinting, were then added by PCR with Phusion DNA polymerase (20 cycles [98°C, 10 s; 60°C, 5 s; 72°C, 10 s]), using the *ermAL1\_opool* or *ermAL1\_opool* libraries in combination with oligonucleotides *T7\_RBS\_ATG\_f* and *Stop\_EcoRV\_r* as templates (1 pmol of each oligonucleotide per 50 µl reaction), and oligonucleotides *T7\_f* and *EcoRV\_r* for amplification (10 pmol of each oligonucleotide per 50 µl reaction; see oligos **Supplementary Table 1**). The two linear expression libraries were purified using a PCR purification kit (Qiagen) according to the manufacturer's instructions prior to quantification with a 2100 Agilent Bioanalyzer and mixing.

### ***In vitro* transcription**

The DNA template contains a T7 promoter followed by a ribosome binding sequence, as specified in the NEB PURExpress system handbook. *In vitro* transcription was performed using

T7 RNA polymerase in a buffer containing 80 mM Tris-HCl, 24 mM MgCl<sub>2</sub>, 2 mM spermidine, and 40 mM DTT, pH 7.6, in the presence of 7.5 mM ATP (Sigma Aldrich), CTP and UTP, 0.3 mM GTP (CTP, UTP, and GTP from Jena Bioscience), and 4.5 mM Thio-Phosphate-GMP (Genaxxon Bioscience). 8 pmol of DNA template were used in 200 µl of reaction volume. *In vitro* transcription was performed at 20°C for 3 h, mRNA was purified using the “RNA Clean & Concentrator<sup>TM</sup>-5” purification kit (ZymoClean Research) according to the manufacturer’s instructions. The final concentration of mRNA was determined using the NanoDrop.

### ***Biotinylation***

Biotin-maleimide (Vectorlabs) was dissolved in dimethylformamide according to the manufacturer’s instructions. 800 pmol mRNA were mixed with 800 nmol biotin-maleimide in 100 mM in Bis-Tris-acetate buffer pH 6.7 and incubated at room temperature for 2.5 h. Unincorporated biotin was removed by washing the mRNA three times with H<sub>2</sub>O (molecular biology grade, Millipore) in an Amicon membrane centrifugal concentrator with a MWCO of 30 kDa (Millipore). mRNA was recovered and the biotinylation efficiency was analyzed using a dot blot.

### ***Dot blot***

H<sup>+</sup> bond membrane (GE Healthcare) was treated with 6× SSC buffer (900 mM NaCl, 90 mM Na<sub>3</sub>-citrate, pH 7.0) for 10 min and dried briefly between two pieces of Whatman paper. Samples and a 5'-biotinylated oligonucleotide standard (Biotin\_standard) were diluted in 6× SSC buffer to 0.5, 1.0, 2.5, and 5.0 µM, and 1 µl of each dilution was pipetted onto the prepared membrane. The membrane was then baked for 2 h at 80°C to adsorb the mRNA to the membrane. The membrane was subsequently blocked in 2.5% dry milk solution in TBS-T (50 mM Tris-HCl, 150 mM NaCl, and 0.05% [vol/vol] Tween-20, pH 7.5) for 1 h at room temperature. The milk solution was removed and the membrane was incubated with a 1:1,000 dilution of streptavidin-alkaline phosphatase antibody (Promega) in TBS-T for 1 h at room temperature. Unbound antibody was removed by washing three times with TBS-T buffer. Colorimetric detection was performed using an NBT/BCIP detection kit (Promega) according to the manufacturer’s instructions. The membrane was imaged immediately on a Bio-Rad Imager. The biotinylation efficiency was estimated by comparing the intensity of the sample dots with the intensity of the standard dots.

### ***Polyadenylation of the mRNA***

Polyadenylation of the biotinylated mRNA was performed using Poly-A polymerase (NEB) using the buffer supplied. The ratio of mRNA to ATP molecules was chosen to be 1:100. The reaction was incubated at 37°C for 2 h and the efficiency of the polyadenylation reaction was assessed by denaturing PAGE (9%). Polyadenylated mRNA was purified using the purification “RNA Clean & Concentrator<sup>TM</sup>-5” kit (ZymoClean Research) according to the manufacturer’s instructions.

### ***Inverse toeprinting***

Inverse toeprinting was performed as described previously, with modifications (Seip et al., 2018). Briefly, *in vitro* translation was carried out with a PURExpress  $\Delta$  RF-123  $\Delta$ Ribosomes kit (NEB), using ~5 pmol of 5'-biotinylated and 3'-polyadenylated mRNA as a template. Erythromycin was supplemented at a final concentration of 50  $\mu$ M in 5  $\mu$ l reactions. Release factors 1 and 3 were added to the translation reaction according to the manufacturer’s instructions. Translation was performed at 37°C for 30 min, after which the samples were placed on ice and 5  $\mu$ l ice-cold  $Mg^{2+}$  buffer (50 mM Hepes-KOH, 100 mM K-glutamate, 87 mM Mg- acetate, and 1 mM DTT, pH 7.5) was added to the reactions, thereby increasing the  $Mg^{2+}$  concentration to 50 mM. 1  $\mu$ l of RNase R (1 mg/ml) was added, followed by an additional incubation for 30 min at 37°C to ensure complete mRNA degradation. 139  $\mu$ l of 1 $\times$  BWT buffer was added to stop the reaction (5 mM Tris-HCl, 0.5 mM EDTA, 1 M NaCl, and 0.05% [vol/vol] Tween- 20, pH 7.5).

### ***In vitro translation conditions***

I translated the *ermCL/ermALI* mutant variant libraries in the presence or absence of 50  $\mu$ M erythromycin and produced ribosome-protected inverse toeprints. The *in vitro* translation reaction is performed using the PURE system (NEB). For these inverse toeprinting assays, the PURE system chosen was lacking release factors and ribosomes (PURExpress  $\Delta$ RF123  $\Delta$ Ribosome system (NEB)) so that they can be added as needed.

### ***mRNA purification and linker ligation***

For each sample, 5  $\mu$ l of a M-280 streptavidin Dynabead (ThermoFisher Scientific) suspension were washed three times with 1 $\times$  BWT buffer in DNA loBind tubes (Eppendorf) and

resuspended in 50 µl of the same buffer. Dynabeads and RNA from the previous step were combined into these tubes and incubated on a tube rotator for 15 min at room temperature to allow binding of the biotinylated mRNA to the streptavidin beads. After incubation, beads were collected using a magnet and the supernatant was discarded. The beads were washed one time with 1× BWT buffer to remove unbound RNA, followed by two washes with H<sub>2</sub>O to remove the 1× BWT buffer. Beads were resuspended in 9.5 µl of linker ligation reaction mixture containing 4 µl of water, 1 µl of T4 RNA ligase2 truncated buffer (10X – NEB), 3 µl of PEG 8000 (50% - NEB), 1 µl of 3'\_linker\_ApoI (10 µM) and 0.5 µl of ligase (T4 RNA ligase 2, truncated - 200 000 U/ml - NEB) per reaction. Linker ligation was allowed to proceed on a tube rotator for 2.5 h at room temperature.

### ***Reverse transcription***

Following ligation of the linker, beads were washed once with H<sub>2</sub>O to remove unincorporated linker oligonucleotide and were resuspended in 18.5 µl of reverse transcription reaction mixture containing 11.5 µl of water, 1 µl of dNTPs (10 mM of each - NEB), 1 µl of Linker\_r oligonucleotide (2 µM), 4 µl of first strand synthesis buffer (5X - ThermoFisher) and 1 µl of DTT (0.1 M - ThermoFisher) per reaction. The samples were incubated for 5 min at 65°C to anneal the primer to the complementary sequence and then placed on ice. 1 µl of reverse transcriptase (Superscript III – 200,000 U/ml – ThermoFisher) was added to each tube and the samples were incubated for 30 min at 55°C in a Thermomixer at 500 rpm to allow reverse transcription of the Dynabead-bound mRNA.

### ***PCR on cDNA, restriction digestion***

Reverse transcribed cDNA was used without further purification as a template for PCR. To generate double stranded DNA for restriction digestion, a fill-up reaction was performed using cDNA\_f oligonucleotide and the reverse transcribed cDNA (10 s denaturation, 10 s annealing at 42°C, and 30 s elongation at 72°C). The resulting double stranded DNA was combined with 1 µl of EcoRV-HF restriction enzyme and the sample was incubated at 37°C for 1 h. To amplify undigested DNA, Linker\_r oligonucleotide was added and a PCR was performed with 10-16 cycles (denaturation at 98°C for 10 s, annealing at 60°C for 10 s, and elongation at 72°C for 10 s). The number of PCR cycles was adjusted to give a visible band on the gel while minimizing non-specific byproducts.

### ***Purification of DNA fragments of interest after PCR***

Bands containing inverse toeprints corresponding to stalled ribosomes were excised from the gel with a clean scalpel. Gel pieces were crushed through a 5 ml syringe into 15 ml Falcon tubes and 5 ml of gel elution buffer (10 mM Tris-HCl, pH 8.0, 500 mM Na-acetate, and 0.5 mM Na-EDTA) were added. The tubes were incubated on a tube rotator at room temperature overnight. Gel debris were separated from the extraction solution by filtering through 0.22 µm centrifugal filters (Millipore). Each sample was then concentrated to ~1 ml using a SpeedVac. DNA was precipitated in 5 ml Eppendorf tubes using 1 ml of isopropanol with 3.7 µl GlycoBlue (Thermo Fisher Scientific) and incubating at -80°C overnight. After precipitation, DNA was recovered by centrifugation in a ThermoScientific Heraeus Multifuge X3R centrifuge at 20,000g for 30 min at 4°C using a Fiberlite F15-8x50cy rotor (ThermoScientific). The supernatant was removed and DNA pellets were resuspended in 20 µl H<sub>2</sub>O (molecular biology grade, Milipore) for subsequent addition of the next-generation sequencing (NGS) adapters.

#### ***Additions of NGS adapters to amplified DNA***

Long NGS adapter oligonucleotides (NGS\_adaptor\_f and the reverse oligonucleotides NGS\_adaptor\_23 through NGS\_adaptor\_23+3) contain Illumina TruSeq adapter sequences followed by 18 nucleotides complementary to the 5' or 3' region of the cDNA. The reverse oligonucleotides also contain barcode sequences for multiplexing according to the TruSeq v1/v2/LT protocol (Illumina). Sequencing libraries were obtained from 12–16 cycles of PCR using 0.02 µM long NGS adapter oligonucleotides (forward and reverse) and 0.2 µM short amplification oligonucleotides (NGS\_f and NGS\_r). PCR products were purified using a Qiagen PCR purification kit. The size and concentration of the fragments obtained were measured using a 2100 Agilent Bioanalyzer with the DNA 1000 kit.

#### ***Next generation sequencing***

Next generation sequencing was performed by the BGI Facility in Hong-Kong, on an Illumina HiSeqXten system in rapid run mode with 150 PE reads.

#### ***Analysis of deep mutational scanning data***

Data analysis was carried out using a series of custom scripts written in-house in Python, which relied on the use of the Biopython package (Cock et al., 2009). Read pairs were assembled using PEAR v0.9.10 (Zhang et al., 2014), with the maximal proportion of uncalled bases in a read set to 0 (-u option) and the upper bound for the resulting quality score set to 126 (-c option). Regions immediately upstream of the start codon and downstream of the point of

cleavage by RNase R were removed using a python script. The 5' flanking region was defined as GTATAAGGAGGAAAAAAT, whereas the 3' flanking region was GGTATCTCGGTGTGACTG. A maximum of two mismatches within each of these flanking regions was tolerated, whereas all other reads were discarded. Trimming of the retained reads resulted in sequences with a start codon directly at the 5' end and the site of RNase R cleavage at the 3' end. Trimmed reads were analyzed in Enrich2 v1.0.0 (Rubin et al., 2017), a general software tool for processing, analyzing, and visualizing data from deep mutational scanning experiments, that generates error estimates for each measurement, capturing both sampling error and consistency between biological and technical replicates. Enrich2 use consisted in a single run with two separate experimental conditions, each consisting of 9 replicates (3 biological x 3 technical) of the libraries obtained following selection in the absence or presence of erythromycin. Reads were required to have a minimum quality score of 30 at all positions and contain no Ns.

### 3.3.2.2. RESULTS

I first compared the size distribution of inverse toeprints with a minimum Q-score of 30 obtained in absence of antibiotic to the size distribution of inverse toeprints obtained in presence of the erythromycin for both *ermCL* and *ermAL1* mutant variant libraries (**Figure 17**). As a reminder, the ErmCL peptide is able to arrest translation in presence of erythromycin when the ribosome reaches the IFVI motifs, where the last I9 of the motif is incorporated to the peptidyl-tRNA located in the P-site and blocks the incorporation of S10. For ErmAL1, the AVVE motif stalls the ribosome once the V8 reaches the P site to inhibit the incorporation of the E9 to the A site. Here, I size-selected the inverse toeprints matching these expectations, and I could therefore obtain a main peak corresponding to ribosomes stalled at codon 9 for ErmCL and at codon 8 for ErmAL1 (**Figure 17**). However, consistent with previous inverse toeprinting results from the laboratory (Seip et al., 2018), I could also observe a second peak for the *ermAL1* condition, corresponding to ribosomes stalled on codon 9 (**Figure 17**).

I then calculated the score representing the enrichment of variants in the presence of erythromycin compared to the negative control condition without antibiotics. To choose the threshold allowing the visualization of significative changes compared to the negative control, I looked at the distribution of the scores given by Enrich2 as a histogram (**Figure 18**). Positive scores in the assay indicate better performance in comparison to the negative control, indicating



that the corresponding variant efficiently stall the ribosome in presence of erythromycin, while negative score indicate worse performance, namely a weaker capability of the variant to stall the ribosome in presence of antibiotic. Scores close to 0 indicate neutral variations, where the variant behaves in presence of erythromycin similarly to the negative control condition. In my inverse toeprinting results, I could observe a bimodal score distribution, with one population around 0 corresponding to the neutral mutations and a second one between -1.5 and -4 corresponding to depleted variants which present a weaker capability to stall the ribosome in presence of antibiotic (**Figure 18**). No population corresponding to enriched variants was observed, meaning that none of the mutants were favorable for the arrest induced by the drug. I set the upper score threshold for a detrimental mutation to -1.5 and plotted the corresponding variants as yellow squares in **Figure 19**.

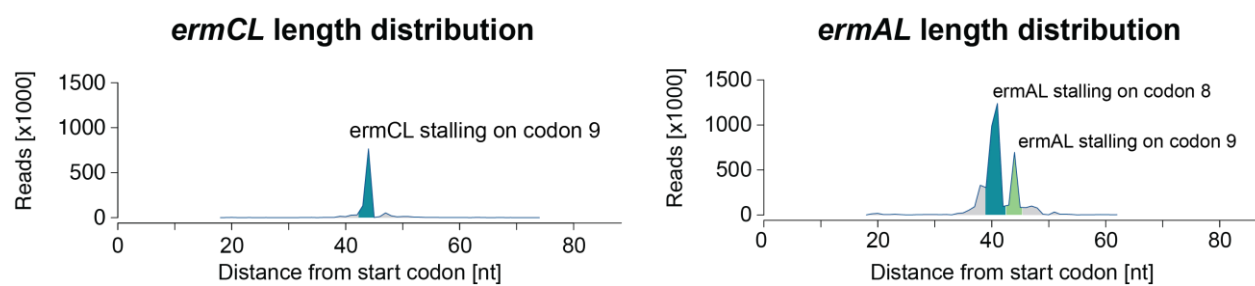


**Figure 17 : Inverse toeprints repartition for *ermCL* and *ermAL1* mutant libraries translated in presence of erythromycin**

The ability of single amino acid variants of ErmCL or ErmAL1 to stall ribosomes on codon 9 or 8, respectively, are shown in **Figure 19**. A positive score (red) indicates mutations that are beneficial for drug-induced stalling, whereas a negative score (blue) indicates detrimental mutations. For ErmCL, the “IFVI” motif is as expected clearly essential for the stalling. The A site (position 9) does not seem appear to be very selective, except for K and I which impair the stalling induced by erythromycin.

One surprising finding is that a stop codon is not tolerated in the A site, meaning that termination is not prevented by the presence of the drug. This observation indicates that only the elongation step is inhibited during ErmCL stalling. For ErmAL1, the arrest motif is less clear except for V7 which cannot be mutated to any residue other than P without losing the ability to undergo arrest. For the A site (position 8), M and aromatic residues are not tolerated (excepted W). This is not entirely in agreement with toeprinting data from (Ramu et al., 2011), where mutating E9 for C, M or F strongly affected the ability of ErmAL1 to stall translation in

presence of erythromycin, while other amino acids such as A, S, T, V or Q moderately affect the inhibition and the others do not affect the ability of ErmAL1 to inhibit translation. Similarly to ErmCL, the stop codon is not tolerated in the A-site.

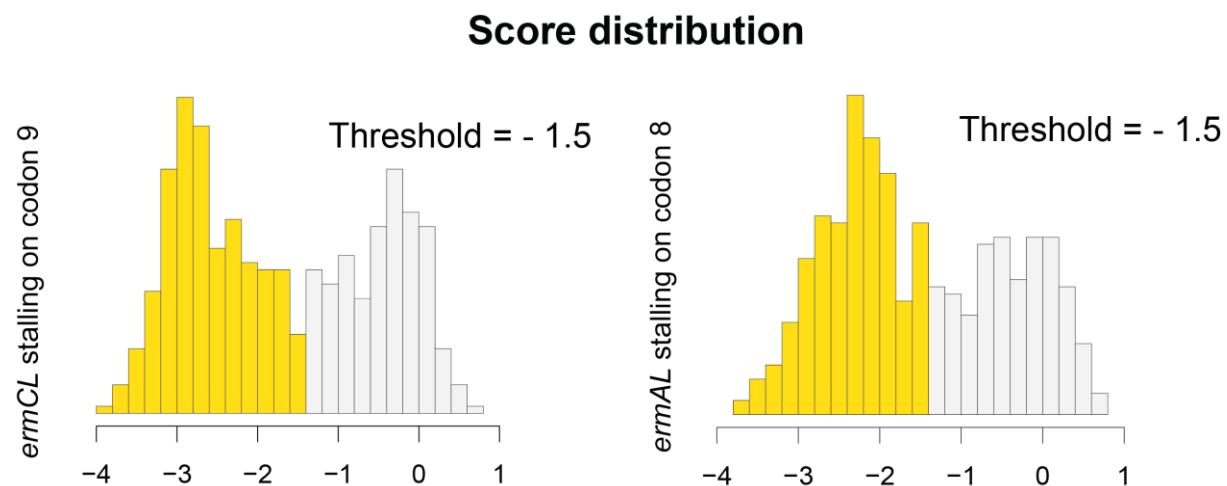
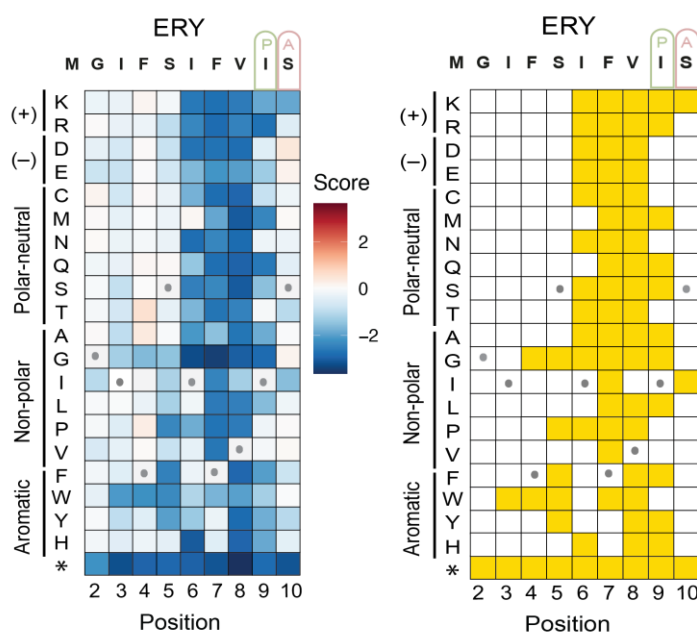


**Figure 18 : Histograms of score distribution furnished by Enrich2 for both ermCL and ermAL1 mutant variant libraries translated in presence of erythromycin**

A threshold of -1.5 separates the bimodal distribution of the scores, and scores lower than the threshold value represent significant depleted variants (yellow bars).

The double mutant analysis for ErmCL stalling on codon 9 and ErmAL1 stalling on codon 8 (**Figure 20**) revealed that the behaviors adopted by the two double mutant variant libraries translated in presence of erythromycin are very similar. In positions 7/6, aromatic residues (H,Y,F) and A are tolerated leading to an absence of selectivity for positions 10 or 9. The others residues at positions 7 or 6 are tolerated only when there are charged amino acids at positions 10 or 9, respectively.

## A Simple mutants (*ermCL* stalling on codon 9)



## B Simple mutants (*ermAL* stalling on codon 8)

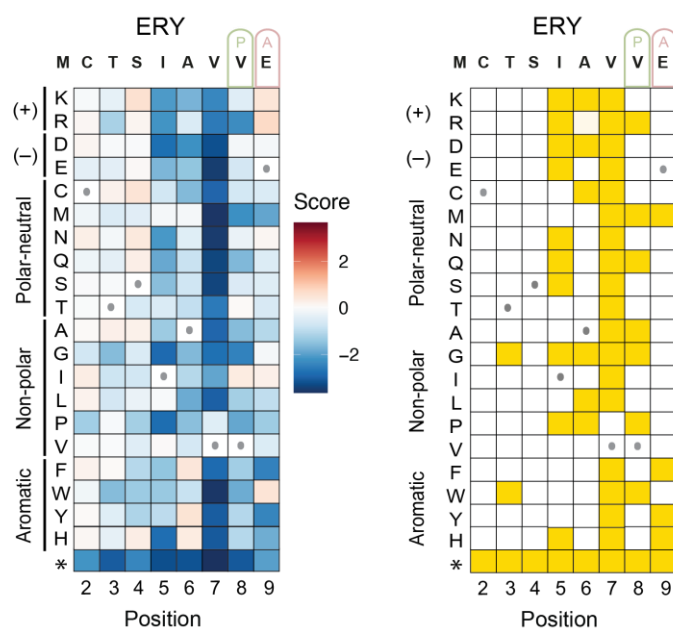
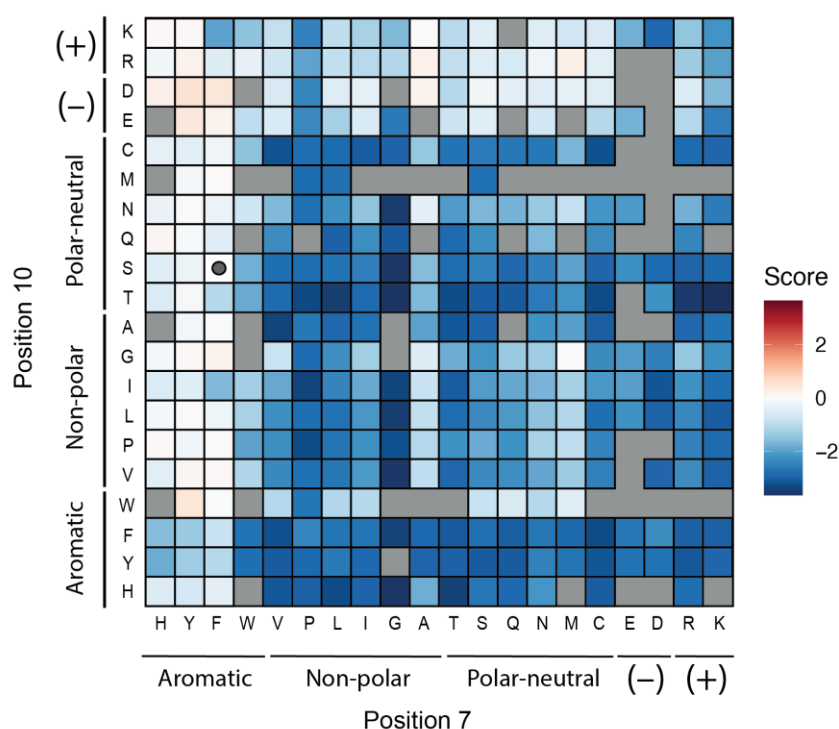


**Figure 19 : Sequence-function map of the *ErmCL* and *ErmAL1* peptides translated in the presence of erythromycin**

Panel A represents the *ErmCL* data and panel B the *ErmAL1* data. Cell color indicates the score for a single amino acid change at a given position, where positive scores (red) indicate better than wild-type translational arrest and negative scores (blue) indicate worse than wild-type performance (left panels). Significant mutations that abolish the arrest (scores < 1.5) are shown in yellow. The ribosomal P (green) and A (pink) sites are indicated above the wild-type *ErmCL* and *ErmAL1* sequences. Squares marked with a grey circle correspond to the wild-type amino acid.

## A 7/10 double mutants (*ermCL* stalling on codon 9)



## B 6/9 double mutants (*ermAL* stalling on codon 8)

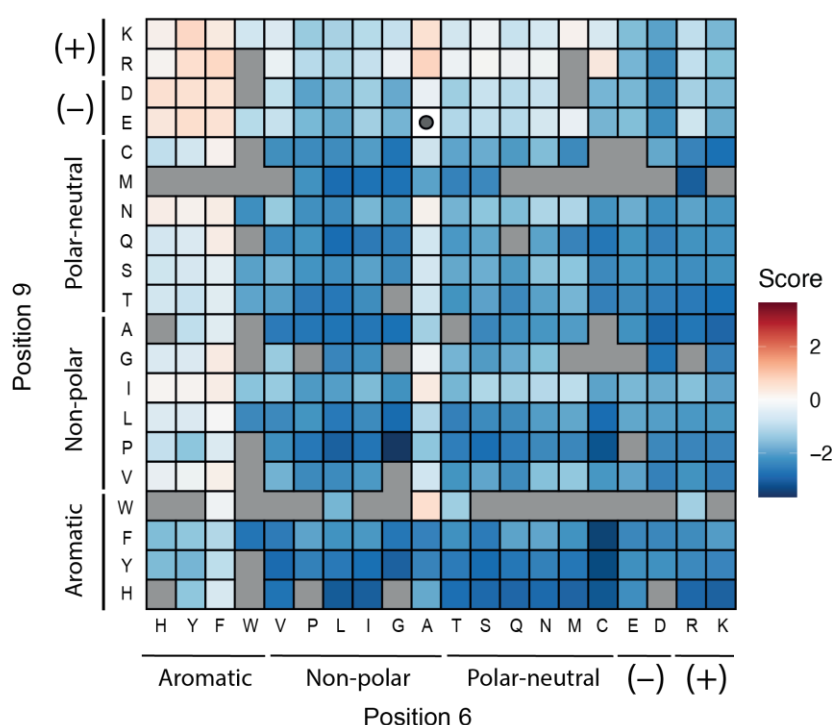


**Figure 20 : Sequence-function map furnished by Enrich2**

Panel A represents the 7/10 *ErmCL* double mutants and Panel B the 6/9 *ErmAL1* double mutants scores. Cell color indicates the score for a single amino acid combination, where positive scores (red) indicate better than wild-type translational arrest and negative scores (blue) indicate worse than wild-type performance. Grey dots correspond to the wildtype variant, and grey squares to missing data.

To verify the correlation between double mutant scores of the two *ermCL* and *ermAL1* libraries, I plotted the scores of each double mutant variant of either ErmAL1 stalling on codon 8 (X axis) or ErmCL stalling on codon 9 (Y axis) (**Figure 21**). I obtained an R squared of 0.72 after linear regression, illustrating a high correlation of the double mutant scores. Following this result, I concluded that ErmCL stalling on codon 9 and ErmAL1 stalling on codon 8 correspond to the same mechanism, where the two peptides respond in presence of erythromycin to the same pattern of amino acids at position 7/6 and 10/9 respectively.

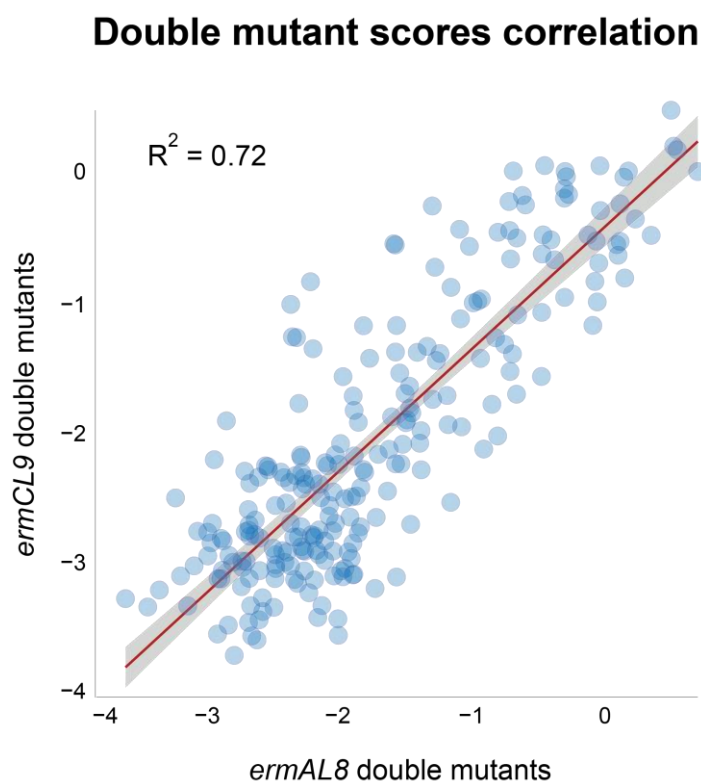


**Figure 21 : Double mutants score correlation plot**

The plot represents Enrich2 score distributions for double mutants of *ermCL* (Y axis) and *ermAL1* (X axis) variants translated in the presence erythromycin. The red line corresponds to the diagonal and represents identical score values between the two libraries scores. The grey surface around the red diagonal corresponds to a linear regression. Enrich2 scores are represented in blue circles.

Looking at the biochemical data together, a picture can be drawn where stalling of ErmCL or ErmAL1 on codon 8 in the presence of erythromycin rely on the same mechanism, involving the P-site tRNA and the -2 residue. The motif observed can roughly be described as: “A/aromatic-V-?-X” or “X-V-?-charged”, where the “?” stands for the P-site amino acid of the motif and where I couldn’t clearly define a common signature between the amino acids able to block the ribosome for this particular position. In other words, the V residue at the -1 position (E-site) is clearly essential for both ErmCL and ErmAL1 arrest, and then, as expected (Ramu

et al., 2011), the nature of amino acid at the -2 position defines the selectivity of the A site. Ala or aromatic residues (excepted W) at the -2 position renders the A site highly restrictive (ErmCL case), whereas other amino acid at the -2 position renders the A site selective for charged residues (ErmAL1 case). The nature of the P-site residue seems to influence the force of the arrest motif, but clearly does not seem to be a key element involved in the process; by looking at the ErmCL cryoEM structure furnished by the literature (Arenz et al., 2014a), the peptidyl-tRNA is shifted to the tunnel, and the rearrangement of A76 positioning from the P-site tRNA seems to be more likely the cause of the PTC inhibition rather than the nature of the C-terminus residue of the nascent peptide. To really assess the importance of the C-terminus residue, more double mutants involving the P-site position would be necessary here.

To complete this picture, I looked at the second stalling site of ErmAL1, where the P site of the ribosome is located on codon E9 of ErmAL1. **Figure 22** represents the score distribution calculated by Enrich2 corresponding to ErmAL1 stalling on codon 9, where the data used correspond to the reads of the second peak of the *ermAL* length distribution (**Figure 17**). I could observe a bimodal distribution of the scores, similarly to the first peak observed for inverse toeprints that corresponded to the ribosomes stalled on codon 8. The first population presented scores around 0 corresponding to the non-significant scores and a second one between -0.5 and -2 corresponding to depleted variants. No major population corresponding to highly enriched variants was observed. I set the upper score threshold for a detrimental mutation to -0.5 and plotted the corresponding variants as yellow squares in **Figure 23**.

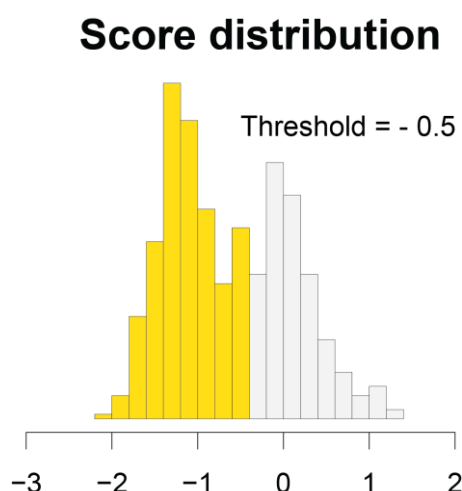


**Figure 22 : Histograms of score distribution furnished by Enrich2 corresponding to ErmAL1 stalling on codon 9**

A threshold of -0.5 separates the bimodal distribution of the scores, and scores lower than the threshold value represent significant depleted variants (yellow bars).

**Figure 23** represents the data corresponding to ribosomes stalled on the 9<sup>th</sup> codon in presence of erythromycin. In the simple mutant analysis (**Figure 23**, panel A) the pattern AVVE seems to be the most important one, where the two V cannot be mutated excepted for I. The P site can contain negatively charged or aromatic residues and L/P/N/Q. The A site does seem very selective, except for stop codon or aromatic residues (F/Y/H) which prevents stalling, and some enrichments observed for charged residues. In parallel, the 6/9 double mutant analysis of ErmAL1 stalling on codon 9 (**Figure 23**, panel B) displays a distinct overall pattern from those presented in **Figure 20** but seems to correspond to the results observed for the simple mutants. Indeed, position 9 corresponding to the P site, can contain negatively charged or aromatic residues and L/P/N. On the other hand, position 6 here does not seem to influence the stalling at position 9 (no vertical pattern observable). In any case, the second stalling site of ErmAL1 and the results of **Figure 23** are difficult to explain because they are influenced by the first stalling on codon 8 of ErmAL1. To better understand the relationships between the first and the second erythromycin-dependent stalling sites of ErmAL1, the ability of the ribosomes to bypass the 8<sup>th</sup> codon needs to be compared to the scores obtained by Enrich2 for the ribosomes stalled on codon 9.

### 3.3.2.3. Discussion

My inverse toeprinting data provided new insights into the mode of action of the ErmCL and ErmAL1 erythromycin-dependent arrest peptides, which actually display a similar functioning. Using two types of libraries, namely a first one containing a single-codon mutagenesis and a second one corresponding to a double mutagenesis of the codons in positions -2 and the A site respectively of the full-length ErmCL and ErmAL1 peptides, I could understand that the erythromycin-dependent stalling of ErmCL and the stalling of ErmAL1 on codon rely actually on the same mechanism, involving the P-site tRNA and the -2 residue. The V residue at the -1 position (E site) is clearly essential for both ErmCL and ErmAL1 arrest, and then, as expected from (Ramu et al., 2011), the nature of amino acid at the -2 position defines the properties of the A site. A or aromatic residues (excepted W) at the -2 position renders the A site highly restrictive (ErmCL case), whereas other amino acid at the -2 position renders the A site selective for charged residues (ErmAL1 case).

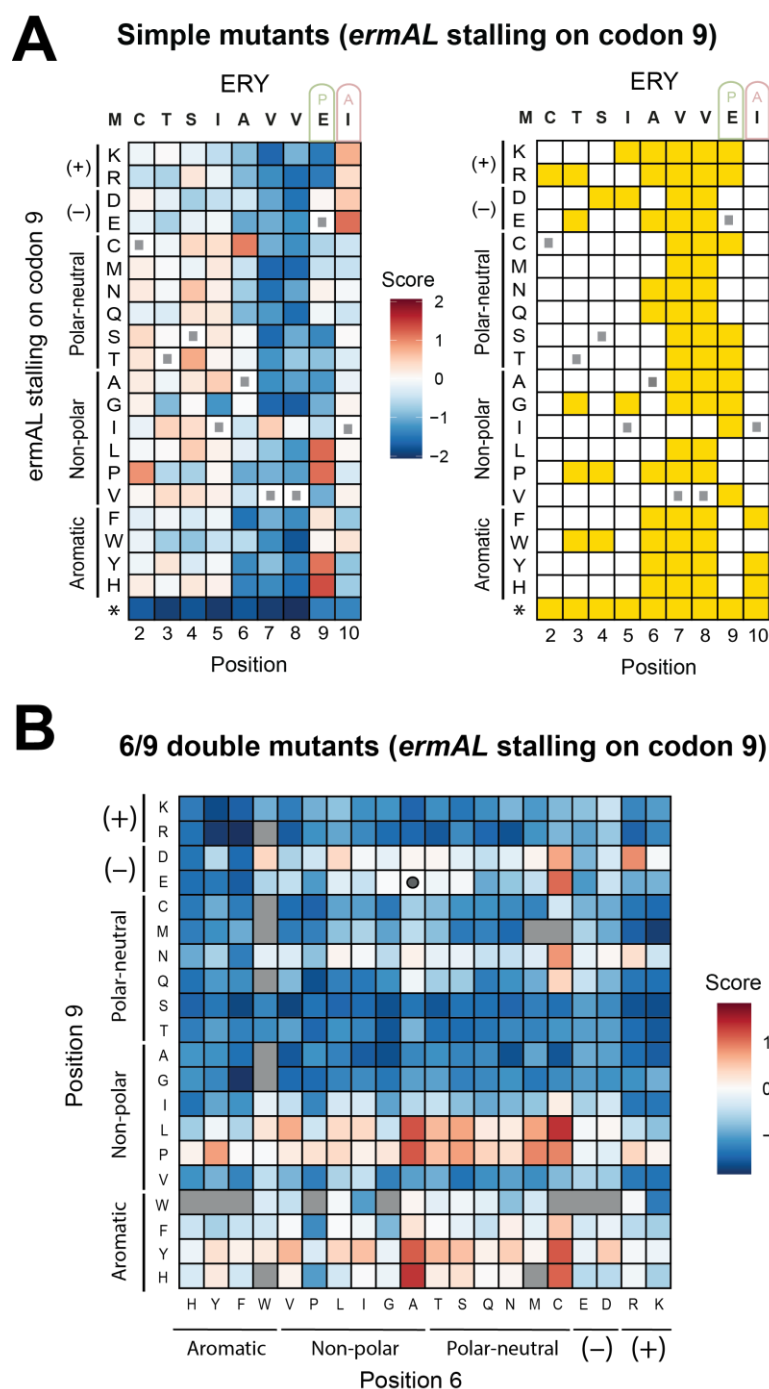


**Figure 23 : Sequence-function analysis of the ErmAL1 erythromycin-dependent arrest on codon 9**

A) Sequence-function map furnished by Enrich2 of the ErmAL1 single mutant peptides translated in the presence of erythromycin. Cell color indicates the score for a single amino acid change at a given position, where positive scores (red) indicate better than wild-type translational arrest and negative scores (blue) indicate worse than wild-type performance (left panels). Significant mutations that abolish the arrest (scores < 0.5) are shown in yellow. The ribosomal P (green) and A (pink) sites are indicated above the wild-type sequence. Squares marked with a grey square correspond to the wild-type amino acid. B) Sequence-function map furnished by Enrich2 of the 6/9 ErmAL1 double mutant peptides translated in the presence of erythromycin. Grey dots correspond to the wildtype variant, and grey squares to missing data.



The nature of the P-site residue seems to influence the force of the arrest motif, but clearly does not seem to be a key element involved in the process; by looking at the ErmCL cryoEM structure from the literature (Arenz et al., 2014a), the peptidyl-tRNA is shifted to the tunnel, and the rearrangement of A76 positioning from the P-site tRNA seems to be more likely the cause of the PTC inhibition rather than the nature of the C-terminus residue of the nascent peptide. To assess the importance of the C-terminus residue, more double mutants involving the P-site position would be necessary here. Finally, from the available structure of the ErmCL peptide (Arenz et al., 2014a), F7 and V8, which are crucial for the arrest in my inverse toeprinting data, are in close contact to U2506 and stabilize a shifted conformation, normally adopted in the induced-state of the PTC, once the aminoacyl tRNA is accommodated into the A site. In this induced-state, U2506 normally interacts with U2585, which also rotates by 19Å upon A-tRNA accommodation. Here, U2585 adopts a dramatically different conformation, such that it is rotated by 80Å compared to the unaccommodated state, and is flipped into a pocket formed by U2584, G2583 and G260, and thus cannot interact with the aminoacyl tRNA within the PTC to stabilize it to allow its accommodation. It is fair to envisage that the interactions between F7 and V8 with U2506 are the key elements at the origin of the different positioning of U2585, which therefore renders the A site restrictive.

To obtain a clear model concerning the mode of action of these arrest peptides, and notably the one of ErmAL1, our collaborators from the laboratory of Prof. Daniel Wilson in Hamburg obtained several cryoEM complexes of ribosomes translating the ErmAL1 or a mutated version of the ErmCL peptides in presence of erythromycin to propose a model explaining how the drug and the peptide interplay with the tunnel and the PTC of the ribosome to modify the properties of the A-site. Once these results are in hand, we will combine our data to compare the two complexes and visualize how the -2 position of the peptide establishes a specific set of interactions in the tunnel to modify the selectivity of the A site in the PTC. In addition, if the position and the role of erythromycin in the tunnel is the same for ErmCL and ErmAL1, it would be interesting to think about the case of ketolides, and to propose a hypothesis concerning the selectivity of this category of antibiotics for the peptide sequence in light of these new structures.

In light of these data and the ones from the literature, one of the remaining outstanding questions concerns the role of ErmAL1; why does the *ermA* gene conserve two uORFs encoding for two leader peptides presenting two different A-site selectivities in presence of erythromycin? As a

reminder, *ermAL1* encodes a 15 amino acid long peptide containing the selective “IAVV” arrest motif and *ermAL2* encodes for a 19 amino acid long peptide containing the restrictive ErmCL-like “IFVI” motif (**Figure 24**) (Murphy, 1985b). Stalling on the ErmAL2 peptide leads to an mRNA conformational change freeing the RBS of *ermA* and leading to its expression (Sandler and Weisblum, 1988); this mode of induction is supported by the fact that the deletion of the upstream *ermAL2* leads to constitutive expression of *ermA* (Murphy, 1985b; Sandler and Weisblum, 1988). The role of *ermAL1* is therefore more difficult to envision, and several hypotheses could explain its conservation.

First, it has been proposed that the ribosomal stalling on *ermAL1* may control the stability of the polycistronic mRNA; the mRNA half-life is strongly decreased when *ermAL1* is deleted from the cassette, whereas the deletion of *ermAL2* does not have any effect (Sandler and Weisblum, 1988). Moreover, this effect on the mRNA stability is related to the translation of the ErmAL1 peptide, as the induction of frameshifting mutations completely abolish the ability of *ermAL1* to stabilize the mRNA (Sandler and Weisblum, 1988). The same effect on the mRNA stability was observed by the deletion of the *ermCL* sequence (Gryczan et al., 1980; Horinouchi and Weisblum, 1980).

As both *ermCL* and *ermAL1* are in the proximity of the 5' end of the transcript (less than 10 nucleotides), it has been proposed that this proximity to the 5' end would be responsible of the mRNA stabilization, by physically blocking the binding of nucleases because of the presence of a stalled ribosome (Sandler and Weisblum, 1988). Second, the presence of two regulatory ORFs may also affect the specificity of *ermA* induction: while *ermAL2* is involved only in macrolide-controlled induction, translation of *ermAL1* appears to respond also to lincosamides (Clarebout et al., 2001; Min et al., 2008). Moreover, deletion of *ermAL2* but preservation of *ermAL1* allows the preservation of the macrolide-inducible mechanism of *ermA*. Taken together, the weaker A-site specificity of ErmAL1 (Ramu et al., 2011) combined with the presence of a second stalling site observed in my data might be necessary to efficiently stall the macrolide-bound ribosome to strongly stabilize the mRNA, while ErmAL2 inhibits the accommodation of any incoming amino acid to ensure the proper expression of *ermA*.



### 3.4. Conclusions and discussion of part III

Despite the several differences observed in the previous sections between the different Erm patterns and their modes of action, the presence of a common feature corresponding to the presence of a specific amino acid arrest motif deciphers the ability of the PTC to incorporate or not certain amino acids in the A-site of the drug-bound ribosome. This common mechanism is used by bacteria to regulate the expression of some of their resistance genes, where the drug acts as an inducer and the ribosome as the mediator of the induction and also as the producer of the resistant protein. Using inverse toeprinting, I obtained new insights concerning the mode of action of three different Erm genes, which represent the three main categories of arrest motifs (“+X+” of ErmDL, the “IFVI” of ErmCL/ErmAL2 and the “AVVE” of ErmAL1). By systematically altering the sequence of the peptide, I demonstrated the importance of key residues, which interact with the nucleobases of the tunnel or of the PTC to regulate the ability of the ribosome to form peptide bonds. In the presence of cladinose-containing macrolides such as erythromycin, the N-terminal part of the ErmDL peptide is able to make several contacts with the tunnel and with the cladinose moiety of erythromycin, which forces the peptide to adopt restrictive conformations in the exit tunnel and prevents at a certain point the accommodation of a new amino acid by the PTC. The high chemical diversity in terms of peptide nature (hydrophobicity, length, charge etc.) can illustrate why macrolide antibiotics are less stringent and block the translation of more proteins than ketolides. In the case of ketolides, the path adopted by the ErmDL peptide is very different that the one observed for macrolide-dependent stallers ErmBL or ErmCL, where the displacement of the peptide by erythromycin promotes movement of the key tunnel bases (U2585, U2586, A2062 or A2602) to impair the activity of the PTC (Arenz et al., 2014a, 2016). Here, rather than extending directly into the tunnel, ErmDL is compacted around the desosamine sugar of telithromycin such that the N-terminal residues can extend into the lumen of the tunnel. On the other side, the C-terminal residues point towards the A-site region where the first Arg of the “+X+” motif of ErmDL extends directly into the PTC, where it sterically and electrostatically clashes with the second arginine side chain of the aminoacyl-tRNA accommodated in the A-site; therefore, in the case of ketolides, the nature of the nascent peptide can inhibit on its own the functioning of the PTC. In presence of macrolide such as erythromycin, ErmDL stabilizes similarly to ErmBL the uninduced state of U2585 within the PTC to inhibit A-site tRNA accommodation. Thus, the nature of the motif in the leader ORF-encoded peptide defines the spectrum of macrolides that can act as inducers of resistance. The recent development and use of certain drugs such as

ketolides raise the point of the apparition of their corresponding arrest motifs. It is conceivable that the proteins containing these motifs were already optimized and adapted to changing environment by their capacity to tune their translation by sensing small molecules, even before their selection induced by the high clinical use of antibiotics. These arrest motifs are maybe already difficult to translate by the ribosome and highly sensitive to small metabolites, allowing their rapid selection and evolution in a competitive milieu.

The main consequence of Erm stalling is the change of conformation of the polycistronic mRNA, leading to the liberation of the RBS of the resistance gene. The *in vivo* kinetics parameters are probably essential in this case to ensure the proper induction by the drug. Moreover, the stalling time of the ribosome on these leader sequences might also be important for the recruitment of the rescuing cellular factors. Indeed, and especially in the case of two uORFs (ErmAL1/ErmAL2 example), the ribosome needs to be stalled on the first leader peptide, to induce the expression of the second leader sequence, to finally free the RBS of the expression gene and lead to its expression; this long process might involve a certain time laps, where avoiding the premature abortion of the stalling process is critical for survival of the bacteria. Therefore, developing strategies to study the kinetic parameters of the *erm* induction inside living cells would be a wonderful tool to study the ribosomal stalling process and help to elucidate and to understand why some of these genes need two uORFs to regulate their expression. Single-molecule kinetics are now possible in living cells, as reviewed by (Elf and Barkefors, 2019). Using *E. coli* cells and various concentrations of macrolide antibiotics, it is fair to imagine a protocol based on the *ermA* operon (**Figure 24**), where the N-terminus part of ErmA would be fused to a reporter protein. By mutating, reordering, or removing the leader sequences or ErmA in presence of various antibiotic conditions, it could be interesting to analyze how *ermA* expression would be or not impacted. Such kinetics information would probably help understanding the need of two uORFs in *ermA* induction, and clarify their role in the expression of the resistance gene.

As macrolides were known to inhibit the elongation step of bacterial translation by promoting the drop-off of peptidyl-tRNA in the P site (Menninger, 1985; Otaka and Kaji, 1975; Tenson et al., 2003), it is quite fascinating to observe the compromise made through the evolution between the requirement to have a peptide of sufficient length for the formation of the stalled complex and the difficulty of polymerizing long amino acid chains by the erythromycin-bound ribosome. It is possible to imagine that the N-terminal part of the nascent part might present also features

which could be more or less conducive to this peptidyl-tRNA drop off. Combining the *in vitro* inverse toeprinting data presented here with biochemical experiments furnishing information about the ability of a given mutant to promote peptidyl drop-off and/or adapting the procedure for an *in vivo* approach would provide strong insights into the molecular mechanism of drug-induced arrest by highlighting the sensitivity of the Erm's system and its ability to respond to small variations of the growing media.

Finally, macrolide and ketolide antibiotics are currently used in human medicine to treat bacterial infections. Thus, it seems fair to be concerned by the ability of these drugs to bind to and inhibit eukaryotic targets. As the bacterial and the mitochondrial ribosomes share a lot of similarities, it would be of great clinical interest to study the effect of macrolides on mitochondrial translation. In addition, preventing translation of individual proteins by using the context-specific action of these drugs could be beneficial for the treatment of human disorders such as cancers, or genetic diseases such as the Creutzfeldt-Jakob disease, where the single mutation leading to the overproduction and the misfolding of a protein, the prion, leads to lethal encephalopathies (<https://www.cdc.gov/prions/cjd/index.html>). A recent paper (Svetlov et al., 2021) demonstrated the ability of macrolide to inhibit a singly mutated yeast ribosome, by binding to the exit tunnel of the eukaryotic ribosome and preferentially stall translation at distinct arrest motifs, and notably the “+X+” arrest motif (Svetlov et al., 2021). The conservation of the context-specificity of macrolide antibiotics observed in bacteria in the eukaryotic ribosome, albeit a mutated one, could pave the way to their use in human medicine. Following this idea, several ribosome profiling data performed on eukaryotic cells by the laboratory of Jamie Cate (Li et al., 2019; Lintner et al., 2017; Travin et al., 2019) demonstrated the tunability of the eukaryotic, and notably the human ribosome, to allow small ligands to specifically inhibit translation of key proteins, thus opening new areas of drug development targeting disease-mediating proteins.

Hypothetically, it would be of great interest in the fight against bacterial pathogens or parasites to engineer new macrolides that are able to completely shut down translation of the whole proteome by abolishing their context-specificity and thereby limiting use of arrest-peptide dependent inducible resistance genes, such as the *erm* systems; at the opposite, for genetic human disorders, tuning molecules able to specifically inhibit the translation of a given protein would provide therapeutic solutions for a high number of diseases.

## Part IV: Revealing the sequence dependence of ribosomal antibiotics

## History and Contributions

The original idea of testing several antibiotics by inverse toeprinting using a random mRNA library came from my supervisor Dr. Axel Innis, but the choice of the antibiotics tested was mine. I firstly decided to test six antibiotics targeting the 30S subunit (capreomycin, neomycin, kanamycin, spectinomycin, streptomycin and tetracycline) using a random library of 15 NNS codons (N stands for aNy nucleotide and S for the Strong G/C ones) that I designed and built. I then performed the inverse toeprinting work and optimized the protocol at the same time with the help of Mélanie Gillard. I prepared and sent the samples for NGS. The reads were assembled and processed by Dr. Axel Innis. I then analyzed the data using a series of Python scripts written by Dr. Axel Innis. The analysis process is detailed in [section 4.2.1](#). From these results, I could observe that capreomycin exhibited preferences for the AAG (K) codon to inhibit the ribosome, but the choice of the NNS library limited the interpretation as the second Lys codon is AAA, and therefore couldn't be observed in these inverse toeprinting dataset. To obtain a complete vision of capreomycin preferences, I decided to go for another inverse toeprinting experiments, using the same *in vitro* conditions but using a library of 15 NNN codons instead, to have access to the 64 codons. From the literature, capreomycin is often compared to viomycin, another tuberactinomycin antibiotic because of their similar structure and binding sites on the ribosome. I therefore decided to also test viomycin in order to see if the preferences exerted by capreomycin for the lysine codon would be related to all tuberactinomycins, or if it would be a particularity of capreomycin. In parallel, from the collaborative exchanges on the work about the ErmDL peptide ([see section 3.3.1](#)), Prof. Daniel Wilson (Hamburg University, Germany) put us in touch with Prof. George Dinos (Patras University, Greece) who kindly provided us with several compounds (pactamycin, gougerotin, sparsomycin and few sparsomycin derivatives), but also with Dr. Ilya Osterman (Skolkovo Institute of Science and Technology, Russia) who provided us with tetracenomycin X. All of these compounds were suspected to be context-dependent by our collaborators. Thus, I designed and built an mRNA library of 15 NNN codons, did the inverse toeprinting experiment for all of these antibiotics, sent the samples to NGS, and analyzed the data using the same approach. From this dataset, I could observe that capreomycin exerted preferences for every lysine codons, but this trend was much less pronounced for viomycin. For the other antibiotics tested, I could observe the sequence-dependency of tetracenomycin X for the “QK” amino acid motif, and similarly, the sequence preferences of pactamycin for certain nucleotides located in the E- and P-sites codons of the mRNA. For the manuscripts concerning capreomycin and tetracenomycin X, Dr. Thibaud Renault took the inverse toeprinting dataset to perform a deeper analysis and implemented a statistical framework in the process, as described in the Materials and Methods sections of the two manuscripts. To complete the inverse toeprinting results, I performed various biochemical experiments with the help of a master student Anaïs Labécot that I supervised (luciferase titration, toeprinting) and used cryoEM to obtain structural insights. For the preparation of the complex visualized by cryoEM, I decided to use the PureSystem (NEB) without purification step and optimized the ribosome dilutions and buffer conditions. For all the cryoEM results presented in this part, Dr. Thomas Perry prepared the grids, froze the samples, and performed the data collection on the Talos Arctica microscope located in our institute (IECB, University of Bordeaux, France). The processing of the images was also done by Dr. Thomas Perry, except



for the capreomycin/viomycin complexes where we shared the work. I then modeled all of the structures presented in this thesis. Finally, for the *in vivo* approach using the blue ring assay, our collaborator Dr. Nora Vazquez-Laslop kindly provided us the  $\Delta acrA/B$  JM109 *E. coli* strain and I designed the cloning protocol for the mutation of the pERMZ $\alpha$  plasmid. The blue ring assays were then done by Dr. Thomas Perry. I finally wrote the two manuscripts of this part, which were then reviewed by Dr. Axel Innis, Dr. Thibaud Renault and Dr. Thomas Perry with whom I shared the preparation and design of the figures.

## 4.1. INTRODUCTION

The increase in multi-drug resistant pathogenic bacteria is making our current arsenal of clinically used antibiotics obsolete, highlighting the urgent need for new molecules with distinct target binding sites to avoid cross-resistance. The majority of currently used antibiotics have been found either serendipitously (such as penicillin) by testing metabolites produced by soil organisms (such as erythromycin) for their ability to inhibit bacterial growth, or by screening libraries of synthetic drugs (such as linezolid); therefore, their optimization has generally not been driven by knowledge of their mechanism of action (Seiple et al., 2016). The lack of recent discoveries (see section 1.1) proves that this method cannot be employed on a long-term basis and acquiring knowledge about how antibiotics work should become a guiding principle for drug discovery. Therefore, innovative approaches are now needed to revive the discovery process. The use of new tools based on the study of functional and biologically relevant complexes would provide key information concerning the precise mode of action of old molecules previously rejected because of their cytotoxic effects or limited antimicrobial activities to bring fresh solutions to the multidrug resistance threat.

As described in the general introduction, the majority of our current arsenal of antibiotics target the bacterial ribosome and most of them were discovered decades ago (see section 1.1). As the context of translation is different at each codon, these antibiotics necessarily encounter ribosomes containing various ribosomal substrates. The nature of these substrates affects the efficiency of translation; tRNAs can bind with distinct kinetics (Dale and Uhlenbeck, 2005; Fahlman et al., 2004), where their nature can influence the level of miscoding by impairing the dynamics of the binding, dissociation and translocation rates (Cochella and Green, 2005; Fei et al., 2011; Konevega et al., 2007; Ranjan and Rodnina, 2017). Within the PTC, the nature of the donor and acceptor amino acids influence the efficiency of peptide bond formation (Johansson et al., 2011; Wohlgemuth et al., 2008). It was therefore fair to imagine the action of macrolide or chloramphenicol antibiotics being dependent of the nature of the nascent peptide by virtue of their proximity in the ribosomal exit tunnel (see sections 1.2.3.2.). From the several examples of sequence specificity of action I mentioned since the beginning of this manuscript, I hypothesized that other families of antibiotics targeting the bacterial ribosome would display a context-specificity of action, particularly those affecting the decoding center, the PTC or the translocation step. In this part of my work, I wanted to assess the sequence dependence of different ribosomal antibiotics targeting steps which might be affected by the nature of the

elongation complex. In order to do so, I used the inverse toeprinting technique in combination with random mRNA libraries. The aim was to characterize the stalling landscape of free and drug-bound *E. coli* ribosomes to obtain a comprehensive list of arrest motifs for different types of antibiotics. In addition, I characterized antibiotic-dependent arrest motifs identified by inverse toeprinting biochemically, and in some cases validated them *in vivo*. From these results, I obtained several cryo-EM structures of the most interesting functional complexes, thus gaining new insights into the mode of action of these antibiotics. The overall methodological approach was the same for all antibiotics and is described in [section 4.4](#). To gain clarity, the results of this part are divided into subsections; the first one gives an overview of the antibiotics tested and of the analysis process, while the three last ones describe individually the results obtained for three categories of antibiotics, namely the tuberactinomycins capreomycin and viomycin, but also tetracenomycin X and pactamycin. The knowledge obtained from this work will enable a greater understanding of how bacterial translation can be inhibited specifically to lead to the development of novel antibiotics.

## 4.2. RESULTS

### 4.2.1. Ribosomal stalling landscapes altered by antibiotics

Our primary hypothesis was that antibiotics interacting with the ribosomal substrates (the mRNA, tRNAs, nascent peptide) are probably affected somehow by the nature of these substrates and might display a context-specific mode of inhibition. I decided to target antibiotics inhibiting the elongation cycle, as variable substrates interplay to allow the translation of a nascent protein (**Figure 25**). The tested drugs are listed in **Table 3**.

In summary, I tested 16 different antibiotics through diverse inverse toeprinting experiments and represent various types of compounds (aminoglycosides and related compounds, nucleotide analogues, cyclic peptides, aromatic polyketides), able to either target the accommodation of the aminoacyl tRNA within the A-site, or to inhibit the formation of the peptide bond within the PTC or still to modify the translocation rate of the tRNA-mRNA complex.

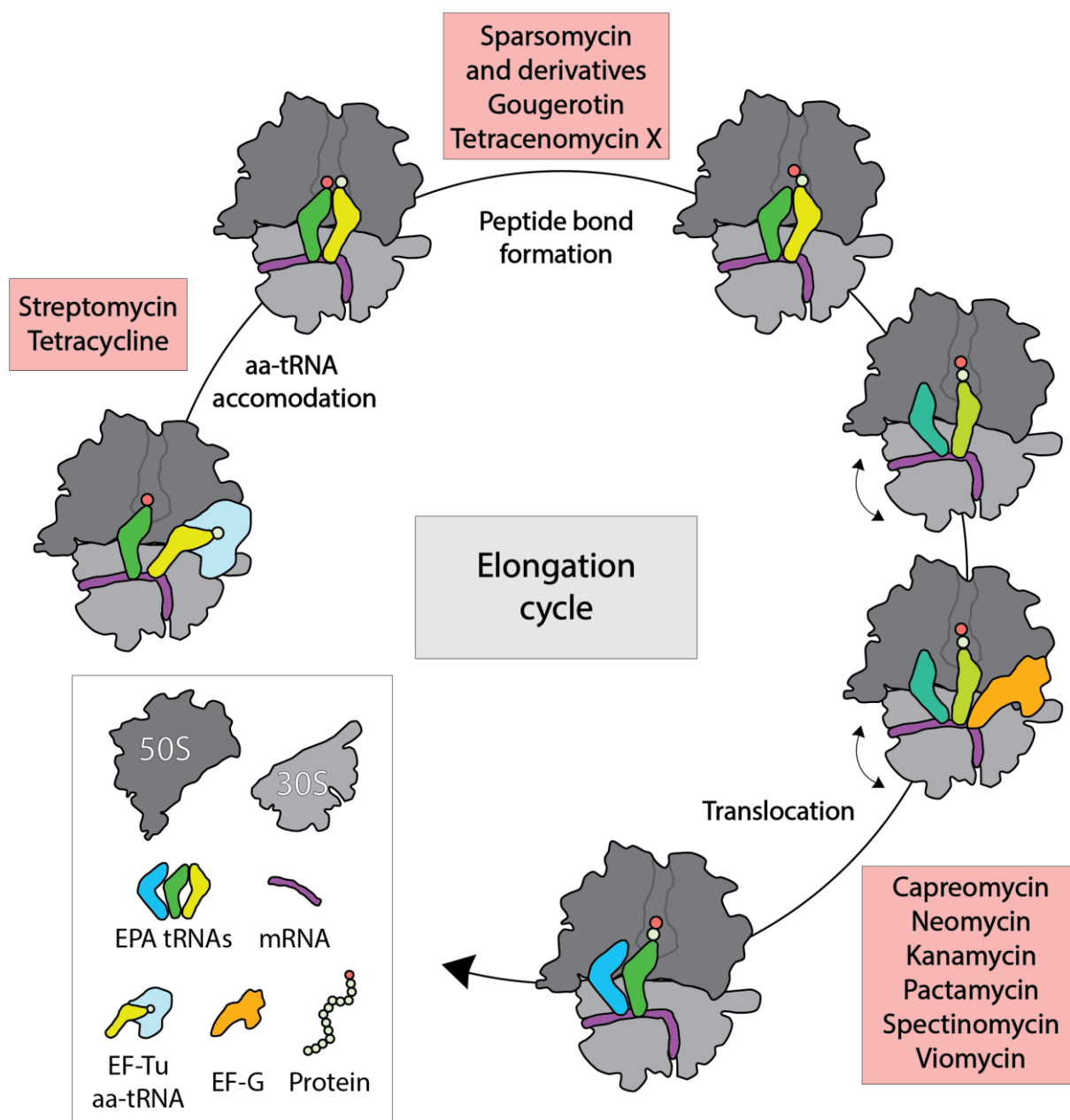


**Figure 25 : Antibiotics tested by inverse toeprinting**

The antibiotics tested target peptide bond formation, tRNAs translocation, or tRNA delivery and accommodation within the A-site of the ribosome during the elongation cycle

To assess how the mode of action of antibiotics targeting the decoding center or translocation process are affected by the nature of the translating complex, I performed two main inverse toeprinting experiments using two DNA libraries encoding peptides composed of 15 random “NNS” (aNy aNy Strong (G/C)) or “NNN” codons, depending of the experiment, fused to a fixed 3’ sequence. For simplification purposes, these libraries are called “NNS15” or “NNN15” for the rest of the manuscript. The “NNS15” library is composed of 32 codons and allows

avoiding the accumulation of ribosomes stalled on the UGA and UAA stop codons, while the use of the “NNN15” library gives access to the 64 codons, which is convenient in the case of antibiotics that interact with the mRNA-tRNAs complexes to determine if the codon or the nucleotides alone are the key elements involved in the drug-induced stalling of the ribosome. Both of the libraries encode for  $\sim 10^{12}$  random peptides, thus furnishing a large variety of sequence motifs that can be tested through inverse toeprinting (**Figure 26**).

Antibiotics	Compound family	Ribosomal binding site	Target
Kanamycin	Six-membered ring aminocyclitol 2-DOS Aminoglycoside	30S - Body domain Decoding center	tRNAs translocation – Induces misreading
Neomycin	Six-membered ring aminocyclitol 2-DOS Aminoglycoside	30S - Body domain Decoding center PDB: 4V52	tRNAs translocation – Induces misreading
Spectinomycin	Six-membered ring aminocyclitol Aminoglycoside-related	30S - Head domain Decoding center PDB: 4V56	tRNAs translocation by destabilizing the aminoacyl tRNA within the A-site
Streptomycin	Six-membered ring aminocyclitol Aminoglycoside-related	30S - Body domain Decoding center PDB: 1FJG	tRNAs translocation by destabilizing the aminoacyl tRNA within the A-site – Induces misreading
Pactamycin	Five-membered ring aminocyclitol	30S - Body domain mRNA path - E-site PDB: 4W2G/H	Blocks the binding of the initiator tRNA - tRNAs translocation – perturbs the mRNA path
Gougerotin	Peptidyl-nucleotide analogue	50S - PTC	Perturbs the positioning of the 3' end of the P-site tRNA
Sparsomycin (And five derivatives)	Nucleotide analogues	50S - PTC PDB : 1M90	Overlaps with the A-site aminoacyl-tRNA – promotes tRNAs translocation
Capreomycin	Tuberactinomycin Cyclic peptide Aminoglycoside-related	30S - Body domain Decoding center PDB: 4V7M	Inhibits tRNAs translocation by stabilizing the aminoacyl tRNA within the A-site
Viomycin	Tuberactinomycin Cyclic peptide Aminoglycoside-related	30S - Body domain Decoding center PDB: 4V7L	Inhibits tRNAs translocation by stabilizing the aminoacyl tRNA within the A-site
Tetracycline	Aromatic polyketide Tetracyclines	30S - Body domain Decoding center PDB: 4V9A	Blocks the accommodation of the aminoacylated-tRNA within the A-site
Tetracenomycin X	Aromatic polyketide Tetracenomycins	50S - Exit tunnel PDB: 6Y69	Inhibits the nascent peptide chain elongation/progression

**Table 3 : Antibiotics tested by inverse toeprinting, their binding site and the molecular mechanism they target**

The drugs are colored according to their chemical nature.

The schematic overview of the inverse toeprinting protocol is presented **Figure 10** and illustrates the most important steps of the protocol. The libraries are *in vitro* transcribed and translated in the presence of 100  $\mu$ M of the antibiotic of interest. The reference is the library translated without antibiotics. The antibiotics and their modes of action are summarized in **Table 3**. Biological triplicates were obtained for each condition and samples were sent for NGS analysis using paired-end Illumina sequencing.

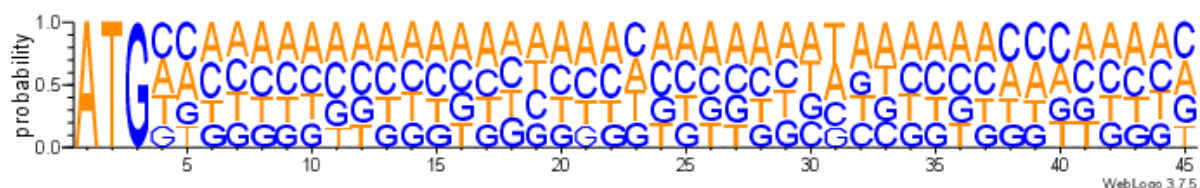


**Figure 26 : DNA template used for inverse toeprinting**

WebLogo obtained for 109572 of the 941716 sequenced reads corresponding to the 15 random codons of the NNN15 library translated in absence of antibiotics (one biological replicate only).

Data analysis was carried out using a series of custom scripts written in-house in Python, which relied on the use of the Biopython package (Cock et al., 2009), as described in (Seip et al., 2018). Briefly, the reads were first processed through several steps. First, reads pairs were assembled using PEAR (Zhang et al., 2014) and the flanking regions located upstream of the start codon and downstream of the RNaseR cleavage site are removed. Second, a quality control is applied and removes the reads that do not match all the customized quality criteria, namely the mandatory presence of an ATG codon as initiation codon, a low amount of repetitive “A” bases and a minimal Phred Q-score of 30. For information, the Phred Q-scores (Q) are defined as following, where P represents the base calling error probabilities.

$$Q = -10 \log_{10} P$$

A Q-score of 30 (Q30) represents a base call accuracy of 99.9%, meaning that the probability of an incorrect base call is 1 in 1000 times. By comparison, Sanger sequencing displays an accuracy of ~Q20. Lower Q scores increase false-positive variant calls resulting in inaccurate conclusions. Finally, the processed reads can be split into codons and then translated in order to analyze the influence of the amino acid sequences on the drug-induced stalled of the ribosome and identify new drug-dependent arrest motifs. After processing of the reads, the analysis of the sequencing revealed a tri-nucleotide periodicity for fragments where RNase R cleavage had occurred 21–48 nucleotides downstream of the start codon (panel B, **Figure 27**). Longer fragments did not follow this size periodicity and were excluded from the dataset.

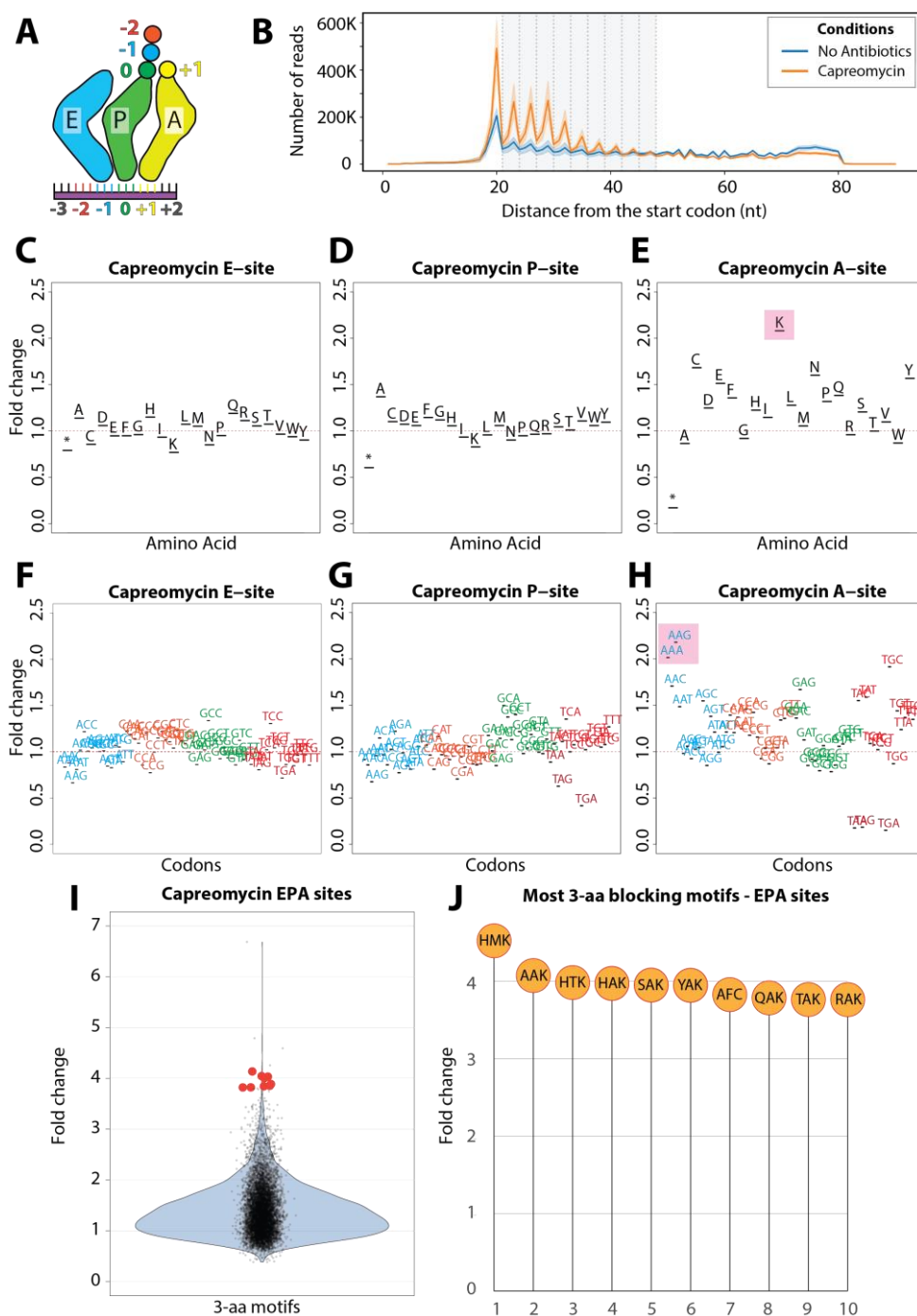


**Figure 27 : Examples of inverse toeprinting data using the results of the NNN15 library translated in presence of capreomycin**

A. Schematic illustration of the nomenclature applied to the different ribosome sites. B. Number of reads obtained in the NGS in function of the distance from the start codon for untreated and capreomycin-treated samples, where the grey area highlights the reads that were selected for the analysis, as this corresponds to the region in which the codons are well defined (grey dotted lines). The error bands show the 95% confidence interval of the average of the three replicates. C/D/E. Fold changes obtained for the amino acid enrichment scores at the three E-, P- and A-sites positions individually. F/G/H. Fold changes obtained for the codon's enrichment scores. I/J. Fold changes obtained for the 3-aa long motifs located within the E/P/A sites of the stalled ribosomes, where panel I represents the overall scores repartition for all the 3-aa motifs, while the panel J focuses on the top 10 capreomycin-dependent arrest motifs.

After preprocessing of the reads, I used more or less the same approach to identify new drug-dependent arrest motifs for all of the antibiotics tested. Several plots illustrating the results of this analysis are shown in panels C to J from **Figure 27** and correspond to the case of the “NNN15” library translated in presence of the tuberactinomycin capreomycin. Capreomycin inhibits tRNA translocation during the elongation phase of bacterial translation (Brilot et al., 2013; Ermolenko et al., 2007b; Holm et al., 2016; Liou and Tanaka, 1976; Modolffil and Vázquez, 1977; Peske et al., 2004; Stanley et al., 2010; Zhang et al., 2020) and binds to the decoding center on the 30S subunit, where 16S rRNA residues A1492 and A1493 adopt a flipped-out conformation (Brilot et al., 2013; Stanley et al., 2010; Zhang et al., 2020) identical to the one observed during the decoding of the aminoacyl-tRNA in the A-site (Ogle et al., 2003). The affinity of capreomycin to the ribosome greatly increases upon binding of an A-site tRNA (Holm et al., 2016; Peske et al., 2004), where the drug stabilizes the rotated conformation of the ribosome with hybrid P/E and A/P tRNAs conformations (Cornish et al., 2008; Ermolenko et al., 2007b; Ly et al., 2010; Pan et al., 2007; Peske et al., 2004; Shoji et al., 2006; Wang et al., 2012).

The first step of the inverse toeprinting analysis is the calculation of the fold change in the frequency of a given sequence motif, that can be one, two or three (or even more) nucleotide(s), codon(s) or amino acid(s), between the condition where the library was translated in the presence of antibiotic and the one translated without. To make use of the three replicates of inverse toeprinting, I calculated the average log-fold change obtained for each motif for each set of translation conditions. As a convention, ribosomal sites are numerated by defining the P site as position 0. From the P site to the 5' side of the mRNA, corresponding to the N-terminus of the nascent peptide, the numbering decreases (the E-site codon/tRNA and the penultimate amino acid of the nascent peptide are defined as position -1). On the other side of the P site, that corresponds to the amino acid that has not been incorporated, the sites are labeled with increasing numbering (the A-site codon/tRNA and the corresponding incoming amino acid are defined as position +1) (see panel A, **Figure 27**).

At first, it is simpler to look at individual ribosome positions, and I always start with the -1/0/+1 positions (E/P/A sites) of the ribosome, as they correspond to the tRNAs/mRNA complexes interacting with the stalled ribosome, but also represent the C-terminal part of the nascent peptide being translated within the PTC. It is nevertheless important to point out that the other sites, namely the -2, -3, etc. positions, also need to be examined, notably for antibiotics able to



bind to the PTC or within the exit tunnel as they often directly interact with the nascent peptide, the incoming amino acid and the tRNAs during translation. For the three E/P/A ribosome positions, I then first compare the fold changes obtained for amino acids and for codons. In the case of capreomycin, it was clear that no amino acid presented high fold changes for the E and P sites of the ribosome (panels C/D, **Figure 27**). However, in the A site, several amino acids displayed fold changes greater than 1.5, most notably K which had a fold change greater than 2, meaning that there were two times more ribosomes stalled with K in the A site in the capreomycin condition than in the negative control without antibiotic (panel E, **Figure 27**). Following this observation, I decided to look at the codon scores for each individual tRNA binding site to determine if both of the K codons, namely AAA and AAG, would stall the ribosome with the same efficiency in presence of the drug (panels F/G/H, **Figure 27**). Consistent with the results obtained for the amino acids fold changes, the E and P sites did not display strong codons preferences to stall the ribosome (panels F/G, **Figure 27**). However, several codons were highly enriched in the A site where the two most blocking codons were the ones coding for K (panel H, **Figure 27**). From the inverse toeprinting data, I could not observe large differences between the two mRNA lysine codons (panel H, **Figure 27**), and the results of the analysis at the nucleotide level were consistent with the results obtained for codons, thus probably indicating the low role of the mRNA substrate in the stalling process. Other amino acids/codons displayed high fold changes in the A-site and notably asparagine (AAT/AAC), cysteine (TGC), or tyrosine (TAT/TAC) (panels E/H, **Figure 27**). On the other hand, alanine (GCN), glycine (GGN) or tryptophan (TGG) displayed fold changes of approximately 1, meaning that they were not able to induce stalling of the ribosome in presence of capreomycin.

I then decided to look at motifs combining two or three codons and/or amino acids. The fold changes obtained for the three amino-acid long motifs located in the E, P and A sites of the ribosome confirmed the observations made for the individual positions, as the best measured (at least 150 reads combined for all three replicates) and most enriched motifs (fold changes higher than 2) contained a lysine residue in the A site (panels I/J, **Figure 27**). Consistent with the analysis of the data for individual ribosome positions, these XXK motifs displaying high-fold changes were followed by motifs containing N, C and Y within the A site (fold changes of +/- 1.5), while the less blocking contained A or G residues (fold changes of +/- 1).

At this step of the analysis, two substrates of the ribosome were candidates to explain the A-site specificities of capreomycin's mode of action (1) the amino acid residue within the PTC

and (2) the tRNA itself. To discriminate between the two candidates, I first considered the capreomycin binding site within the decoding center of the ribosome. The incoming amino acid brought by the A-site tRNA is located within the PTC of the 50S subunit of the ribosome, thus far from the binding site of capreomycin within the decoding center of the 30S subunit (Brilot et al., 2013; Stanley et al., 2010; Zhang et al., 2020). If the amino acid was responsible for the A-site specificities, that would involve that the A-site amino acid would have a long-distance allosteric effect on the drug mode of action. Second, the lack of evident common chemical features not only between the amino acids displaying high fold changes (e.g. K/N that have a long charged or polar side chain, C that is a small and polar amino acid and Y that has a large aromatic side chain), but also with amino acids displaying fold changes close to 1 (e.g. A/G that have small non-polar side chains or W that is the largest aromatic amino acid), led me to conclude that the amino acid located in the A-site of the PTC was probably not the substrate responsible for the capreomycin specificities, even if this possibility couldn't be excluded. Therefore, I hypothesized that the nature of the tRNA located in the A-site of the ribosome would influence the arrest induced by capreomycin as the drug was particularly able to inhibit the ribosome in presence of the K-tRNA, but also N/C/Y-tRNAs, while it was particularly not the case in presence of A/G/W tRNAs.

The approach used for the study of capreomycin was employed for all the antibiotics tested, with modifications depending of the drug's mode of action and binding site, and allowed me to identify which antibiotics were worth pursuing further. From the antibiotics presented in **Figure 25** and **Table 3**, most of the drugs tested did not clearly display any context-dependence by performing similar analyses. However, four of them, namely the tuberactinomycins capreomycin and viomycin (see section 0), the aromatic polyketide tetracenomycin X (see section 4.2.3), and the five-membered ring aminocyclitol antibiotic pactamycin (see section 4.2.4), displayed various sequence dependencies in my inverse toeprinting data. As a consequence, more detailed analyses of the inverse toeprinting data were performed subsequently for these antibiotics and are described in the following sections.

#### 4.2.2. The tuberactinomycins capreomycin and viomycin

Capreomycin and viomycin belong to the tuberactinomycin family, a group of non-ribosomal cyclic peptide antibiotics containing several non-canonical amino acids, which are produced by non-ribosomal peptide synthetases (NRPSs) (Thomas et al., 2003). The various members of the tuberactinomycin family differ in their residue side chain modifications, including aminoacylation with  $\beta$ -lysine (Yamada et al., 1981). Additionally, capreomycin is a mixture of four isoforms where isoforms IA and IB containing a  $\beta$ -lysine moiety represent more than 90% of the mixture (Liu et al., 2018), while viomycin is a single molecule containing also a  $\beta$ -lysine moiety at a different position. Tuberactinomycins are mostly used as second-line treatments against *Mycobacterium tuberculosis* (Jain and Dixit, 2008; Johansen et al., 2006) due to their toxicity. Viomycin is produced by various *Streptomyces* species, and was first reported in 1951 as the first member of the tuberactinomycins (Ma et al., 2007). It was used to treat tuberculosis until it was replaced by the less toxic, but structurally related compound, capreomycin, isolated in 1961 from *Streptomyces capreolus*. The tuberactinomycins are characterized as translation inhibitors for their ability to inhibit the bacterial ribosome (Polikanov et al., 2018; Wilson, 2014).

The primary mechanism of tuberactinomycin action is the inhibition of tRNA translocation (Brilot et al., 2013; Ermolenko et al., 2007b; Holm et al., 2016; Liou and Tanaka, 1976; Modolffl and Vázquez, 1977; Peske et al., 2004; Stanley et al., 2010; Zhang et al., 2020). Tuberactinomycins bind to the decoding center, at the interface between h44 and H69 of the 30S and 50S subunit, respectively, where 16S rRNA residues A1492 and A1493 adopt a flipped-out conformation (Brilot et al., 2013; Stanley et al., 2010; Zhang et al., 2020). Tuberactinomycins also affect the position of 23S rRNA residue A1913 which adopts a position where it forms one hydrogen bond with the A-site tRNA (Stanley et al., 2010; Zhang et al., 2020). This explains why the affinity of tuberactinomycin to the ribosome greatly increases upon binding of an A-site tRNA (Holm et al., 2016; Peske et al., 2004). Although the crystal structures of capreomycin and viomycin were on non-rotated ribosomes (Stanley et al., 2010), biophysical studies indicate that viomycin stabilizes a rotated conformation of the ribosome with hybrid P/E and A/P tRNAs conformations (Cornish et al., 2008; Ermolenko et al., 2007b; Ly et al., 2010; Pan et al., 2007; Peske et al., 2004; Shoji et al., 2006; Wang et al., 2012). Recent cryo-EM structures confirmed these results, but revealed additional drug binding sites at the interface between the two ribosomal subunits, that were proposed to stabilize the rotated

ribosome (Zhang et al., 2020). Therefore, it was proposed that viomycin inhibits translation by trapping the ribosome in an intermediate state on the translocation pathway. Importantly, viomycin does not prevent the binding of EF-G to the ribosome, nor GTP hydrolysis by EF-G (Belardinelli et al., 2021; Holm et al., 2016; Modolffl and Vázquez, 1977; Peske et al., 2004), and even seems to stabilize EF-G binding (Salsi et al., 2014; Savelsbergh et al., 2003). A pre-translocation complex with A/P and P/E hybrid site tRNAs and EF-G trapped by viomycin has been in fact visualized by cryo-electron microscopy (Brilot et al., 2013; Carbone et al., 2021).

Considering the overall effect of tuberactinomycins on the retention of tRNA in the A site, I hypothesized that the nature of the A-site tRNA, rather than the nature of the amino acid, might have an impact on the ability of tuberactinomycins to inhibit translocation. Moreover, most of the studies concerning the mode of action of tuberactinomycin relied on the use of viomycin, but only little is actually known concerning capreomycin, despite the fact that capreomycin is the one used in clinics. To explore these issues, I performed three biological replicates of inverse toeprinting using capreomycin or viomycin, and the “NNN15” template library (**Figure 26**). By doing so, I could observe that capreomycin inhibits translation in a manner dependent on the nature of the transfer RNAs, while viomycin exhibited also A-site specificities but with slight differences. Using a combination of biochemical and structural approaches, I could shed light onto the mode of actions of tuberactinomycins, and the results are presented in the following manuscript.

# Mechanism and context-dependence of ribosome inhibition by the antituberculosis drugs viomycin and capreomycin

Elodie C. Leroy<sup>1,2</sup>, Thomas N. Perry<sup>1,2</sup>, Mélanie Gillard-Bocquet<sup>1</sup>, Thibaud T. Renault<sup>1\*</sup> & C. Axel Innis<sup>1\*</sup>

<sup>1</sup> Univ. Bordeaux, Centre National de la Recherche Scientifique, Institut National de la Santé et de la Recherche Médicale, ARNA, UMR 5320, U1212, Institut Européen de Chimie et Biologie, F-33600 Pessac, France.

<sup>2</sup> These authors contributed equally.

\* To whom correspondence should be addressed: axel.innis@inserm.fr; thibaud.renault@u-bordeaux.fr

## ABSTRACT

**Viomycin (Vio) and capreomycin (Cap) are members of the tuberactinomycin family and display excellent activity against *Mycobacterium tuberculosis*, including multidrug resistant strains. Both antibiotics bind across the ribosomal subunit interface and are translocation inhibitors that stabilize the pre-translocation state of the ribosome. Here we show using inverse toeprinting that Cap and Vio exhibit preferences for the nature of the A-site tRNA-mRNA complex. To understand these differences, several cryo-EM structures of *E. coli* Cap and Vio-bound ribosomes arrested by these A-site complexes were obtained at high resolution (around 3Å). We found that a single molecule of Cap or Vio was sufficient to not only target both the classical and rotated conformations of the EF-G-free ribosomes during the pre-translocation states, but also to impede the proper accommodation of EF-G into the A-site, thus inhibiting translocation. Our findings shed light onto the mode of action of tuberactinomycins where the nature of the A-site tRNA, combined to the structure and concentration of the drug, define the drug ability to inhibit translocation. Clarifying the mode of action of these highly used anti-tuberculosis treatments may lead to a more accurate understanding of their mechanisms of translation inhibition and provide new approaches to fight antimicrobial resistance.**

## INTRODUCTION

The spread of multidrug resistant *Mycobacterium tuberculosis* (*M. tuberculosis*) strains and the decrease in new antibiotic entering the market make tuberculosis a considerable threat to public health. Each year, *M. tuberculosis* is responsible for the death of 1.5 million people, and for the infection of 10 million more worldwide, despite the availability of several antimicrobial treatments (global tuberculosis report, WHO, 2019). Viomycin (Vio) and capreomycin (Cap) are members of the tuberactinomycin family and are produced by non-ribosomal peptide synthetases (NRPSs) found in various *Streptomyces* species (Thomas et al., 2003). They display excellent activity against *M. tuberculosis*, including multidrug resistant strains (Johansen et al., 2006). All tuberactinomycins contain the same cyclic pentapeptide core, composed of L-serine and the non-proteinogenic amino acids 2,3-diaminopropionate, L-capreomycidine, and  $\beta$ -ureidodehydro-alanine (Thomas et al., 2003), but differ in their residue side chain modifications, including aminoacylation at different positions with  $\beta$ -lysine. Vio was the first member of the tuberactinomycin family to be identified (Nagata et al., 1968) and most of the studies aimed at understanding the molecular mode of action of tuberactinomycins were therefore carried out with this drug. Cap is less toxic and more effective *in vivo* against wild-type and multi-resistant *M. tuberculosis* strains (Guire; Sutton et al., 1966).

Unlike Vio, which consists of a single molecular species, Cap is a mixture of four different isoforms (**Figure 1a**).

Tuberactinomycins primarily block bacterial protein synthesis by preventing the tRNA-mRNA translocation during the elongation phase of translation (Ermolenko et al., 2007a; Holm et al., 2016; Liou and Tanaka, 1976; Modolffl and Vázquez, 1977; Peske et al., 2004). During tRNA-mRNA translocation, a deacylated tRNA moves from the P site to the E site and peptidyl-tRNA moves from the A site to the P site, vacating the A site for the next incoming aminoacylated tRNA. Elongation factor G (EF-G) facilitates translocation through GTP hydrolysis and translocation occurs via the formation of tRNA hybrid states, relative rotation of the ribosomal subunits, and movement of the L1 stalk (Belardinelli et al., 2016a, 2016b; Cornish et al., 2008; Fei et al., 2008, 2009; Munro et al., 2010; Petrychenko et al., 2021; Rundlet et al., 2021; Trabuco et al., 2010). Pre-steady-state kinetic studies examining the mode of action of Vio reveal that elongating ribosomes present two Vio-sensitive states, and that Vio and EF-G compete for binding to the pre-translocation ribosome (Holm et al., 2016). Moreover, Vio induces few, if any, translational misreading errors (Akbergenov et al., 2011; Marrero et al., 1980), suggesting that translocation inhibition, rather than error induction, is the major cause of cell growth inhibition by this antibiotic (Holm et al., 2019).

Crystal structures of the *T. thermophilus* 70S ribosome in complex with three tRNAs, mRNA and Cap or Vio, show that the 16S ribosomal RNA (rRNA) monitoring bases A1492 and A1493, together with residue A1913 of the 23S rRNA, flip out to create a binding site for a single drug molecule at the conserved inter-subunit bridge (B2a) formed between rRNA helices h44 and H69 (Stanley et al., 2010). This is consistent with the observation that the affinity of Vio for the ribosome is greatly increased upon the binding of tRNA to the A-site, which also stabilizes these residues in their flipped out conformation, where the decoding center is said to be in a locked state (Holm et al., 2019). In these structures, the ribosome is maintained in the non-rotated classical state (PRE-C) by the crystal lattice. However, cryo-EM structures of Vio-containing complexes show the ribosome in a rotated conformation (Brilot et al., 2013; Zhang et al., 2020), albeit in the presence of fusidic acid, which traps EF-G in its GDP-bound form on the ribosome (Brilot et al., 2013), or in the absence of A-site tRNA (Zhang et al., 2020). Moreover, high concentrations of Vio were used to obtain these complexes, resulting in the binding of four additional drug molecules (Zhang et al., 2020). Such discrepancies also extend to single-molecule FRET (smFRET) studies, where Vio is shown to trap the ribosome in a rotated state and stabilize tRNAs in a P/E-A/P hybrid state in one study (Cornish et al., 2008; Ermolenko et al., 2007a), while the same drug appears to favor the classical state in another (Kim et al., 2007). Interestingly, another smFRET study shows that Vio preferentially stabilizes different tRNA states depending on the drug concentration, and that additional Vio binding sites might be present at high drug concentrations (Feldman et al., 2010).

Coupled to the growing realization that certain ribosome-targeting antibiotics can exhibit context-dependent effects (Vázquez-Laslop and Mankin, 2018), these discrepancies prompted us to revisit the molecular mechanism underlying tuberactinomycin action, first by establishing whether these drugs prevent the translocation of all tRNAs equally, and second by focusing our structural efforts on translating ribosomes under drug concentrations and protein synthesis conditions as close as possible to those experienced *in vivo*. In doing so, we found that Cap displays a marked sequence dependence by preferentially blocking the translocation of certain A-site tRNAs, whereas Vio exhibits considerable weaker context dependence. In addition, we obtained several cryo-EM structures of *E. coli* 70S ribosomes blocked during translation *in vitro* by the addition of low concentrations of Cap or Vio, which confirm the existence of multiple drug-sensitive states. Collectively, our findings shed light on the states of the ribosome targeted by tuberactinomycins during early translocation, and highlight how differences in the sequence and/or

modification pattern of tRNAs may impact the ability of antibiotics targeting the decoding center to inhibit bacterial translation.

## RESULTS

### Cap and Vio globally block tRNA translocation with a preference for certain A-site tRNAs

We used inverse toeprinting (Seip et al., 2018) to measure the extent to which Cap or Vio cause ribosomes translating different combinations of tRNAs to stall. Inverse toeprinting relies on a highly processive 3' to 5' RNA exonuclease (RNase R) to map the position of ribosomes stalled on mRNA with codon resolution. Unlike ribosome profiling, for which ribosome-protected mRNA footprints must be mapped to a reference genome, inverse toeprinting does not require a priori knowledge of the transcript sequences and may be used on libraries of any size and complexity (**Figure 1B**). Here, we performed inverse toeprinting on a collection of short open reading frames (ORFs) featuring a stretch of 15 degenerate NNN codons, following translation in vitro in the absence or presence of Cap or Vio. For this experiment, we chose a drug concentration of 100  $\mu$ M, that is  $\sim$ 8–25x greater than the MIC of Cap against *M. tuberculosis* (4–12  $\mu$ M) (Dijkstra et al., 2018; Monshupanee et al., 2012), to ensure complete translation inhibition. We first calculated the enrichment in each amino acid for all positions in the nascent peptide. For this, we counted the reads in which a given sequence was observed in the stalled ribosomes, and computed the enrichment in presence of the antibiotic (defined as the log2 fold change:  $\log_2(n_{\text{reads}}^{\text{antibiotic}}/n_{\text{reads}}^{\text{untreated}})$ ). Positive values indicate sequences for which the ribosome is stalled in the presence of the antibiotic. We observed that both antibiotics induced general translation arrest irrespective of the nature of the translated sequence (**Figure 1C**). However, a closer analysis of the enrichment values indicated that despite this global trend, there was a mild preference for specific tRNAs in the A-site (**Figure 1C/1D**). Interestingly, while most amino acids demonstrated a similar enrichment for both antibiotics relative to the untreated condition, a few residues were differentially enriched. Proline was specifically enriched for Vio while lysine and asparagine were more strongly enriched in presence of Cap. Alanine, glycine, and tryptophan displayed a lesser enrichment for both antibiotics. Given the central nature of the P- and A-site tRNAs during translocation, we confirmed this tendency by analyzing the enrichment of motifs of two amino acids in the P- and A-sites (**Figure 1E**). Of note, we also performed the enrichment analysis at the codon level, but could not observe particular biases for certain codons (**Figure S2**). At this stage, two substrates of the ribosome were candidates to explain the A-site specificities of tuberactinomycin's mode of action (1) the amino acid residue within the PTC and (2) the mRNA-tRNA complex. If the amino acid was responsible for the A-site specificities, it would first involve that the amino acid would have a long-distance allosteric effect on the drug mode of action. Second, the lack of evident common chemical features not only between the amino acids displaying high log2 fold changes, but also between amino acids displaying low log2 fold changes, led us to conclude that the amino acid located in the A-site of the PTC was probably not the substrate responsible for the tuberactinomycin specificities, even if this possibility couldn't be excluded. Therefore, we hypothesized that the nature of the mRNA-tRNA complex located in the A-site of the ribosome would influence the arrest induced by Cap or Vio.

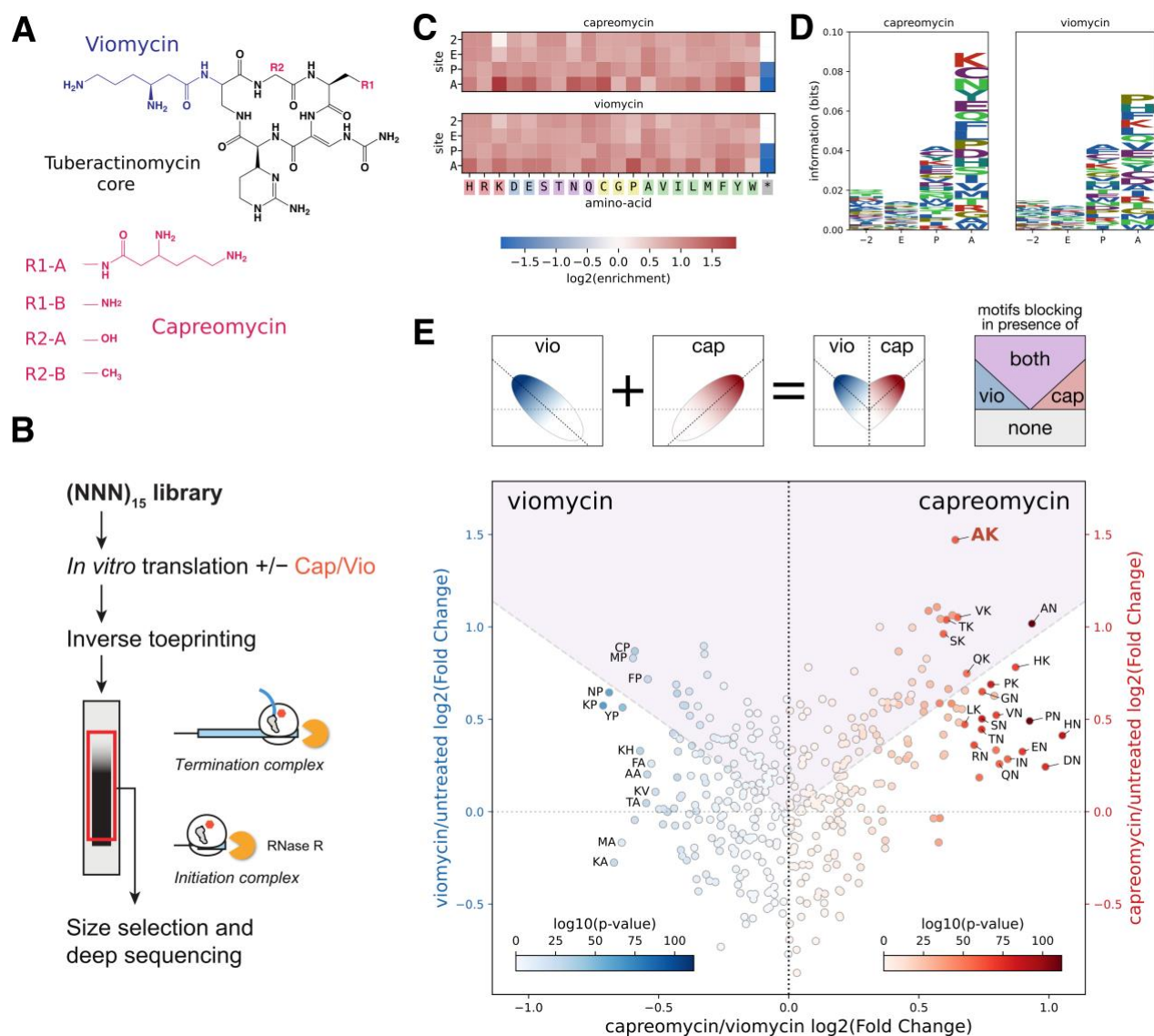


**Figure 1: Inverse toeprinting analysis.**

A. Structure of the studied antibiotics. Cap and Vio share the common tubercidin core, with variable chemical moieties. B. Overview of the inverse toeprinting procedure. A random (NNN)<sub>15</sub> library is translated in the absence or presence of the antibiotics, stalled ribosomes are purified and the blocking sequences are identified by next-generation sequencing. C. enrichment at the amino acid level in the -2/E/P/A sites in the presence of either Cap or Vio, relative to the untreated condition. D. Amino acid information logo demonstrating a mild bias at the A-site. The maximum information value (0.08 bits) should be put in perspective of the theoretical maximal information of 4.3 bits for amino acids. E. Heart plot of 2-amino acid motif enrichment in the presence of Cap or Vio relative to the untreated condition (Y-axis) as a function of the enrichment of Cap relative to Vio.

### Low and high concentrations of drug inhibit the ribosome differently

Having determined that the nature of the translation complex impacts the ability of tubercidinomycins to block translation *in vitro*, we next sought to identify whether other factors might account for the discrepancies surrounding the mechanism of ribosome inhibition by this family of antibiotics.



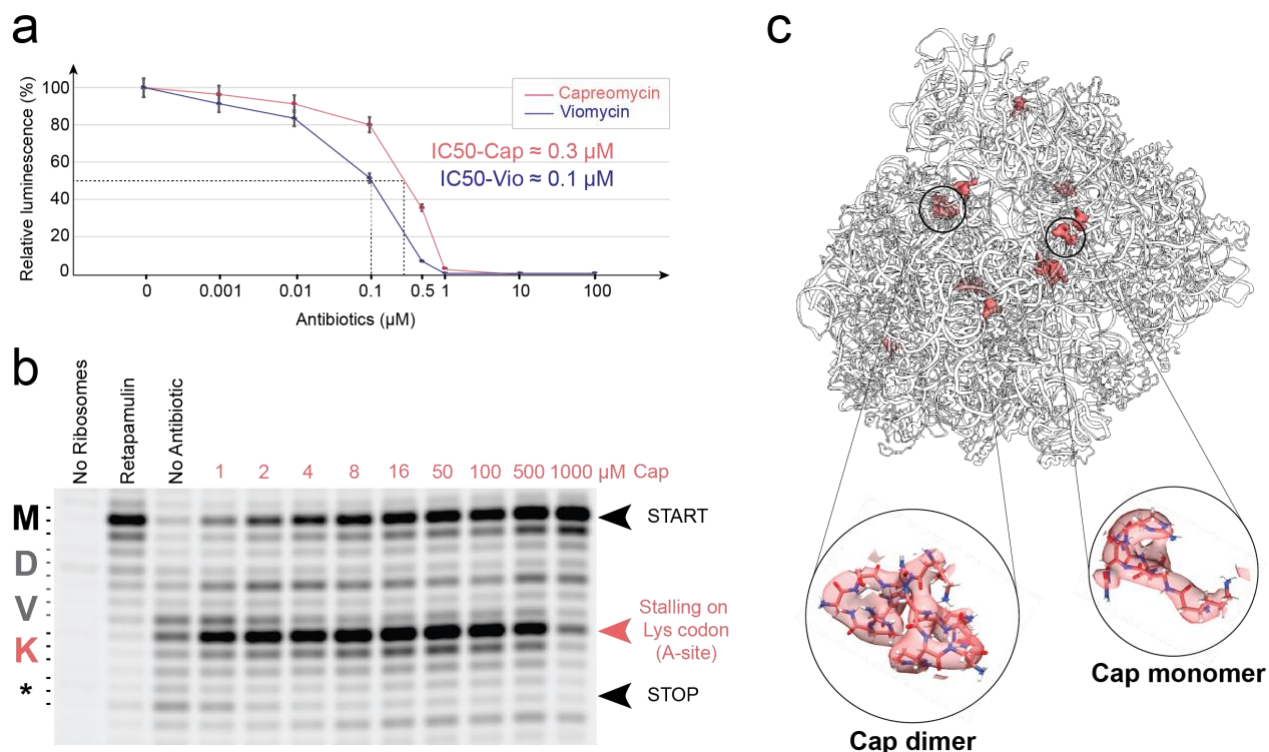


**Figure 2: Influence of Cap concentration on its mode of action.**

A. Protein synthesis inhibition with increasing concentrations of Cap (Cap) (salmon) and Vio (Vio) (blue) using an *in vitro* cell-free translation system, where the error bars represent the 5% error amount for three independent experiments. B. Cap concentration-dependent translation inhibition showed by an *in vitro* toeprinting assay. The Cap-dependent arrest on AAG codon is marked by the salmon arrow, while ribosomal arrest on start and stop codons are indicated by black arrows. C. Molecular model of the cryo-EM structure of the 70S-(AAG)<sub>5</sub>-Cap complex (colored in white) with isolated densities highlighting 13 Cap molecules (salmon) bound to the ribosome in the presence of 1 mM Cap, with close-ups on one Cap monomer and one dimer modeled into their corresponding map densities.

In particular, the fact that translation of most codons was impacted in the presence of 100  $\mu\text{M}$  Cap or Vio suggested that the inhibition observed by inverse toeprinting might be the result of two distinct, concentration-dependent modes of action for these antibiotics: a context-specific one at low drug concentration, and a context-independent one at high drug concentrations. To address this issue, we first measured the effect of concentrations ranging from 1  $\mu\text{M}$  to 1 mM of Cap or Vio on the *in vitro* synthesis of luciferase by monitoring bioluminescence. Consistent with previous results (Ermolenko et al., 2007b; Holm et al., 2016, 2019; Liou and Tanaka, 1976; Modolffl and Vázquez, 1977; Peske et al., 2004), we found that Cap and Vio are efficient inhibitors of protein synthesis, blocking luciferase production with half-maximal inhibitory concentrations ( $\text{IC}_{50}$ ) of 0.3  $\mu\text{M}$  and 0.1  $\mu\text{M}$ , respectively, and reaching complete inhibition of luciferase production at concentrations greater than 10  $\mu\text{M}$  (**Figure 2a**). Next, we chose to more closely study the effect of antibiotic concentration on the translation of individual codons. To do so, we selected the combination of drug and A-site codon that resulted in the strongest stalling observed by inverse toeprinting, and used classical toeprinting (Orelle et al., 2013) to monitor the position of ribosomes stalled during translation of a short open reading frame (ORF) containing an AAG codon in the presence of Cap (**Figure 2b**). As long as the concentration of Cap increases, the number of ribosomes stalled on the start codon also increases, suggesting that the ribosome may become immobilized by the addition of new

and non-specific binding sites. Once the concentration of Cap reaches 1 mM, translation is greatly impaired and ribosomes are predominantly stalled on the start codon (**Figure 2b**). From these data, we hypothesized that tuberactinomycins may inhibit translation through distinct mechanisms depending on the concentration of drug: a specific one at low drug concentration (1-100  $\mu$ M), where the ribosome starts translating until the lysine codon reaches the A-site, and a non-specific one at high drug concentrations (> 500  $\mu$ M), where the ribosome stalls directly on the start codon.

A recent cryo-EM structure of an *E. coli* 70S ribosome in a rotated state revealed five Vio molecules bound to the inter-subunit interface, which was taken as an indication that the binding of multiple drug molecules may be responsible for stabilizing the ribosome in the rotated state (Zhang et al., 2020). However, this structure was obtained using very high drug concentrations (0.5 mM), raising the possibility that the rotation observed was a direct consequence of exposure to a non-physiological concentration of drug. Moreover, the ribosomes used for cryo-EM analysis did not contain an A-site tRNA, which is required for high affinity binding of the drug to the decoding center on the 30S subunit (Peske et al., 2004). To test whether exposure of translating ribosomes to high concentrations of Cap might lead to spurious, non-specific binding of the antibiotic and lock the ribosome in a rotated state, we translated a short AUG-(AAG)<sub>5</sub> ORF in the presence of this antibiotic, and diluted the translation reaction with a solution containing 1 mM Cap and 25 mM Mg<sup>2+</sup> prior to structural analysis by cryo-EM.

A high concentration of magnesium is known to stabilize the ribosome in the non-rotated classical state, but does not entirely abolish subunit rotation and hybrid state formation (Kim et al., 2007). Thus, we would expect that if the binding of multiple antibiotic molecules stabilizes the rotated state, we should observe such ribosomes within our sample. We therefore determined a cryo-EM structure of the resulting 70S-(AAG)<sub>5</sub>-Cap complex to an average resolution of 3.3 Å and could observe a major class of particles (25.8%) with three tRNAs bound to the ribosome in the classical PRE-state (**Supp Figure 2**), with no class corresponding to rotated pre-translocation ribosomes. Although clear density for the cyclic pentapeptide core and side chains of Cap could be seen within the previously described binding site near the decoding center (Brilot et al., 2013; Stanley et al., 2010; Zhang et al., 2020), we could also detect 13 additional Cap molecules scattered over the entire ribosome and at the ribosomal subunit interface (**Figure 2c**), including three Cap dimers and seven monomers. Like the three Vio molecules previously observed in the structure of a rotated *E. coli* 70S ribosome in complex with a deacylated P-site tRNA (Zhang et al., 2020), one of these dimers is located within a crevice formed by helix h44 of the 16S rRNA and helices H69 and H71 of the 23S rRNA. However, the large number of bound drug molecules suggests that the majority of these sites only exist at high drug concentrations, and result from the propensity of a cyclic peptide like Cap to fill suitably-sized cavities in the rRNA (Polikanov et al., 2018). Given the MIC of Cap for *M. tuberculosis* (4 to 8  $\mu$ M) (Akbergenov et al., 2011) and for *E. coli* (128  $\mu$ M) (Monshupanee et al., 2012), we conclude that the mode of inhibition involving multiple drug molecules and occurring at high concentrations of antibiotic is not likely to be relevant *in vivo*.

## A single tuberactinomycin molecule binds to both the classical and hybrid PRE-states

To understand why Cap preferentially blocks translation when a lysine codon is in the ribosomal A-site, we set out to analyze translating ribosomes stalled by low drug concentrations (10  $\mu$ M) by cryo-EM. Using toeprinting to select an mRNA construct that would result in a homogeneous population of stalled ribosomes, we tested the effect of positioning a single lysine codon at various distances from the start codon. As expected from our inverse toeprinting data, adding one or several non-blocking alanine codons between the start and lysine codons led to a majority of ribosomes becoming stalled with the lysine codon in the A-site in the presence of 10  $\mu$ M Cap (**Figure 3a**). We thus chose a template encoding the peptide MAAK to prepare ribosomal complexes for cryo-EM and determined their structure following translation *in vitro* in the presence of 10  $\mu$ M Cap. Two major classes of particles were observed, corresponding to the non-rotated (PRE-C) (18.7 % particles) and rotated (PRE-H) (7.6 % particles) pre-translocation states (**Supp Figure 2**). These classes could be refined to 3.2 and 3.5 Å-resolution, respectively, to yield the PRE-C-MAAK-Cap and PRE-H-MAAK-Cap structures featuring MAAK-tRNA<sup>Lys</sup> in the A-site.

At this low concentration of Cap, we only observed density for a single Cap molecule near the decoding center, in the same location described previously (Stanley et al., 2010) (**Figure 3b**). To see whether the same held true for Vio, we also prepared 70S-MAAK complexes stalled by this antibiotic and determined the structures of the two main particle classes in this sample (**Supp Figure 2**), PRE-C-MAAK-Vio (27.3% particles) and PRE-H-MAAK-Vio (18.1% particles), at an overall resolution of 3.2 Å and of 3.3 Å, respectively (**Figure 3c**). Unlike a recent cryo-EM structure obtained after incubating ribosomes with 0.5 mM Vio, in which five bound drug molecules were observed (Zhang et al., 2020), we could only see a single Vio molecule bound to the decoding center on the 30S subunit. We therefore confirmed that the additional drug binding pockets seen in the 70S-(AAG)<sub>5</sub>-Cap structure and in the earlier structure of a ribosome-Vio complex (Zhang et al., 2020) are low affinity sites that contribute to the non-specific ribosome inhibition observed at high drug concentrations.

As expected from earlier structural data, the PRE-C-MAAK-Cap and PRE-C-MAAK-Vio structures were nearly identical (**Figure 3d**), with the exception of the bound drug molecule which made different contacts with the decoding center. The increased map quality and resolution compared to the previous structures enabled us to accurately model the  $\beta$ -lysine side chain of both Cap and Vio. In the case of Cap, several salt bridges between the  $\beta$ -lysine modification and the backbone phosphate of residue t6A37 and A38 of the A-site tRNA<sup>Lys</sup>, but also with A1913 of the 23S rRNA, were clearly visible in the PRE-C-MAAK-Cap density (**Figure 3e**). These contacts, which are absent in the case of Vio, are maintained during the transition to the PRE-H state and may contribute to the drug-dependent specificities observed for Cap. However, the near perfect overlap between the PRE-H-MAAK-Cap and PRE-H-MAAK-Vio structures, together with the lack of any visible structural backbone differences between the A-site bound tRNA<sup>Lys</sup> (Arenz et al., 2016; Rundlet et al., 2021) and other tRNAs did not allow us to identify structural elements that might be responsible for such sequence-dependent effects.

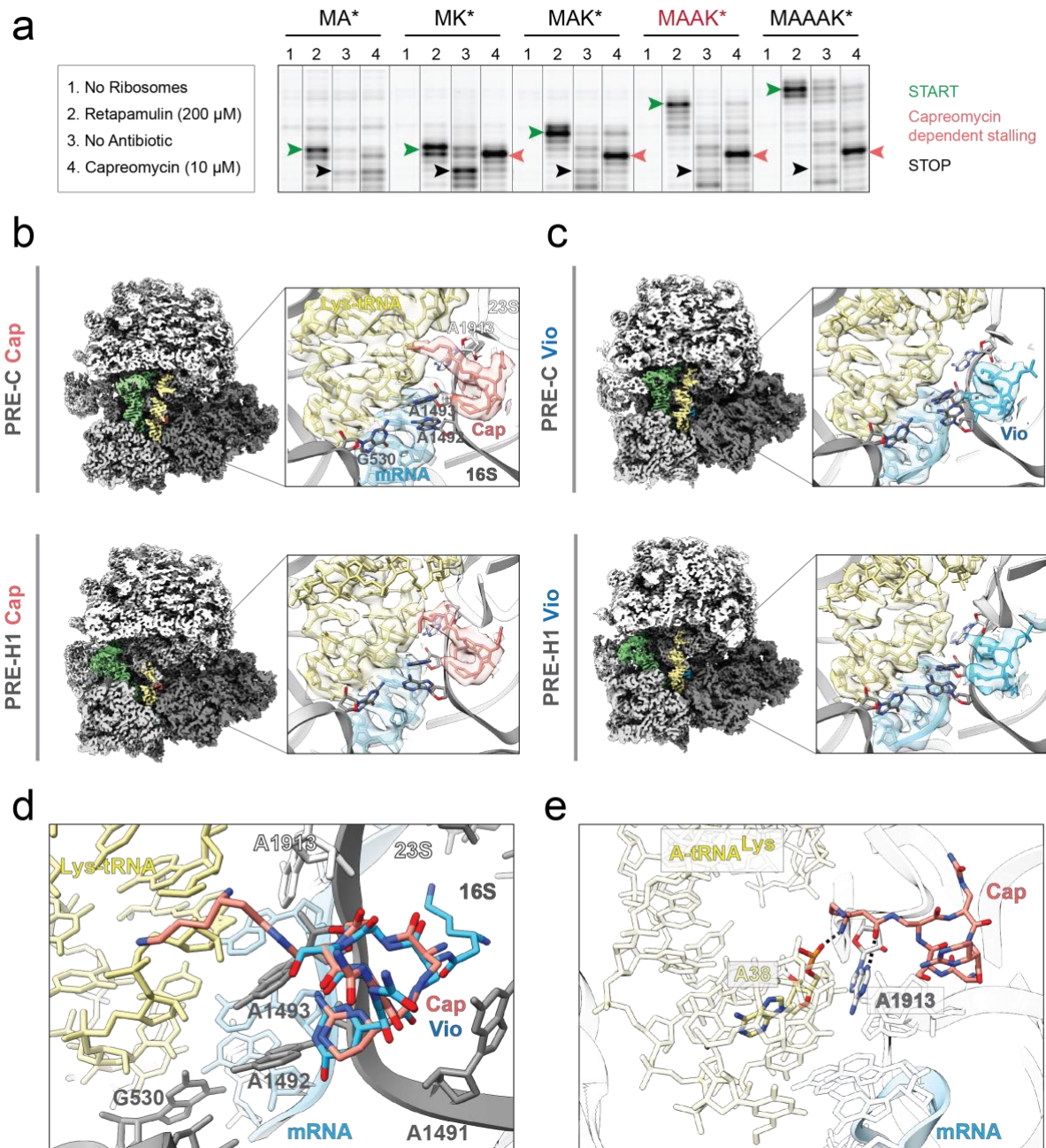


**Figure 3: Cryo-EM structures of PRE-H-MAAK-70S and PRE-H-MAAK-70S complexes bound to Cap or Vio.**

**a.** *In vitro* toeprinting assay of template encoding for alanine and/or lysine using 10  $\mu$ M Cap. The Cap-dependent arrest on the AAG codon is marked by salmon arrows, while ribosomal arrest on start and stop codons are indicated by green and black arrows respectively. **b/c.** Transverse section of the cryo-EM map and zoom-in of the decoding center for the PRE-C and PRE-H complexes stalled by Cap (**b**) or Vio (**c**) with isolated densities highlighting the 30S head (light grey), the 30S body (grey) and the 50S (white) subunits, the peptidyl-tRNA (yellow), the deacyl-tRNA (green), the mRNA (light blue), and Cap (salmon) or Vio (blue). **d.** Superimposition of Cap (salmon) and Vio (blue) PRE-C models within the decoding center. **E.** The  $\beta$ -lysine moiety of cap makes salt bridges interactions with the backbone A38 base of the A-site tRNA (yellow), and with A1913 of the 23S rRNA, within the decoding center of the *E. coli* ribosome



### The decoding center locking inhibits the accommodation of the EF-G domain IV to the tuberactinomycin-bound ribosome

Based on the cryo-EM data described above, we could not identify a class containing EF-G. Given that an earlier study had reported an EF-G-bound ribosome in the presence of Vio and fusidic acid (Brilot et al., 2013), we sought to determine whether such a state could be detected in the absence of additional inhibitors used to trap EF-G on the ribosome. In order to do so, we prepared ribosomal complexes translating MAAK in the presence of 10  $\mu$ M Cap and incubated them with a 15-molar excess of EF-G in the presence of GTP, prior to determining their structures using cryo-EM. Although we could observe the same PRE-C and PRE-H structures as before, a minor class of ribosomes in a rotated state also contained EF-G together with tRNAs in the A/P and P/E states (2,6% particles). This class corresponds to the structure observed by Brilot et al., 2013 at lower resolution and, despite the low resolution of our map, we could observe that the decoding center is locked, with A1492, A1493 and A1913 in their flipped-out conformations. Moreover, tRNA<sup>Lys</sup> in this EF-G-MAAK-Cap structure is more advanced along the translocation coordinate compared to the PRE-H-MAAK-Cap structure, indicating that the binding of EF-G is possible but is not stabilized in the presence of Cap.

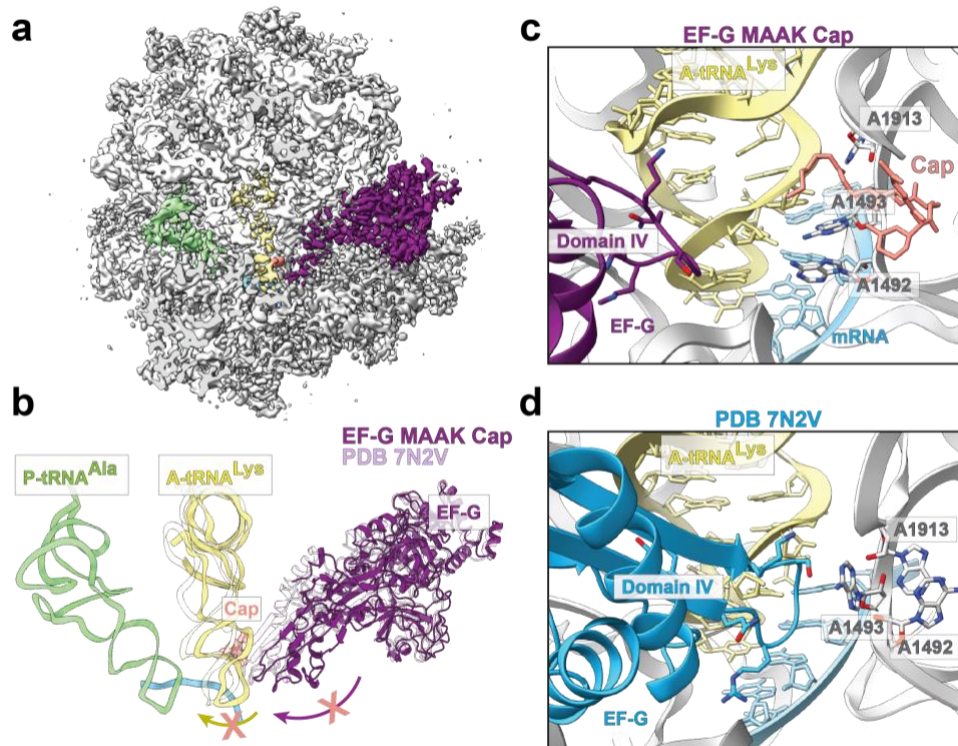


**Figure 3: Cryo-EM structures of EF-G-MAAK-Cap complex bound to Cap.**

a. Transverse section of the cryo-EM map and zoom-in of the decoding center for the EF-G complex stalled by Cap with isolated densities highlighting EF-G (purple), the peptidyl-tRNA (yellow), the deacyl-tRNA (green), the mRNA (light blue), and Cap (salmon). b. Superimposition of our EF-G-MAAK-Cap model to a corresponding intermediate complex of translocation bound to EF-G and stalled by spectinomycin (PDB 7N2V). c. Zoomed view to the decoding center of the EF-G-MAAK-Cap model, with bases A1493, A1492 of the 16S RNA and A1913 of the 23S RNA locked in their flipped-out conformations by the binding of Cap. d. Same zoomed view as panel c to the decoding center of the 7N2V model, with bases A1493, A1492 and A1913 in their canonical flipped-in conformations allowing the proper accommodation of EF-G domain IV within the A-site.

## DISCUSSION

Although kinetic data on the effect of Vio on elongation have indicated that two Vio-sensitive states exist during translocation (Holm et al., 2016), the available structural and biophysical data disagree on the exact state of the ribosome that is targeted and on the number of drug molecules that bind to the elongation complex (Brilot et al., 2013; Ermolenko et al., 2007b; Stanley et al., 2010; Zhang et al., 2020). Here, we show that a single molecule of Vio or Cap is sufficient to block translation at physiological drug concentrations (10  $\mu$ M), and that the drug-bound pre-translocation ribosome is free to explore the PRE-C, PRE-H states and EF-G-bound PRE-state during translation in the presence of these antibiotics. In addition, we show that very high drug concentrations, well above the MIC of *M. tuberculosis* or *E. coli*, lead to the binding of a large number of drug molecules to the ribosome, which prevent a majority of the initiation complexes from entering elongation. Such abnormally high drug concentrations and the lack of an A-site tRNA are likely to have caused the subunit rotation previously observed in response to Vio (Ermolenko et al., 2007b; Zhang et al., 2020), which is unlikely to reflect the major mode of translation inhibition by tuberactinomycins.

The structures of the drug-bound PRE-C, PRE-H and EF-G-bound complexes isolated here from a complete *in vitro* translation reaction allow us to propose a structural model for the mechanism of action of tuberactinomycins (**Figure 4**). The first drug-sensitive state identified through kinetic studies of Vio action (Holm et al., 2016) is the PRE-C state, previously observed in crystal structures of the *T. thermophilus* 70S ribosome in complex with three tRNAs and Cap or Vio (Stanley et al., 2010), and in a cryo-EM structure of the *M. tuberculosis* 70S ribosome in complex with Vio (Yang et al., 2017). Although the ribosomes in these structures are trapped in the PRE-C conformation by the crystal lattice, our data provides structural confirmation that this state does exist in solution. During normal translation in the absence of drug, the pre-translocation ribosome is free to explore a number of different hybrid states in addition to the PRE-C state. In the presence of Cap or Vio, we could only observe a single PRE-H state, that is situated in between the PRE-H2\* and PRE-H1 states observed previously along the translocation coordinate (Rundlet et al., 2021). Moreover, we could identify a sparsely populated drug- and EF-G-bound state that closely resembles the low-resolution structure of an EF-G-bound ribosome trapped in the PRE-state by the addition of Vio and fusidic acid (Brilot et al., 2013). A similar complex obtained by time-resolved cryo-EM in the presence of Vio but in the absence of additional antibiotics or non-hydrolyzable GTP analogues has been described (Carbone et al., 2021), and represents the second Vio sensitive state described by kinetic studies (Holm et al., 2016). Thus, it is clear that both Vio and Cap can remain associated with the pre-translocation ribosome following the initial decoding event until EF-G arrival and GTP hydrolysis. Although both the drug and EF-G can coexist on the ribosome, phosphate release leads to the rearrangement of switches I on EF-G, thereby weakening its interaction with the 30S subunit in the rotated state. In the absence of drug, this initiates a series of coupled structural changes that result in the net movement of the tRNA-mRNA module to reach the POST state: (i) backwards rotation of the 30S subunit body, (ii) rearrangement of the sarcin-ricin loop (SRL) back to a ground state, (iii) rotation of EF-G together with the SRL to roll on the shoulder of the 30S subunit and stabilize the non-rotated state, and (iv) binding of the domain IV of EF-G to the decoding center, which stabilize the head of the 30S subunit in the swiveled state (Carbone et al., 2021; Petrychenko et al., 2021; Rundlet et al., 2021). In the presence of drug however, the decoding center remains locked and the weakening of the interaction between EF-G and the 30S subunit following phosphate release likely results in EF-G(GDP) dropping off from the ribosome (Belardinelli et al., 2021; Carbone et al., 2021; Petrychenko et al., 2021). A new EF-G(GTP) can then bind to the ribosome, leading to additional futile cycles of GTP hydrolysis. If the drug dissociates from the ribosome first, then translocation can proceed normally.

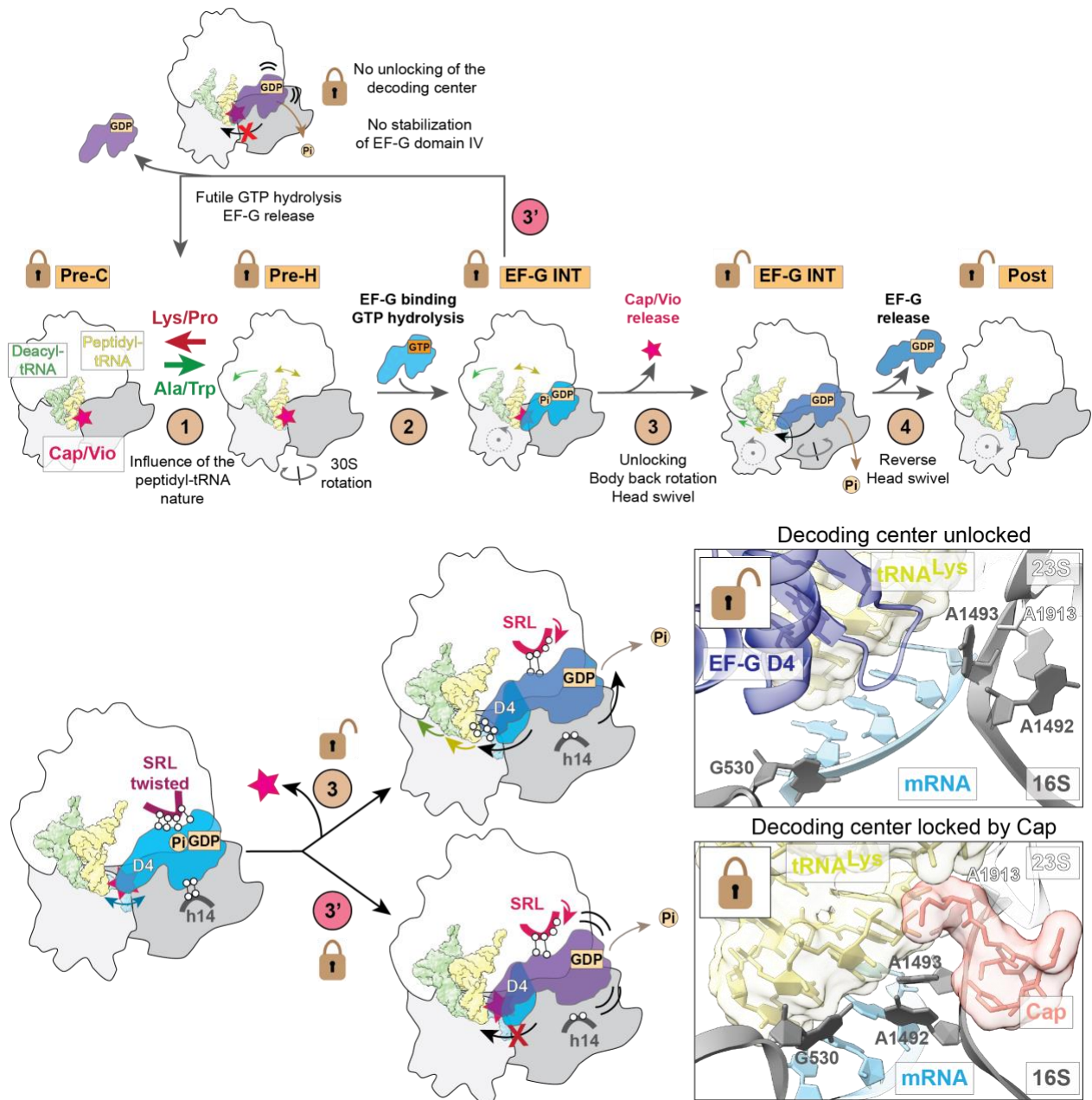


**Figure 4: Mechanism of tuberactinomycin-induced translocation inhibition.**

Translocation process and rearrangements of ribosomal subunits, EF-G and tRNAs in presence of Cap/Vio. Cap and Vio can bind to the Pre-C and Pre-H states of translocation. In presence of tuberactinomycin bound to the ribosome, the transition from Pre-C to Pre-H (1) requires movements of the deacyl- and peptidyl-tRNAs, which can possibly be affected by the nature of the peptidyl-tRNA located in the A-site. EF-G can bind to the Pre-H ribosome. Under free-antibiotic conditions, EF-G accommodates within the A-site (2) after GTP hydrolysis. The following step is the release of Pi from EF-G that is accompanied by the loss of interactions with the SRL of the 50S subunit and h14 of the 16S RNA within the 30S; this allows EF-G domain IV to interact with the A-site tRNA, the mRNA and the decoding center in order to promote translocation (3). After translocation and before complete reverse swivel of the 30S head domain, EF-G can leave the post-translocation state of the ribosome. However, in presence of Cap/Vio, the accommodation of EF-G domain IV that normally occurs in step (3) is restrained by the presence of the drug which stabilizes the locked conformation of the decoding center (3'). Coupled to the loss of interactions with the 50S and

30S subunits, EF-G is completely destabilized after Pi release and leaves the ribosome without promoting translocation (3'), thus inhibiting EF-G catalyzed translocation.

Our in-depth characterization of the *in vitro* translational pausing landscape of free and tuberactinomycin-bound ribosomes showed that translation inhibition is sequence-dependent in the case of Cap and, to a lesser extent, Vio, in a manner that appears to be tRNA-dependent. To understand why the presence of tRNA<sup>Lys</sup> in the A-site results in strong translation inhibition in the presence of Cap, we obtained structures of ribosomes stalled during translation of an ORF encoding MAAK in the presence of Cap or Vio. Although both antibiotics could bind to the PRE-C and PRE-H states, we could not observe any difference in the conformations of the tRNA<sup>Lys</sup> in the absence (Rundlet et al., 2021) or presence of either drug. As a result, we could not identify the molecular basis for this sequence specificity on the basis of the structural data alone. Nevertheless, we could observe a general trend for the sequence and modification pattern at positions 34, 37 and 39 of the ASL when we ranked A-site tRNA sequences according to their ability to arrest translation in response to Cap or Vio, suggesting that these tRNA elements could be responsible for this behavior (**Supp Figure 6**). Chemical modifications within the anticodon are important to ensure the redundancy of the genetic code, decoding accuracy, and maintenance of the reading frame (Agris, 2004, 2008; Murphy et al., 2004). Additionally, the anticodon domain contributes to the global structure and the dynamics of the tRNA during its accommodation and translocation (Lorenz et al., 2017; Zhang et al., 2014). In fact, anticodon stem loops containing high A/U contents, such as that of tRNA<sup>Lys</sup>, are stabilized and rigidified by the presence of modified nucleosides at key positions, which increase the number of hydrogen bonds formed within the tRNA and with the ribosome (Motorin and Helm, 2010; Ranjan and Rodnina, 2017; Sundaram et al., 2000). It is conceivable that the nature of the peptidyl-tRNA located in the A-site impairs the rate of transition between the Pre-C and Pre-H states (**Figure 4**); as the binding of EF-G is possible only on the Pre-H state (Carbone et al., 2021; Petrychenko et al., 2021), a low-population of Pre-H ribosomes could add an additional effect on tuberactinomycin-induced translocation inhibition by disfavoring the binding of EF-G to the ribosomes. It is unclear whether a similar drug-dependent behavior would be observed with *M. tuberculosis* ribosomes and tRNAs. Complementary studies to study the effect of these drugs on translation in *E. coli* or *M. tuberculosis* strains or to analyze tRNA dynamics during translocation in the presence of Cap or Vio by smFRET will therefore be necessary to understand the basis for this sequence dependence. Revealing the detailed modes of action for different tuberactinomycins may eventually help to develop new compounds that are effective against multi-drug resistant or extremely drug-resistant *Mycobacterium tuberculosis* strains.



## **ACKNOWLEDGEMENTS**

E.C.L., M.G-B. and C.A.I. have received funding for this project from the European Research Council (ERC) under the European Union's Horizon 2020 research and innovation program (Grant Agreement No. 724040). C.A.I. is an EMBO YIP and has received funding from the Fondation Bettencourt-Schueller. T.N.P. has received funding for this project from the Agence Nationale de la Recherche (ANR) under the frame of the Joint JPI-EC-AMR Project "Ribotarget – Development of novel ribosome-targeting antibiotics". We thank the cryo-EM platform of the European Institute for the data collection time on the Talos Arctica microscope.

## **AUTHOR CONTRIBUTIONS**

C.A.I. designed the study. E.C.L. and M.G-B. performed inverse toeprinting experiments. E.C.L., T.T.R. and C.A.I. processed and analyzed the inverse toeprinting data. E.C.L. performed the toeprinting and luciferase inhibition assays. E.C.L. prepared the complexes for cryo-EM; T.N.P. prepared the cryo-EM grids and performed data collection on the Talos Arctica. T.N.P., C.A.I. and E.C.L. processed the cryo-EM data and E.C.L. built the models. E.C.L., T.N.P., T.T.R. and C.A.I. wrote the paper, reviewed and edited the manuscript.

## **COMPETING FINANCIAL INTERESTS**

The authors declare no competing financial interests. Correspondence and requests for materials should be addressed to C.A.I. ([axel.innis@inserm.fr](mailto:axel.innis@inserm.fr)) or T.T.R. ([thibaud.renault@u-bordeaux.fr](mailto:thibaud.renault@u-bordeaux.fr)).

## METHODS

### General experimental procedures for inverse toeprinting

DNA and RNA products at various points in the inverse toeprinting protocol were analyzed on 9% acrylamide (19:1) TBE (90 mM Tris, 90 mM boric acid, and 2 mM EDTA) gels and stained with SyBR Gold (Invitrogen). Inverse toeprints were excised from 12% acrylamide TBE gels using a clean scalpel. RNA gel electrophoresis was performed under denaturing conditions (8 M urea in the gel). All reactions were performed using molecular biology grade H<sub>2</sub>O (Millipore). Oligonucleotides used in this study are listed above.

### 15 codons random library generation

A random variant library containing 15 'NNN' codon (aNy aNy, aNy) was designed and ordered to Eurogentec under the form of a single stranded oligonucleotide called 'iTP\_NNN15\_random-library'. This expression cassette was obtained by polymerase chain reaction (PCR) with Phusion DNA polymerase (6 cycles [98°C, 10 s; 62°C, 5 s; 72°C, 10 s]), using the 'iTP\_NNN15\_random-library' oligonucleotide in combination with oligonucleotides 'iTP/TP\_T7\_RBS\_ATG\_f' and 'iTP\_Stop\_EcoRV\_r' as templates (0.1 pmol of each oligonucleotide per 50 µl reaction) and oligonucleotides 'iTP/TP\_T7\_f' and 'iTP\_EcoRV\_r' for amplification (1 pmol of each oligonucleotide per 50 µl reaction). The final sequence of the expression cassette is:

CGATCGAATTCTAATACGACTCACTATAGGGCTTAAGTATAAGGAGGAAAAATATG**NNNNNNNNNNNNNNNNNN**  
**NNNNNNNNNNNNNNNNNNNNNNNNNNNNNNNGCGATCTCGGTGTGATGAGATATCAATATCAAAAAGGATCCA**  
TATA

(the T7 promoter is underlined, random expression region is in **bold**; the EcoRV site is in *italics*). Linear expression cassettes were purified using a PCR purification kit (Qiagen) according to the manufacturer's instructions prior to quantification with a 2100 Agilent Bioanalyzer and mixing.

### *In vitro* transcription

The DNA template contains a T7 promoter followed by a ribosome binding sequence, as specified in the NEB PURExpress system handbook. *In vitro* transcription was performed using T7 RNA polymerase in a buffer containing 80 mM Tris-HCl, 24 mM MgCl<sub>2</sub>, 2 mM spermidine, and 40 mM DTT, pH 7.6, in the presence of 7.5 mM ATP (Sigma Aldrich), CTP and UTP, 0.3 mM GTP (CTP, UTP, and GTP from Jena Bioscience), and 4.5 mM Thio-Phosphate-GMP (Genaxxon Bioscience). 8 pmol of DNA template were used in 200 µl of reaction volume. *In vitro* transcription was performed at 20°C for 3 h, mRNA was purified using the "RNA Clean & Concentrator<sup>TM</sup>-5" purification kit (ZymoClean Research) according to the manufacturer's instructions. The final concentration of mRNA was determined using the NanoDrop.

### Biotinylation

Biotin-maleimide (Vectorlabs) was dissolved in dimethylformamide according to the manufacturer's instructions. 800 pmol mRNA were mixed with 800 nmol biotin-maleimide in 100 mM in Bis-Tris-acetate buffer pH 6.7 and incubated at room temperature for 2.5 h. Unincorporated biotin was removed by washing the mRNA three times with H<sub>2</sub>O (molecular biology grade, Millipore) in an Amicon membrane centrifugal concentrator with a MWCO of 30 kDa (Millipore). mRNA was recovered and the biotinylation efficiency was analyzed using a dot blot.

### Dot blot

H<sup>+</sup> bond membrane (GE Healthcare) was treated with 6× SSC buffer (900 mM NaCl, 90 mM Na<sub>3</sub>-citrate, pH 7.0) for 10 min and dried briefly between two pieces of Whatman paper. Samples and a 5'-biotinylated oligonucleotide standard (Biotin\_standard) were diluted in 6× SSC buffer to 0.5, 1.0, 2.5, and 5.0 μM, and 1 μl of each dilution was pipetted onto the prepared membrane. The membrane was then baked for 2 h at 80°C to adsorb the mRNA to the membrane. The membrane was subsequently blocked in 2.5% dry milk solution in TBS-T (50 mM Tris-HCl, 150 mM NaCl, and 0.05% [vol/vol] Tween-20, pH 7.5) for 1 h at room temperature. The milk solution was removed and the membrane was incubated with a 1:1,000 dilution of streptavidin-alkaline phosphatase antibody (Promega) in TBS-T for 1 h at room temperature. Unbound antibody was removed by washing three times with TBS-T buffer. Colorimetric detection was performed using an NBT/BCIP detection kit (Promega) according to the manufacturer's instructions. The membrane was imaged immediately on a Bio-Rad Imager. The biotinylation efficiency was estimated by comparing the intensity of the sample dots with the intensity of the standard dots.

### Polyadenylation of the mRNA

Polyadenylation of the biotinylated mRNA was performed using Poly-A polymerase (NEB) using the buffer supplied. The ratio of mRNA to ATP molecules was chosen to be 1:100. The reaction was incubated at 37°C for 2 h and the efficiency of the polyadenylation reaction was assessed by denaturing PAGE (9%). Polyadenylated mRNA was purified using the purification "RNA Clean & Concentrator"<sup>TM</sup>-5" kit (ZymoClean Research) according to the manufacturer's instructions.

### Inverse toeprinting

Inverse toeprinting was performed as described previously, with modifications (Seip *et al.* 2018). Briefly, *in vitro* translation was carried out with a PURExpress Δ RF-123 Δ Ribosomes kit (NEB), using ~5 pmol of 5'-biotinylated and 3'-polyadenylated mRNA as a template. Antibiotic (Cap or Vio) was supplemented at a final concentration of 100 μM in 5 μl reactions. Release factors 1 and 3 were added to the translation reaction according to the manufacturer's instructions. Translation was performed at 37°C for 30 min, after which the samples were placed on ice and 5 μl ice-cold Mg<sup>2+</sup> buffer (50 mM Hepes-KOH, 100 mM K-glutamate, 87 mM Mg- acetate, and 1 mM DTT, pH 7.5) was added to the reactions, thereby increasing the Mg<sup>2+</sup> concentration to 50 mM. 1 μl of RNase R (1 mg/ml) was added, followed by an additional incubation for 30 min at 37°C to ensure complete mRNA degradation. 139 μl of 1× BWT buffer was added to stop the reaction (5 mM Tris-HCl, 0.5 mM EDTA, 1 M NaCl, and 0.05% [vol/vol] Tween- 20, pH 7.5).

### mRNA purification and linker ligation

For each sample, 5 μl of a M-280 streptavidin Dynabeads (ThermoFisher Scientific) suspension were washed three times with 1× BWT buffer in DNA loBind tubes (Eppendorf) and resuspended in 50 μl of the same buffer. Dynabeads and RNA from the previous step were combined into these tubes and incubated on a tube rotator for 15 min at room temperature to allow binding of the biotinylated mRNA to the streptavidin beads. After incubation, beads were collected using a magnet and the supernatant was discarded. The beads were washed one time with 1× BWT buffer to remove unbound RNA, followed by two washes with H<sub>2</sub>O to remove the 1× BWT buffer. Beads were resuspended in 9.5 μl of linker ligation reaction mixture containing 4 μl of water, 1 μl of T4 RNA ligase2 truncated buffer (10X – NEB), 3 μl of PEG 8000 (50% - NEB), 1 μl of 'iTP\_3'\_linker\_ApoI '(10 μM) and 0.5 μl of ligase (T4 RNA ligase 2, truncated - 200 000 U/ml - NEB) per reaction. Linker ligation was allowed to proceed on a tube rotator for 2.5 h at room temperature.

### **Reverse transcription**

Following ligation of the linker, beads were washed once with H<sub>2</sub>O to remove unincorporated linker oligonucleotide and were resuspended in 18.5 µl of reverse transcription reaction mixture containing 11.5 µl of water, 1 µl of dNTPs (10 mM of each - NEB), 1 µl of 'iTP\_Linkers\_r' oligonucleotide (2 µM), 4 µl of first strand synthesis buffer (5X - ThermoFisher) and 1 µl of DTT (0.1 M - ThermoFisher) per reaction. The samples were incubated for 5 min at 65°C to anneal the primer to the complementary sequence and then placed on ice. 1 µl of reverse transcriptase (Superscript III – 200,000 U/ml – ThermoFisher) was added to each tube and the samples were incubated for 30 min at 55°C in a Thermomixer at 500 rpm to allow reverse transcription of the Dynabead-bound mRNA.

### **PCR on cDNA, restriction digestion**

Reverse transcribed cDNA was used without further purification as a template for PCR. To generate double stranded DNA for restriction digestion, a fill-up reaction was performed using 'iTP\_cDNA\_f' oligonucleotide and the reverse transcribed cDNA (10 s denaturation, 10 s annealing at 42°C, and 30 s elongation at 72°C). The resulting double stranded DNA was combined with 1 µl of EcoRV-HF restriction enzyme and the sample was incubated at 37°C for 1 h. To amplify undigested DNA, 'iTP\_Linkers\_r' oligonucleotide was added and a PCR was performed with 10-16 cycles (denaturation at 98°C for 10 s, annealing at 60°C for 10 s, and elongation at 72°C for 10 s). The number of PCR cycles was adjusted to give a visible band on the gel while minimizing non-specific byproducts.

### **Purification of DNA fragments of interest after PCR**

Bands containing inverse toeprints corresponding to stalled ribosomes from the initiation codon to the last 'NNN' codon were excised from the gel with a clean scalpel. Gel pieces were crushed through a 5 ml syringe into 15 ml Falcon tubes and 10 ml of gel elution buffer (10 mM Tris-HCl, pH 8.0, 500 mM Na-acetate, and 0.5 mM Na-EDTA) were added. The tubes were incubated on a tube rotator at room temperature overnight. Gel debris were separated from the extraction solution by filtering through 0.22 µm centrifugal filters (Millipore). Each sample was then concentrated to ~1 ml using a SpeedVac. DNA was precipitated in 5 ml Eppendorf tubes using 1 ml of isopropanol with 3.7 µl GlycoBlue (Thermo Fisher Scientific) and incubating at -80°C overnight. After precipitation, DNA was recovered by centrifugation in a ThermoScientific Heraeus Multifuge X3R centrifuge at 20,000g for 30 min at 4°C using a Fiberlite F15-8x50cy rotor (ThermoScientific). The supernatant was removed and DNA pellets were resuspended in 20 µl H<sub>2</sub>O (molecular biology grade, Millipore) for subsequent addition of the next-generation sequencing (NGS) adapters.

### **Additions of NGS adaptors to amplified DNA**

Long NGS adapter oligonucleotides ('NGS\_adaptor\_f' and the reverse oligonucleotides 'NGS\_adaptor\_index\_number') contain Illumina TruSeq adapter sequences followed by 18 nucleotides complementary to the 5' or 3' region of the cDNA. The reverse oligonucleotides also contain barcode sequences for multiplexing according to the TruSeq v1/v2/LT protocol (Illumina). Sequencing libraries were obtained from 12–16 cycles of PCR using 0.02 µM long NGS adapter oligonucleotides (forward and reverse) and 0.2 µM short amplification oligonucleotides ('NGS\_f' and 'NGS\_r'). PCR products were purified using a Qiagen PCR purification kit. The size and concentration of the fragments obtained were measured using a 2100 Agilent Bioanalyzer with the DNA 1000 kit.

### **Next generation sequencing**

Next generation sequencing was performed by the BGI Facility in Hong-Kong, on an Illumina HiSeqXten system in rapid run mode with 150 PE reads.

### Toeprinting assays

Toeprinting was performed as described previously (Orelle et al, 2013). Briefly, DNA templates containing a T7 promoter, a ribosome binding site, the expression cassette and the NV1 sequence (Vazquez-Laslop et al, 2008) were generated by PCR using as templates oligonucleotides 'iTP/TP\_frag1\_T7\_RBS\_ATG\_f', 'TP\_frag2\_r', 'TP\_frag2\_NV1\_r' and the corresponding expression cassette oligo (0.1 pmol of each oligonucleotide per 50 µl reaction) and the short primers 'iTP/TP\_frag1\_T7\_f' and 'TP\_short\_r' for amplification (1 pmol of each oligonucleotide per 50 µl reaction) (see Key Resources Table for the sequences of oligonucleotides used).

For instance, the final sequence of the 'MAAK\*' expression cassette is:

CGATCGAATTCTAATACGACTCACTATAGGGCTTAAGTATAAGGAGGAAAAAAT**ATGGCAGCAAAGTGAAGCGAA**  
TAATAACTGACTCTGAACAACATCCGTACTCTTCGTGCGCAGGCAAGGTTAATAAGCAAAATTCATTATAACC (the  
T7 promoter is underlined, the 'MAAK\*' expression region is in **bold**; the NV1 sequence is in *italics*).

DNA templates were transcribed and translated *in vitro* using the PURExpress Δ RF123 Δ Ribosomes Kit (New England Biolabs). Ligands were dissolved in water and added as needed at the beginning of the reaction. The Yakima Yellow-labelled probe complementary to the NV1 sequence ('TP\_RT\_yakima-yellow\_r') was added to the 5 µl reaction after incubating for 15 min at 37 °C (2 µM) and the sample was incubated for another 5 min at the same temperature. Reverse transcription is then performed with 50 U of Avian Myeloblastosis Virus reverse transcriptase (Promega Corporation) for 20 min at 37 °C. RNA was degraded by adding 0.5 µl of a 10 M NaOH stock at 37 °C for 15 min. Samples were neutralized with 0.7 µl of a 7.5 M HCl stock and the remaining complementary DNA was purified using a nucleotide removal kit (QIAGEN). Sequencing reactions were performed using a commercial kit designed to be used with fluorescent dye-labeled primers (#792601KT – ThermoFischer Scientific). To purify the PCR product, the ExoSAP-IT reagent (#PN 78200 – ThermoFischer Scientific) is used, to remove the excess dNTPs and primers before starting the sequencing. This purification step is performed following the manufacturer's instructions. For the sequencing procedure, 4 µl of purified PCR product (or approximately 0,5 – 1 pmol of DNA) and 2 pmol of the 5'-labeled oligonucleotide are used to prepare the master reaction following the manufacturer's instructions. Once the PCR product is purified and the sequencing reactions are prepared, the following sequencing PCR program is used: [30 s denaturation, 15 s annealing at 50°C, and 60 s elongation at 72°C], 25 cycles. 2 µl of formamide loading dye from the kit are then added to each Sanger reaction. Sanger reactions are heated for 3 min at 75°C to denature the cDNA, while the toeprinting samples were denatured at 95 °C for 5 min. 3.5µl of the sequencing reactions and 3 µl of the toeprinting reactions were separated by 7.5% sequencing polyacrylamide gel electrophoresis (2,000 V, 40 W for 2–2.5 h) followed by detection on an Amersham Typhoon Gel and Blot Imaging System (GE Healthcare Life Sciences).

### Luciferase inhibition assays

Dilutions of Cap and Vio were made from 1 nM to 1 mM. For each dilution, 2 µL were dried in the speed vacuum for 15 minutes to eliminate the solvent. *In vitro* translation reactions were made in PURExpress system (NEB), each reaction in 5 µl, supplied with 200 ng of luciferase mRNA and the dried antibiotic at the desired concentration. The reactions were incubated for 15 minutes at 37°C to allow the translation to proceed. The d-luciferin (Luciferase substrate Steady-Glo, Promega, #2510) was then diluted by mixing 400 µL of luciferase buffer (70mM Hepes pH 7.7, 7mM MgSo4; 3mM DTT, 1% BSA) with 40 µL of d-luciferin. 50 µL of this substrate dilution were dispensed onto each reaction tube at the end of the incubation time. Each reaction was transferred into a 96 wells black plate and the luminescence was measured on plate reader CLARIOstar (BMG Labtech) at 550-570 nm. Each

experiment was done in three biological replicates to calculate the half-maximal inhibitory concentration (IC<sub>50</sub>).

### **Preparation of *E. coli* 70S complexes for cryo-EM**

#### *70S-(AAG)<sub>5</sub>-Cap complex:*

The complexes were translated *in vitro* using 2.2  $\mu$ M of homemade reassociated 70S ribosomes from *E. coli* KC6 strain, 200  $\mu$ M of Cap, 5 pmol of AUG-(AAG)<sub>5</sub> mRNA and the PURExpress  $\Delta$  Ribosomes Kit (New England Biolabs) at 37°C for 20 min then diluted to a final concentration of ribosomes of 200 nM in buffer A (50 mM HEPES-KOH pH 7.5, 100 mM K-acetate, 25 mM Mg-acetate, and 1 mM Cap) for immediate grid preparation.

#### *70S-PRE-H/PRE-C-MAAK complexes:*

The complexes were translated *in vitro* using 2.2  $\mu$ M of homemade reassociated 70S ribosomes from *E. coli* KC6 strain, 10  $\mu$ M of Cap or Vio, 5 pmol of MAAK-mRNA and the PURExpress  $\Delta$  Ribosomes Kit (New England Biolabs) at 37°C for 20 min then diluted to a final concentration of ribosomes of 300 nM in buffer B (30 mM HEPES-KOH pH 7.5, 5 mM MgCl<sub>2</sub>, 50 mM NH<sub>4</sub>Cl, 5 mM 2-mercaptoethanol, 2 mM spermidine and 5 mM putrescine, and 10  $\mu$ M of Cap or Vio) for immediate grid preparation.

#### *70S-EF-G-MAAK-Cap complex:*

The complex was translated *in vitro* using 2.2  $\mu$ M of homemade reassociated 70S ribosomes from *E. coli* KC6 strain, 10  $\mu$ M of Cap, 5 pmol of MAAK-mRNA and the PURExpress  $\Delta$  Ribosomes Kit (New England Biolabs) at 37°C for 20 min then diluted to a final concentration of ribosomes of 300 nM in buffer B (30 mM HEPES-KOH pH 7.5, 5 mM MgCl<sub>2</sub>, 50 mM NH<sub>4</sub>Cl, 5 mM 2-mercaptoethanol, 2 mM spermidine and 5 mM putrescine, and 10  $\mu$ M of Cap). 20  $\mu$ l of this dilution and 2  $\mu$ l of a solution containing 55  $\mu$ M of homemade purified *E. coli* EF-G and 11 mM GTP (both diluted in buffer B containing 10  $\mu$ M Cap) were mixed and incubated for 5 min at 37°C, and finally placed on ice for immediate grid preparation. End concentrations of each components in the cryoEM sample: 273 nM ribosomes, 10  $\mu$ M Cap, 5  $\mu$ M EF-G, 1 mM GTP.

### **Cryo-EM grid preparation**

For cryo-EM analyses, 3.5  $\mu$ l of sample was deposited on glow-discharged Quantifoil carbon grids (QF-R2/2-Cu) coated with a thin carbon layer of 2 nm using an Edwards Vacuum Carbon Coater E306. After waiting for 30 seconds and blotting with filter paper to remove excess sample for 2.5 s, grids were plunge-frozen in liquid ethane using a FEI Vitrobot Mark IV (Thermo Fisher) with a blotting force of 5 in an environment with 100% humidity and 4 °C temperature.

### **Cryo-EM data acquisition**

Cryo-EM images were collected in counting mode on a Talos Arctica (Thermo Fisher) operated at 200 kV and equipped with a K2 Summit direct electron detector (Gatan) in Nanoprobe mode at the IECB in Bordeaux (France). Images of 70S-(AAG)<sub>3</sub>-Cap, MAAK-Cap and MAAK-Vio complexes were recorded with SerialEM with a magnified pixel size of 0.93 Å at a magnification of 45,000 to record 38 movies frames with an exposure time of 3.8 seconds using a dose rate of 1.32, 0.92 and 0.89 electron per Å<sup>2</sup> per frame for a total accumulated dose of 50.16, 34.96 and 33.82 electrons per Å<sup>2</sup>, respectively. The final datasets were composed of micrographs with defocus values ranging from -0.2 to -1.8  $\mu$ m.

## QUANTIFICATION AND STATISTICAL ANALYSIS

### Analysis of inverse toeprinting data

Unless indicated otherwise, data analysis was carried out using a series of custom python scripts. Read pairs were assembled using PEAR v0.9.10 (Zhang et al, 2014) on a computer with a 2.7 GHz Intel Core i7 processor and 16 GB 1,600 MHz DDR3 memory, with the maximal proportion of uncalled bases in a read set to 0 (`-u` option) and the upper bound for the resulting quality score set to 126 (`-c` option). The 5' flanking region was defined as GTATAAGGAGGAAAAAAT, whereas the 3' flanking region was GGTATCTCGGTGTGACTG. A maximum of two mismatches within each of these flanking regions was tolerated, whereas all other reads were discarded. Trimming of the retained reads resulted in sequences with a start codon directly at the 5' end and the site of RNase R cleavage at the 3' end (**Supplementary Data Figure 1**). Reads were required to have a minimum quality score of 30 at all positions and contain no Ns. The data underlying the volcano plots was analyzed using a custom python3 script to count the reads per motif, and DESeq2 to compute the statistics. The graphs were produced with matplotlib 3.3.2.

### Cryo-EM image processing

Data were processed in Relion v3.1 according to the scheme presented in **Supplementary Data Figure 3**. Briefly, the raw movie frames were summed and corrected for drift and beam-induced motion at the micrograph level using MotionCor2 v1.3.1 in Relion v3.1. The resolution range of each micrograph and the contrast transfer function (CTF) were estimated with Gctf v1.18. Best two-dimensional classes were selected by subsequent rounds of two-dimensional classifications of the particles obtained by automated picking in Relion v3.1. Three-dimensional classification was performed in Relion v3.1 in two steps: (1) unsupervised classification with particles downsized four times; (2) focused classification on all three tRNA sites for non-rotated 70S ribosomes (Pre-C), and on A-/E- tRNA sites for rotated 70S ribosomes (Pre-H) with background subtraction and particles downsized twice. Classes containing Pre-C and Pre-H ribosome conformations were further selected for 3D reconstruction and CTF refinement in Relion v3.1, followed by Bayesian polishing. The final reconstruction was sharpened by applying a negative sharpening B-factor of -10 in Relion v3.1. The resolution for the electron density map was estimated using the "gold standard" criterion (FSC=0.143). Local-resolution estimation was done using Relion v3.1 **Supplementary Data Figure 4**. Pixel size was optimized by generating maps with different pixel sizes and assessing the correlation in Chimera v1.14. The same processing was applied to the EF-G-MAAK-Cap complex but using Relion v4.0 instead of Relion v3.1 (**Supplementary Data Figure 5**).

### Atomic model building and refinement

An initial model of each complex was obtained by placing the coordinates for an *E. coli* 70S ribosome (PDB: 6TBV) or for EF-G (PDB: 4V7D) into the cryo-EM density map with Coot v0.8.9.2, and was refined using the rigid body refinement procedure in Phenix v1.17.1. Cap and Vio models were generated using Phenix eLBOW v1.19.2 and were manually fitted into the map using Coot v0.8.9.2. The nascent chain, mRNA and A-, P- and E-site tRNAs were de novo modeled into the corresponding density using Coot v0.8.9.2. Automatic map sharpening was performed in Phenix v1.17.1 and the final combined molecular model were then refined through multiple rounds of real space refinement procedure in Phenix v1.17.1 with restraints and manual rebuilding in Coot v0.8.9.2. The model was validated with MolProbity v4.5.1.

### Figure preparation

The inverse-toeprinting plots were produced with python3 and matplotlib 3.3.2. The sharpened map from Phenix v1.17.1 was used to prepare all figures for which a post-processed map from Relion v3.1 or Relion

v4.0 was used. Figures showing cryo-EM density or atomic models were prepared using Chimera v.1.14, ChimeraX v.0.91 or PyMOL v.1.7.4 (Schrödinger).



## REFERENCES

- Agris, P.F. (2004). Decoding the genome: a modified view. *Nucleic Acids Res.* **32**, 223–238.
- Agris, P.F. (2008). Bringing order to translation: the contributions of transfer RNA anticodon-domain modifications. *EMBO Rep.* **9**, 629–635.
- Akbergenov, R., Shcherbakov, D., Matt, T., Duscha, S., Meyer, M., Wilson, D.N., and Böttger, E.C. (2011). Molecular Basis for the Selectivity of Antituberculosis Compounds Capreomycin and Viomycin. *Antimicrob. Agents Chemother.* **55**, 4712–4717.
- Arenz, S., Bock, L.V., Graf, M., Innis, C.A., Beckmann, R., Grubmüller, H., Vaiana, A.C., and Wilson, D.N. (2016). A combined cryo-EM and molecular dynamics approach reveals the mechanism of ErmBL-mediated translation arrest. *Nat. Commun.* **7**.
- Belardinelli, R., Sharma, H., Caliskan, N., Cunha, C.E., Peske, F., Wintermeyer, W., and Rodnina, M.V. (2016a). Choreography of molecular movements during ribosome progression along mRNA. *Nat. Struct. Mol. Biol.* **23**, 342–348.
- Belardinelli, R., Sharma, H., Peske, F., Wintermeyer, W., and Rodnina, M.V. (2016b). Translocation as continuous movement through the ribosome. *RNA Biol.* **13**, 1197–1203.
- Belardinelli, R., Sharma, H., Peske, F., and Rodnina, M.V. (2021). Perturbation of ribosomal subunit dynamics by inhibitors of tRNA translocation. *RNA N. Y. N* **27**, 981–990.
- Boccaletto, P., Machnicka, M.A., Purta, E., Piątkowski, P., Bagiński, B., Wirecki, T.K., de Crécy-Lagard, V., Ross, R., Limbach, P.A., Kotter, A., et al. (2018). MODOMICS: a database of RNA modification pathways. 2017 update. *Nucleic Acids Res.* **46**, D303–D307.
- Brilot, A.F., Korostelev, A.A., Ermolenko, D.N., and Grigorieff, N. (2013). Structure of the ribosome with elongation factor G trapped in the pretranslocation state. *Proc. Natl. Acad. Sci. U. S. A.* **110**, 20994–20999.
- Carbone, C.E., Loveland, A.B., Gamper, H., Hou, Y.-M., Demo, G., and Korostelev, A.A. (2021). Time-resolved cryo-EM visualizes ribosomal translocation with EF-G and GTP.
- Cornish, P.V., Ermolenko, D.N., Noller, H.F., and Ha, T. (2008). Spontaneous Intersubunit Rotation in Single Ribosomes. *Mol. Cell* **30**, 578–588.
- Dijkstra, J.A., van der Laan, T., Akkerman, O.W., Bolhuis, M.S., de Lange, W.C.M., Kosterink, J.G.W., van der Werf, T.S., Alffenaar, J.W.C., and van Soolingen, D. (2018). In Vitro Susceptibility of *Mycobacterium tuberculosis* to Amikacin, Kanamycin, and Capreomycin. *Antimicrob. Agents Chemother.* **62**, e01724-17.
- Ermolenko, D.N., Majumdar, Z.K., Hickerson, R.P., Spiegel, P.C., Clegg, R.M., and Noller, H.F. (2007a). Observation of Intersubunit Movement of the Ribosome in Solution Using FRET. *J. Mol. Biol.* **370**, 530–540.
- Ermolenko, D.N., Spiegel, P.C., Majumdar, Z.K., Hickerson, R.P., Clegg, R.M., and Noller, H.F. (2007b). The antibiotic viomycin traps the ribosome in an intermediate state of translocation. *Nat. Struct. Mol. Biol.* **14**, 493–497.

- Fei, J., Kosuri, P., MacDougall, D.D., and Gonzalez, R.L. (2008). Coupling of ribosomal L1 stalk and tRNA dynamics during translation elongation. *Mol. Cell* 30, 348–359.
- Fei, J., Bronson, J.E., Hofman, J.M., Srinivas, R.L., Wiggins, C.H., and Gonzalez, R.L. (2009). Allosteric collaboration between elongation factor G and the ribosomal L1 stalk directs tRNA movements during translation. *Proc. Natl. Acad. Sci. U. S. A.* 106, 15702–15707.
- Feldman, M.B., Terry, D.S., Altman, R.B., and Blanchard, S.C. (2010). Aminoglycoside activity observed on single pre-translocation ribosome complexes. *Nat. Chem. Biol.* 6, 54–62.
- Guire, J.M.M. EARL B. HERR, JR. , ROBERT L. INHVAENMTIOLRSL. 10.
- Holm, M., Borg, A., Ehrenberg, M., and Sanyal, S. (2016). Molecular mechanism of viomycin inhibition of peptide elongation in bacteria. *Proc. Natl. Acad. Sci.* 113, 978–983.
- Holm, M., Mandava, C.S., Ehrenberg, M., and Sanyal, S. (2019). The mechanism of error induction by the antibiotic viomycin provides insight into the fidelity mechanism of translation. *ELife* 8, e46124.
- Johansen, S.K., Maus, C.E., Plikaytis, B.B., and Douthwaite, S. (2006). Capreomycin Binds across the Ribosomal Subunit Interface Using tlyA-Encoded 2'-O-Methylations in 16S and 23S rRNAs. *Mol. Cell* 23, 173–182.
- Kim, H.D., Puglisi, J.D., and Chu, S. (2007). Fluctuations of Transfer RNAs between Classical and Hybrid States. *Biophys. J.* 93, 3575–3582.
- Liou, Y.-F., and Tanaka, N. (1976). Dual actions of viomycin on the ribosomal functions. *Biochem. Biophys. Res. Commun.* 71, 477–483.
- Lorenz, C., Lünse, C.E., and Mörl, M. (2017). tRNA Modifications: Impact on Structure and Thermal Adaptation. *Biomolecules* 7.
- Marrero, P., Cabañas, M.J., and Modolell, J. (1980). Induction of translational errors (misreading) by tuberactinomycins and capreomycins. *Biochem. Biophys. Res. Commun.* 97, 1047–1042.
- Modolffl, J., and Vázquez, D. (1977). The Inhibition of Ribosomal Translocation by Viomycin. *Eur. J. Biochem.* 81, 491–497.
- Monshupanee, T., Johansen, S.K., Dahlberg, A.E., and Douthwaite, S. (2012). Capreomycin susceptibility is increased by TlyA-directed 2'-O-methylation on both ribosomal subunits. *Mol. Microbiol.* 85, 1194–1203.
- Motorin, Y., and Helm, M. (2010). tRNA Stabilization by Modified Nucleotides. *Biochemistry* 49, 4934–4944.
- Munro, J.B., Altman, R.B., Tung, C.-S., Sanbonmatsu, K.Y., and Blanchard, S.C. (2010). A fast dynamic mode of the EF-G-bound ribosome. *EMBO J.* 29, 770–781.
- Murphy, F.V., Ramakrishnan, V., Malkiewicz, A., and Agris, P.F. (2004). The role of modifications in codon discrimination by tRNA(Lys)UUU. *Nat. Struct. Mol. Biol.* 11, 1186–1191.

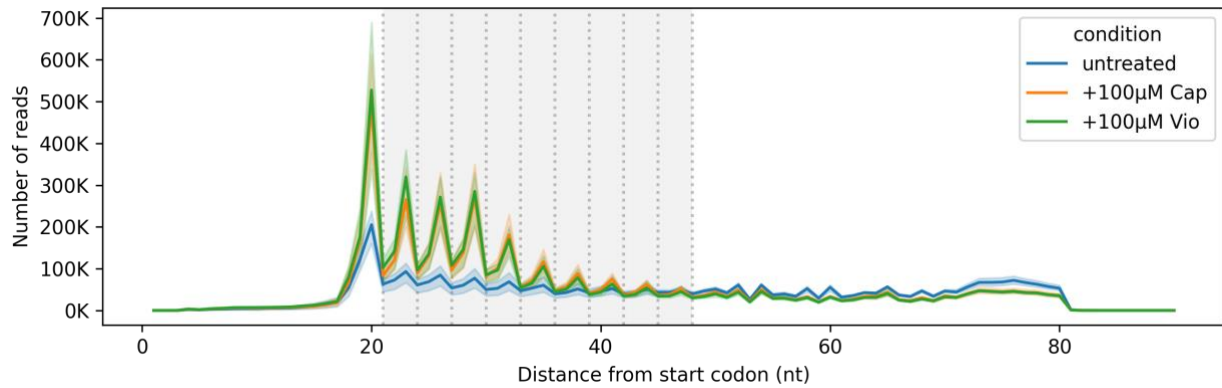
- Nagata, A., Ando, T., Izumi, R., Sakakibara, H., and Take, T. (1968). Studies on tuberactinomycin (tuberactin), a new antibiotic. I. Taxonomy of producing strain, isolation and characterization. *J. Antibiot. (Tokyo)* **21**, 681–687.
- Orelle, C., Carlson, S., Kaushal, B., Almutairi, M.M., Liu, H., Ochabowicz, A., Quan, S., Pham, V.C., Squires, C.L., Murphy, B.T., et al. (2013). Tools for Characterizing Bacterial Protein Synthesis Inhibitors. *Antimicrob. Agents Chemother.* **57**, 5994–6004.
- Peske, F., Savelsbergh, A., Katunin, V.I., Rodnina, M.V., and Wintermeyer, W. (2004). Conformational Changes of the Small Ribosomal Subunit During Elongation Factor G-dependent tRNA–mRNA Translocation. *J. Mol. Biol.* **343**, 1183–1194.
- Petrychenko, V., Peng, B.-Z., de A P Schwarzer, A.C., Peske, F., Rodnina, M.V., and Fischer, N. (2021). Structural mechanism of GTPase-powered ribosome-tRNA movement. *Nat. Commun.* **12**, 5933.
- Polikanov, Y.S., Aleksashin, N.A., Beckert, B., and Wilson, D.N. (2018). The Mechanisms of Action of Ribosome-Targeting Peptide Antibiotics. *Front. Mol. Biosci.* **5**, 48.
- Ranjan, N., and Rodnina, M.V. (2017). Thio-Modification of tRNA at the Wobble Position as Regulator of the Kinetics of Decoding and Translocation on the Ribosome. *J. Am. Chem. Soc.* **139**, 5857–5864.
- Rundlet, E.J., Holm, M., Schacherl, M., Natchiar, S.K., Altman, R.B., Spahn, C.M.T., Myasnikov, A.G., and Blanchard, S.C. (2021). Structural basis of early translocation events on the ribosome. *Nature* **1–5**.
- Seip, B., Sacheau, G., Dupuy, D., and Innis, C.A. (2018). Ribosomal stalling landscapes revealed by high-throughput inverse toeprinting of mRNA libraries. *Life Sci. Alliance* **1**.
- Stanley, R.E., Blaha, G., Grodzicki, R.L., Strickler, M.D., and Steitz, T.A. (2010). The structures of the anti-tuberculosis antibiotics viomycin and capreomycin bound to the 70S ribosome. *Nat. Struct. Mol. Biol.* **17**, 289–293.
- Sundaram, M., Durant, P.C., and Davis, D.R. (2000). Hypermodified Nucleosides in the Anticodon of tRNA<sup>Lys</sup> Stabilize a Canonical U-Turn Structure,. *Biochemistry* **39**, 12575–12584.
- Sutton, W.B., Gordee, R.S., Wick, W.E., and Stanfield, L. (1966). In Vitro and in Vivo Laboratory Studies on the Antituberculous Activity of Capreomycin. *Ann. N. Y. Acad. Sci.* **135**, 947–959.
- Thomas, M.G., Chan, Y.A., and Ozanick, S.G. (2003). Deciphering tuberactinomycin biosynthesis: isolation, sequencing, and annotation of the viomycin biosynthetic gene cluster. *Antimicrob. Agents Chemother.* **47**, 2823–2830.
- Trabuco, L.G., Schreiner, E., Eargle, J., Cornish, P., Ha, T., Luthey-Schulten, Z., and Schulten, K. (2010). The role of L1 stalk:tRNA interaction in the ribosome elongation cycle. *J. Mol. Biol.* **402**, 741–760.
- Vázquez-Laslop, N., and Mankin, A.S. (2018). Context-Specific Action of Ribosomal Antibiotics. *Annu. Rev. Microbiol.* **72**, 185–207.

Yang, K., Chang, J.-Y., Cui, Z., Li, X., Meng, R., Duan, L., Thongchol, J., Jakana, J., Huwe, C.M., Sacchettini, J.C., et al. (2017). Structural insights into species-specific features of the ribosome from the human pathogen *Mycobacterium tuberculosis*. *Nucleic Acids Res.* *45*, 10884–10894.

Zhang, L., Wang, Y.-H., Zhang, X., Lancaster, L., Zhou, J., and Noller, H.F. (2020). The structural basis for inhibition of ribosomal translocation by viomycin. *Proc. Natl. Acad. Sci.* *117*, 10271–10277.

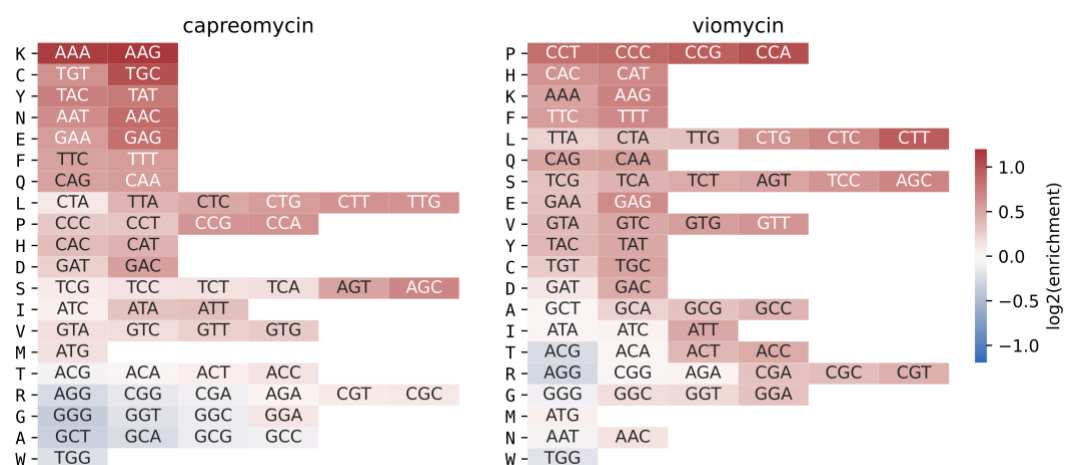
Zhang, X., Walker, R.C., Phizicky, E.M., and Mathews, D.H. (2014). Influence of Sequence and Covalent Modifications on Yeast tRNA Dynamics. *J. Chem. Theory Comput.* *10*, 3473–3483.

## SUPPLEMENTARY DATA



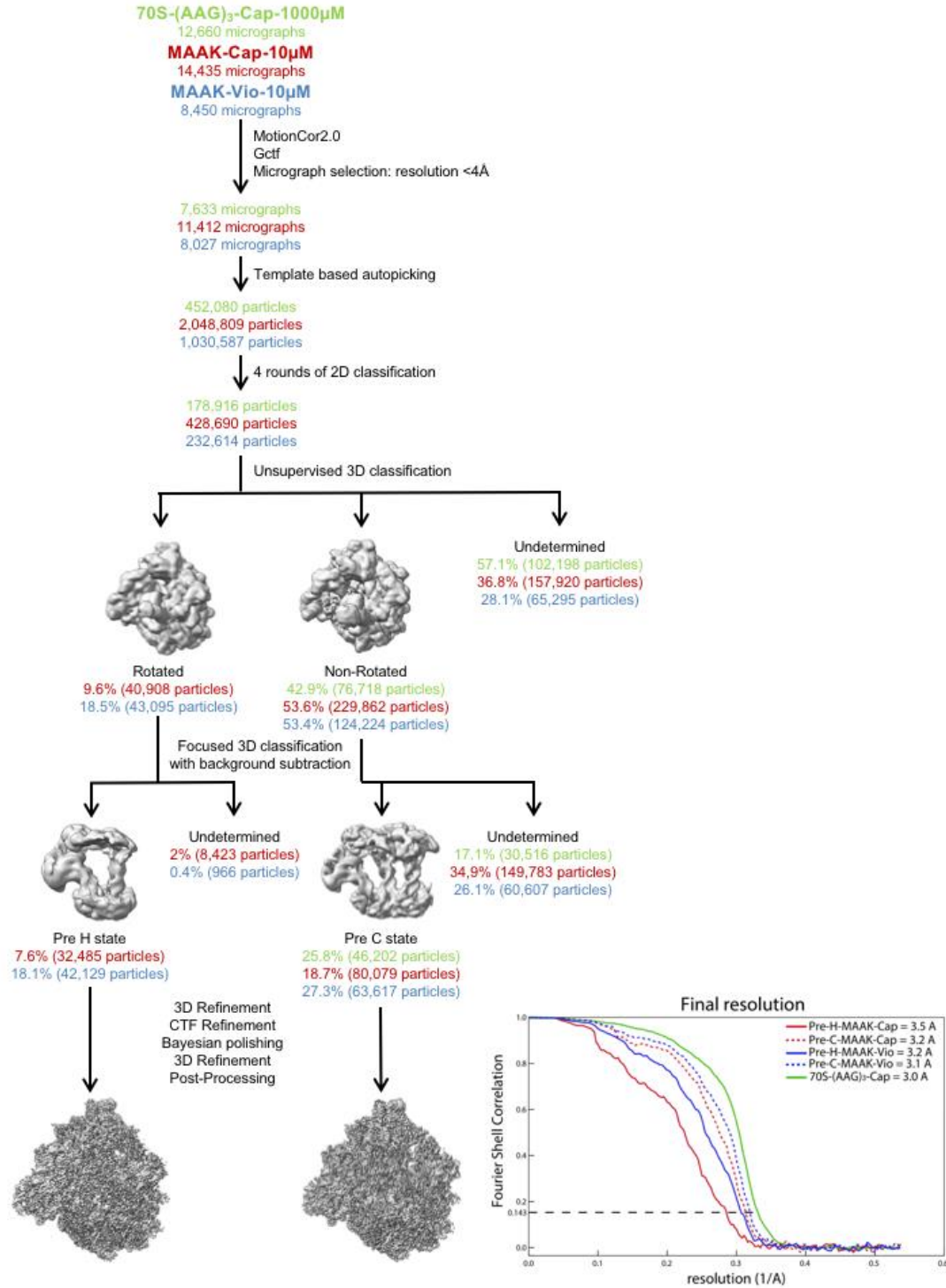
### Supplementary Figure 1: Inverse toeprints analysis.

Number of reads obtained in the NGS in function of the distance from the start codon for untreated and Cap- (orange line) or Vio- (green line) treated samples. The grey area highlights the reads that were selected for further analysis, as this corresponds to the region in which the codons are well defined (grey dotted lines). The error bands show the 95% confidence interval of the average of the 3 replicates.



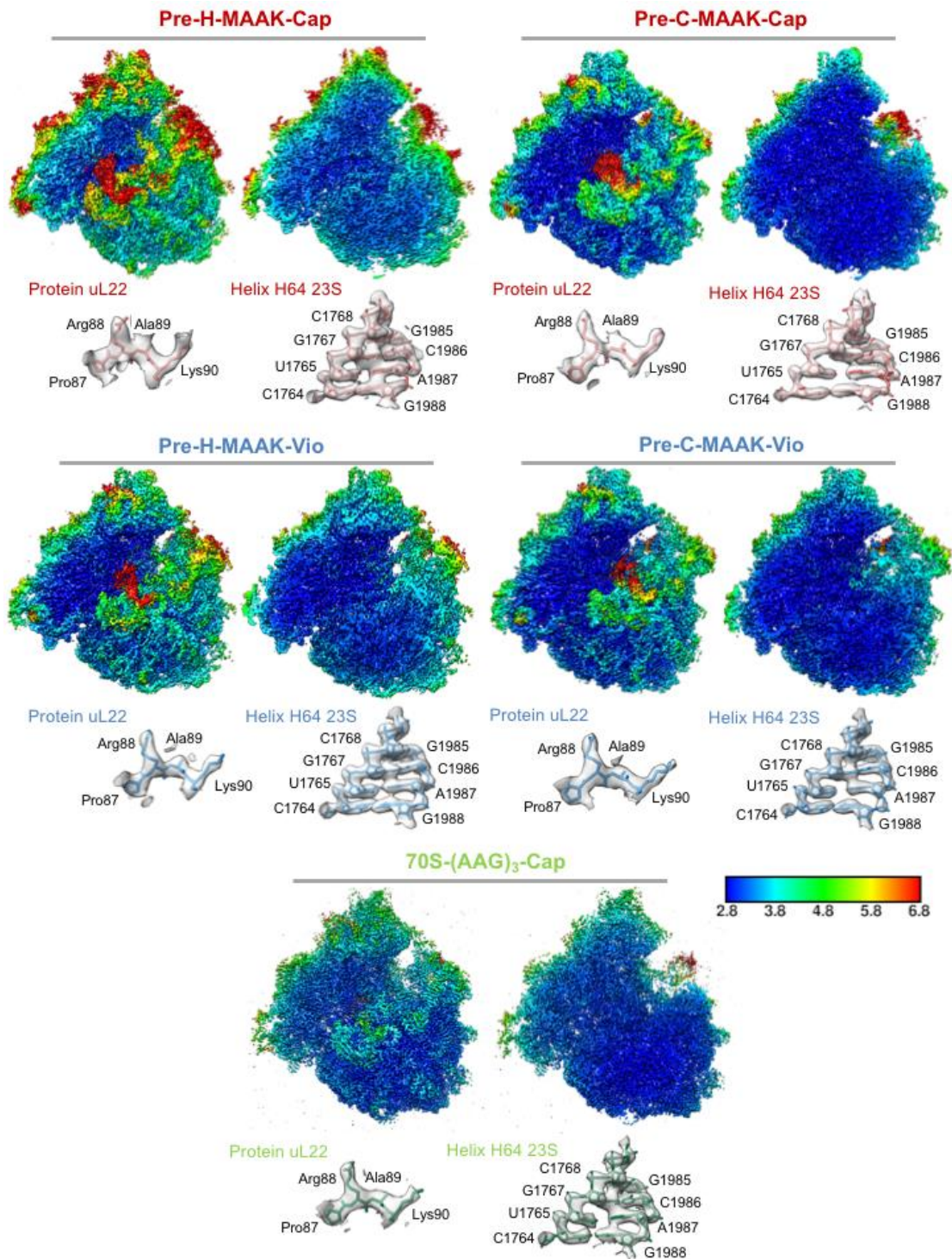
## Supplementary Figure 2: Enrichment at the codon level

Enrichment at the codon level for Cap and Vio relative to the untreated condition



**Supplementary Figure 3: Flowchart of cryo-EM data processing for the 70S-(AAG)<sub>3</sub>-Cap, MAAK-Cap and MAAK-Vio datasets.**

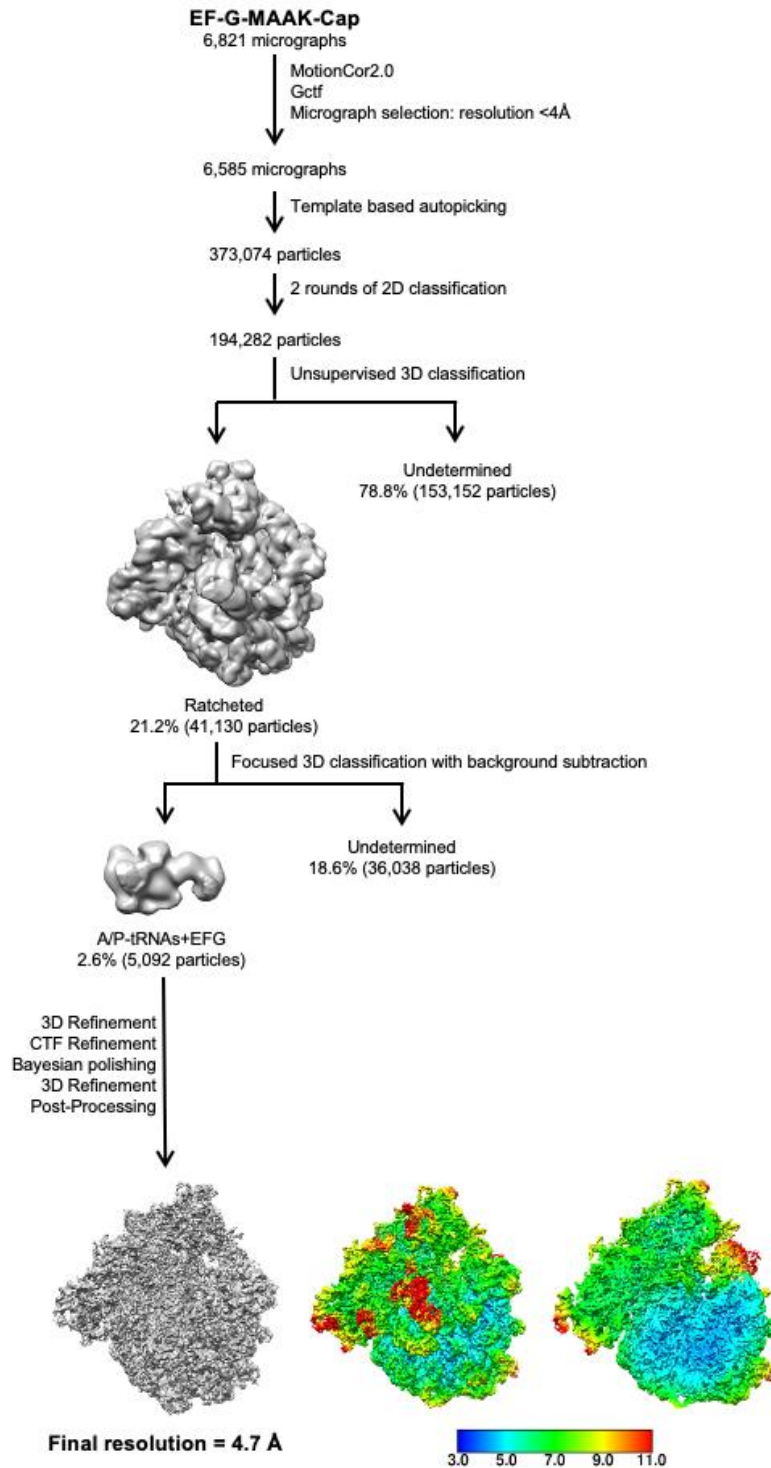
The flowchart shows the workflow used to process and analyze cryo-EM data using Relion 3.1. Steps for 70S-(AAG)<sub>3</sub>-Cap, MAAK-Cap and MAAK-Vio are shown in green, red and blue respectively. Fourier Shell Correlation (FSC) curves of the final reconstructions are shown as calculated by the Relion 3.1 post-processing algorithm.



**Supplementary Figure 4: Quality of the cryo-EM reconstructions.**

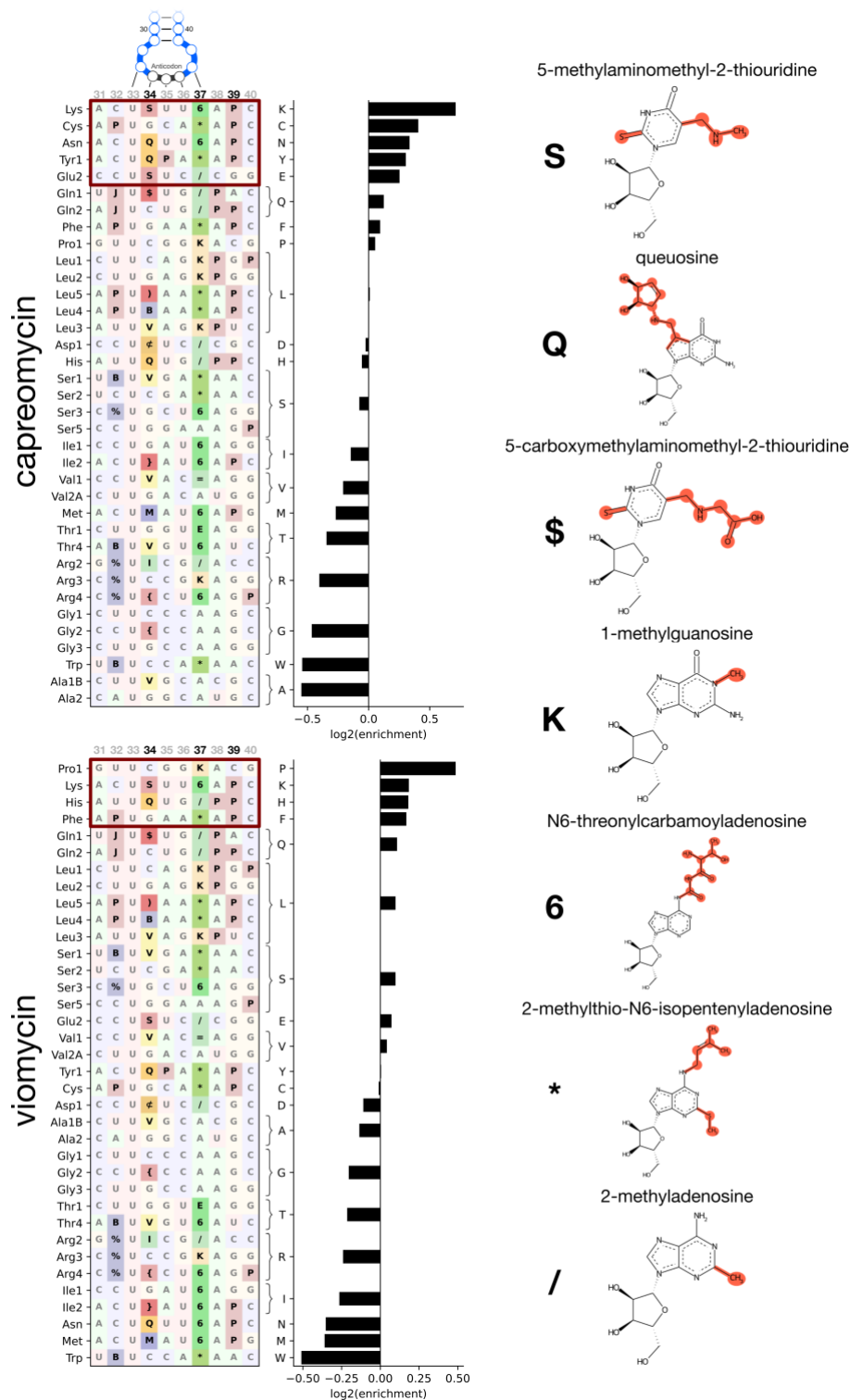
Refined cryo-EM density map obtained in Relion 3.1 filtered and colored by local resolution estimation values in Chimera for each complex. A cross-section of the same map is also shown, as a representative cryo-EM density for the tunnel extension of ribosomal protein uL22 and helix H64 of the 23S rRNA.





### Supplementary Figure 5: Quality of the cryo-EM reconstructions.

The flowchart shows the workflow used for the EF-G-MAAK-cap complex to process and analyze cryo-EM data using Relion 4.0. Refined cryo-EM density map obtained in Relion 4.0 filtered and colored by local resolution estimation values in Chimera for each complex. A cross-section of the same map is also shown.



**Supplementary Figure 6: tRNAs alignment based on the log2fold changes obtained in the inverse toeprinting datasets.**

Enrichment at the tRNA level in the A-site in the presence of either Cap or Vio, relative to the untreated condition. The red squares surround the most blocking tRNAs. Chemical structures of the modifications found in the most blocking tRNA sequences (Modomics database, (Boccalletto et al., 2018)).

**Supplementary Table: Reagents and oligonucleotides**

REAGENT or RESOURCE	SOURCE	IDENTIFIER
Chemicals, Peptides, and Recombinant Proteins		
Acrylamide/Bis-Acrylamide 37.5:1, 40%	Biosolve	Cat#014223
Ammonium persulfate	Sigma-Aldrich	Cat#A3678-25G
Bromophenol blue	Fisher Scientific	Cat#1010223280
Boric acid	Sigma-Aldrich	Cat#B7901-500G
Deoxynucleotide (dNTP) Solution Mix 10mM	New England Biolabs	Cat#N0447S
Diethyl Pyrocarbonate for DEPC water	Sigma-Aldrich	Cat#D5758-100ML
Merck™ Ultrapure Water for Molecular Biology	FisherScientific	Cat#15161735
Adenosine 5'-triphosphate disodium salt hydrate	Sigma-Aldrich	Cat#A2383-25G
CTP	Jena Bioscience	Cat#NU-1011-1G
GTP	Jena Bioscience	Cat#NU-1012-1G
UTP	Jena Bioscience	Cat#NU-1013-1G
Guanosine-5'-thiophosphatedisodium salt	Genaxxon Bioscience	Cat#S5402.0025
SYBR Gold nucleic acid gel stain	Invitrogen	Cat#S11494
Trizma Base	Sigma-Aldrich	Cat#T1503-1KG
Acetic acid	Sigma-Aldrich	Cat#33209-1L
Trisodium citrate dihydrate	Sigma-Aldrich	Cat#S1804-500G
Ethanol	Sigma-Aldrich	Cat#32221-2.5L-M
N,N,N',N'-Tetramethylethylenediamine	Euromedex	Cat#50406-A
Urea	Sigma-Aldrich	Cat#U5378-1KG
Magnesium chloride hexahydrate	Sigma-Aldrich	Cat#M2670-1KG
Magnesium acetate tetrahydrate	Sigma-Aldrich	Cat#M5661-250G
Potassium glutamate	Sigma-Aldrich	Cat#49601-100G
Spermidine	Sigma-Aldrich	Cat#S2626-5G
NH <sub>4</sub> -acetate	Sigma-Aldrich	Cat#A1542-500G
Biotin (Long Arm) maleimide	Vectorlabs	Cat#SP-1501
Bis-Tris	Sigma-Aldrich	Cat#B7535-500G
N,N-Dimethylformamide	Sigma-Aldrich	Cat#D4551-250ML
Sodium chloride	VWR	Cat#27788.366
Tween 20	Sigma-Aldrich	Cat#P1379-100ML
Cap	Sigma-Aldrich	Cat#C4142-1G
Vio	TOCRIS (a biotechne brand)	Cat#3787
Dynabeads M-280 Streptavidin	ThermoFisher Scientific	Cat#11205D
HEPES	Sigma-Aldrich	Cat#H4034-1KG

Potassium hydroxide	Sigma-Aldrich	Cat#P1767-250G
Hydrochloric acid	Sigma-Aldrich	Cat#30721-2.5L-M
Phusion polymerase	Recombinant	
Phusion HF buffer Pack 5X	New England Biolabs	Cat#B0518S
<i>E. coli</i> Poly(A) Polymerase supplied with 10X Poly(A) Polymerase buffer	New England Biolabs	Cat#M0276L
T7 RNA polymerase (P266L)	Recombinant	
Ribonuclease R	Recombinant, kind gift from Dr. Arun Malhotra (University of Miami)	
T4 RNA ligase 2, truncated supplied with 10X T4 RNA ligase reaction buffer and 50 % PEG8000	New England Biolabs	Cat#M0242L
SuperScript™ III Reverse Transcriptase supplied with a vial (1 mL) of 5X first-strand buffer and a vial (500 µL) of 100 mM DTT	ThermoFisher	Cat#18080044
EcoRV-HF	New England Biolabs	Cat#R3195S
Agilent High Sensitivity DNA Kit	Agilent	Cat#5067-4626
Powdered milk	Régilait	N/A
Streptavidin-Alkaline Phosphatase	Promega	Cat#V5591
NBT/BCIP detection kit	Promega	Cat#S3771
Xylene Cyanol	Biosolve	Cat#242223
DNA Ladder: Low Molecular Weight DNA Ladder	New England Biolabs	Cat#N3233S
RNA Ladder: Century-Plus RNA Marker	ThermoFisher Scientific	Cat#AM7145
MinElute PCR Purification Kit™	Qiagen	Cat#28006
RNA Clean & Concentrator™-5	Zymo research	Cat#R1015
Isopropanol	Sigma-Aldrich	Cat#I9516-4L
GlycoBlue coprecipitant	ThermoFisher Scientific	Cat#AM9515
MiliporeSigma™ Ultrapure water for Molecular Biology	Fisher Scientific	Cat#09-739-006
Avian Myeloblastosis Virus Reverse Transcriptase	Promega	Cat#M5101
Sodium Hydroxide	Sigma-Aldrich	Cat#221465

QIAquick Nucleotide removal Kit <sup>TM</sup>	Qiagen	Cat#28304
Dideoxy-nucleotides	GE Healthcare Life Sciences	Cat#27-2045-01
Thermo Sequenase Dye Primer Manual Cycle Sequencing Kit	ThermoFisher Scientific	Cat#792601KT
ExoSAP-IT reagent	ThermoFisher Scientific	Cat#PN78200
d-luciferin (Luciferase substrate Steady-Glo)	Promega	Cat#2510
Critical Commercial Assays		
PURExpress Δ RF123 Δ Ribosomes Kit	New England Biolabs	Cat#E6850ZZ
Oligonucleotides		
iTP/TP_frag1_T7_RBS_ATG_f CGA-TCG-AAT-TCT-AAT-ACG-ACT- CAC-TAT-AGG-GCT-TAA-GTA- TAA-GGA-GGA-AAA-AAT-ATG	Seip et al., 2018	Eurogentec custom synthesis
Stop_EcoRV_r TAT-ATG-GAT-CCT-TTT-TGA-TAT- TGA-TAT-CTC-ATC-ACA-CCG-AGA- TCG	Seip et al., 2018	Eurogentec custom synthesis
iTP/TP_frag1_T7_f CGA-TCG-AAT-TCT-AAT-ACG-ACT- CAC-TAT-AG	Seip et al., 2018	Eurogentec custom synthesis
iTP_EcoRV_r TAT-ATG-GAT-CCT-TTT-TGA-TAT- TGA-TA	Seip et al., 2018	Eurogentec custom synthesis
iTP_NNN15_random-library GGA-GGA-AAA-AAT-ATG-NNN- NNN-NNN-NNN-NNN-NNN-NNN- NNN-NNN-NNN-NNN-NNN-NNN- NNN-NNN- GCG-ATC-TCG-GTG- TGA	This work	Eurogentec custom synthesis
iTP_3'_linker_Apol /5rAPP/GGT-ATC-TCG-GTG-TGA- CTG-ACT-GAA-AAT-TTC-TGT-AGG- CAC-CAT-CAA-T/ddC	Seip et al., 2018	Eurogentec custom synthesis
iTP_Linker_r ATT-GAT-GGT-GCC-TAC-AG	Seip et al., 2018	IDT custom synthesis
iTP_cDNA_f GTA-TAA-GGA-GGA-AAA-AAT- ATG	Seip et al., 2018	Eurogentec custom synthesis
iTP_Biotin_standard /5Biosg/AAA-AAA-AAA-AAA-AAT- TAA-CTC-CAT-CTA-A	Seip et al., 2018	Eurogentec custom synthesis

iTP_NGS_f AAT-GAT-ACG-GCG-ACC-ACC-G	Seip et al., 2018	Eurogentec custom synthesis
iTP_NGS_r CAA-GCA-GAA-GAC-GGC-ATA- CGA-G	Seip et al., 2018	Eurogentec custom synthesis
iTP_NGS_adapter_f AAT-GAT-ACG-GCG-ACC-ACC- GAG-ATC-TAC-ACT-CTT-TCC-CTA- CAC-GAC-GCT-CTT-CCG-ATC-TGT- ATA-AGG-AGG-AAA-AAA-TAT-G	Seip et al., 2018	Eurogentec custom synthesis
iTP_NGS_adapter_index1 CAA-GCA-GAA-GAC-GGC-ATA- CGA-GAT-CGT-GAT-GTG-ACT- GGA-GTT-CAG-ACG-TGT-GCT- CTT-CCG-ATC-GAT-TGA-TGG-TGC- CTA-CAG	This work	Eurogentec custom synthesis
iTP_NGS_adapter_index2 CAA-GCA-GAA-GAC-GGC-ATA- CGA-GAT-ACA-TCG-GTG-ACT- GGA-GTT-CAG-ACG-TGT-GCT- CTT-CCG-ATC-GAT-TGA-TGG-TGC- CTA-CAG	This work	Eurogentec custom synthesis
iTP_NGS_adapter_index3 CAA-GCA-GAA-GAC-GGC-ATA- CGA-GAT-GCC-TAA-GTG-ACT- GGA-GTT-CAG-ACG-TGT-GCT- CTT-CCG-ATC-GAT-TGA-TGG-TGC- CTA-CAG	This work	Eurogentec custom synthesis
iTP_NGS_adapter_index4 CAA-GCA-GAA-GAC-GGC-ATA- CGA-GAT-TGG-TCA-GTG-ACT- GGA-GTT-CAG-ACG-TGT-GCT- CTT-CCG-ATC-GAT-TGA-TGG-TGC- CTA-CAG	This work	Eurogentec custom synthesis
iTP_NGS_adapter_index5 CAA-GCA-GAA-GAC-GGC-ATA- CGA-GAT-CAC-TGT-GTG-ACT- GGA-GTT-CAG-ACG-TGT-GCT- CTT-CCG-ATC-GAT-TGA-TGG-TGC- CTA-CAG	This work	Eurogentec custom synthesis
iTP_NGS_adapter_index6 CAA-GCA-GAA-GAC-GGC-ATA- CGA-GAT-ATT-GGC-GTG-ACT- GGA-GTT-CAG-ACG-TGT-GCT- CTT-CCG-ATC-GAT-TGA-TGG-TGC- CTA-CAG	This work	Eurogentec custom synthesis

iTP_NGS_adapter_index7 CAA-GCA-GAA-GAC-GGC-ATA- CGA-GAT-GAT-CTG-GTG-ACT- GGA-GTT-CAG-ACG-TGT-GCT- CTT-CCG-ATC-GAT-TGA-TGG-TGC- CTA-CAG	This work	Eurogentec custom synthesis
iTP_NGS_adapter_index8 CAA-GCA-GAA-GAC-GGC-ATA- CGA-GAT-TCA-AGT-GTG-ACT- GGA-GTT-CAG-ACG-TGT-GCT- CTT-CCG-ATC-GAT-TGA-TGG-TGC- CTA-CAG	This work	Eurogentec custom synthesis
iTP_NGS_adapter_index9 CAA-GCA-GAA-GAC-GGC-ATA- CGA-GAT-CTG-ATC-GTG-ACT- GGA-GTT-CAG-ACG-TGT-GCT- CTT-CCG-ATC-GAT-TGA-TGG-TGC- CTA-CAG	This work	Eurogentec custom synthesis
TP_frag2_r CTT-GCC-TGC-GCA-CGA-AGA- GTA-CGG-ATG-TTG-TTC-AGA- GTC-AGT-TAT-TAT-TCG-CT	This work	Eurogentec custom synthesis
TP_frag2_NV1_r GGT-TAT-AAT-GAA-TTT-TGC-TTA- TTA-ACC-TTG-CCT-GCG-CAC-G	This work	Eurogentec custom synthesis
TP_short_r GGT-TAT-AAT-GAA-TTT-TGC-TT	This work	Eurogentec custom synthesis
TP_RT_yakima-yellow_r /5YakYel/GGT-TAT-AAT-GAA-TTT- TGC-TTA-TTA-AC	This work	Eurogentec custom synthesis
TP_polyAAG_fwd CGA-TCG-AAT-TCT-AAT-ACG-ACT- CAC-TAT-AGG-GCT-TAA-GTA- TAA-GGA-GGA-AAA-AAT-ATG- AAG-AAG-AAG-AAG-AAG-TAG- AGC-GAA-TAA-TAA-CTG-ACT- CTG-AAC-AAC-ATC-CGT-ACT-CTT- CGT-GCG-CAG-GCA-AGG-TTA- ATA-AGC-AAA-ATT-CAT-TAT-AAC- C	This work	IDT G-blocks custom synthesis
TP_cap_MA*_fwd GTA-TAA-GGA-GGA-AAA-AAT- ATG-GCA-TGA-AGC-GAA-TAA- TAA-CTG-ACT-CTG	This work	Eurogentec custom synthesis
TP_cap_MK*_fwd GTA-TAA-GGA-GGA-AAA-AAT- ATG-AAG-TGA-AGC-GAA-TAA- TAA-CTG-ACT-CTG	This work	Eurogentec custom synthesis

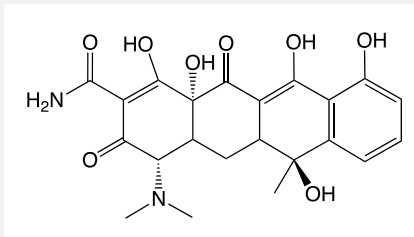
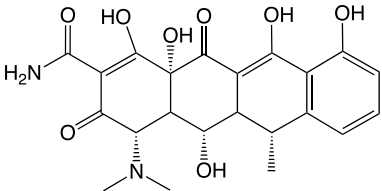
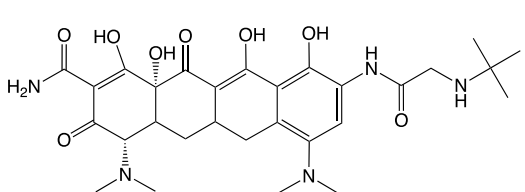
TP_cap_MAK*_fwd GTA-TAA-GGA-GGA-AAA-AAT- ATG-GCA-AAG-TGA-AGC-GAA- TAA-TAA-CTG-ACT-CTG	This work	Eurogentec custom synthesis
TP_cap_MAAK*_fwd GTA-TAA-GGA-GGA-AAA-AAT- ATG-GCA-GCA-AAG-TGA-AGC- GAA-TAA-TAA-CTG-ACT-CTG	This work	Eurogentec custom synthesis
TP_cap_MAAAK*_fwd GTA-TAA-GGA-GGA-AAA-AAT- ATG-GCA-GCA-GCA-AAG-TGA- AGC-GAA-TAA-TAA-CTG-ACT-CTG	This work	Eurogentec custom synthesis
Software and Algorithms		
Image Lab	Bio-RAD	<a href="https://www.bio-rad.com/webroot/web/pdf/lsr/literature/10000076953.pdf">https://www.bio-rad.com/webroot/web/pdf/lsr/literature/10000076953.pdf</a>
python 3.8		<a href="https://www.python.org/">https://www.python.org/</a>
numpy 1.19.2		<a href="https://numpy.org/">https://numpy.org/</a>
pandas 1.1		<a href="https://pandas.pydata.org/">https://pandas.pydata.org/</a>
matplotlib 3.3.2		<a href="https://matplotlib.org/">https://matplotlib.org/</a>
seaborn 0.11		<a href="https://seaborn.pydata.org/">https://seaborn.pydata.org/</a>
scipy 1.5		<a href="https://www.scipy.org/">https://www.scipy.org/</a>



### 4.2.3. The aromatic polyketide tetracenomycin X

Polyketides are a large group of secondary metabolites present in the three kingdoms of life, meaning that the absence of such metabolites does not directly lead to immediate death but can limit the survival, fertility or appearance of the host organism (Huang et al., 2018; Katz and Baltz, 2016; Wang et al., 2020; Zhang et al., 2017). Among this large and diverse group of metabolites, aromatic polyketides form a large number of subfamilies that are used as antimicrobials or as antitumor agents (Katz and Baltz, 2016).

A well-characterized group of aromatic polyketides displaying antibiotic activity are the tetracyclines (Wilson, 2014). Tetracyclines are natural antibiotics which target the bacterial ribosome and inhibit translation. They have been clinically used since the 1940s and are broad-spectrum antibiotics. The best-known molecule belonging to this family is the antibiotic tetracycline, which binds near the decoding center on the 30S ribosomal subunit (Brodersen et al., 2000), at a position that prevents the accommodation of the anticodon stem-loop of incoming aminoacyl-tRNAs into the A site (Brodersen et al., 2000; Olson et al., 2006). However, several other binding sites located on the 30S subunit were identified (Pioletti et al., 2001). In addition to blocking aminoacyl-tRNA delivery to the A site, tetracyclines were also shown to inhibit the initiation step of translation (Barrenechea et al., 2021). The widespread use of tetracyclines across the world has favored the spread of tetracycline-resistant pathogenic bacteria, making it necessary to develop second- and third- generation tetracycline derivatives (Jenner et al., 2013; Olson et al., 2006; Wilson, 2014). Among these, doxycycline is largely used in human medicine and is a second-generation derivative. The third and last generation of tetracyclines are the glycylcyclines, such as tigecycline, which display a higher affinity for the 30S subunit and have enhanced antibacterial activity compared to first- and second-generation tetracyclines, including against resistant strains (Grossman, 2016; Jenner et al., 2013; Olson et al., 2006). Recent crystal structures of tetracycline–70S and tigecycline–70S complexes at 3.1–3.3 Å revealed that both drugs bind to the 70S exclusively at the primary binding site previously detected on the 30S subunit (Jenner et al., 2013). Tetracycline, doxycycline and tigecycline represent the three generations of tetracyclines I cited above and are classified as critically important for human medicine by the World Health Organization (<https://www.who.int/>) (Table 4).

Generation	Examples	Clinical use
<b>FIRST</b>	<b>Tetracycline</b> 	Broad-spectrum Acne, cholera, brucellosis, plague, and syphilis
<b>SECOND</b>	<b>Doxycycline</b> 	Broad-spectrum Bacterial pneumonia, acne, chlamydia infections, Lyme disease, cholera, typhus, and syphilis
<b>THIRD</b>	<b>Tigecycline</b> 	Broad-spectrum including Antibiotic resistant bacteria such as <i>Staphylococcus aureus</i> , <i>Acinetobacter baumannii</i> , and <i>E. coli</i>

**Table 4 : Three generations of tetracycline antibiotics, their structure and clinical use**

Aromatic polyketides also comprise a substantial number of anticancer agents, such as the anthracyclines (Katz and Baltz, 2016). Anthracyclines were isolated from *Streptomyces* strains and are widely used to treat many cancers, including leukemias, lymphomas, breast, stomach, uterine, ovarian and lung cancers. The most important molecules in terms of clinical use are doxorubicin, daunorubicin (the first anthracycline discovered), epirubicin and idarubicin. The well-characterized doxorubicin drug was originally isolated from the bacterium *Streptomyces peucetius* and was approved for medical use in the United States in the 1980s. Doxorubicin intercalates with DNA and thereby inhibits DNA replication and RNA transcription by interfering with topoisomerase II function (Agudelo et al., 2014, 2014, 2016). Cytotoxicity is primarily due to the ability of the drug to intercalate between two DNA base pairs through the planar aromatic chromophore portion of the molecule, while the sugar sits within the minor groove of the DNA and interacts with adjacent base pairs (Tacar et al., 2013). The binding of the drug then leads to the stabilization of the topoisomerase II complex after it has broken the DNA chain for replication, preventing the DNA double helix from being resealed and leading to cell death.

A less characterized subfamily of aromatic polyketides are the tetracenomycins, which display very high chemical structure similarities with tetracycline or doxorubicin. Tetracenomycin C was the first member of this subfamily to be discovered. It was originally isolated from the soil-dwelling bacterium *Streptomyces glaucescens* and was shown to display broad antimicrobial activity against actinomycetes and streptomycetes (Weber et al., 1979). Despite its activity as antimicrobial, its chemical structure is highly similar to that of the anthracyclines, as it is composed of four aromatic rings fused together and bound to a sugar moiety (Anderson et al., 1989; Egert et al., 1992; Lazar et al., 1981). This similarity might explain its previously reported antitumor activity against leukemia cells in mice (Weber et al., 1979). More recent chemical screening resulted in the discovery of another anthracycline-like antibiotic closely related to tetracenomycin C called elloramycin (Rohr and Zeeck, 1990). Elloramycin is produced by *Streptomyces olivaceus* and features an additional l-rhamnose attached to the tetracyclic chromophore through a phenolic alpha-glycosidic linkage (Anderson et al., 1989; Drautz et al., 1985) (

**Figure 28**). It is active against a variety of Gram-positive bacteria, especially streptomycetes (Drautz et al., 1985). The antibacterial activity of both compounds is comparable, but elloramycin displays a weaker antitumor activity compared to tetracenomycin C (Drautz et al., 1985; Rohr and Zeeck, 1990). However, while these compounds were discovered and characterized a few decades ago, only little is known regarding their precise mode of action, which is only assumed to be analogous to that of the anthracycline doxorubicin on the basis that the tetracyclic chromophore of tetracenomycins is flat and therefore optimal for intercalating between two DNA base pairs. This is not the case with the tetracyclic chromophore of tetracyclines (Agudelo et al., 2014; Egert et al., 1992; Rohr and Zeeck, 1990; Wilson, 2014). The characterization and optimization of tetracenomycins may lead to the development of potential new antimicrobial or anticancer agents (Adinarayana et al., 2006).

A recent study focused on the characterization of another member of this subfamily called tetracenomycin X (TcmX) (Osterman et al., 2020). TcmX is the 12a-O-methyl ester of tetracenomycin C (

**Figure 28**), and is produced by *Nocardia mediterranei*. TcmX was recently identified by PCR-based gene sequence analysis from the marine-derived actinomycete *Saccharothrix sp* (Liu et al., 2014). Two high-resolution cryo-EM structures were obtained of tetracenomycin X bound to the prokaryotic 70S ribosome and to the eukaryotic 80S ribosome (Osterman et al., 2020). The tetracyclic chromophore of tetracenomycin X binds in both structures to the nascent

polypeptide exit tunnel and, similarly to tetracycline, inhibits protein synthesis in bacteria and human lysates, but does not trigger the SOS response due to DNA damage and does not inhibit thymine incorporation in living cells, as it is the case for the anthracycline doxorubicin (Osterman et al., 2020). The binding site of tetracenomycin X is located on the opposite surface of the ribosomal tunnel compared to that of the macrolides (Osterman et al., 2020; Vázquez-Laslop and Mankin, 2018a). Interestingly, no cross-resistance to tetracenomycin X by A2058G could be observed (Osterman et al., 2020), which is of high interest since mutation or methylation of A2058 is one of the main determinants for clinical resistance to macrolides, lincosamides and streptogramin B (MLSB) antibiotics (Leclercq, 2002). Finally, from toeprinting experiments using an mRNA template coding for the macrolide-dependent arrest peptide ErmBL (Arenz et al., 2014b, 2016; Vázquez-Laslop and Mankin, 2018a), tetracenomycin X appears to stall translation in a nascent peptide-dependent manner but the sequence-specificity of stalling for tetracenomycin X seems to be distinct from that observed for macrolide antibiotics (Osterman et al., 2020). Collectively, the binding mode, mechanism of action X and lack of cross-resistance of tetracenomycin with other antibiotics, make tetracenomycin X an attractive compound for the development of new antimicrobial agents.

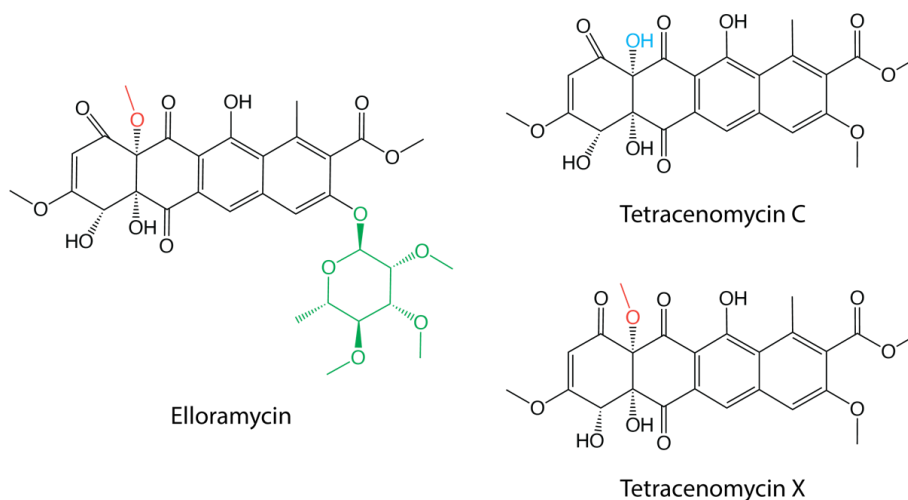


**Figure 28 : Chemical structures of Elloramycin, Tetracenomycin C and Tetracenomycin X.**  
The chemical groups differing between the three drugs are colored in dark orange, cyan and green.

To study the context-dependent mode of action of tetracenomycin X, I decided to perform inverse toeprinting on an *in vitro* translation reaction carried out in the presence of tetracenomycin X, using the “NNN15” library (**Figure 26**). I could observe that tetracenomycin X could inhibit translation only in presence of a small subset of specific peptides. Using a similar combination of biochemical and structural approaches as done for the work on

tuberactinomycins (section 0), I could describe a previously unseen mode of inhibition of the PTC induced by tetracenomycin X, which is presented in the following manuscript.

# The mechanism of context-dependent translation inhibition by the polyketide antibiotic Tetracenomycin X

Elodie C. Leroy<sup>1,4</sup>, Thomas N. Perry<sup>1,4</sup>, Ilya A. Osterman<sup>2,3</sup>, Thibaud T. Renault<sup>1</sup> & C. Axel Innis<sup>1\*</sup>

<sup>1</sup> Univ. Bordeaux, Centre National de la Recherche Scientifique, Institut National de la Santé et de la Recherche Médicale, ARNA, UMR 5320, U1212, Institut Européen de Chimie et Biologie, F-33600 Pessac, France.

<sup>2</sup> Center of Life Sciences, Skolkovo Institute of Science and Technology, Skolkovo, Russia.

<sup>3</sup> Department of Chemistry, Faculty of Bioengineering and Bioinformatics and Belozersky Institute of Physico-Chemical Biology, Lomonosov Moscow State University, Moscow, Russia.

<sup>4</sup> Equal contribution

\* To whom correspondence should be addressed: axel.innis@inserm.fr; thibaud.renault@u-bordeaux.fr

## ABSTRACT

**For the last few decades, the number of multidrug resistant pathogens has increased steadily whereas the number of new antibiotics entering the market has decreased dramatically, highlighting the urgent need to discover new antimicrobials. Here we report that the recently discovered antibiotic tetracenomycin X (TcmX) allows translation of most oligopeptides and, similarly to macrolide antibiotics, only inhibits translation of specific nascent peptides containing blocking motifs. TcmX binds within the nascent polypeptide exit tunnel of the ribosome, adjacent to the binding site of macrolide antibiotics like erythromycin. Despite the mechanistic similarities with macrolides, we show that TcmX inhibits peptide bond formation in the PTC through a novel context-dependent mechanism, whereby nascent peptides containing a Gln-Lys (QK) motif are retained within the exit tunnel and trapping the 3' adenosine of the P-site lysyl-tRNA towards the tunnel-bound drug. Our study provides mechanistic insights into the mode of action of TcmX on the prokaryotic ribosome, paving the way for the development of novel antimicrobial molecules based on a common aromatic polyketide scaffold.**

## INTRODUCTION

New antimicrobial resistance mechanisms are emerging and spreading worldwide, rendering our current arsenal of clinically used antibiotics obsolete and threatening our ability to treat common infectious diseases. Therefore, there is an urgent need for new lead compounds with distinct target binding sites to prevent cross-resistance. Polyketides are a large group of secondary metabolites present in all three kingdoms of life (Huang et al., 2018; Katz and Baltz, 2016; Wang et al., 2020; Zhang et al., 2017). Among these, aromatic polyketides feature a large number of subfamilies used as antimicrobials or antitumor agents (Katz and Baltz, 2016), such as tetracycline or doxorubicin, respectively, or the lesser known, structurally related, tetracenomycins (Zhang et al., 2017). Therefore, characterization and

optimization of tetracenomycins may facilitate the development of new antimicrobial or anticancer agents (Adinarayana et al., 2006).

Recently, Tetracenomycin X (TcmX) (**Figure 1A**) was shown to exert moderate antimicrobial activity against drug-resistant pathogens, including methicillin-resistant *Staphylococcus aureus* and vancomycin-resistant *Enterococci* (Liu et al., 2014), and some degree of cytotoxic activity against human cell lines (Liu et al., 2014; Osterman et al., 2020; Qiao et al., 2019). Unlike the anthracycline doxorubicin, with whom it shares a planar tetracyclic core, TcmX does not trigger the SOS response and does not inhibit DNA synthesis in living cells (Osterman et al., 2020). Like tetracycline, however, (Jenner et al., 2013), TcmX inhibits protein synthesis in bacteria and in human lysates (Osterman et al., 2020), suggesting that the ribosome and protein synthesis are the physiological targets for this drug. Accordingly, point mutations of U2586, U2609 and U1782 of the *E. coli* 23S ribosomal RNA (rRNA) located within the exit tunnel of the ribosome confer resistance to TcmX. Similarly, cytoplasmic protein synthesis, rather than intercalation with DNA, was the reported cause of cytotoxicity of tetracenomycins against HEK293T cells and other human cell lines (Osterman et al., 2020). High-resolution cryogenic electron microscopy (cryo-EM) structures of TcmX bound to the prokaryotic 70S and eukaryotic 80S ribosomes show that the tetracyclic chromophore of TcmX stacks onto the non-canonical base pair formed between residues U2586 and U1782 of the 23S rRNA (*E. coli* numbering), within the nascent polypeptide exit tunnel of the ribosome (Osterman et al., 2020). Together, the binding mode and mechanism of action of TcmX, as well as its cytotoxic activity against various cell lines, make TcmX an attractive compound for the development of new therapeutic molecules.

It was previously suggested that the mode of action of TcmX could be similar to that of macrolide antibiotics (*e.g.*, erythromycin or telithromycin) and would arise from ribosome stalling resulting from the translation of problematic nascent amino acid motifs (Arenz et al., 2014a, 2016; Beckert et al., 2021). Indeed, ribosomes translating the *ermBL* (Arenz et al., 2014b) or *trpL* leader sequences in the presence of TcmX undergo sequence-dependent stalling on Leu-Lys (LK) motifs, which differ from the +X+ arrest motifs observed for macrolides (Beckert et al., 2021; Kannan et al., 2014; Osterman et al., 2020). In order to explore this phenomenon and gain deeper insights into the mechanism of protein synthesis inhibition by TcmX, we used inverse toeprinting (Seip et al., 2018) to characterize the stalling landscapes of free and TcmX-bound *Escherichia coli* ribosomes engaged in the translation of a random transcript library *in vitro*. We found that TcmX could primarily inhibit the ribosome in presence of QK-containing motifs. To further understand how interactions between the drug and the nascent peptide lead to the arrest of translation, we obtained a high-resolution cryo-EM structure of a TcmX-bound *E. coli* 70S ribosome translating an mRNA that encodes an amino acid motif capable of inducing strong ribosome stalling. We show that TcmX inhibits bacterial translation at QK motifs through a mechanism that is distinct from that of other context-dependent antibiotics. Indeed, TcmX inhibits peptide bond formation in the PTC by forcing the nascent peptide to occupy the A-site crevice and by trapping the 3' end of the P-site peptidyl tRNA to the exit tunnel of the ribosome. In this configuration, the distance between the  $\alpha$ -amine of the aminoacyl tRNA and the carbon of the ester carbonyl of the peptidyl tRNA is increased, preventing formation of the peptide bond. Our work therefore provides the necessary detailed molecular and structural insights to develop TcmX derivatives with potent antimicrobial activity.

## RESULTS

### TcmX primarily inhibits bacterial translation at QK motifs

To characterize the translational pausing landscape of free and TcmX-bound ribosomes, we used inverse toeprinting (Seip et al., 2018), an *in vitro* profiling method that locates stalled ribosomes on the mRNA with codon-level resolution (**Figure 1B**). This technique is based on the use of a highly processive 3' to 5' RNA nuclease (RNase R) (Vincent and Deutscher, 2006), such that the leading ribosome paused or stalled on a given transcript protects the mRNA upstream of the pause site from degradation. Since the entire peptide-encoding sequence is preserved, prior knowledge of the transcript sequences is not required. Here, we used a random library to produce  $\sim 10^{12}$  peptides with an N-terminal variable region encoded by 15 NNN codons, where N denotes equal proportions of the four possible canonical nucleotides. This library was translated *in vitro* using a reconstituted PURE translation system (Hartz et al., 1988; Shimizu et al., 2001) containing *E. coli* ribosomes and elongation factor P (EF-P), in the absence or presence of 100  $\mu$ M TcmX. RNase R digestion of the transcripts following *in vitro* translation yielded inverse toeprints which were then reverse-transcribed, amplified by PCR, and analyzed by next-generation sequencing. We collected about  $2.5 \times 10^6$  reads per sample in triplicate. The read counts for each variant of the motifs were normalized to total reads and the counts ratio of antibiotic-treated samples to untreated was defined as the enrichment. This process was applied both at the nucleotide and amino acid levels, and either for individual positions relative to the ribosomal P-site or for groups of consecutive amino acids. As expected from the presence of EF-P in the translation reaction, we did not observe a significant enrichment of polyproline (PP) motifs, and only observed a limited overall amino acid preference at the single residue level, with a mild enrichment in hydrophobic amino acids in the E- and P-sites (**Supp. Figure 2**). However, we observed a strong enrichment for the combination of glutamine (Q) and lysine (K), when these amino acids are located in the E- and P-sites of the ribosome, respectively (**Figure 1C**). To a lesser extent, we also observed enrichment in the combinations of P/Q residues (-2/E sites), and K/C residues (P/A sites) (**Supp. Figure 2**). These results confirm that TcmX can trigger ribosome stalling in response to specific sequence motifs within the ribosome.

To further characterize the drug-dependent blocking motifs, we calculated the enrichment of four amino acid-long motifs in the presence of TcmX within our inverse toeprinting dataset. Interestingly, nearly all of the motifs that underwent strong translational arrest contained a QK motif in the E/P sites (**Figure 1D**). In addition, proline (P) in the -2 site and cysteine (C) in the A-site were enriched, and the four-amino acid PQKC motif was the most enriched arrest motif (**Figure 1D**). The LK amino acid combination in the P- and A-sites reported by Osterman *et al.*, however, did not demonstrate a general ability to induce ribosome stalling in our data (**Supp. Figures 2/3**). This may indicate that LK must form part of a longer arrest motif, with residues preceding it providing a specific context that is necessary for stalling to occur, as observed for the erythromycin- dependent stalling induced by ErmDL variants lacking a +X+ motif (Beckert et al., 2021), or the importance of the sequence preceding PP-motifs for polyproline-mediated stalling (Starosta et al., 2014).



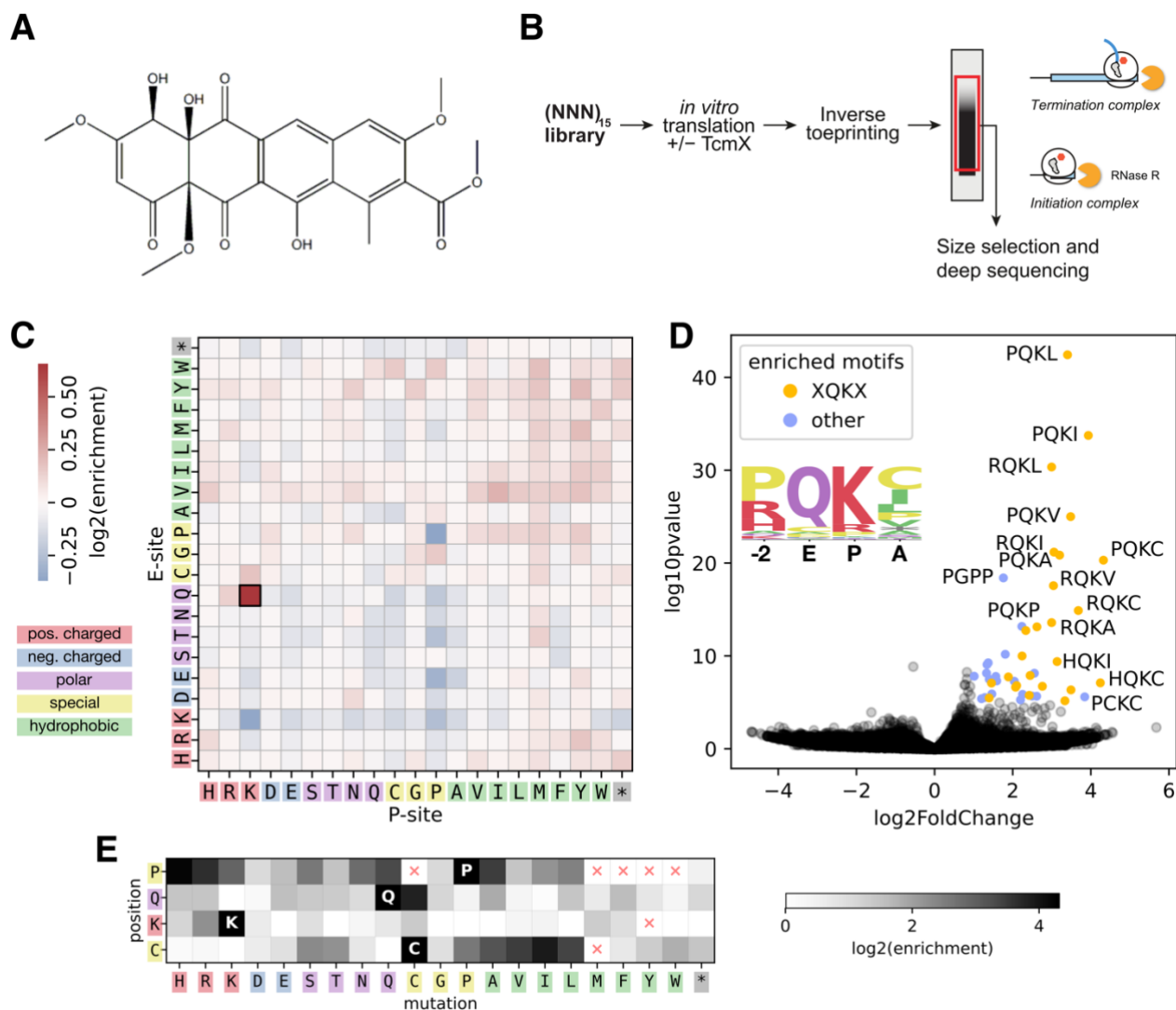


**Figure 1: Inverse toeprinting analysis of the NNN15 library translated in presence of TcmX.**

**A.** chemical structure of tetracenomycin X (TcmX). **B.** Summary of the inverse toeprinting procedure. The experiment was replicated on three independent days. On average ~2.5M reads were obtained per condition (2.7M, 2.3M, 2.6M reads without antibiotic, and 2.8M, 2.5M, 2.3M reads in presence of TcmX). **C.** Heatmap of the enriched E/P-sites motifs in presence of TcmX. Enrichment (or log2FoldChange) was calculated using the log2 ratio of the number of matching motifs:  $enrichment = \log_2\left(\frac{N_{reads_{TcmX}}}{N_{reads_{untreated}}}\right)$ . **D.** Volcano plot of statistical significance against enrichment (log2FoldChange) for 4 amino-acids motifs in the -2 to A-site. The most enriched and statistically significant motifs demonstrate a conservation of sequence. Albeit not absolute, a strong enrichment in the QK combination of amino-acids (at positions E/P) is observed for many of the motifs (yellow points). Thresholds of 1 log2FoldChange and 5 log10pvalue were used to highlight the enriched motifs. **E.** Analysis of single amino-acid variants of the PQKC motif highlights that, although some variability is tolerated on the first and last position, efficient stalling in presence of TcmX is dependent on the amino-acid sequence of the nascent peptide.

To measure the contribution of each amino acid in the PQKC motif to stalling, we analyzed all point variants of the motif in our inverse toeprinting dataset. A majority of the substitutions strongly decreased stalling efficiency, with a tolerance in a few particular cases (**Figure 1E & Supp. Figure 4**). The -2 position accommodated positively charged residues (H,R,K), alanine, or to a lesser extent polar residues (Q,N,S).

The -1 position (E-site) could be substituted with cysteine. The 0 position (P-site) only tolerated substitution to arginine, with a substantial decrease in stalling efficiency. Finally, the +1 position (A-site) had tolerance for medium-sized hydrophobic (A,V,I,L) and polar (S,T) residues. This confirmed the hypothesis that the QK residues form the core of the stalling motif with, nevertheless, a global contribution of all residues. Considering the proximity of the drug-binding site to the PTC, and the similar enrichment among codons encoding the same amino acid, we hypothesized that TcmX inhibits the ribosome in response to specific amino acids motifs present within the nascent peptide.

### **The PQKC motif undergoes strong TcmX-dependent arrest *in vitro* and *in vivo***

To assess the ability of TcmX to inhibit translation in a sequence-dependent manner, we performed a toeprinting assay on a MAAAPQKCAAA\* sequence (**Figure 2A**), which validated that TcmX induces ribosome stalling when K is in the P-site. In addition, we performed a  $\beta$ -galactosidase complementation assay in *E. coli* (**Figure 2B**) with a construction involving the pERMZ $\alpha$  plasmid containing the *ermCL-ermC* operon fused in frame with the *lacZ $\alpha$*  reporter (Bailey et al., 2008). Programmed macrolide-dependent arrest on the *ermCL* leader sequence triggers conformational changes of the *ermCL-ermC* intergenic region, thus liberating the Shine Dalgarno sequence of *ermC* and allowing the expression of the reporter gene. Here, we replaced the first nine codons of the *ermCL* sequence with a nucleotide sequence encoding a non-blocking AAA spacer and the PQKC motif, which preserved the *ermCL-ermC* intergenic region necessary for the induction of the *lacZ $\alpha$*  gene as well as the position of the stalling site (**Figure 2B**). This plasmid was then inserted into an *E. coli* JM109 strain from which the *acrAB* operon had been deleted. AcrAB is a general drug efflux pump, whose removal helps to maintain a stable cytoplasmic concentration of the antibiotic (Tikhonova and Zgurskaya, 2004). The blue halo observed in the drug-diffusion assay (**Figure 2B**) indicated that TcmX can activate stalling-dependent expression of the *ermC-lacZ $\alpha$*  reporter, thus validating *in vivo* translation arrest within the leader sequence encoding for the PQKC motif.

### **TcmX blocks translation at QK motifs by trapping residue A76 of the P-site tRNA inside the exit tunnel**

To understand the structural basis of the context specificity of TcmX-mediated translation inhibition at QK motifs, we determined the cryo-EM structure of a ribosome stalled during translation of a PQKC motif in the presence of 100  $\mu$ M TcmX, at an overall resolution of 2.8 Å (**Supp. Figure 6**).

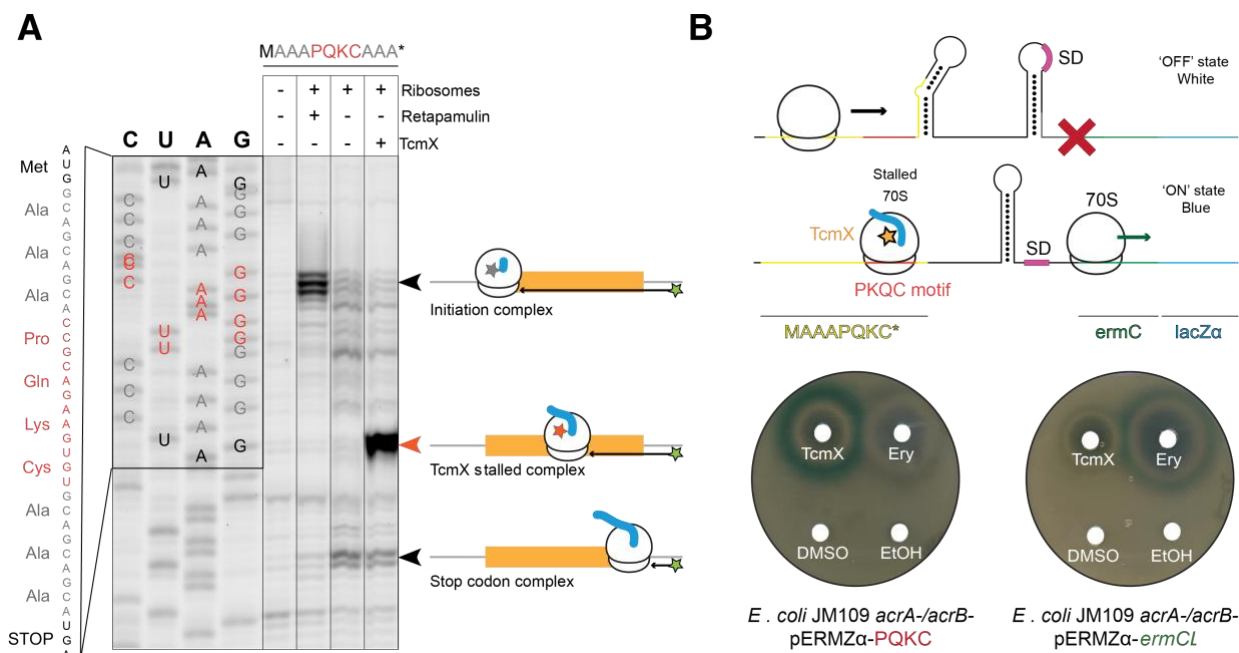


**Figure 2: *In vitro* and *in vivo* validation of ribosome stalling on the PQC motif in presence of TcmX.**

A. Toeprint assay demonstrate stalling on the PQC motif. B. top: principle of the *ermZ*-α reporter system. A modified version of the *pERMZ*-α plasmid (Bailey et al., 2008) was used, in which the PQC sequence was inserted directly upstream of the bistable RNA loops of the reporter. Upon stalling of the ribosome on the motif, the RBS (SD) of the ErmC-LacZα reporter is made accessible by the reorganization of the bistable loop, which enable translation of the reporter and α-complementation that is visible as blue rings on X-gal plates. Bottom: visualization of blue rings in presence of TcmX, erythromycin (Ery) or the respective solvents e.g. DMSO and ethanol (EtOH).

In order to prepare this complex, we translated an mRNA template encoding the MAAAPQKCAAA\* peptide in a PURE translation system and applied a dilution of this reaction mixture to grids immediately after translation, without any additional purification step. We observed a major class accounting for 34% of the particles and showing clear density for tRNA<sup>Gln</sup>, tRNA<sup>Lys</sup> and tRNA<sup>Cys</sup> in the ribosomal E-, P- and A-sites, respectively, as confirmed by the presence of tRNA specific modifications. As expected, TcmX binds within the nascent polypeptide exit tunnel in the large ribosomal subunit, by stacking against the non-canonical base pair formed by 23S rRNA residues U2586 and U1782 (**Figure 3A and 3B**). Clear density was also visible for residues 3–7 of the nascent peptide (AAPQK) and for the Cys residue attached to the A-site tRNA (**Figure 3B**). The local resolution of ~2.7 Å for the nascent peptide enabled us to unambiguously model the side chains of all of the residues observed (**Supp. Figure 6**). Thus, the last residue incorporated into the nascent peptide was Lys-7, in agreement with our inverse and classical toeprinting data.

To our surprise, residue A76 of the P-site tRNA<sup>Lys</sup> occupies a cavity that normally accommodates the side chain of the C-terminal amino acid of the nascent peptide. In our structure, the base of A76 is stabilized in this pocket through van der Waals interactions with the drug and through a non-canonical *trans* Hoogsteen–Hoogsteen interaction with residue A2439 of the 23S rRNA (**Figure 3C**), while residues C74 and C75 of the P-site tRNA form the usual Watson-Crick

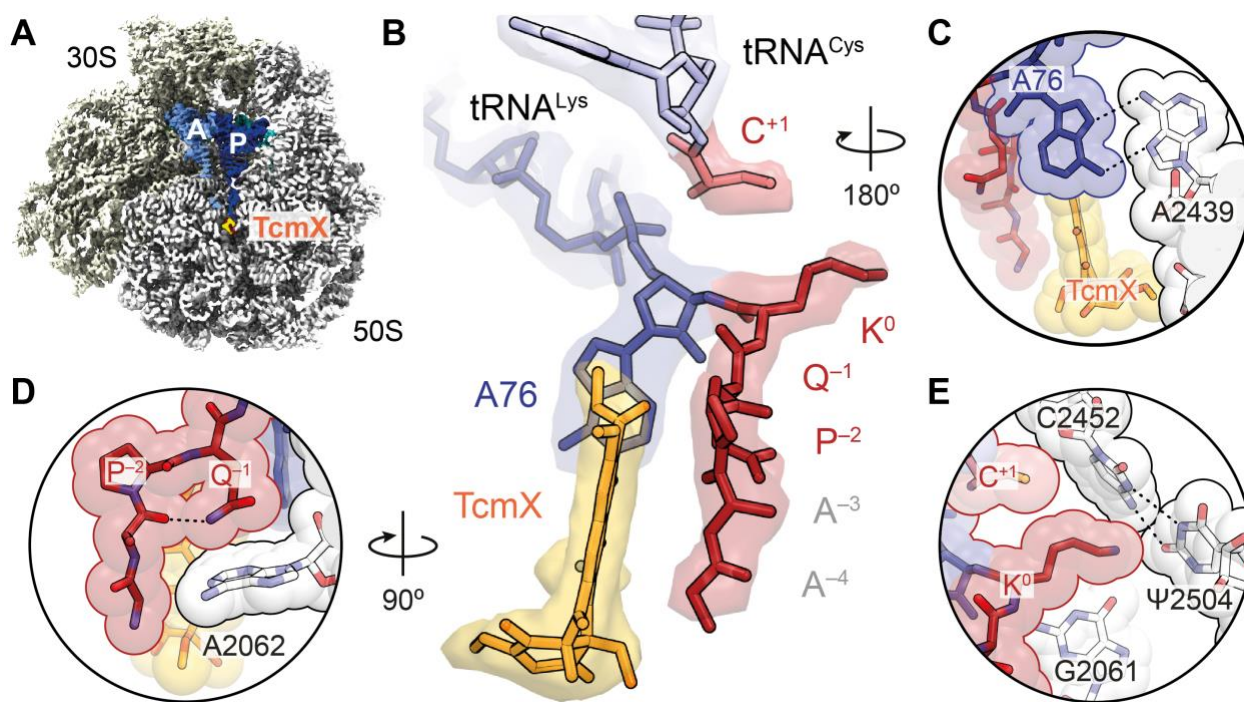


**Figure 3: Cryo-EM structures of the MA<sub>3</sub>PQKCA<sub>3</sub>\*-TcmX-70S complex.**

A. Transverse section of the cryo-EM map of the MA<sub>3</sub>PQKCA<sub>3</sub>\*-TcmX-70S with isolated densities highlighting the 30S (light yellow) and 50S (white) subunits, P-site tRNA (dark blue), A-site tRNA (light blue), MA<sub>3</sub>PQKCA<sub>3</sub>\* nascent chain (red) and TcmX (yellow). B. Molecular model and surrounding map densities of MA<sub>3</sub>PQKCA<sub>3</sub>\* nascent chain (red), P-site tRNA (dark blue), A-site tRNA (light blue) and TcmX (yellow). C. A76 of the CCA end of the P-site tRNA is stabilized in the A-site pocket a non-canonical trans Hoogsteen–Hoogsteen interaction with residue A2439 of the 23S rRNA. D. The P<sup>-2</sup> residue allows the nascent peptide to adopt an elbow conformation that facilitates the folding of the peptide around A2062 of the 23S rRNA, where the Q<sup>-1</sup> side chain stacks upon A2062 and forms a hydrogen bond with the backbone carbonyl oxygen of the nascent peptide, which contributes to stabilize the ribosome/peptide/antibiotic complex. E. The K<sup>0</sup> residue still attached to the A76 base is displaced into the A-site crevice, thus impeding the positioning that is required to form the peptidyl bond with the incoming C<sup>+1</sup> amino-acid. K<sup>0</sup> side chain is stabilized through a network of interactions involving the carbonyl oxygen of K7 and the N2 atom of G2061 and the C2452-ψ2504 base pair.

base pairs with the bases of 23S rRNA residues O2'-methyl-G2251 and G2252, respectively. These cytosines are also slightly pulled towards the tunnel in comparison to a classical peptidyl-tRNA bound to the P-site in the state preceding peptide bond formation (Polikanov et al., 2014). This shift of approximately 2 Å of the two cytosines allows U2602 to form a hydrogen bond with the ribose of residue A73 of tRNA<sup>Lys</sup>, thus stabilizing the conformation adopted by the CCA of the P-site tRNA. To the best of our knowledge, a similar conformation for residue A76 has not been observed in the structures of the ribosome compared to other antibiotics that silence the PTC or prevent the progression of the peptide through the nascent polypeptide exit tunnel (Beckert et al., 2021; Polikanov et al., 2015; Svidritskiy and Korostelev, 2018).

Next, we looked at the position of the other ribosomal bases known to play a functional role within the PTC. In our structure, the mobile bases of 23S rRNA residues U2585 and U2506 are in their induced conformation (Schmeing et al., 2005), while the side chain amide of Q6 from the nascent peptides stacks against 23S rRNA residue A2062 (**Figure 3D**), which would not be optimal with the shorter side chain of an asparagine residue. The atypical position of A76 within the PTC displaces the K7 residue — still attached to the A76 base — into the A-site crevice, thus impeding the positioning that is required to form a peptide bond with the incoming amino acid. This position of K7 is stabilized through a network of interactions formed with the ribosome, notably involving the carbonyl oxygen of K7 and the N2 atom of G2061 (**Figure 3E**).

Under physiological conditions, the  $\alpha$ -amino group of the aminoacyl-tRNA is deprotonated to yield a nucleophilic  $\alpha$ -NH<sub>2</sub> moiety capable of attacking the ester bond connecting the C-terminal amino acid of the nascent peptide and the tRNA bound to the P-site. For peptide bond formation to occur, the two amino acids must be located within an ideal distance of  $\sim 3.2$  Å from one another. In our structure, the position of the components of the ribosome, nascent peptide, and tRNAs, increases the distance between the  $\alpha$ -amine of the incoming amino acid C8 and the carbon of the carbonyl group of residue K7 from the nascent peptide to 5.3 Å, which is no longer favorable to the reaction (**Figure 4**). In addition, the environment around the  $\alpha$ -amine of residue C8 suggests that it could be protonated, which would induce the residue to form a salt bridge with the phosphate group of A76, and likely contribute to render C8 unable to form a new peptide bond.

Our structure also sheds light on the overall contribution of the motif in the stalling. Residue Q6 from the nascent peptide forms intramolecular hydrogen bonds with the backbone carbonyl oxygen and the amine of residue A4, and one hydrogen bond with atom O4 of TcmX, which contribute to stabilizing the interaction between the ribosome, nascent peptide and antibiotic (**Figure 3D**). These bonds seem to be intrinsically dependent on the length, orientation and chemical composition of the glutamine side chain as other possible hydrogen bond donors (N, S, T, R, K...) were not found to induce stalling according to our inverse toeprinting results. The P5 residue forms a kink in the nascent peptide that could orient the peptide in a favorable conformation to form these hydrogen bonds (**Figure 3D**). However, our inverse toeprinting data indicate, that proline is not strictly required at this position, even though it may contribute to stalling efficiency.

## DISCUSSION

Our data reveal the principal mode of action for TcmX, a recently discovered antibiotic that targets the ribosomal exit tunnel. We employed inverse toeprinting to characterize the stalling landscape of TcmX-bound *E. coli* ribosomes, and could observe that the translational inhibition induced by the drug relies on the sequence of the nascent peptide being translated, both *in vitro* and *in vivo*. Using complementary biochemical and structural approaches, we could identify how the nascent peptide interacts with the ribosome and the drug to inhibit peptide bond formation at the PTC. TcmX inhibits translation through a novel mechanism, by sequestering the A76 base of the CCA end of the P-site tRNA inside the nascent

polypeptide exit tunnel of the ribosome. As a result, A76 occupies the space normally dedicated to the last residue of the nascent peptide, and the C-terminal lysine residue of the QK motif is thus forced to occupy the A-site crevice of the PTC. This movement increases the distance between the amino-acyl moiety of the A-site tRNA and the peptidyl of the P-site tRNA to inhibit peptide bond formation (**Figure 4**).

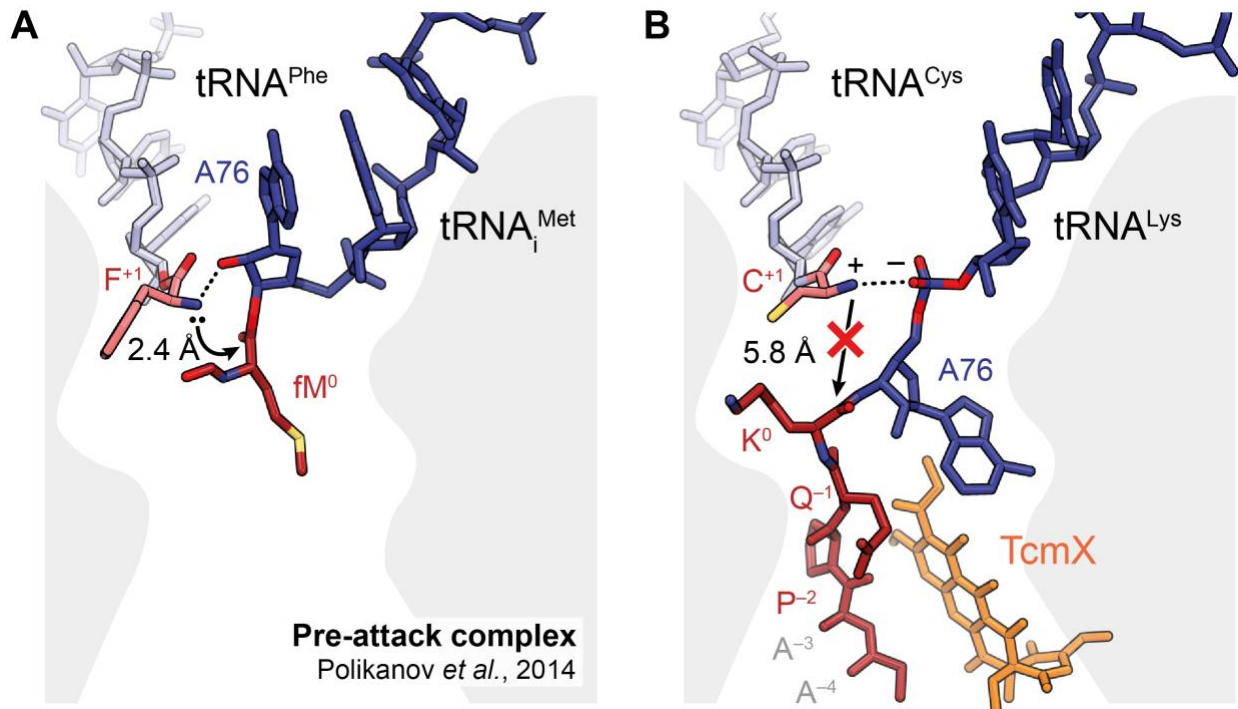


**Figure 4: Mechanism of TcmX-induced translation inhibition.**

A. In the absence of TcmX, the nascent chain containing the “PQK” motif adopts a canonical conformation within the exit tunnel of the ribosome, where the distance of 2.4 Å between the amino-acyl moiety of the A-site tRNA and the peptidyl of the P-site tRNA is favorable for the reaction of peptide bond formation. (PDB 1VY4) B. In the presence of TcmX, the shifted conformation of the nascent peptide traps the A76 base of the CCA end of the P-site tRNA into the exit tunnel of the ribosome. As a consequence, A76 occupies the space normally dedicated to the last residue of the nascent peptide, where the lysine residue of the motif is thus forced to occupy the A-site crevice of the PTC. This conformation of the nascent peptide increases the distance to 5.8 Å between the amino-acyl moiety of the A-site tRNA and the peptidyl of the P-site tRNA, thus inhibiting peptide bond formation.

This atypical position of residue A76 of the P-site tRNA is distinct from those observed in other structures of ribosome-antibiotic complexes presenting abnormal conformations of the CCA end of the P-site bound tRNA. A crystal structure of 70S ribosomes from *Thermus thermophilus* bound to the antibiotic blasticidin S shows that this antibiotic inhibits protein synthesis by displacing the 3' end of the P-site tRNA and moving residue C75 away from the drug and towards the A-site. In this case, the deformation of the 3'-CCA end of the peptidyl tRNA strongly inhibits peptide bond formation and peptidyl-tRNA hydrolysis normally catalyzed by release factors (Mondal et al., 2014; Svidritskiy and Korostelev, 2018). In the case of hygromycin A, the drug prevents the proper accommodation of residue A76 of the A-site tRNA, causing it to adopt a conformation that stabilizes 23S rRNA residue A2602 in a rotated state through a base-stacking



interaction (Polikanov et al., 2015). As a consequence, the nucleotides of the 3' strand of the acceptor arm of the A-site tRNA re-adjust their positions to account for the unaccommodated A76 position (Polikanov et al., 2015). Therefore, hygromycin A interferes with the productive docking of the CCA end of the deacetylated A-site tRNA at the PTC and causes the A-site tRNA to oscillate between the A/T-like configuration and partially accommodated states for an extended period of time, preventing the full accommodation of the A-site tRNA at the PTC. Our work reports a novel situation, whereby the antibiotic sequesters the CCA-end of the P-site tRNA inside the tunnel instead of pushing it away from the PTC and therefore the ribosome.

The mode of action of TcmX is reminiscent of the mechanism of ribosome inhibition by macrolide antibiotics, with which it shares similarities (Vázquez-Laslop and Mankin, 2018). First, both TcmX and macrolides bind to the portion of the exit tunnel near the PTC; unlike erythromycin however, TcmX binds on the opposite surface of the ribosomal tunnel (Osterman et al., 2020; Vázquez-Laslop and Mankin, 2018). The distinct binding sites of TcmX and erythromycin is consistent with the finding that the A2058G mutation within the 23S rRNA confers erythromycin but not TcmX resistance, whereas mutations in U2586 or U1782 that confer TcmX resistance, do not confer erythromycin resistance (Osterman et al., 2020). The lack of cross-resistance to TcmX by A2058G is of high importance since mutation or methylation of A2058 represents one of the main determinants for clinical resistance to macrolides, lincosamides and streptogramin B (MLSB) antibiotics (Leclercq, 2002). Additionally, both macrolides and TcmX also inhibit translation in a peptide sequence-dependent manner (Vázquez-Laslop and Mankin, 2018). In the presence of macrolides, ribosomes can stall at the RLR (+X+) arrest motif, a motif found in several macrolide-dependent arrest peptides, such as ErmDL (Beckert et al., 2021). To stall the drug-bound ribosome, ErmDL adopts a conformation where the first arginine of the motif occupies the A-site crevice and therefore clashes with the accommodation of the second arginine in the A-site (Beckert et al., 2021). In ErmDL, the guanidinium moiety of the arginine side chain plays an important role to make stacking interactions that stabilize the complex. This group is however not present in lysine and, accordingly, this residue is less common in +X+ motifs of the Erm leader peptides family (Ramu et al., 2009). The opposite appears to hold true when the ribosome is stalled with TcmX due to the different position of the lysine residue of the PQKC motif within the PTC. We believe that in this case lysine is more favorable for stalling than arginine, as the bulkier side chain of the latter would likely clash with the C2452-Ψ2504 and A2451-G2061 base pairs of the 23S rRNA.

In summary, our findings reveal strong insights into the mechanism by which TcmX inhibits bacterial translation in a manner that is dependent on the sequence of the nascent peptide. Other members of the tetracenomycin class could be studied using the approach detailed here, such as elloramycin or tetracenomycin C, which display a similar tetracyclic chromophore core and also exert antimicrobial activity against a variety of *Actinomyces* and *Streptomyces* species (Anderson et al., 1989; Drautz et al., 1985; Egert et al., 1992; Rohr and Zeeck, 1990; Weber et al., 1979). Indeed, the high structural homology of tetracenomycins and tetracyclines/anthracyclines, and the mode of action of TcmX which is strongly reminiscent of that of macrolides, suggest a high therapeutic potential for this family of drugs. Moreover, TcmX can also bind the human ribosome (Osterman et al., 2020), raising the possibility that context-dependent ribosome stalling could also be induced by this drug in eukaryotes, as was recently

reported for macrolides and ketolides in a yeast model in which the ribosomes were rendered susceptible to these antibiotics (Svetlov et al., 2021). The ability of TcmX to inhibit eukaryotic translation may limit its usefulness as an antibiotic, but could be of high interest for chemotherapy, as suggested by the high structural similarity between TcmX and the widely used anticancer drug doxorubicin. Further characterization and optimization of tetracenomycins is therefore needed to develop this promising class of antimicrobial and/or anticancer drugs.



## ACKNOWLEDGEMENTS

We thank Nora Vázquez-Laslop (University of Illinois, Chicago, Illinois) for providing the JM109  $\Delta$ *acrA/acrB* *E. coli* strain. We also thank Anaïs Labécot for preliminary experiments. E.C.L. and C.A.I. have received funding for this project from the European Research Council (ERC) under the European Union's Horizon 2020 research and innovation program (Grant Agreement No. 724040). C.A.I. is an EMBO YIP and has received funding from the Fondation Bettencourt-Schueller. T.N.P. has received funding for this project from the Agence Nationale de la Recherche (ANR) under the frame of the Joint JPI-EC-AMR Project "Ribotarget – Development of novel ribosome-targeting antibiotics". We thank the cryo-EM facility of the European Institute for Chemistry and Biology for the data collection time on the Talos Arctica microscope.

## AUTHOR CONTRIBUTIONS

C.A.I. designed the study. I.A.O. isolated and purified TcmX. E.C.L. performed inverse toeprinting experiments. E.C.L. and T.T.R. processed and analyzed the inverse toeprinting data. E.C.L. generated toeprinting analysis. T.N.P. performed the blue ring assays. E.C.L. prepared the cryo-EM complexes; T.N.P. prepared grids and performed cryo-EM data collection. T.N.P. and C.A.I. processed the cryo-EM data and E.C.L. built the models. E.C.L., T.N.P., T.T.R. and C.A.I. wrote the manuscript. All authors reviewed and edited the manuscript.

## COMPETING FINANCIAL INTERESTS

The authors declare no competing financial interests. Correspondence and requests for materials should be addressed to C.A.I. ([axel.innis@inserm.fr](mailto:axel.innis@inserm.fr)) or T.T.R. ([thibaud.renault@u-bordeaux.fr](mailto:thibaud.renault@u-bordeaux.fr)).

## METHODS

### General experimental procedures for inverse toeprinting

DNA and RNA products at various points in the inverse toeprinting protocol were analyzed on 9% acrylamide (19:1) TBE (90 mM Tris, 90 mM boric acid, and 2 mM EDTA) gels and stained with SyBR Gold (Invitrogen). Inverse toeprints were excised from 12% acrylamide TBE gels using a clean scalpel. RNA gel electrophoresis was performed under denaturing conditions (8 M urea in the gel). All reactions were performed using molecular biology grade H<sub>2</sub>O (Millipore). Oligonucleotides used in this study are listed above.

### 15 codons random library generation

A random variant library containing 15 'NNN' codon (aNy aNy, aNy) was designed and ordered to Eurogentec under the form of a single stranded oligonucleotide called 'iTP\_NNN15\_random-library'. This expression cassette was obtained by polymerase chain reaction (PCR) with Phusion DNA polymerase (6 cycles [98°C, 10 s; 62°C, 5 s; 72°C, 10 s]), using the 'iTP\_NNN15\_random-library' oligonucleotide in combination with oligonucleotides 'iTP/TP\_T7\_RBS\_ATG\_f' and 'iTP\_Stop\_EcoRV\_r' as templates (0.1 pmol of each oligonucleotide per 50 µl reaction) and oligonucleotides 'iTP/TP\_T7\_f' and 'iTP\_EcoRV\_r' for amplification (1 pmol of each oligonucleotide per 50 µl reaction). The final sequence of the expression cassette is:

CGATCGAATTCTAATACGACTCACTATAGGGCTTAAGTATAAGGAGGAAAAAATATG**NNNNNNNNNNNNNNNNNN**  
**NNNNNNNNNNNNNNNNNNNNNNNNNNNNNN**NGCGATCTCGGTGTGATGAGATATCAATATCAAAAAGGATCCA  
TATA

(the T7 promoter is underlined, random expression region is in **bold**; the EcoRV site is in *italics*). Linear expression cassettes were purified using a PCR purification kit (Qiagen) according to the manufacturer's instructions prior to quantification with a 2100 Agilent Bioanalyzer and mixing.

### *In vitro* transcription

The DNA template contains a T7 promoter followed by a ribosome binding sequence, as specified in the NEB PURExpress system handbook. *In vitro* transcription was performed using T7 RNA polymerase in a buffer containing 80 mM Tris-HCl, 24 mM MgCl<sub>2</sub>, 2 mM spermidine, and 40 mM DTT, pH 7.6, in the presence of 7.5 mM ATP (Sigma Aldrich), CTP and UTP, 0.3 mM GTP (CTP, UTP, and GTP from Jena Bioscience), and 4.5 mM Thio-Phosphate-GMP (Genaxxon Bioscience). 8 pmol of DNA template were used in 200 µl of reaction volume. *In vitro* transcription was performed at 20°C for 3 h, mRNA was purified using the "RNA Clean & Concentrator<sup>TM</sup>-5" purification kit (ZymoClean Research) according to the manufacturer's instructions. The final concentration of mRNA was determined using the NanoDrop.

### Biotinylation

Biotin-maleimide (Vectorlabs) was dissolved in dimethylformamide according to the manufacturer's instructions. 800 pmol mRNA were mixed with 800 nmol biotin-maleimide in 100 mM in Bis-Tris-acetate buffer pH 6.7 and incubated at room temperature for 2.5 h. Unincorporated biotin was removed by washing the mRNA three times with H<sub>2</sub>O (molecular biology grade, Millipore) in an Amicon membrane centrifugal concentrator with a MWCO of 30 kDa (Millipore). mRNA was recovered and the biotinylation efficiency was analyzed using a dot blot.

### Dot blot

H<sup>+</sup> bond membrane (GE Healthcare) was treated with 6× SSC buffer (900 mM NaCl, 90 mM Na<sub>3</sub>-citrate, pH 7.0) for 10 min and dried briefly between two pieces of Whatman paper. Samples and a 5'-biotinylated oligonucleotide standard (Biotin\_standard) were diluted in 6× SSC buffer to 0.5, 1.0, 2.5, and 5.0 μM, and 1 μl of each dilution was pipetted onto the prepared membrane. The membrane was then baked for 2 h at 80°C to adsorb the mRNA to the membrane. The membrane was subsequently blocked in 2.5% dry milk solution in TBS-T (50 mM Tris-HCl, 150 mM NaCl, and 0.05% [vol/vol] Tween-20, pH 7.5) for 1 h at room temperature. The milk solution was removed and the membrane was incubated with a 1:1,000 dilution of streptavidin-alkaline phosphatase antibody (Promega) in TBS-T for 1 h at room temperature. Unbound antibody was removed by washing three times with TBS-T buffer. Colorimetric detection was performed using an NBT/BCIP detection kit (Promega) according to the manufacturer's instructions. The membrane was imaged immediately on a Bio-Rad Imager. The biotinylation efficiency was estimated by comparing the intensity of the sample dots with the intensity of the standard dots.

### Polyadenylation of the mRNA

Polyadenylation of the biotinylated mRNA was performed using Poly-A polymerase (NEB) using the buffer supplied. The ratio of mRNA to ATP molecules was chosen to be 1:100. The reaction was incubated at 37°C for 2 h and the efficiency of the polyadenylation reaction was assessed by denaturing PAGE (9%). Polyadenylated mRNA was purified using the purification "RNA Clean & Concentrator"<sup>TM</sup>-5" kit (ZymoClean Research) according to the manufacturer's instructions.

### Inverse toeprinting

Inverse toeprinting was performed as described previously, with modifications (Seip et al., 2018). Briefly, *in vitro* translation was carried out with a PURExpress Δ RF-123 Δ Ribosomes kit (NEB), using ~5 pmol of 5'-biotinylated and 3'-polyadenylated mRNA as a template. Antibiotic (TcmX) was supplemented at a final concentration of 100 μM in 5 μl reactions. Release factors 1 and 3 were added to the translation reaction according to the manufacturer's instructions. Translation was performed at 37°C for 30 min, after which the samples were placed on ice and 5 μl ice-cold Mg<sup>2+</sup> buffer (50 mM Hepes-KOH, 100 mM K-glutamate, 87 mM Mg- acetate, and 1 mM DTT, pH 7.5) was added to the reactions, thereby increasing the Mg<sup>2+</sup> concentration to 50 mM. 1 μl of RNase R (1 mg/ml) was added, followed by an additional incubation for 30 min at 37°C to ensure complete mRNA degradation. 139 μl of 1× BWT buffer was added to stop the reaction (5 mM Tris-HCl, 0.5 mM EDTA, 1 M NaCl, and 0.05% [vol/vol] Tween- 20, pH 7.5).

### mRNA purification and linker ligation

For each sample, 5 μl of a M-280 streptavidin Dynabeads (ThermoFisher Scientific) suspension were washed three times with 1× BWT buffer in DNA loBind tubes (Eppendorf) and resuspended in 50 μl of the same buffer. Dynabeads and RNA from the previous step were combined into these tubes and incubated on a tube rotator for 15 min at room temperature to allow binding of the biotinylated mRNA to the streptavidin beads. After incubation, beads were collected using a magnet and the supernatant was discarded. The beads were washed one time with 1× BWT buffer to remove unbound RNA, followed by two washes with H<sub>2</sub>O to remove the 1× BWT buffer. Beads were resuspended in 9.5 μl of linker ligation reaction mixture containing 4 μl of water, 1 μl of T4 RNA ligase2 truncated buffer (10X – NEB), 3 μl of PEG 8000 (50% - NEB), 1 μl of 'iTP\_3'\_linker\_ApoI '(10 μM) and 0.5 μl of ligase (T4 RNA ligase 2, truncated - 200 000 U/ml - NEB) per reaction. Linker ligation was allowed to proceed on a tube rotator for 2.5 h at room temperature.

### **Reverse transcription**

Following ligation of the linker, beads were washed once with H<sub>2</sub>O to remove unincorporated linker oligonucleotide and were resuspended in 18.5 µl of reverse transcription reaction mixture containing 11.5 µl of water, 1 µl of dNTPs (10 mM of each - NEB), 1 µl of 'iTP\_Linkers\_r' oligonucleotide (2 µM), 4 µl of first strand synthesis buffer (5X - ThermoFisher) and 1 µl of DTT (0.1 M - ThermoFisher) per reaction. The samples were incubated for 5 min at 65°C to anneal the primer to the complementary sequence and then placed on ice. 1 µl of reverse transcriptase (Superscript III – 200,000 U/ml – ThermoFisher) was added to each tube and the samples were incubated for 30 min at 55°C in a Thermomixer at 500 rpm to allow reverse transcription of the Dynabead-bound mRNA.

### **PCR on cDNA, restriction digestion**

Reverse transcribed cDNA was used without further purification as a template for PCR. To generate double stranded DNA for restriction digestion, a fill-up reaction was performed using 'iTP\_cDNA\_f' oligonucleotide and the reverse transcribed cDNA (10 s denaturation, 10 s annealing at 42°C, and 30 s elongation at 72°C). The resulting double stranded DNA was combined with 1 µl of EcoRV-HF restriction enzyme and the sample was incubated at 37°C for 1 h. To amplify undigested DNA, 'iTP\_Linkers\_r' oligonucleotide was added and a PCR was performed with 10-16 cycles (denaturation at 98°C for 10 s, annealing at 60°C for 10 s, and elongation at 72°C for 10 s). The number of PCR cycles was adjusted to give a visible band on the gel while minimizing non-specific byproducts.

### **Purification of DNA fragments of interest after PCR**

Bands containing inverse toeprints corresponding to stalled ribosomes from the initiation codon to the last 'NNN' codon were excised from the gel with a clean scalpel. Gel pieces were crushed through a 5 ml syringe into 15 ml Falcon tubes and 10 ml of gel elution buffer (10 mM Tris-HCl, pH 8.0, 500 mM Na-acetate, and 0.5 mM Na-EDTA) were added. The tubes were incubated on a tube rotator at room temperature overnight. Gel debris were separated from the extraction solution by filtering through 0.22 µm centrifugal filters (Millipore). Each sample was then concentrated to ~1 ml using a SpeedVac. DNA was precipitated in 5 ml Eppendorf tubes using 1 ml of isopropanol with 3.7 µl GlycoBlue (Thermo Fisher Scientific) and incubating at -80°C overnight. After precipitation, DNA was recovered by centrifugation in a ThermoScientific Heraeus Multifuge X3R centrifuge at 20,000g for 30 min at 4°C using a Fiberlite F15-8x50cy rotor (ThermoScientific). The supernatant was removed and DNA pellets were resuspended in 20 µl H<sub>2</sub>O (molecular biology grade, Millipore) for subsequent addition of the next-generation sequencing (NGS) adapters.

### **Additions of NGS adaptors to amplified DNA**

Long NGS adapter oligonucleotides ('NGS\_adaptor\_f' and the reverse oligonucleotides 'NGS\_adaptor\_index\_number') contain Illumina TruSeq adapter sequences followed by 18 nucleotides complementary to the 5' or 3' region of the cDNA. The reverse oligonucleotides also contain barcode sequences for multiplexing according to the TruSeq v1/v2/LT protocol (Illumina). Sequencing libraries were obtained from 12–16 cycles of PCR using 0.02 µM long NGS adapter oligonucleotides (forward and reverse) and 0.2 µM short amplification oligonucleotides ('NGS\_f' and 'NGS\_r'). PCR products were purified using a Qiagen PCR purification kit. The size and concentration of the fragments obtained were measured using a 2100 Agilent Bioanalyzer with the DNA 1000 kit.

### Next generation sequencing

Next generation sequencing was performed by the BGI Facility in Hong-Kong, on an Illumina HiSeqXten system in rapid run mode with 150 PE reads.

### Toeprinting assays

Toeprinting was performed as described previously (Orelle et al., 2013). Briefly, DNA templates containing a T7 promoter, a ribosome binding site, the expression cassette and the NV1 sequence (Vazquez-Laslop et al., 2008) were generated by PCR using as templates oligonucleotides 'iTP/TP\_frag1\_T7\_RBS\_ATG\_f', 'TP\_frag2\_r', 'TP\_frag2\_NV1\_r' and the corresponding expression cassette oligo (0.1 pmol of each oligonucleotide per 50 µl reaction) and the short primers 'iTP/TP\_frag1\_T7\_f' and 'TP\_short\_r' for amplification (1 pmol of each oligonucleotide per 50 µl reaction) (see Key Resources Table for the sequences of oligonucleotides used). For instance, the final sequence of the 'MAAAPQKCAA\*' expression cassette is:

CGATCGAATTCTAATACGACTCACTATAGGGCTTAAGTATAAGGAGGAAAAAAT**ATGGCAGCAGCACCGCAGAAGTGTGCAGCAGCATGAAGCGAATAATAACTGACTCTGAACAACATCCGTACTTCTCGTGCGCAGGCAAGGTTAATAAGCAAATTCATTATAACC**

(the T7 promoter is underlined, the 'MAAAPQKCAA\*' expression region is in **bold**; the NV1 sequence is in *italics*).

DNA templates were transcribed and translated *in vitro* using the PURExpress Δ RF123 Δ Ribosomes Kit (New England Biolabs). Ligands were dissolved in water and added as needed at the beginning of the reaction. The Yakima Yellow-labelled probe complementary to the NV1 sequence ('TP\_RT\_yakima-yellow\_r') was added to the 5 µl reaction after incubating for 15 min at 37 °C (2 µM) and the sample was incubated for another 5 min at the same temperature. Reverse transcription is then performed with 50 U of Avian Myeloblastosis Virus reverse transcriptase (Promega Corporation) for 20 min at 37 °C. RNA was degraded by adding 0.5 µl of a 10 M NaOH stock at 37 °C for 15 min. Samples were neutralized with 0.7 µl of a 7.5 M HCl stock and the remaining complementary DNA was purified using a nucleotide removal kit (QIAGEN). Sequencing reactions were performed using a commercial kit designed to be used with fluorescent dye-labeled primers (#792601KT – ThermoFischer Scientific). To purify the PCR product, the ExoSAP-IT reagent (#PN 78200 – ThermoFischer Scientific) is used, to remove the excess dNTPs and primers before starting the sequencing. This purification step is performed following the manufacturer's instructions. For the sequencing procedure, 4 µl of purified PCR product (or approximately 0,5 – 1 pmol of DNA) and 2 pmol of the 5'-labeled oligonucleotide are used to prepare the master reaction following the manufacturer's instructions. Once the PCR product is purified and the sequencing reactions are prepared, the following sequencing PCR program is used: [30 s denaturation, 15 s annealing at 50°C, and 60 s elongation at 72°C], 25 cycles. 2 µL of formamide loading dye from the kit are then added to each Sanger reaction. Sanger reactions are heated for 3 min at 75°C to denature the cDNA, while the toeprinting samples were denatured at 95 °C for 5 min. 3.5µl of the sequencing reactions and 3 µl of the toeprinting reactions were separated by 7.5% sequencing polyacrylamide gel electrophoresis (2,000 V, 40 W for 2–2.5 h) followed by detection on an Amersham Typhoon Gel and Blot Imaging System (GE Healthcare Life Sciences).

### β-galactosidase assay

To test for *in vivo* activity, a translational reporter pERMZα plasmid containing the ermCL-ermC operon in frame with the lacZα reporter was used. The sequence coding for the AAAPQKC\* motif was inserted in the place of the first ninth codons of the ermCL sequence by mutation using the QuikChange Lightning Site-Directed Mutagenesis Kit (Agilent Technologies, Inc). Briefly, oligonucleotides (pZα\_MAAAPQKC\_fwd) and (pZα\_MAAAPQKC\_rvs) were used to mutate and linearize the pERMZα plasmid by PCR amplification. The PCR product was incubated 5 minutes at 37°C with the DpnI enzyme to digest parental supercoiled and

methyated dsDNA. The nicked vector DNA containing the desired mutations was then transformed into *E. coli* XL10-Gold. The plasmids were transformed into *E. coli* JM109 deleted for the operon *acrAB* to reduce drug efflux. The cells were grown in lysogeny broth (LB) at 37°C (180 rpm) with ampicillin (100 µg/ml) until they reached an optical density of 0.5 at 600 nm. 1 ml of the cell culture were added to 4 ml of 0.6% LB-agar at 50 °C and plated onto 1.5% LB-agar plates supplemented with ampicillin, 0.5 mM Isopropyl-β-D-1-thiogalactopyranoside (IPTG) and 0.5 mM 5-bromo-4-chloro-3-indolyl-beta-D-galactopyranoside (X-gal). Once the soft agar had solidified, 6-mm-diameter Whatmann paper discs (GE Healthcare) were placed on top of the plate and wetted with 5 µl of a solution at 10 mM of tetracenomycin X diluted in DMSO or 300 µg of erythromycin diluted in 10 µl of ethanol. The plates were then incubated at 30°C overnight and pictures were taken the next day.

#### **Preparation of an *E. coli* 70S complex for cryo-EM**

The complexes were translated *in vitro* using 2.2 µM of homemade 70S *E. coli* ribosomes, 100 µM of tetracenomycin X, 5 pmol of mRNA and the PURExpress Δ Ribosomes Kit (New England Biolabs) at 37°C for 20 min and then diluted in a 0.22 µM filtered storage buffer (50 mM Hepes KOH pH 7.5, 100 mM K-Acetate, 25 mM Mg-Acetate, 10 µM tetracenomycin X) to yield a final concentration of 300 nM of ribosome.

#### **Cryo-EM grid preparation**

For cryo-EM analyses, 3.5 µl of sample was deposited on glow-discharged Quantifoil carbon grids (QF-R2/2-Cu) coated with a thin carbon layer of 2 nm using an Edwards Vacuum Carbon Coater E306. After waiting for 30 seconds and blotting with filter paper to remove excess sample for 2.5 s, grids were plunge-frozen in liquid ethane using a FEI Vitrobot Mark IV (Thermo Fisher) with a blotting force of 5 in an environment with 100% humidity and 4 °C temperature.

#### **Cryo-EM data acquisition**

Cryo-EM images were collected in counting mode on a Talos Arctica (Thermo Fisher) operated at 200 kV and equipped with a K2 Summit direct electron detector (Gatan) in Nanoprobe mode at the IECB in Bordeaux (France). Images were recorded with SerialEM with a magnified pixel size of 0.93 Å at a magnification of 45,000 to record 38 movies frames with an exposure time of 3.8 seconds using a dose rate of 0.94 electron per Å<sup>2</sup> per frame for a total accumulated dose of 35.71 electrons per Å<sup>2</sup>. The final datasets were composed of 7,450 micrographs with defocus values ranging from -0.2 to -1.8 µm.

### **QUANTIFICATION AND STATISTICAL ANALYSIS**

#### **Analysis of inverse toeprinting data**

Unless indicated otherwise, data analysis was carried out using a series of custom python scripts. Read pairs were assembled using PEAR v0.9.10 (Zhang et al, 2014) on a computer with a 2.7 GHz Intel Core i7 processor and 16 GB 1,600 MHz DDR3 memory, with the maximal proportion of uncalled bases in a read set to 0 (–u option) and the upper bound for the resulting quality score set to 126 (–c option). The 5' flanking region was defined as GTATAAGGAGGAAAAAAT, whereas the 3' flanking region was GGTATCTCGGTGTGACTG. A maximum of two mismatches within each of these flanking regions was tolerated, whereas all other reads were discarded. Trimming of the retained reads resulted in sequences with a start codon directly at the 5' end and the site of RNase R cleavage at the 3' end (**Supplementary Data Figure 1**). Reads were required to have a minimum quality score of 30 at all positions and contain no Ns. The data underlying the volcano plots was analyzed using a custom python3 script to count the reads per motif, and DESeq2 to compute the statistics. The graphs were produced with matplotlib 3.3.2.

### **Cryo-EM image processing**

Data were processed in Relion v3.1 according to the scheme presented in **Supplementary Data Figure 5**. Briefly, the raw movie frames were summed and corrected for drift and beam-induced motion at the micrograph level using MotionCor2 v1.3.1 in Relion v3.1. The resolution range of each micrograph and the contrast transfer function (CTF) were estimated with Gctf v1.18. Best two-dimensional classes were selected by subsequent rounds of two-dimensional classifications of the particles obtained by automated picking in Relion v3.1. Three-dimensional classification was performed in Relion v3.1 in two steps: (1) unsupervised classification with particles downsized four times; (2) focused classification on all three tRNA sites and EF-Tu protein with background subtraction and particles downsized twice. Classes containing A-, P- and E-site tRNAs were further selected for 3D reconstruction and CTF refinement in Relion v3.1, followed by Bayesian polishing. The final reconstruction was sharpened by applying a negative sharpening B-factor of -10 in Relion v3.1. The resolution for the electron density map was estimated using the “gold standard” criterion (FSC=0.143) resulting in a final reconstruction of 2.8 Å. Local-resolution estimation was done using Relion v3.1. Pixel size was optimized by generating maps with different pixel sizes and assessing the correlation in Chimera v1.14.

### **Atomic model building and refinement**

An initial model of the TcmX-70S complex was obtained by placing the coordinates for an E. coli 70S ribosome (PDB: 6TBV) and for the TcmX antibiotic (PDB: 6Y69) into the cryo-EM density map with Coot v0.8.9.2, and was refined using the rigid body refinement procedure in Phenix v1.17.1. The nascent chain, mRNA and A-, P- and E-site tRNAs were de novo modeled into the corresponding density using Coot v0.8.9.2. Automatic map sharpening was performed in Phenix v1.17.1 and the final combined molecular model were then refined through multiple rounds of real space refinement procedure in Phenix v1.17.1 with restraints and manual rebuilding in Coot v0.8.9.2. The model was validated with MolProbity v4.5.1.

### **Figure preparation**

The inverse-toe-printing plots were produced with python3 and matplotlib 3.3.2. The sharpened map from Phenix v1.17.1 was used to prepare all figures except **Supplementary Data Figure 6.A**, for which a post-processed map from Relion v3.1 was used. Figures showing cryo-EM density or atomic models were prepared using Chimera v.1.14, ChimeraX v.0.91 or PyMOL v.1.7.4 (Schrödinger).

## REFERENCES

- Adinarayana, G., Venkateshan, M.R., Bapiraju, V.V.S.N.K., Sujatha, P., Premkumar, J., Ellaiah, P., and Zeeck, A. (2006). [Cytotoxic compounds from the marine actinobacterium]. *Bioorg. Khim.* 32, 328–334.
- Anderson, M.G., Khoo, C.L.-Y., and Rickards, R.W. (1989). OXIDATION PROCESSES IN THE BIOSYNTHESIS OF THE TETRACENOMYCIN AND ELLORAMYCIN ANTIBIOTICS. *J. Antibiot. (Tokyo)* 42, 640–643.
- Arenz, S., Meydan, S., Starosta, A.L., Berninghausen, O., Beckmann, R., Vázquez-Laslop, N., and Wilson, D.N. (2014a). Drug sensing by the ribosome induces translational arrest via active site perturbation. *Mol. Cell* 56, 446–452.
- Arenz, S., Ramu, H., Gupta, P., Berninghausen, O., Beckmann, R., Vázquez-Laslop, N., Mankin, A.S., and Wilson, D.N. (2014b). Molecular basis for erythromycin-dependent ribosome stalling during translation of the ErmBL leader peptide. *Nat. Commun.* 5, 3501.
- Arenz, S., Bock, L.V., Graf, M., Innis, C.A., Beckmann, R., Grubmüller, H., Vaiana, A.C., and Wilson, D.N. (2016). A combined cryo-EM and molecular dynamics approach reveals the mechanism of ErmBL-mediated translation arrest. *Nat. Commun.* 7.
- Bailey, M., Chettiath, T., and Mankin, A.S. (2008). Induction of erm(C) expression by noninducing antibiotics. *Antimicrob. Agents Chemother.* 52, 866–874.
- Beckert, B., Leroy, E.C., Sothiselvam, S., Bock, L.V., Svetlov, M.S., Graf, M., Arenz, S., Abdelshahid, M., Seip, B., Grubmüller, H., et al. (2021). Structural and mechanistic basis for translation inhibition by macrolide and ketolide antibiotics. *Nat. Commun.* 12, 4466.
- Dratz, H., Reuschenbach, P., Zähler, H., Rohr, J., and Zeeck, A. (1985). Metabolic products of microorganisms. 225. Elloramycin, a new anthracycline-like antibiotic from *Streptomyces olivaceus*. Isolation, characterization, structure and biological properties. *J. Antibiot. (Tokyo)* 38, 1291–1301.
- Egert, E., Noltemeyer, M., Siebers, J., Rohr, J., and Zeeck, A. (1992). THE STRUCTURE OF TETRACENOMYCIN C. *J. Antibiot. (Tokyo)* 45, 1190–1192.
- Hartz, D., McPheeters, D.S., Traut, R., and Gold, L. (1988). Extension inhibition analysis of translation initiation complexes. *Methods Enzymol.* 164, 419–425.
- Huang, C., Yang, C., Zhu, Y., Zhang, W., Yuan, C., and Zhang, C. (2018). Marine Bacterial Aromatic Polyketides From Host-Dependent Heterologous Expression and Fungal Mode of Cyclization. *Front. Chem.* 0.
- Jenner, L., Starosta, A.L., Terry, D.S., Mikolajka, A., Filonava, L., Yusupov, M., Blanchard, S.C., Wilson, D.N., and Yusupova, G. (2013). Structural basis for potent inhibitory activity of the antibiotic tigecycline during protein synthesis. *Proc. Natl. Acad. Sci.* 110, 3812–3816.
- Kannan, K., Kanabar, P., Schryer, D., Florin, T., Oh, E., Bahroos, N., Tenson, T., Weissman, J.S., and Mankin, A.S. (2014). The general mode of translation inhibition by macrolide antibiotics. *Proc. Natl. Acad. Sci.* 111, 15958–15963.



Katz, L., and Baltz, R.H. (2016). Natural product discovery: past, present, and future. *J. Ind. Microbiol. Biotechnol.* **43**, 155–176.

Leclercq, R. (2002). Mechanisms of Resistance to Macrolides and Lincosamides: Nature of the Resistance Elements and Their Clinical Implications. *Clin. Infect. Dis.* **34**, 482–492.

Liu, B., Tan, Y., Gan, M.-L., Zhou, H.-X., Wang, Y.-G., Ping, Y.-H., Li, B., Yang, Z.-Y., and Xiao, C.-L. (2014). [Identification of tetracenomycin X from a marine-derived *Saccharothrix* sp. guided by genes sequence analysis]. *Yao Xue Xue Bao* **49**, 230–236.

Mondal, S., Pathak, B.K., Ray, S., and Barat, C. (2014). Impact of P-Site tRNA and Antibiotics on Ribosome Mediated Protein Folding: Studies Using the *Escherichia coli* Ribosome. *PLOS ONE* **9**, e101293.

Orelle, C., Carlson, S., Kaushal, B., Almutairi, M.M., Liu, H., Ochabowicz, A., Quan, S., Pham, V.C., Squires, C.L., Murphy, B.T., et al. (2013). Tools for Characterizing Bacterial Protein Synthesis Inhibitors. *Antimicrob. Agents Chemother.* **57**, 5994–6004.

Osterman, I.A., Wieland, M., Maviza, T.P., Lashkevich, K.A., Lukianov, D.A., Komarova, E.S., Zakalyukina, Y.V., Buschauer, R., Shiriaev, D.I., Leyn, S.A., et al. (2020). Tetracenomycin X inhibits translation by binding within the ribosomal exit tunnel. *Nat. Chem. Biol.* **16**, 1071–1077.

Polikanov, Y.S., Steitz, T.A., and Innis, C.A. (2014). A proton wire to couple aminoacyl-tRNA accommodation and peptide-bond formation on the ribosome. *Nat. Struct. Mol. Biol.* **21**, 787–793.

Polikanov, Y.S., Starosta, A.L., Juetter, M.F., Altman, R.B., Terry, D.S., Lu, W., Burnett, B.J., Dinos, G., Reynolds, K.A., Blanchard, S.C., et al. (2015). Distinct tRNA Accommodation Intermediates Observed on the Ribosome with the Antibiotics Hygromycin A and A201A. *Mol. Cell* **58**, 832–844.

Qiao, X., Gan, M., Wang, C., Liu, B., Shang, Y., Li, Y., and Chen, S. (2019). Tetracenomycin X Exerts Antitumour Activity in Lung Cancer Cells through the Downregulation of Cyclin D1. *Mar. Drugs* **17**, 63.

Ramu, H., Mankin, A., and Vazquez-Laslop, N. (2009). Programmed drug-dependent ribosome stalling. *Mol. Microbiol.* **71**, 811–824.

Rohr, J., and Zeeck, A. (1990). Structure-activity relationships of elloramycin and tetracenomycin C. *J. Antibiot. (Tokyo)* **43**, 1169–1178.

Schmeing, T.M., Huang, K.S., Strobel, S.A., and Steitz, T.A. (2005). An induced-fit mechanism to promote peptide bond formation and exclude hydrolysis of peptidyl-tRNA. *Nature* **438**, 520–524.

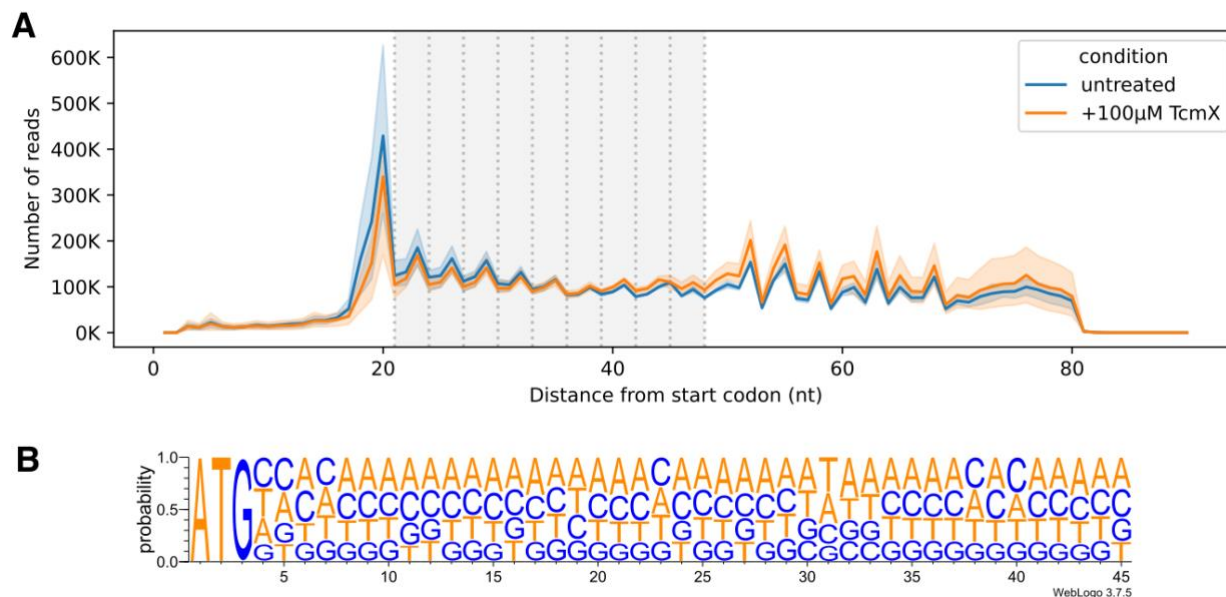
Seip, B., Sacheau, G., Dupuy, D., and Innis, C.A. (2018). Ribosomal stalling landscapes revealed by high-throughput inverse toeprinting of mRNA libraries. *Life Sci. Alliance* **1**.

Shimizu, Y., Inoue, A., Tomari, Y., Suzuki, T., Yokogawa, T., Nishikawa, K., and Ueda, T. (2001). Cell-free translation reconstituted with purified components. *Nat. Biotechnol.* **19**, 751–755.

Starosta, A.L., Lassak, J., Peil, L., Atkinson, G.C., Virumäe, K., Tenson, T., Remme, J., Jung, K., and Wilson, D.N. (2014). Translational stalling at polyproline stretches is modulated by the sequence context upstream of the stall site. *Nucleic Acids Res.* **42**, 10711–10719.

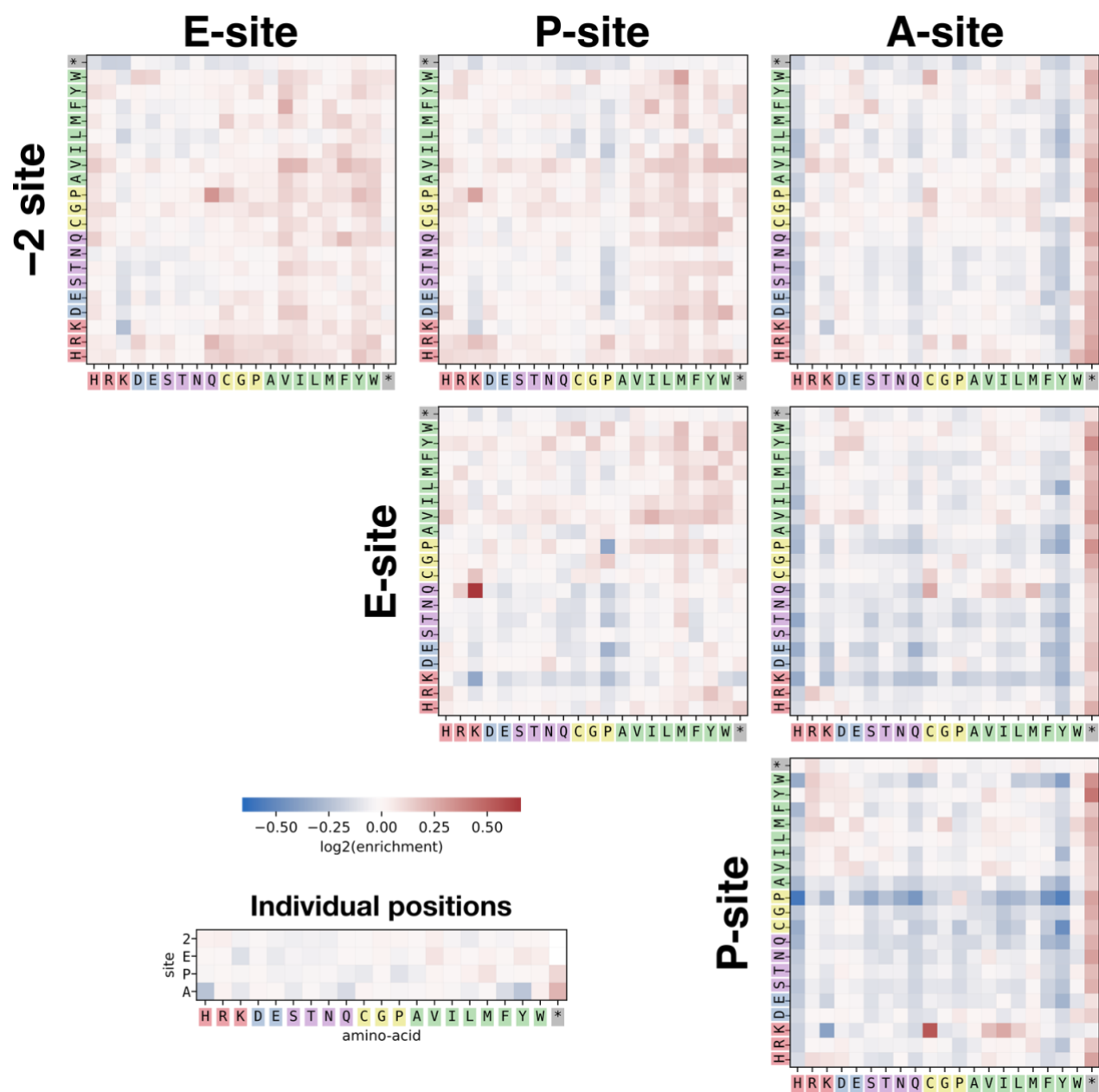
- Svetlov, M.S., Koller, T.O., Meydan, S., Shankar, V., Klepacki, D., Polacek, N., Guydosh, N.R., Vázquez-Laslop, N., Wilson, D.N., and Mankin, A.S. (2021). Context-specific action of macrolide antibiotics on the eukaryotic ribosome. *Nat. Commun.* **12**, 2803.
- Svidritskiy, E., and Korostelev, A.A. (2018). Mechanism of Inhibition of Translation Termination by Blasticidin S. *J. Mol. Biol.* **430**, 591–593.
- Tikhonova, E.B., and Zgurskaya, H.I. (2004). AcrA, AcrB, and TolC of *Escherichia coli* Form a Stable Intermembrane Multidrug Efflux Complex \*. *J. Biol. Chem.* **279**, 32116–32124.
- Vázquez-Laslop, N., and Mankin, A.S. (2018). How Macrolide Antibiotics Work. *Trends Biochem. Sci.* **43**, 668–684.
- Vazquez-Laslop, N., Thum, C., and Mankin, A.S. (2008). Molecular Mechanism of Drug-Dependent Ribosome Stalling. *Mol. Cell* **30**, 190–202.
- Vincent, H.A., and Deutscher, M.P. (2006). Substrate Recognition and Catalysis by the Exoribonuclease RNase R\*. *J. Biol. Chem.* **281**, 29769–29775.
- Wang, J., Zhang, R., Chen, X., Sun, X., Yan, Y., Shen, X., and Yuan, Q. (2020). Biosynthesis of aromatic polyketides in microorganisms using type II polyketide synthases. *Microb. Cell Factories* **19**, 110.
- Weber, W., Zähler, H., Siebers, J., Schröder, K., and Zeeck, A. (1979). [Metabolic products of microorganisms. 175. Tetracenomycin C (author's transl)]. *Arch. Microbiol.* **121**, 111–116.
- Zhang, Z., Pan, H.-X., and Tang, G.-L. (2017). New insights into bacterial type II polyketide biosynthesis. *F1000Research* **6**, 172.

## SUPPLEMENTARY DATA

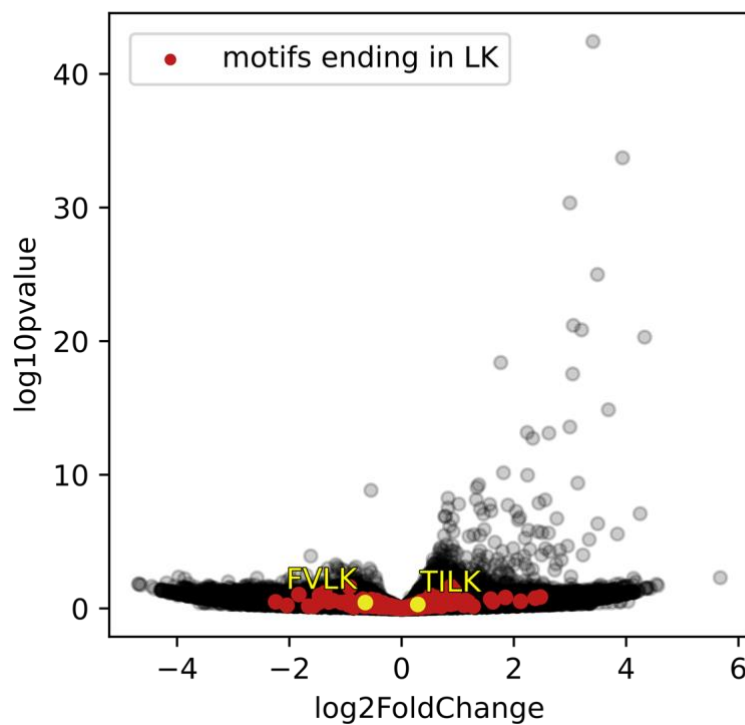


### Supplementary Figure 1: Inverse toeprints analysis.

A. Number of reads obtained in the NGS in function of the distance from the start codon for untreated and TcmX treated samples. The grey area highlights the reads that were selected for further analysis, as this corresponds to the region in which the codons are well defined (grey dotted lines). The error bands show the 95% confidence interval of the average of the 3 replicates. B. Nucleotide frequency of the raw reads confirm that the (NNN)15 library was unbiased. The initial ATG is the start codon.

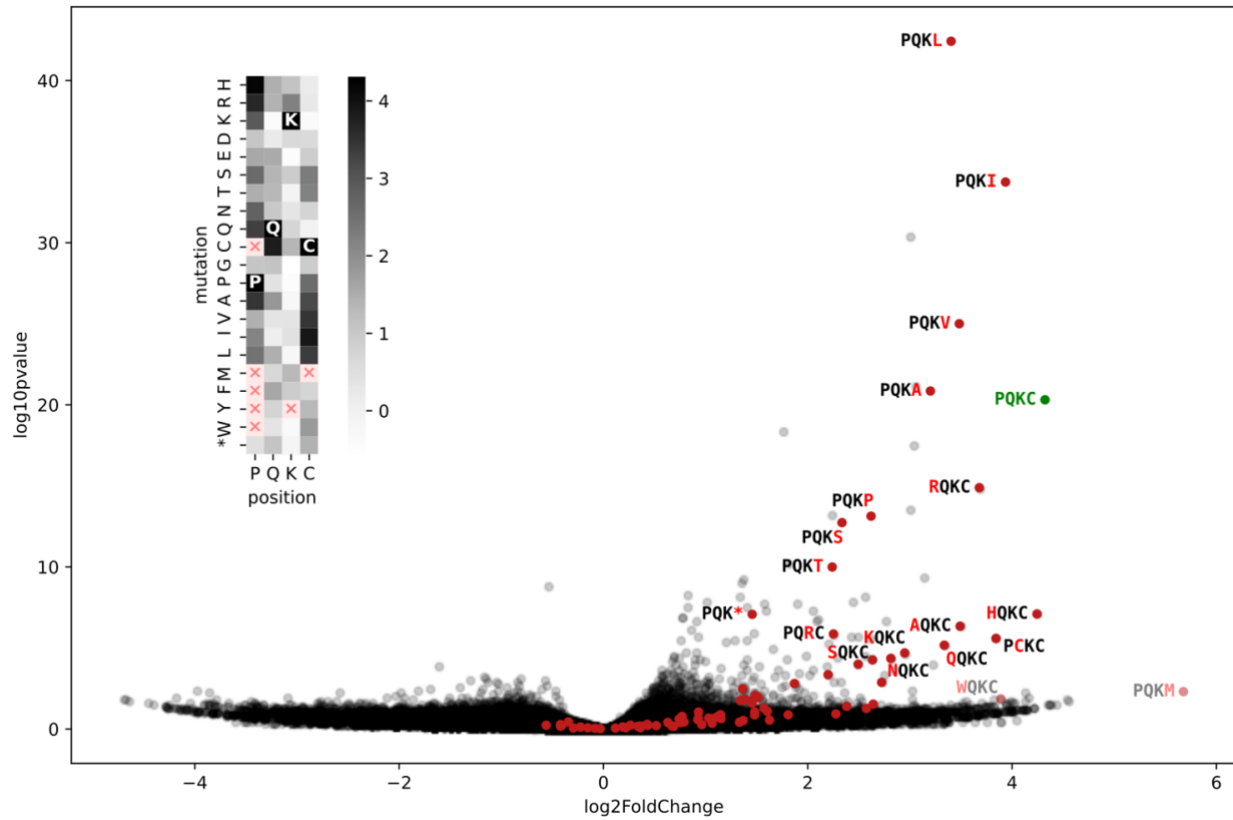


Supplementary Figure 2: Heatmaps of the log<sub>2</sub>(TcmX/Untreated) enrichment for individual -2/E/P/A positions and combinations thereof.



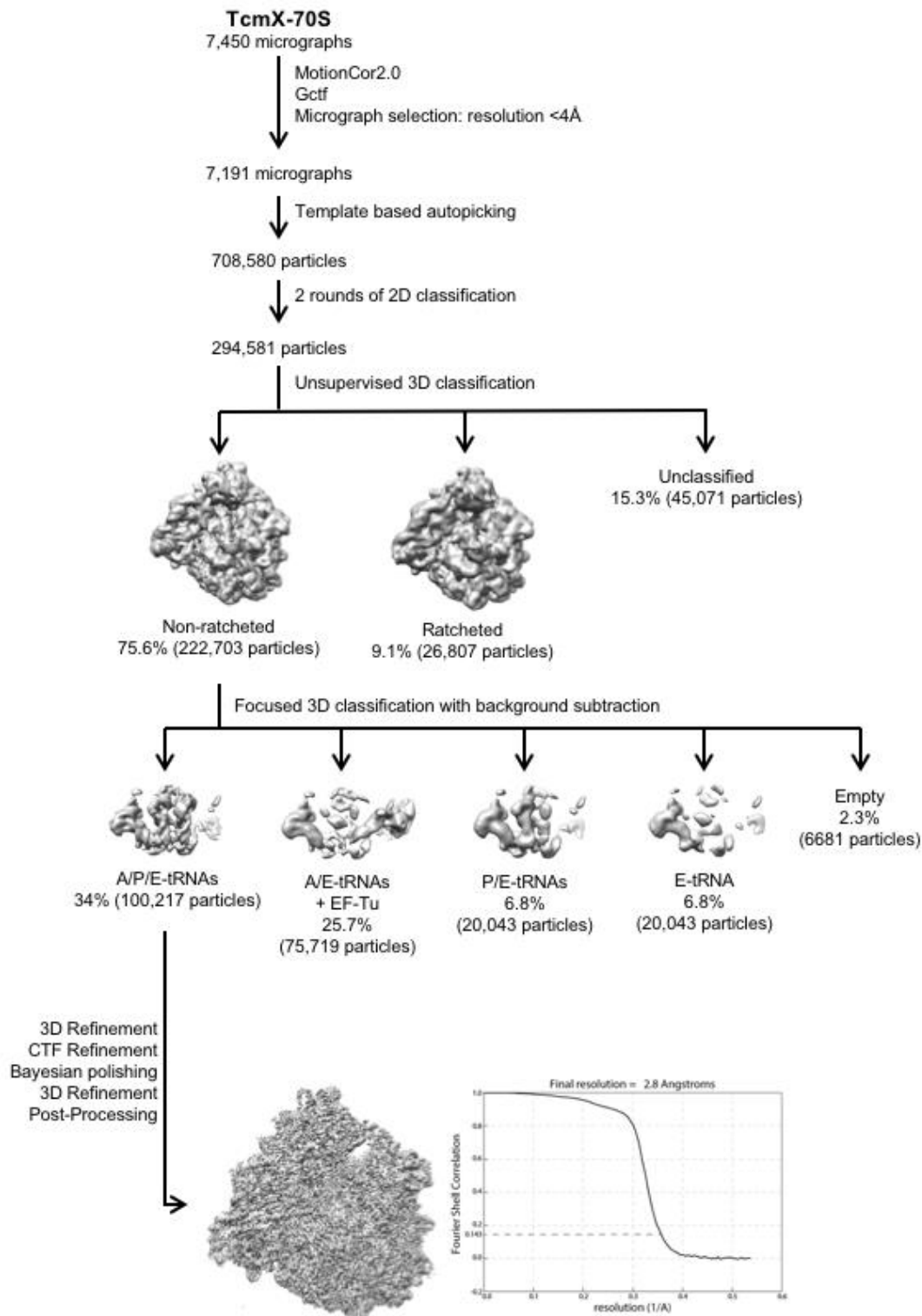
**Supplementary Figure 3: Peptides with LK in the P/A-sites are not strong blockers.**

Volcano plot of statistical significance against enrichment ( $\log_2\text{FoldChange}$ ) for 4 amino-acids motifs (-2 to A-sites). The points in red are the motifs ending in LK and yellow the two motifs described in (Osterman et al., 2020).

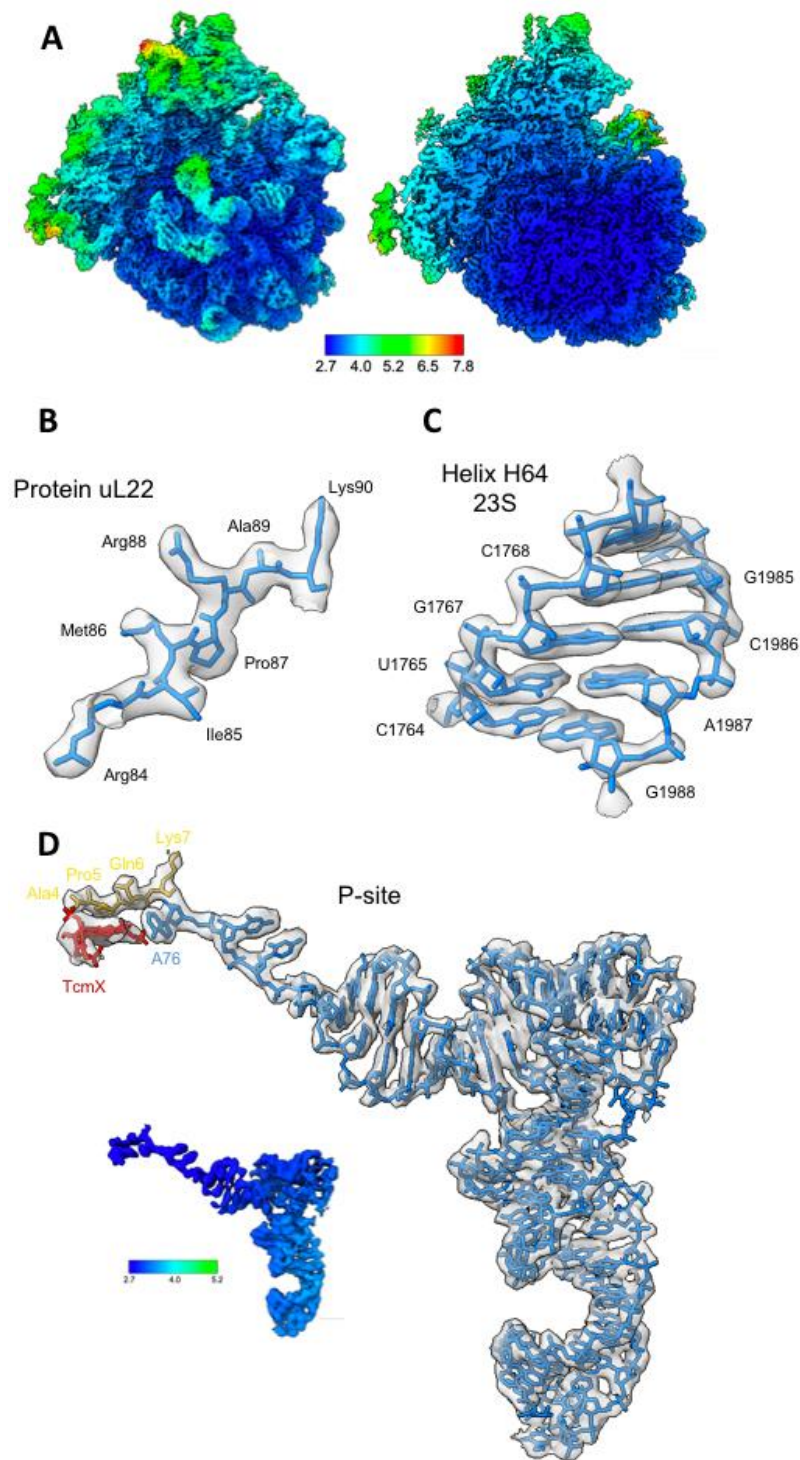


**Supplementary Figure 4: Single amino-acid variants of the PQKC motif.**

Volcano plot of statistical significance against enrichment (log2FoldChange) for 4 amino-acids motifs (-2 to A-sites). The points in red are the point amino-acid variants of the PQKC motif (in green). Most of the variants that conserved stalling efficiency are variants of the last position to hydrophobic amino-acids.



**Supplementary Figure 5: Flowchart of cryo-EM data processing for MA<sub>3</sub>PQKCA<sub>3</sub>\*-TcmX-70S complex the datasets.** The flowchart shows the workflow used to process and analyze cryo-EM data using Relion 3.1. Structure of MA<sub>3</sub>PQKCA<sub>3</sub>\*-TcmX-70S complex could be refined to an overall resolution of 2.8 Å using a Fourier shell correlation (FSC) cutoff of 0.143.



**Supplementary Figure 6: Quality of the cryo-EM reconstructions.**

A. Refined cryo-EM density map obtained in *Relion* v3.1 filtered and colored by local resolution estimation values in *Chimera* v1.14. A cross-section of the same map is also shown. B,C and D. Representative cryo-EM densities for (B) the tunnel extension of ribosomal protein uL22, (C) helix H64 of the 23S rRNA, and (D) P-site tRNA with the nascent peptide and TcmX. A refined cryo-EM density map of the P-site tRNA filtered and colored by local resolution estimation is also shown.



**Supplementary Table: Reagents and oligonucleotides**

REAGENT or RESOURCE	SOURCE	IDENTIFIER
Chemicals, Peptides, and Recombinant Proteins		
Acrylamide/Bis-Acrylamide 37.5:1, 40%	Biosolve	Cat#014223
Ammonium persulfate	Sigma-Aldrich	Cat#A3678-25G
Bromophenol blue	Fisher Scientific	Cat#1010223280
Boric acid	Sigma-Aldrich	Cat#B7901-500G
Deoxynucleotide (dNTP) Solution Mix 10mM	New England Biolabs	Cat#N0447S
Diethyl Pyrocarbonate for DEPC water	Sigma-Aldrich	Cat#D5758-100ML
Merck™ Ultrapure Water for Molecular Biology	FisherScientific	Cat#15161735
Adenosine 5'-triphosphate disodium salt hydrate	Sigma-Aldrich	Cat#A2383-25G
CTP	Jena Bioscience	Cat#NU-1011-1G
GTP	Jena Bioscience	Cat#NU-1012-1G
UTP	Jena Bioscience	Cat#NU-1013-1G
Guanosine-5'-thiophosphatedisodium salt	Genaxxon Bioscience	Cat#S5402.0025
SYBR Gold nucleic acid gel stain	Invitrogen	Cat#S11494
Trizma Base	Sigma-Aldrich	Cat#T1503-1KG
Acetic acid	Sigma-Aldrich	Cat#33209-1L
Trisodium citrate dihydrate	Sigma-Aldrich	Cat#S1804-500G
Ethanol	Sigma-Aldrich	Cat#32221-2.5L-M
N,N,N',N'-Tetramethylethylenediamine	Euromedex	Cat#50406-A
Urea	Sigma-Aldrich	Cat#U5378-1KG
Magnesium chloride hexahydrate	Sigma-Aldrich	Cat#M2670-1KG
Magnesium acetate tetrahydrate	Sigma-Aldrich	Cat#M5661-250G
Potassium glutamate	Sigma-Aldrich	Cat#49601-100G
Spermidine	Sigma-Aldrich	Cat#S2626-5G
NH4-acetate	Sigma-Aldrich	Cat#A1542-500G
Biotin (Long Arm) maleimide	Vectorlabs	Cat#SP-1501
Bis-Tris	Sigma-Aldrich	Cat#B7535-500G
N,N-Dimethylformamide	Sigma-Aldrich	Cat#D4551-250ML
Sodium chloride	VWR	Cat#27788.366
Tween 20	Sigma-Aldrich	Cat#P1379-100ML
Dynabeads M-280 Streptavidin	ThermoFisher Scientific	Cat#11205D
HEPES	Sigma-Aldrich	Cat#H4034-1KG
Potassium hydroxide	Sigma-Aldrich	Cat#P1767-250G
Hydrochloric acid	Sigma-Aldrich	Cat#30721-2.5L-M
Phusion polymerase	Recombinant	
Phusion HF buffer Pack 5X	New England Biolabs	Cat#B0518S
<i>E. coli</i> Poly(A) Polymerase supplied with 10X Poly(A) Polymerase buffer	New England Biolabs	Cat#M0276L
T7 RNA polymerase (P266L)	Recombinant	

Ribonuclease R	Recombinant, kind gift from Dr. Arun Malhotra (University of Miami)	
T4 RNA ligase 2, truncated supplied with 10X T4 RNA ligase reaction buffer and 50 % PEG8000	New England Biolabs	Cat#M0242L
SuperScript™ III Reverse Transcriptase supplied with a vial (1 mL) of 5X first-strand buffer and a vial (500 µL) of 100 mM DTT	ThermoFisher	Cat#18080044
EcoRV-HF	New England Biolabs	Cat#R3195S
Agilent High Sensitivity DNA Kit	Agilent	Cat#5067-4626
Powdered milk	Régilait	N/A
Streptavidin-Alkaline Phosphatase	Promega	Cat#V5591
NBT/BCIP detection kit	Promega	Cat#S3771
Xylene Cyanol	Biosolve	Cat#242223
DNA Ladder: Low Molecular Weight DNA Ladder	New England Biolabs	Cat#N3233S
RNA Ladder: Century-Plus RNA Marker	ThermoFisher Scientific	Cat#AM7145
MinElute PCR Purification Kit™	Qiagen	Cat#28006
RNA Clean & Concentrator™-5	Zymo research	Cat#R1015
Isopropanol	Sigma-Aldrich	Cat#I9516-4L
GlycoBlue coprecipitant	ThermoFisher Scientific	Cat#AM9515
MiliporeSigma™ Ultrapure water for Molecular Biology	Fisher Scientific	Cat#09-739-006
Avian Myeloblastosis Virus Reverse Transcriptase	Promega	Cat#M5101
Sodium Hydroxide	Sigma-Aldrich	Cat#221465
QIAquick Nucleotide removal Kit™	Qiagen	Cat#28304
Dideoxy-nucleotides	GE Healthcare Life Sciences	Cat#27-2045-01
Thermo Sequenase Dye Primer Manual Cycle Sequencing Kit	ThermoFisher Scientific	Cat#792601KT
ExoSAP-IT reagent	ThermoFischer Scientific	Cat#PN78200
QuikChange Lightning Site-Directed Mutagenesis Kit	Agilent Technologies	Cat#210518
Critical Commercial Assays		
PURExpress Δ RF123 Δ Ribosomes Kit	New England Biolabs	Cat#E6850ZZ
Oligonucleotides		
iTP/TP_frag1_T7_RBS_ATG_f CGA-TCG-AAT-TCT-AAT-ACG-ACT-CAC-TAT-AGG-GCT- TAA-GTA-TAA-GGA-GGA-AAA-AAT-ATG	Seip et al., 2018	Eurogentec custom synthesis



iTP_NGS_adapter_index22+2 CAA-GCA-GAA-GAC-GGC-ATA-CGA-GAT-CGT-ACG-GTG- ACT-GGA-GTT-CAG-ACG-TGT-GCT-CTT-CCG-ATC-GAT- TGA-TGG-TGC-CTA-CAG	This work	Eurogentec custom synthesis
TP_frag2_r CTT-GCC-TGC-GCA-CGA-AGA-GTA-CGG-ATG-TTG-TTC- AGA-GTC-AGT-TAT-TAT-TCG-CT	This work	Eurogentec custom synthesis
TP_frag2_NV1_r GGT-TAT-AAT-GAA-TTT-TGC-TTA-TTA-ACC-TTG-CCT- GCG-CAC-G	This work	Eurogentec custom synthesis
TP_short_r GGT-TAT-AAT-GAA-TTT-TGC-TT	This work	Eurogentec custom synthesis
TP_RT_yakima-yellow_r /5YakYel/GGT-TAT-AAT-GAA-TTT-TGC-TTA-TTA-AC	This work	Eurogentec custom synthesis
TP_MAAAPQKCAAA*_f GTA-TAA-GGA-GGA-AAA-AAT-ATG-GCA-GCA-GCA-CCG- CAG-AAG-TGT- GCA-GCA-GCA-TGA-AGC-GAA-TAA-TAA- CTG-ACT-CTG	This work	Eurogentec custom synthesis
pZ $\alpha$ _MAAAPQKC_fwd TAA-TTA-AGT-CTT-ATA-AGG-AGG-AAA-ACA-TAT-GGC- AGC-AGC-ACC-GCA-GAA-GTG-TAC-AGT-TCA-TTA-TCA- ACC-AAA-CAA-AAA-ATA-AG	This work	Eurogentec custom synthesis
pZ $\alpha$ _MAAAPQKC_rvs CTT-ATT-TTT-TGT-TTG-GTT-GAT-AAT-GAA-CTG-TAC- ACT-TCT-GCG-GTG-CTG-CTG-CCA-TAT-GTT-TTC-CTC- CTT-ATA-AGA-CTT-AAT-TA	This work	Eurogentec custom synthesis
Software and Algorithms		
Image Lab	Bio-RAD	<a href="https://www.bio-rad.com/webroot/web/pdf/lsr/literature/10000076953.pdf">https://www.bio-rad.com/webroot/web/pdf/lsr/literature/10000076953.pdf</a>
python 3.8		<a href="https://www.python.org/">https://www.python.org/</a>
numpy 1.19.2		<a href="https://numpy.org/">https://numpy.org/</a>
pandas 1.1		<a href="https://pandas.pydata.org/">https://pandas.pydata.org/</a>
matplotlib 3.3.2		<a href="https://matplotlib.org/">https://matplotlib.org/</a>
seaborn 0.11		<a href="https://seaborn.pydata.org/">https://seaborn.pydata.org/</a>
scipy 1.5		<a href="https://www.scipy.org/">https://www.scipy.org/</a>

#### 4.2.4. The five-membered ring aminocyclitol antibiotic pactamycin

Pactamycin is a five-membered ring aminocyclitol, and is therefore structurally related to aminoglycoside antibiotics which are six-membered aminocyclitol compounds. Pactamycin is an antibiotic produced by *Streptomyces pactum* and is active against a variety of Gram-positive and Gram-negative microorganisms, and against several animal tumor lines in culture or *in vivo* (Bhuyan, 1962; White, 1962). Pactamycin is today only used as a tool for biochemical research because of its toxicity and also because it targets protein synthesis in bacteria, archaea, and eukaryotes by binding to the small ribosomal subunit (Brodersen et al., 2000; Egebjerg and Garrett, 1991; Mankin, 1997; Woodcock et al., 1991). Despite the fact that pactamycin was discovered almost seven decades ago, its detailed mechanism of action is still unclear. Pactamycin was originally viewed as a specific inhibitor of initiation (Gale, 1981), but was more recently described as an inhibitor of translocation (Brodersen et al., 2000; Dinos et al., 2004). Several observations support this idea, beginning with the available structural data. The single binding site for pactamycin on the bacterial ribosome was first identified from an X-ray crystallographic structure of the 30S subunit of *Thermus thermophilus* determined at 3.4 Å resolution (Brodersen et al., 2000). Pactamycin binds between the anticodon stem loop of the E-site tRNA and the mRNA. The two distal rings of pactamycin stack upon each other and G693 at the tip of h23b of the 16S rRNA, while the central ring interacts with C795 and C796 in h24a. By doing so, pactamycin mimics the last two nucleotides of the mRNA E-site codon and displaces it by over 12 Å. This displacement of the mRNA leads to the inhibition of its movement and therefore blocks translocation. In addition, two recent crystal structures show pactamycin bound to the complete *E. coli* 70S ribosome and reveal that this antibiotic can displace the mRNA within the E site (**Figure 29**) (Polikanov et al., 2014b). In agreement with these structural data, pactamycin protects the universally conserved bases G693 and C795 of the 16S rRNA from chemical modification (Egebjerg and Garrett, 1991; Woodcock et al., 1991). In addition, pactamycin-resistant mutants of the archaeon *Halobacterium halobium* were identified at corresponding positions, namely A694G, C795U, and C796U (Mankin, 1997). More interestingly, by analyzing the effect of pactamycin on the steps of translation initiation and elongation on *E. coli* ribosomes, pactamycin was shown to block the translocation of certain acylated-tRNAs from A to P site completely (tRNA<sup>Val</sup>, tRNA<sup>Lys</sup>), whereas acylated-tRNA<sup>Phe</sup> remained unaffected (Dinos et al., 2004). This observation suggested that the inhibition of pactamycin might depend on the nature of the mRNA/tRNA complex. In addition, tRNA binding to the P site was suggested to be dictated by the conformational state of the universally

conserved residues G693 and C795 of the 16S rRNA (Dinos et al., 2004). Finally, *in vitro* translation of several model genes was shown to be arrested at specific sites by pactamycin, confirming its ability to block translation in a context-dependent manner (Orelle et al., 2013). None of the currently available structural data explain how the nature of the mRNA codon, the tRNA body, and/or the nascent chain might influence the action of pactamycin, and the precise sequence dependent of this drug's effect on the ribosome remains unknown.

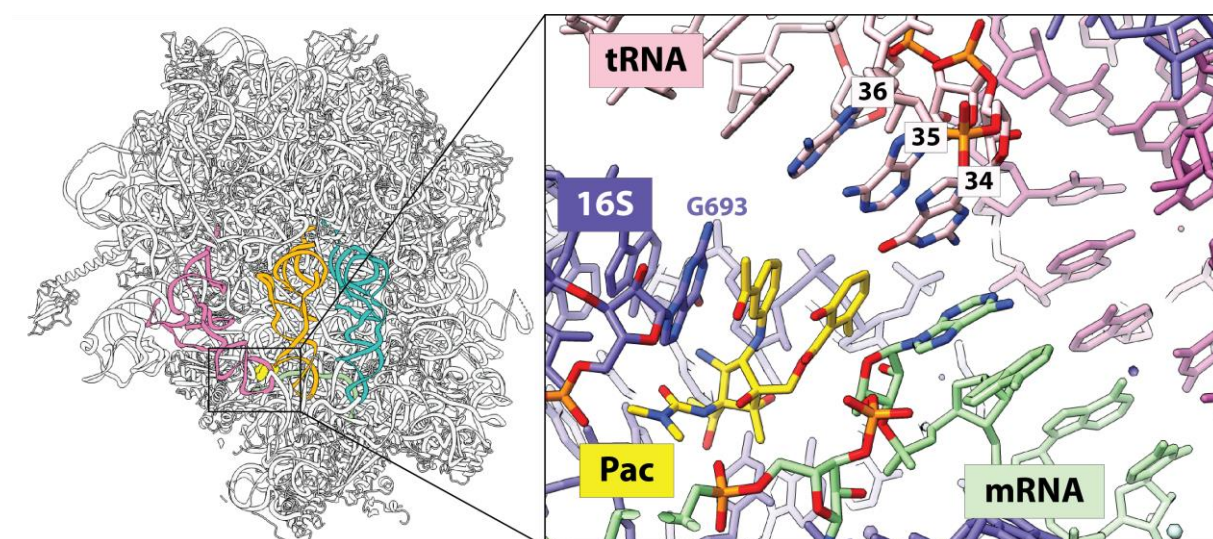


**Figure 29 : Pactamycin binding site**

Pactamycin (Pac) (colored in yellow) binds to the 70S ribosome (grey) in the path of the mRNA (pale green) and stacks upon G693 of the 16S rRNA (blue) such that two of the ring moieties of pactamycin mimic the last two nucleotides of the E-site codon. The E-site tRNA is colored in pink, the P-site tRNA is colored in light orange and the A-site tRNA is colored in cyan. PDB 4W2G (Polikanov et al., 2014b).

In light of these preliminary data, I decided to perform inverse toeprinting experiments to visualize how the addition of pactamycin alters the *in vitro* translational landscape of *E. coli* ribosomes. To do so, I translated the NNN15 library in the absence or presence of 100  $\mu$ M of pactamycin and performed three biological replicates of the experiment. The samples were sent for NGS to obtain 26,526,619 reads in total for the negative control condition and 39,256,251 reads for the pactamycin condition. The reads were then processed and reads displaying Q-scores lower than 30 were eliminated (see section 4.2.1 for more details). The details concerning the evolution of the reads number are presented in **Table 5**. After processing, I compared the size distribution of inverse toeprints obtained in the absence of antibiotic to the size distribution of inverse toeprints obtained in the presence of pactamycin and only the reads matching the 3-nucleotides periodicity were size-selected and kept for the analysis (**Figure 30**).

SAMPLES	NUMBER OF READS			
	After sequencing	After processing	After selection	Final total (3 replicates)
NNN15_NoAB-I	9,807,745	7,517,369	2,707,649	7,623,256
NNN15_NoAB-II	8,947,224	6,980,613	2,320,570	
NNN15_NoAB-III	7,771,650	6,774,980	2,595,037	
NNN15_Pactamycin-I	9,703,268	7,986,775	2,442,313	7,646,600
NNN15_Pactamycin-II	8,608,701	7,848,884	2,298,117	
NNN15_Pactamycin-III	20,944,282	9,064,716	2,906,170	

**Table 5: Summary of reads processing**

Repartition of the reads obtained for the three biological replicates of the NNN15 library translated in absence or presence of pactamycin directly after NGS, after processing (assembling/trimming/quality control, see section 4.2.1) and after size selection of the inverse toeprints matching the 3-nucleotides periodicity.

Pactamycin addition leads to a strong increase in stalled ribosomes at first codons positions, and notably at the start codon, compared to the no antibiotic control (**Figure 30**). This observation is consistent with previous studies showing that pactamycin inhibits the transition from initiation to elongation (Gale, 1981) but also with studies showing that pactamycin inhibits the elongation phase (Brodersen et al., 2000; Dinos et al., 2004).

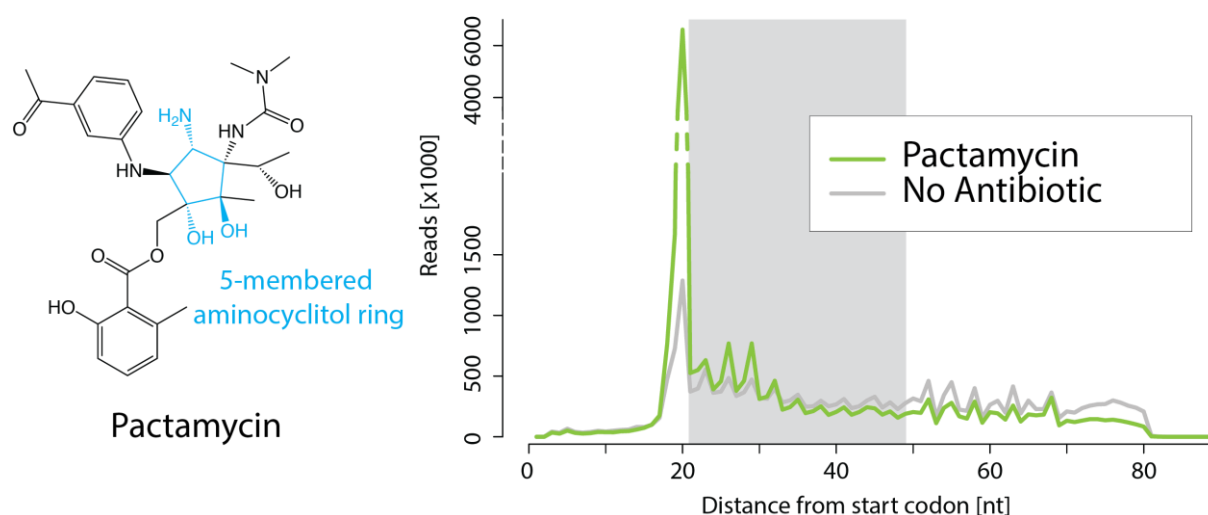


**Figure 30 : Structure of pactamycin and size distribution of inverse toeprints**

Structures of pactamycin. Repartition of the inverse toeprints obtained in the NGS in function of the distance from the start codon for untreated (grey line) and pactamycin-treated (green line) samples, where the grey area highlights the reads that were selected for the analysis, as this corresponds to the region in which the codons are well defined. Ribosomes stalled on the start codon were excluded from the analysis.

From the inverse toeprints following the 3-nucleotide periodicity (initiation codon excluded), I calculated the fold change in the frequencies of all possible codons in the A, P and E sites of the ribosome in the presence of pactamycin relative to their frequency in the absence of drug. Since the antibiotic is known to be positioned between the E-site tRNA and the mRNA (**Figure 29**), I expected to see significant changes in the frequency of the E and/or P site codons.

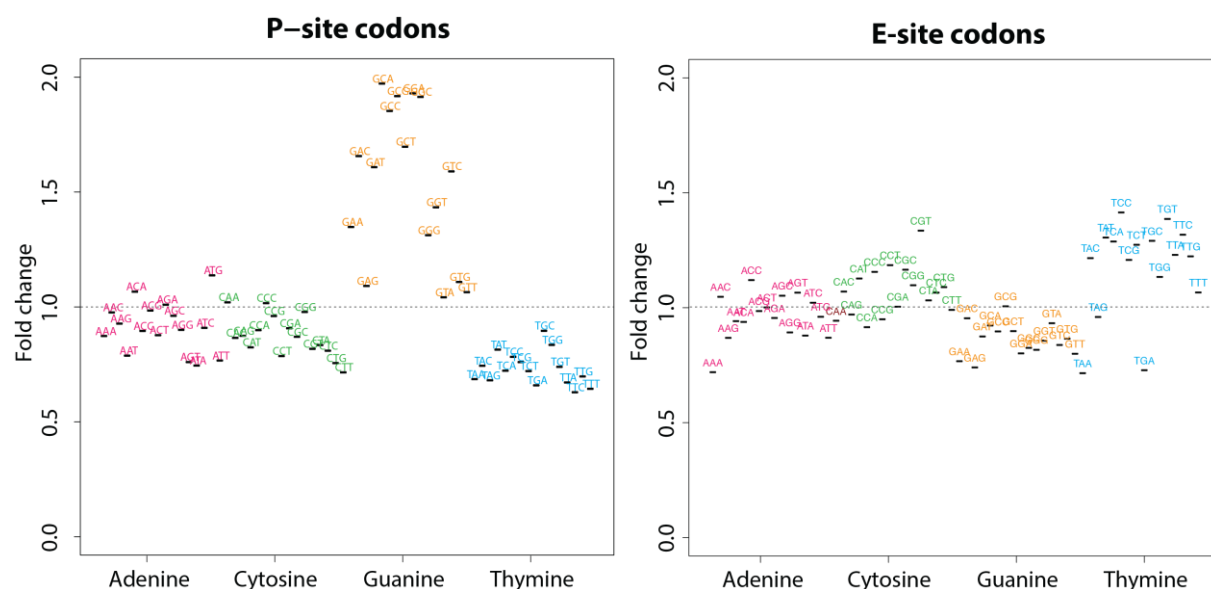


**Figure 31 : Nucleotides enrichments scores obtained in presence of pactamycin**

Codons fold changes obtained from the inverse toeprints translated in presence of 100  $\mu$ M pactamycin at the two P- (right panel) and E- (right panel) sites positions individually.

Accordingly, I could observe high fold changes (between 1.5 and 2) for most of the codons starting by a guanine (**Figure 31**). Moreover, weaker fold changes (between 1.2 and 1.5) were also observed for the in the E-site, for codons starting by a thymine (equivalent to a uridine within the mRNA translated by the pactamycin-bound ribosome) (**Figure 31**). Looking at the data in detail, I chose a three-codon pattern matching these observations that was able to strongly inhibit the ribosome: “**TGT-GCC-CCG**”, encoding the amino acid motif “CAP”. I then decided to test this sequence by toeprinting to see how the ribosome would translate this motif in the presence or absence of pactamycin. The toeprinting assay confirmed that pactamycin induces strong ribosomal arrest on the start codon (as observed **Figure 30**), but also induces a specific arrest on the “CAP” motif, where the GCC codon encoding the alanine residue of the motif was located in the ribosomal P-site (**Figure 32**).



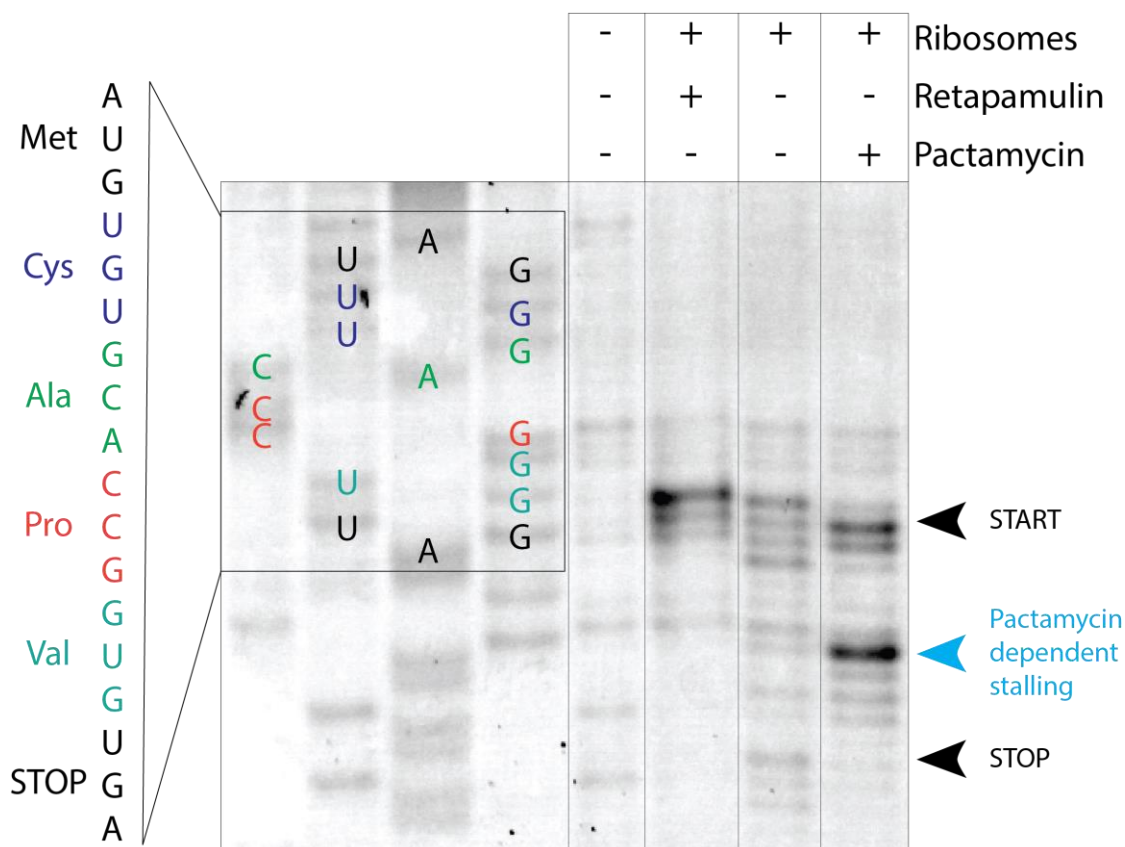


**Figure 32 : Toeprinting analysis of *E. coli* ribosomes translating an mRNA template encoding for the “CAP” motif in presence of pactamycin.**

Although this work is still in progress and will need to be complemented by a detailed structural analysis of ribosomes translating the CAP motif in the presence of drug, I could show that pactamycin action is dependent on the sequence of the mRNA codons located in the E and P sites of the ribosome. These observations are consistent with the binding site of the drug (Brodersen et al., 2000; Dinos et al., 2004), but not with the proposed mechanism by which pactamycin inhibits translocation in a manner dependent on the nature of the A-site tRNA (Orelle et al., 2013; Vázquez-Laslop and Mankin, 2018b). It may therefore be necessary to gain additional insights by using ribosome profiling to examine the effect of pactamycin on bacterial translation *in vivo* at a genome-wide level. In addition, the high conservation of the 16S rRNA residues interacting with the drug between the three domains of life would predict that the pactamycin binding site is the same on the eukaryotic ribosome and might explain its cytotoxicity (Bhuyan, 1962; White, 1962). Given the ability of pactamycin to block prokaryotic and eukaryotic protein synthesis, it is difficult to imagine pactamycin as a promising antibiotic molecule. However, an increased understanding of the mechanism by which pactamycin blocks translation coupled to its the ability to inhibit cancerous cell lines (Bhuyan, 1962; White, 1962)

may eventually provide a suitable basis on which to develop anticancer agents for human medicine.

### 4.3. Perspectives and discussion

The large-scale use of the inverse toeprinting methodology during my thesis revealed how several ribosome-targeting antibiotics inhibit bacterial translation in a context-dependent manner. Although most of the antibiotics described to date as context-dependent affect the PTC and have an inhibitory activity that depends on the nature of the incoming amino acid and the nascent peptide within the exit tunnel, I showed that the nature of the tRNAs and the mRNA could also influence the inhibition induced by antibiotics that target the 30S subunit. Among the antibiotics which I tested targeting the decoding center, only the tuberactinomycins capreomycin and viomycin appeared to be capable of inhibiting translation in a manner dependent on context. From the insights provided by the literature and our structural data, we know that only capreomycin is able to directly interact with a ribosomal substrate, in this case the A-site tRNA, in comparison to viomycin or aminoglycosides for example. This observation raises the question of the necessity of a direct contact between the antibiotic and a ribosomal substrate for the drug to be context-dependent. Although I did not test this by inverse toeprinting, I would expect that removing the  $\beta$ -lysine moiety of capreomycin, by purifying for example the minor isoforms IIA or IIB, would abolish the preferences of capreomycin for the lysine-tRNA in the A-site. Following this idea, pactamycin binds to the mRNA tunnel within the 30S subunit, and therefore directly interacts with the E-site tRNA and the mRNA. Without considering its effect on initiation, if we focus on the preferences of pactamycin for certain nucleotides at key positions of the mRNA in the elongation inhibition, we may also suppose that a direct contact, or at least a close proximity, is necessary between the drug and the substrate(s) to observe context-dependent translation inhibition. In parallel, kasugamycin binds closely to pactamycin within the mRNA path, and also appears to be dependent to the mRNA to inhibit translation initiation, thus confirming the hypothesis that a close proximity might be necessary for a drug to be context-dependent, despite the possibility of allosteric effects being at the origin of the context-dependence cannot be ruled out in most of the cases studied (see section 1.2.3.2.) (Vázquez-Laslop and Mankin, 2018b). Future drug design approaches on antibiotics targeting the 30S subunit and more precisely on the ones binding to the proximity of the RNA substrates, need to consider these facts to improve their efficiency by rendering these drugs insensitive to the context of translation.

A particularly exciting outcome of my PhD work was to elucidate the mode of action of tetracenomycin X, an antibiotic targeting the nascent polypeptide exit tunnel of the ribosome that blocks translation by a novel mechanism, entirely distinct from that of the macrolides. It is quite fascinating, in light of the knowledge brought by the study into the mechanisms of action of macrolides and ketolides) and by my work on tetracenomycin X, to observe how a few key amino acids within the nascent peptide can, in the presence of a drug obstructing the exit tunnel, completely abolish the ability of the ribosome to catalyze peptide bond formation. The different inhibition mechanisms revealed for tetracenomycin X and macrolide antibiotics provide promising tracks to optimize our medicines; first, by rendering these drugs less specific, we may enhance their antimicrobial activity to obtain better antimicrobial compounds, and second, developing highly specific inhibitors capable of precisely targeting the translation of problematic proteins within human cells, could prove highly useful for cancer therapy or for the treatment of genetic diseases (as discussed in section 3.4).

A limit in the inverse toeprinting approach I employed is the number of reads per biological replicate necessary after deep sequencing to obtain the statistically relevant number of each variant, especially in sequence motifs longer than four amino acids. For a first screening, we decided to use between three and five million reads for each biological replicate using the NNN15 library, which allowed us to look at motifs of three to four-amino acids long maximum. In the case of tetracenomycin X, we cannot exclude the possibility that the drug might be specific to other peptide sequences, which would be longer and therefore could not be detected because of a too low number of reads within the three biological replicates. A simple solution would be to increase the number of reads sequenced for each inverse toeprinting replicate, but this would strongly reduce the number of conditions that can be analyzed per deep sequencing, thus limiting the “screening approach” I employed.

In the studies concerning the context-dependency of ribosomal antibiotics, almost all of the *in vivo* experiments rely on ribosome profiling. Another possibility to combine the advantages of the *in vitro* screening approach offered by inverse toeprinting to the ones obtained by a more focused *in vivo* technique such as ribosome profiling, could be to add a second step at the inverse toeprinting protocol. The first *in vitro* screening would first select the most antibiotic-dependent blocking sequences to reduce the number of sequences tested. Then the second step would consist in their cloning into plasmids to transform bacterial cells, where a reporter gene would select the sequences which are also able to *in vivo* inhibit the bacterial ribosome. Such

protocol would solve the problem raised by the differences between *in vitro* and *in vivo* conditions, but also reduce the depth of sequencing necessary to highlight potential antibiotic-dependent arrest motifs.

As a conclusion, the results of my work encourage the pursuit of the studies concerning the mode of actions of ribosome-targeting antibiotics, and notably those interacting with the substrates of the ribosome. Knowledge-based approaches will help the optimization or the design of novel compounds, which could be used as antimicrobials to fight the alarming resistance threat, but also as medicines to treat numerous non-pathogenic human diseases.

#### 4.4. Materials and Methods

##### 4.4.1. Inverse toeprinting to characterize *in vitro* the stalling landscapes of drug-bound *E. coli* ribosomes

The protocol was done as described in the inverse toeprinting manuscript (Seip et al., 2018) with the following specificities. Oligonucleotides used in this study are listed in **Supplementary Table 2**.

##### *Randomized libraries design:*

The libraries of random mRNA sequences were generated by polymerase chain reaction (PCR) with Phusion DNA polymerase. The sequence of the expression cassette is:

CGATCGAATTCTTAATACGACTCACTATAGGGGCTTAAGTATAAGGAGGAAAAAAT  
**ATG** - (NNS or NNN) \* **15** – GCG – ATC – TCG – GTG – **TGA** – TGA *GATATC*  
AATATCAAA AAGGATCCATATA

(the T7 promoter is underlined, the randomized region is in **bold**; the EcoRV site is in *italics*).

##### *In vitro translation conditions:*

The randomized libraries are translated in presence or absence of 100  $\mu$ M of drug to produce ribosome-protected inverse toeprints. The *in vitro* translation reaction is performed using the PURE system, a reconstituted *in vitro* cell free translation system. The PURE system chosen was lacking release factors and ribosomes (PURExpress  $\Delta$ RF123  $\Delta$ Ribosome system (New England Biolabs)) so that they can be added as needed. The rescue elongation factor P (EF-P) from *E. coli* was added to a final concentration of 25  $\mu$ M to avoid the accumulation of ribosomes arrested on non-specific arrest motifs (poly-prolines motifs for example). The inverse toeprints were size-selected on acrylamide gels, purified and the subsequent addition of

the NGS adaptors was performed as described in the inverse toeprinting manuscript (Seip et al., 2018) before sending to NGS.

#### ***Data processing and analysis:***

Next generation sequencing was performed by the BGI Facility in Hong-Kong, on an Illumina HiSeqXten system in rapid run mode with 150 PE reads. Data processing and analysis was carried out following the protocol of the original paper (Seip et al., 2018).

#### **4.4.2. Toeprinting technique for the study of the effect of mutations on ribosomal stalling**

Toeprinting is an *in vitro* method to identify the position of an arrested ribosome along a mRNA with nucleotide resolution. Originally the reaction was performed using an S30 cell extract (Hartz et al., 1988), but recent developments led to a protocol using the PURE system (NEB) (Orelle et al., 2013). During the toeprinting reaction, a 5' fluorescently labeled oligonucleotide complementary to the 3' end of the template mRNA is extended using a reverse transcriptase until the enzyme reaches the arrested ribosome. The synthesized cDNA is then purified and analyzed on a denaturing gel.

Several controls are necessary to analyze properly the ribosomal toeprints. First, to identify the codon where the ribosome is at, a sequencing reaction is performed and deposited in the gel. Second, a reaction lacking ribosomes shows toeprints corresponding to the secondary structure of the mRNA. Third, lack of release factors and antibiotics allows the determination of the positioning of the stop codon on the sequencing gel. Finally, to easily locate the initiation codon, a reaction is made in presence of retapamulin (200  $\mu$ M), an antibiotic able to inhibit the initiation step (Meydan et al., 2021).

#### ***DNA template preparation***

5' and 3' extremities containing for example the T7 promoter, the RBS, and the NV1 sequence that are required for toeprinting, were then added by PCR with Phusion DNA polymerase (20 cycles [98°C, 10 s; 60°C, 5 s; 72°C, 10 s]), using the *TP\_Pac\_MCAPV\*\_fwd* oligo containing the drug-dependent arrest motif in combination with oligonucleotides *Fragment1\_fwd*, *TP\_frag2\_rev* and *TP\_frag2\_NV\_rev* as templates (1 pmol of each oligonucleotide per 50  $\mu$ l reaction), and oligonucleotides *Fwd\_short* and *TP\_rev\_short* for amplification (10 pmol of each

oligonucleotide per 50 µl reaction; see oligos **Supplementary Table 2**). The two linear expression libraries were purified using a PCR purification kit (Qiagen) according to the manufacturer's instructions prior to quantification with a 2100 Agilent Bioanalyzer and mixing. The sequence of the DNA template is:

CGATCGAATTCTTAATACGACTCACTATAGGGCTTAAGTATAAGGAGGAAAAAAT  
**ATGTGTGCACCGGTGTGA**AGCGAATAATAACTGACTCTGAACAACATCCGTACT  
CTTCGTGCGCAGGCAAG**GTTAATAAGCAAAATTCATTATAACC**

(the T7 promoter is underlined, the drug-dependent arrest motif tested is in **bold**; the NV1 sequence is colored in grey and the YakimaYellow sequence is colored in yellow).

### ***In vitro transcription***

The DNA template contains a T7 promoter followed by a ribosome binding sequence, as specified in the NEB PURExpress system handbook. *In vitro* transcription was performed using T7 RNA polymerase in a buffer containing 80 mM Tris-HCl, 24 mM MgCl<sub>2</sub>, 2 mM spermidine, and 40 mM DTT, pH 7.6, in the presence of 7.5 mM ATP (Sigma Aldrich), CTP, GTP and UTP 7.5 mM (CTP, UTP, and GTP from Jena Bioscience). 8 pmol of DNA template were used in 200 µl of reaction volume. *In vitro* transcription was performed at 37°C for 3 h, mRNA was purified using the “RNA Clean & Concentrator<sup>TM</sup>-5” purification kit (ZymoClean Research) according to the manufacturer's instructions. The final concentration of mRNA was determined using the NanoDrop.

### ***In vitro translation, reverse transcription and purification***

The drug-induced translational arrest of *E. coli* ribosomes was tested using the PURE system ΔRF1,2,3 kit. The reactions are assembled as recommended for a total volume of 5 µL per reaction. Additionally, 2 pmol of Yakima-yellow labeled DNA oligonucleotide (*TP\_rev\_YakimaYellow*, see **Supplementary Table 2**), which is a reverse complement oligo to the 3' end of the mRNA, 5 pmol of mRNA template and 1 to 1000 µM of antibiotic are added to the translation mixture. The reaction compositions are listed **Table 6**.

REACTION	LACKING COMPONENTS	REACTION MIX	CONTROLS/TESTS
<b>ΔRIBOSOMES</b>	Δribosomes ΔRF1,2,3	2 μl Solution A 0,6 μl Factor Mix 1 μl mRNA - 5 pmol Water QSP 5 μl	Secondary structure of mRNA
<b>RETAPAMULIN</b>	ΔRF1,2,3	2 μl Solution A 0,6 μl Factor Mix 1 μl mRNA - 5 pmol 0,9 μl ribosomes - 2,3 μM end concentration 1 μl retapamulin (dried) - 200 μM end concentration Water QSP 5 μl	Start codon
<b>- ANTIBIOTICS</b>	ΔRF1,2,3	2 μl Solution A 0,6 μl Factor Mix 1 μl mRNA - 5 pmol 0,9 μl ribosomes - 2,3 μM end concentration Water QSP 5 μl	Stop codon
<b>+ ANTIBIOTICS</b>	ΔRF1,2,3	2 μl Solution A 0,6 μl Factor Mix 1 μl mRNA - 5 pmol 0,9 μl ribosomes - 2,3 μM end concentration 1 μl antibiotics (dried - various concentrations) Water QSP 5 μl	Drug-induced ribosomal arrest

**Table 6 : Reaction mixture of toeprinting reactions**

All components are combined and the reaction is incubated for 15 min at 37°C to allow translation. To locate the ribosomes stalled on the mRNA, the mRNA is reverse transcribed using a 5' labeled oligonucleotide. 1 μL of reverse transcriptase mix (100 μM dNTPs, four volumes of PURE system buffer (9 mM Mg(CH<sub>3</sub>CO<sub>2</sub>)<sub>2</sub>, 5 mM K-phosphate pH 7.3, 95 mM K-glutamate, 5 mM NH<sub>4</sub>Cl, 0.5 mM CaCl<sub>2</sub>, 1 mM spermidine, 8 mM putrescine, 1 mM DTT) and five volumes of AMV reverse transcriptase) are added to the reaction which is then incubated for further 20 min at 37°C. The next step corresponds to the degradation of the mRNA by the addition of 0.5 M NaOH and incubation at 37°C for 15 minutes. The reaction is

neutralized with 0.5 M HCl and diluted with a resuspension buffer (300 mM Na(CH<sub>3</sub>CO<sub>2</sub>) pH 5.5, 5 mM EDTA, 0.5% SDS) (Orelle et al., 2013). Proteins and nucleotides are removed using a nucleotide removal kit (Qiagen). 200 µL PNI buffer are added per reaction, which are then loaded onto the spin columns provided by the kit. Subsequently, the column is washed once with 750 µL PE buffer. The cDNA is eluted with 50 µL molecular biology grade water (Merck) and dried by vacuum centrifugation. The dried cDNA is resuspended in 6 µL of toeprinting loading dye. Samples are heated before loading for 5 min at 95°C to denature the cDNA.

To be able to determine the exact arrest position of the ribosome on the mRNA, a Sanger sequencing reaction is performed using a commercial kit designed to be used with fluorescent dye-labeled primers. This kit contains the Thermo Sequenase DNA Polymerase, an enzyme engineered for DNA sequencing. This enzyme is thermostable and exonuclease-free. It readily incorporates dideoxynucleotide triphosphates, resulting in much more uniform band intensities. The enzyme is formulated as a mixture with thermostable inorganic pyrophosphatase (TAP) cloned from the *Thermoplasma acidophilum*. TAP hydrolyzes the inorganic pyrophosphate product of nucleotide polymerization preventing pyrophosphorolysis from occurring. Pyrophosphorolysis can result in faint bands, which can affect the accuracy of base calling. In order to obtain high quality sequence information, it is essential that original PCR products used for the sequencing are of high quality and quantity. In order to do so, I use the ExoSAP-IT reagent (#PN 78200 – ThermoFischer Scientific), which can efficiently remove the excess dNTPs and primers before starting the sequencing. This purification step is performed following the manufacturer's instructions. For the sequencing procedure, 4 µl of purified PCR product (or approximatively 0,5 – 1 pmol of DNA) and 2 pmol of the 5'-labeled oligonucleotide are used to prepare the master reaction following the manufacturer's instructions. Once the PCR product is purified and the sequencing reactions are prepared, the sequencing PCR program presented **Table 7** is used.

Temperature	Time	Step	Cycles
95 °C	30 s	Denaturation of PCR fragments	25x
50 °C	15 s	Primer annealing	
72 °C	60 s	Primer extension	
12 °C	∞	Incubation until further usage	1x

**Table 7 : Program for sequencing reaction**



2  $\mu$ L of formamide loading dye from the kit are added to each Sanger reaction. Samples are heated for 3 min at 75°C to denature the cDNA. The samples are loaded onto a denaturing sequencing PAGE that was prepared according to the protocol **Table 8**.

#### **Sequencing PAGE**

TBE buffer (180 mM Tris, 180 mM Boric acid, 4 mM EDTA)  
7,5% (w/v) acrylamide (19:1)  
8 M Urea  
0,075% (w/v) APS  
0,075% (v/v) TEMED

**Table 8 : Gel mix for sequencing PAGE**

The sequencing PAGE is run at 40 W for 2.5 h at room temperature. The bands are detected using a fluorescent scanner (Amersham<sup>TM</sup> Typhoon, GE Healthcare) using the green laser, detecting +3 mm and default settings.

#### **4.4.3. Structural characterization of 70S ribosomal complexes blocked in the presence of the drug of interest**

To understand how the previously arrest motifs identified by inverse toeprinting and characterized by toeprinting would stall the ribosome in presence of the drug of interest, we decided to do cryo-electron microscopy to get structural insights concerning the interactions between the drug and the arrest motif inside the ribosomal complex. The cryo-EM complexes formed to study drug-induced ribosomal arrest are composed of the same mixture as the reaction made for toeprinting experiments for the “+ Antibiotics” condition (see Table 5) with the exception of the use of homemade reassociated (Blaha et al., 2000) 70S ribosomes from *E. coli* KC6 strain (Calhoun and Swartz, 2006). This reaction is incubated 15-20 min at 37 °C to let the translation process occur and is then diluted to a final concentration of ribosomes of 250-300 nM in buffer A (50 mM HEPES-KOH pH 7.5, 100 mM K-acetate, 25 mM Mg-acetate, and drug of interest at the desired concentration) or in buffer B (30 mM HEPES-KOH pH 7.5, 5 mM MgCl<sub>2</sub>, 50 mM NH<sub>4</sub>Cl, 5 mM 2-mercaptoethanol, 2 mM spermidine and 5 mM putrescine, and drug of interest at the desired concentration) depending of the complex, for immediate grid preparation.

The details of the samples freezing, data imaging and processing and the modeling are described in the sections containing cryoEM results (see sections 0. and 4.2.3.).

## Part V: General conclusions and perspectives

My thesis work focused on understanding how certain antibiotics inhibit bacterial translation in a context-dependent manner.

The first part of my work revisited the mechanism of action of macrolide and ketolide antibiotics, which interact with the nascent peptide during the elongation phase of translation to inhibit the PTC. Through a collaborative approach combining several technical approaches, I could show using inverse toeprinting that ribosomes synthesizing the ErmDL peptide undergo translational arrest through distinct mechanisms in response to erythromycin or telithromycin. In addition, my data provided additional evidence that erythromycin displays a less stringent sequence-specificity to inhibit the ribosome in comparison to telithromycin, but also explained more generally how the widespread +X+ stalling motif shuts down the PTC in the presence of macrolide or ketolide antibiotics. Using the same inverse toeprinting-based approach, I showed that ErmCL and ErmAL1 peptides likely inhibit the ribosome through the same mode of action, as suggested by the fact that similar amino acid changes at two key positions in the nascent peptide abolish, restrict or allow the translation of the full-length peptides by macrolide-bound ribosomes. These new insights raised several questions concerning the role of such sequence variations within the inducer leader peptide sequences among the *erm* genes; the differences observed in terms of translation selectivity are probably crucial *in vivo* to tightly regulate the expression of the resistance gene, and reduce the fitness cost induced by such expression. Addressing the issues concerning the importance of such variety of leader sequences among macrolide-resistance strains would help the understanding of *erm* inducible expression, and help the development of less specific macrolide and ketolide antibiotics in order to limit the apparition of multi-resistant strains.

In the second part of my work, I studied how other categories of antibiotics targeting the elongation process may inhibit the ribosome in a context-dependent manner. While a majority of the antibiotics I tested appeared to inhibit the ribosome in a similar manner regardless of the composition of the translating complex, several antibiotics displayed a previously unknown context-dependent mode of action. Using a combination of inverse toeprinting and high-resolution structural analysis by cryo-EM, I showed that the inhibition induced by the antituberculosis antibiotic capreomycin depends on the nature of the A-site tRNA. To my knowledge, it is the first time that the mode of action of an antibiotic has been shown to rely on the nature of a tRNA; which is surprising considering that kinetic and thermodynamic properties do not differ from one tRNA to another, despite their sequence and structural

differences (Ledoux and Uhlenbeck, 2008). In addition, the work performed on capreomycin raised the questions of the choice of the in vitro conditions to study the mode of action of antibiotics. Indeed, I could show using various concentrations of antibiotic, that the mode of action of capreomycin could strongly vary depending of the conditions used for the experiment. These observations reminded the importance of limiting very artificial conditions (high concentrations of salts/drugs for example) to study antibiotics mode of action. Another antibiotic which exhibited a context-dependent mode of action was TcmX, a recently described antibiotic that targets the exit tunnel of prokaryotic and eukaryotic ribosomes. Using inverse toeprinting, I could show that TcmX inhibits the translation of a few short peptide motifs, similarly to what was already described for macrolide and ketolide antibiotics, except here that the blocking motifs are different. These results provided new insights into how the ribosomal exit tunnel, the nascent peptide and the drug alter the conformation of the PTC and the tRNAs to block peptide bond formation. Using cryo-EM, I could show that translation inhibition induced by TcmX at QK motifs occurs through a novel mechanism, whereby the 3'CCA end of the P-site tRNA is not only deformed, but also pulled into the exit tunnel, which prevents peptide bond formation by increasing the distance between the peptidyl-tRNA and the aminoacyl-tRNA. Finally, the antibiotic pactamycin, originally described as an initiation inhibitor and then placed in the category of the elongation inhibitors, was thought to be dependent of the nature of the A-site tRNA. Contrary to this view, my inverse toeprinting data showed that the action of the pactamycin was actually dependent of the nature of key nucleotide positions of the mRNA codons located in the E- and P-sites of the ribosome. A collaborative work with the team of George Dinos, using again inverse toeprinting and also cryoEM is currently underway and should lead to an increased understanding of the mode of action of pactamycin. All of my results concerning this part led me to the hypothesis that a close contact was necessary between the drug and ribosomal substrate(s) for the drug to be context-dependent.

My recent work on pactamycin gave me several ideas of additional antibiotics to study. First, edeine and kasugamycin bind similarly to pactamycin within the mRNA path of the 30S subunit; thus, their activity could also possibly depend on the nature of the mRNA, or of the nature of the tRNAs bound to the ribosome. Consistent with this idea, we already know that kasugamycin inhibits differently the translation of leader and leaderless mRNAs ([see section 1.2.3.2.](#)); therefore, it could be interesting to adapt the protocol of inverse toeprinting to play with the initiation sites instead of the sequence being translated, and see in details how the

nature of the 5'-UTR mRNA influences the mode of action of kasugamycin. In the case of edeine, the drug binds similarly to pactamycin within the mRNA path on the 30S subunit, and could also display a preference for the mRNA sequence. On the other side on the 50S subunit, lincosamides, pleuromutilins and streptogramins bind within the PTC in a site which is located between the macrolide's binding site within the exit tunnel, and the phenicols/oxazolidinones binding site within the PTC. The last three categories of antibiotics inhibit the ribosome in a peptide-dependent manner (Vázquez-Laslop and Mankin, 2018b). It is therefore fair to assume that antibiotics binding adjacently to macrolides or phenicols could also exhibit a context-dependent mode of action, which would probably also rely on the nascent peptide or the peptidyl tRNA and/or on the aminoacyl moiety of the tRNA located in the A-site.

For an antibiotic, displaying a context-dependent mode of inhibition might reduce its effectiveness in terms of antimicrobial activity, as the drug does not prevent complete inhibition of the ribosome. This weakness has been exploited by bacteria to develop inducible-mechanisms to express antibiotic resistance genes. This phenomenon has been indeed observed for macrolide antibiotics (*erm* genes) or chloramphenicol (*cat* genes), (see sections 1.2.3.2.), but also for numerous antibiotic-responsive leader peptides that control antibiotic resistance genes in pathogens and in the human microbiome (Dar et al., 2016). It would be thus very complementary to combine the insights provided by inverse toeprinting concerning the preferences of arrest motifs of a drug of interest, to genomic analyses of resistant strains, in order to study if the expression of other kinds of resistance genes rely on such context-dependent mechanisms.

In summary, studying the precise mode of action of antibiotics is of high importance to fight the global antibiotic resistance threat, as it provides promising ideas to enhance and optimize the activity of our current therapeutics by 1. Reducing their specificity during bacterial translation to have better antibiotics, 2. Increasing this specificity to have interesting anticancer compounds or inhibit translation of specific proteins within the human cell in case of genetic diseases for example and 3. Improving their pharmaceutical properties, to reduce as much as possible the onset of resistance. The insights provided by such studies will pave the way to develop knowledge-based approaches in order to replace our current screening assays and restart the antibiotic discovery process.

## REFERENCES

- Adinarayana, G., Venkateshan, M.R., Bapiraju, V.V.S.N.K., Sujatha, P., Premkumar, J., Ellaiah, P., and Zeeck, A. (2006). [Cytotoxic compounds from the marine actinobacterium]. *Bioorg. Khim.* 32, 328–334.
- Adio, S., Senyushkina, T., Peske, F., Fischer, N., Wintermeyer, W., and Rodnina, M.V. (2015). Fluctuations between multiple EF-G-induced chimeric tRNA states during translocation on the ribosome. *Nat. Commun.* 6, 7442.
- Agrawal, R.K., and Burma, D.P. (1996). Sites of ribosomal RNAs involved in the subunit association of tight and loose couple ribosomes. *J. Biol. Chem.* 271, 21285–21291.
- Agrawal, R.K., Lata, R.K., and Frank, J. (1999). Conformational variability in *Escherichia coli* 70S ribosome as revealed by 3D cryo-electron microscopy. *Int. J. Biochem. Cell Biol.* 31, 243–254.
- Agris, P.F. (2004). Decoding the genome: a modified view. *Nucleic Acids Res.* 32, 223–238.
- Agris, P.F. (2008). Bringing order to translation: the contributions of transfer RNA anticodon-domain modifications. *EMBO Rep.* 9, 629–635.
- Agudelo, D., Bourassa, P., Bérubé, G., and Tajmir-Riahi, H.-A. (2014). Intercalation of antitumor drug doxorubicin and its analogue by DNA duplex: Structural features and biological implications. *Int. J. Biol. Macromol.* 66, 144–150.
- Agudelo, D., Bourassa, P., Bérubé, G., and Tajmir-Riahi, H.A. (2016). Review on the binding of anticancer drug doxorubicin with DNA and tRNA: Structural models and antitumor activity. *J. Photochem. Photobiol. B* 158, 274–279.
- Almutairi, M.M., Park, S.R., Rose, S., Hansen, D.A., Vázquez-Laslop, N., Douthwaite, S., Sherman, D.H., and Mankin, A.S. (2015). Resistance to ketolide antibiotics by coordinated expression of rRNA methyltransferases in a bacterial producer of natural ketolides. *Proc. Natl. Acad. Sci. U. S. A.* 112, 12956–12961.
- Almutairi, M.M., Svetlov, M.S., Hansen, D.A., Khabibullina, N.F., Klepacki, D., Kang, H.-Y., Sherman, D.H., Vázquez-Laslop, N., Polikanov, Y.S., and Mankin, A.S. (2017). Co-produced natural ketolides methymycin and pikromycin inhibit bacterial growth by preventing synthesis of a limited number of proteins. *Nucleic Acids Res.* 45, 9573–9582.
- Aminov, R.I. (2010). A Brief History of the Antibiotic Era: Lessons Learned and Challenges for the Future. *Front. Microbiol.* 1.
- Anderson, M.G., Khoo, C.L.-Y., and Rickards, R.W. (1989). Oxidation processes in the biosynthesis of the tetracenomycin and elloramycin antibiotics. *J. Antibiot. (Tokyo)* 42, 640–643.
- Antoun, A., Pavlov, M.Y., Andersson, K., Tenson, T., and Ehrenberg, M. (2003). The roles of initiation factor 2 and guanosine triphosphate in initiation of protein synthesis. *EMBO J.* 22, 5593–5601.
- Antoun, A., Pavlov, M.Y., Lovmar, M., and Ehrenberg, M. (2006a). How initiation factors maximize the accuracy of tRNA selection in initiation of bacterial protein synthesis. *Mol. Cell* 23, 183–193.
- Antoun, A., Pavlov, M.Y., Lovmar, M., and Ehrenberg, M. (2006b). How initiation factors tune the rate of initiation of protein synthesis in bacteria. *EMBO J.* 25, 2539–2550.

- Arenz, S., Meydan, S., Starosta, A.L., Berninghausen, O., Beckmann, R., Vázquez-Laslop, N., and Wilson, D.N. (2014a). Drug sensing by the ribosome induces translational arrest via active site perturbation. *Mol. Cell* 56, 446–452.
- Arenz, S., Ramu, H., Gupta, P., Berninghausen, O., Beckmann, R., Vázquez-Laslop, N., Mankin, A.S., and Wilson, D.N. (2014b). Molecular basis for erythromycin-dependent ribosome stalling during translation of the ErmBL leader peptide. *Nat. Commun.* 5, 3501.
- Arenz, S., Nguyen, F., Beckmann, R., and Wilson, D.N. (2015). Cryo-EM structure of the tetracycline resistance protein TetM in complex with a translating ribosome at 3.9-Å resolution. *Proc. Natl. Acad. Sci. U. S. A.* 112, 5401–5406.
- Arenz, S., Bock, L.V., Graf, M., Innis, C.A., Beckmann, R., Grubmüller, H., Vaiana, A.C., and Wilson, D.N. (2016). A combined cryo-EM and molecular dynamics approach reveals the mechanism of ErmBL-mediated translation arrest. *Nat. Commun.* 7.
- Bahal, N., and Nahata, M.C. (1992). The new macrolide antibiotics: azithromycin, clarithromycin, dirithromycin, and roxithromycin. *Ann. Pharmacother.* 26, 46–55.
- Ban, N., Nissen, P., Hansen, J., Moore, P.B., and Steitz, T.A. (2000). The Complete Atomic Structure of the Large Ribosomal Subunit at 2.4 Å Resolution. *Science* 289, 905–920.
- Barraud, P., Schmitt, E., Mechulam, Y., Dardel, F., and Tisné, C. (2008). A unique conformation of the anticodon stem-loop is associated with the capacity of tRNA<sup>fMet</sup> to initiate protein synthesis. *Nucleic Acids Res.* 36, 4894–4901.
- Barrenechea, V., Vargas-Reyes, M., Quiliano, M., and Milón, P. (2021). A Complementary Mechanism of Bacterial mRNA Translation Inhibition by Tetracyclines. *Front. Microbiol.* 12, 682682.
- Bassett, E.J., Keith, M.S., Armelagos, G.J., Martin, D.L., and Villanueva, A.R. (1980). Tetracycline-labeled human bone from ancient Sudanese Nubia (A.D. 350). *Science* 209, 1532–1534.
- Belardinelli, R., Sharma, H., Caliskan, N., Cunha, C.E., Peske, F., Wintermeyer, W., and Rodnina, M.V. (2016a). Choreography of molecular movements during ribosome progression along mRNA. *Nat. Struct. Mol. Biol.* 23, 342–348.
- Belardinelli, R., Sharma, H., Peske, F., Wintermeyer, W., and Rodnina, M.V. (2016b). Translocation as continuous movement through the ribosome. *RNA Biol.* 13, 1197–1203.
- Belardinelli, R., Sharma, H., Peske, F., and Rodnina, M.V. (2021). Perturbation of ribosomal subunit dynamics by inhibitors of tRNA translocation. *RNA N. Y. N* 27, 981–990.
- Benjin, X., and Ling, L. (2020). Developments, applications, and prospects of cryo-electron microscopy. *Protein Sci.* 29, 872–882.
- Beringer, M., Adio, S., Wintermeyer, W., and Rodnina, M. (2003). The G2447A mutation does not affect ionization of a ribosomal group taking part in peptide bond formation. *RNA N. Y. N* 9, 919–922.
- Beringer, M., Bruell, C., Xiong, L., Pfister, P., Bieling, P., Katunin, V.I., Mankin, A.S., Böttger, E.C., and Rodnina, M.V. (2005). Essential mechanisms in the catalysis of peptide bond formation on the ribosome. *J. Biol. Chem.* 280, 36065–36072.
- Bhuyan, B. (1962). Pactamycin, a new antitumor antibiotic. I. Discovery and biological properties. *Antimicrob Agents Chemother* 1961, 184–190.

- Bieling, P., Beringer, M., Adio, S., and Rodnina, M.V. (2006). Peptide bond formation does not involve acid-base catalysis by ribosomal residues. *Nat. Struct. Mol. Biol.* *13*, 423–428.
- Blaha, G., Stelzl, U., Spahn, C.M., Agrawal, R.K., Frank, J., and Nierhaus, K.H. (2000). Preparation of functional ribosomal complexes and effect of buffer conditions on tRNA positions observed by cryoelectron microscopy. *Methods Enzymol.* *317*, 292–309.
- Blanchard, S.C., Kim, H.D., Gonzalez, R.L., Puglisi, J.D., and Chu, S. (2004). tRNA dynamics on the ribosome during translation. *Proc. Natl. Acad. Sci. U. S. A.* *101*, 12893–12898.
- Brilot, A.F., Korostelev, A.A., Ermolenko, D.N., and Grigorieff, N. (2013). Structure of the ribosome with elongation factor G trapped in the pretranslocation state. *Proc. Natl. Acad. Sci. U. S. A.* *110*, 20994–20999.
- Brodersen, D.E., Clemons, W.M., Carter, A.P., Morgan-Warren, R.J., Wimberly, B.T., and Ramakrishnan, V. (2000). The Structural Basis for the Action of the Antibiotics Tetracycline, Pactamycin, and Hygromycin B on the 30S Ribosomal Subunit. *Cell* *103*, 1143–1154.
- Bryskier, A. (2000). Ketolides-telithromycin, an example of a new class of antibacterial agents. *Clin. Microbiol. Infect. Off. Publ. Eur. Soc. Clin. Microbiol. Infect. Dis.* *6*, 661–669.
- Bulkley, D., Innis, C.A., Blaha, G., and Steitz, T.A. (2010). Revisiting the structures of several antibiotics bound to the bacterial ribosome. *Proc. Natl. Acad. Sci.* *107*, 17158–17163.
- Calhoun, K.A., and Swartz, J.R. (2006). Total amino acid stabilization during cell-free protein synthesis reactions. *J. Biotechnol.* *123*, 193–203.
- Carbone, C.E., Loveland, A.B., Gamper, H., Hou, Y.-M., Demo, G., and Korostelev, A.A. (2021). Time-resolved cryo-EM visualizes ribosomal translocation with EF-G and GTP.
- Chang, B., Halgamuge, S., and Tang, S.-L. (2006). Analysis of SD sequences in completed microbial genomes: non-SD-led genes are as common as SD-led genes. *Gene* *373*, 90–99.
- Chaudhary, D.K., Khulan, A., and Kim, J. (2019). Development of a novel cultivation technique for uncultured soil bacteria. *Sci. Rep.* *9*, 6666.
- Cheng, Y. (2015). Single-Particle Cryo-EM at Crystallographic Resolution. *Cell* *161*, 450–457.
- Chin, K., Shean, C.S., and Gottesman, M.E. (1993). Resistance of lambda cI translation to antibiotics that inhibit translation initiation. *J. Bacteriol.* *175*, 7471–7473.
- Choi, J., Marks, J., Zhang, J., Chen, D.-H., Wang, J., Vázquez-Laslop, N., Mankin, A.S., and Puglisi, J.D. (2020). Dynamics of the context-specific translation arrest by chloramphenicol and linezolid. *Nat. Chem. Biol.* *16*, 310–317.
- Clarebout, G., Nativelle, E., and Leclercq, R. (2001). Unusual inducible cross resistance to macrolides, lincosamides, and streptogramins B by methylase production in clinical isolates of *Staphylococcus aureus*. *Microb. Drug Resist. Larchmt. N* *7*, 317–322.
- Cochella, L., and Green, R. (2005). An Active Role for tRNA in Decoding Beyond Codon:Anticodon Pairing. *Science* *308*, 1178–1180.
- Cock, P.J.A., Antao, T., Chang, J.T., Chapman, B.A., Cox, C.J., Dalke, A., Friedberg, I., Hamelryck, T., Kauff, F., Wilczynski, B., et al. (2009). Biopython: freely available Python tools for computational molecular biology and bioinformatics. *Bioinforma. Oxf. Engl.* *25*, 1422–1423.



- Collins, D.A., Wu, Y., Tateda, K., Kim, H.-J., Vickers, R.J., and Riley, T.V. (2021). Evaluation of the antimicrobial activity of ridinilazole and six comparators against Chinese, Japanese and South Korean strains of *Clostridioides difficile*. *J. Antimicrob. Chemother.* *76*, 967–972.
- Contreras, A., and Vazquez, D. (1977). Cooperative and Antagonistic Interactions of Peptidyl-tRNA and Antibiotics with Bacterial Ribosomes. *Eur. J. Biochem.* *74*, 539–547.
- Cornish, P.V., Ermolenko, D.N., Noller, H.F., and Ha, T. (2008). Spontaneous Intersubunit Rotation in Single Ribosomes. *Mol. Cell* *30*, 578–588.
- Counter, F.T., Ensminger, P.W., Preston, D.A., Wu, C.Y., Greene, J.M., Felty-Duckworth, A.M., Paschal, J.W., and Kirst, H.A. (1991). Synthesis and antimicrobial evaluation of dirithromycin (AS-E 136; LY237216), a new macrolide antibiotic derived from erythromycin. *Antimicrob. Agents Chemother.* *35*, 1116–1126.
- Dale, T., and Uhlenbeck, O.C. (2005). Amino acid specificity in translation. *Trends Biochem. Sci.* *30*, 659–665.
- Dallas, A., and Noller, H.F. (2001). Interaction of translation initiation factor 3 with the 30S ribosomal subunit. *Mol. Cell* *8*, 855–864.
- Dao Duc, K., Batra, S.S., Bhattacharya, N., Cate, J.H.D., and Song, Y.S. (2019). Differences in the path to exit the ribosome across the three domains of life. *Nucleic Acids Res.* *47*, 4198–4210.
- Dar, D., and Sorek, R. (2017). Regulation of antibiotic-resistance by non-coding RNAs in bacteria. *Curr. Opin. Microbiol.* *36*, 111–117.
- Dar, D., Shamir, M., Mellin, J.R., Koutero, M., Stern-Ginossar, N., Cossart, P., and Sorek, R. (2016). Term-seq reveals abundant ribo-regulation of antibiotics resistance in bacteria. *Science* *352*, aad9822–aad9822.
- Darken, M.A. (1964). Puromycin inhibition of protein synthesis. *Pharmacol. Rev.* *16*, 223–243.
- Davis, A.R., Gohara, D.W., and Yap, M.-N.F. (2014). Sequence selectivity of macrolide-induced translational attenuation. *Proc. Natl. Acad. Sci.* *111*, 15379–15384.
- Denis, A., Agouridas, C., Auger, J.M., Benedetti, Y., Bonnefoy, A., Bretin, F., Chantot, J.F., Dussarat, A., Fromentin, C., D'Ambrières, S.G., et al. (1999). Synthesis and antibacterial activity of HMR 3647 a new ketolide highly potent against erythromycin-resistant and susceptible pathogens. *Bioorg. Med. Chem. Lett.* *9*, 3075–3080.
- Depardieu, F., Podglajen, I., Leclercq, R., Collatz, E., and Courvalin, P. (2007). Modes and modulations of antibiotic resistance gene expression. *Clin. Microbiol. Rev.* *20*, 79–114.
- Diaconu, M., Kothe, U., Schlünzen, F., Fischer, N., Harms, J.M., Tonevitsky, A.G., Stark, H., Rodnina, M.V., and Wahl, M.C. (2005). Structural basis for the function of the ribosomal L7/12 stalk in factor binding and GTPase activation. *Cell* *121*, 991–1004.
- Dijksteel, G.S., Ulrich, M.M.W., Middelkoop, E., and Boekema, B.K.H.L. (2021). Review: Lessons Learned From Clinical Trials Using Antimicrobial Peptides (AMPs). *Front. Microbiol.* *12*, 616979.
- D'Imprima, E., and Kühlbrandt, W. (2021). Current limitations to high-resolution structure determination by single-particle cryoEM. *Q. Rev. Biophys.* *54*.
- Dinos, G.P. (2017). The macrolide antibiotic renaissance. *Br. J. Pharmacol.* *174*, 2967–2983.

- Dinos, G., Wilson, D.N., Teraoka, Y., Szaflarski, W., Fucini, P., Kalpaxis, D., and Nierhaus, K.H. (2004). Dissecting the Ribosomal Inhibition Mechanisms of Edeine and Pactamycin: The Universally Conserved Residues G693 and C795 Regulate P-Site RNA Binding. *Mol. Cell* *13*, 113–124.
- Doern, G.V. (2006). Macrolide and Ketolide Resistance with *Streptococcus pneumoniae*. *Med. Clin. North Am.* *90*, 1109–1124.
- Dönhöfer, A., Franckenberg, S., Wickles, S., Berninghausen, O., Beckmann, R., and Wilson, D.N. (2012). Structural basis for TetM-mediated tetracycline resistance. *Proc. Natl. Acad. Sci. U. S. A.* *109*, 16900–16905.
- Dorner, S., Polacek, N., Schulmeister, U., Panuschka, C., and Barta, A. (2002). Molecular aspects of the ribosomal peptidyl transferase. *Biochem. Soc. Trans.* *30*, 1131–1136.
- Dorner, S., Panuschka, C., Schmid, W., and Barta, A. (2003). Mononucleotide derivatives as ribosomal P-site substrates reveal an important contribution of the 2'-OH to activity. *Nucleic Acids Res.* *31*, 6536–6542.
- Dorner, S., Brunelle, J.L., Sharma, D., and Green, R. (2006). The hybrid state of tRNA binding is an authentic translation elongation intermediate. *Nat. Struct. Mol. Biol.* *13*, 234–241.
- Drautz, H., Reuschenbach, P., Zähner, H., Rohr, J., and Zeeck, A. (1985). Metabolic products of microorganisms. 225. Elloramycin, a new anthracycline-like antibiotic from *Streptomyces olivaceus*. Isolation, characterization, structure and biological properties. *J. Antibiot. (Tokyo)* *38*, 1291–1301.
- Dunkle, J.A., Xiong, L., Mankin, A.S., and Cate, J.H.D. (2010). Structures of the *Escherichia coli* ribosome with antibiotics bound near the peptidyl transferase center explain spectra of drug action. *Proc. Natl. Acad. Sci.* *107*, 17152–17157.
- Durand, G.A., Raoult, D., and Dubourg, G. (2019). Antibiotic discovery: history, methods and perspectives. *Int. J. Antimicrob. Agents* *53*, 371–382.
- Duval, M., Simonetti, A., Caldelari, I., and Marzi, S. (2015). Multiple ways to regulate translation initiation in bacteria: Mechanisms, regulatory circuits, dynamics. *Biochimie* *114*, 18–29.
- Egebjerg, J., and Garrett, R.A. (1991). Binding sites of the antibiotics pactamycin and celesticetin on ribosomal RNAs. *Biochimie* *73*, 1145–1149.
- Egert, E., Noltemeyer, M., Siebers, J., Rohr, J., and Zeeck, A. (1992). The structure of tetracenomycin C. *J. Antibiot. (Tokyo)* *45*, 1190–1192.
- Elf, J., and Barkefors, I. (2019). Single-Molecule Kinetics in Living Cells. *Annu. Rev. Biochem.* *88*, 635–659.
- Embley, T.M., and Stackebrandt, E. (1994). The molecular phylogeny and systematics of the actinomycetes. *Annu. Rev. Microbiol.* *48*, 257–289.
- Emmerson, A.M., and Jones, A.M. (2003). The quinolones: decades of development and use. *J. Antimicrob. Chemother.* *51 Suppl 1*, 13–20.
- Erlacher, M.D., Lang, K., Shankaran, N., Wotzel, B., Hüttenhofer, A., Micura, R., Mankin, A.S., and Polacek, N. (2005). Chemical engineering of the peptidyl transferase center reveals an important role of the 2'-hydroxyl group of A2451. *Nucleic Acids Res.* *33*, 1618–1627.

- Erlacher, M.D., Lang, K., Wotzel, B., Rieder, R., Micura, R., and Polacek, N. (2006). Efficient ribosomal peptidyl transfer critically relies on the presence of the ribose 2'-OH at A2451 of 23S rRNA. *J. Am. Chem. Soc.* *128*, 4453–4459.
- Ermolenko, D.N., Majumdar, Z.K., Hickerson, R.P., Spiegel, P.C., Clegg, R.M., and Noller, H.F. (2007a). Observation of Intersubunit Movement of the Ribosome in Solution Using FRET. *J. Mol. Biol.* *370*, 530–540.
- Ermolenko, D.N., Spiegel, P.C., Majumdar, Z.K., Hickerson, R.P., Clegg, R.M., and Noller, H.F. (2007b). The antibiotic viomycin traps the ribosome in an intermediate state of translocation. *Nat. Struct. Mol. Biol.* *14*, 493–497.
- Fahlman, R.P., Dale, T., and Uhlenbeck, O.C. (2004). Uniform Binding of Aminoacylated Transfer RNAs to the Ribosomal A and P Sites. *Mol. Cell* *16*, 799–805.
- Farrell, D.J., Mendes, R.E., and Jones, R.N. (2015). Antimicrobial activity of solithromycin against serotyped macrolide-resistant *Streptococcus pneumoniae* isolates collected from U.S. medical centers in 2012. *Antimicrob. Agents Chemother.* *59*, 2432–2434.
- Fei, J., Richard, A.C., Bronson, J.E., and Gonzalez, R.L. (2011). Transfer RNA-mediated regulation of ribosome dynamics during protein synthesis. *Nat. Struct. Mol. Biol.* *18*, 1043–1051.
- Felmingham, D., Cantón, R., and Jenkins, S.G. (2007). Regional trends in  $\beta$ -lactam, macrolide, fluoroquinolone and telithromycin resistance among *Streptococcus pneumoniae* isolates 2001–2004. *J. Infect.* *55*, 111–118.
- Fernandes, P., Martens, E., Bertrand, D., and Pereira, D. (2016). The solithromycin journey-It is all in the chemistry. *Bioorg. Med. Chem.* *24*, 6420–6428.
- Foulds, G., Shepard, R.M., and Johnson, R.B. (1990). The pharmacokinetics of azithromycin in human serum and tissues. *J. Antimicrob. Chemother.* *25 Suppl A*, 73–82.
- Frank, J., and Agrawal, R.K. (2000). A ratchet-like inter-subunit reorganization of the ribosome during translocation. *Nature* *406*, 318–322.
- Frank, J., Zhu, J., Penczek, P., Li, Y., Srivastava, S., Verschoor, A., Radermacher, M., Grassucci, R., Lata, R.K., and Agrawal, R.K. (1995). A model of protein synthesis based on cryo-electron microscopy of the *E. coli* ribosome. *Nature* *376*, 441–444.
- Frank, J., Gao, H., Sengupta, J., Gao, N., and Taylor, D.J. (2007). The process of mRNA-tRNA translocation. *Proc. Natl. Acad. Sci. U. S. A.* *104*, 19671–19678.
- Freistroffer, D.V., Pavlov, M.Y., MacDougall, J., Buckingham, R.H., and Ehrenberg, M. (1997). Release factor RF3 in *E. coli* accelerates the dissociation of release factors RF1 and RF2 from the ribosome in a GTP-dependent manner. *EMBO J.* *16*, 4126–4133.
- Gale, E.F. (1981). Antibiotic inhibitors of ribosome function. *Mol. Basis Antibiot. Action* 402–547.
- Giegé, R., Ebel, J.P., Springer, M., and Grunberg-Manago, M. (1973). Initiation of protein synthesis with mischarged tRNA<sup>fet</sup> from *E. coli*. *FEBS Lett.* *37*, 166–169.
- Girard, A.E., Girard, D., English, A.R., Gootz, T.D., Cimochowski, C.R., Faiella, J.A., Haskell, S.L., and Retsema, J.A. (1987). Pharmacokinetic and in vivo studies with azithromycin (CP-62,993), a new macrolide with an extended half-life and excellent tissue distribution. *Antimicrob. Agents Chemother.* *31*, 1948–1954.

- Girshovich, A.S., Bochkareva, E.S., and Vasiliev, V.D. (1986). Localization of elongation factor Tu on the ribosome. *FEBS Lett.* *197*, 192–198.
- Goldstein, J.L., and Caskey, C.T. (1970). Peptide chain termination: effect of protein S on ribosomal binding of release factors. *Proc. Natl. Acad. Sci. U. S. A.* *67*, 537–543.
- Gould, K. (2016). Antibiotics: from prehistory to the present day. *J. Antimicrob. Chemother.* *71*, 572–575.
- Goyal, A., Belardinelli, R., Maracci, C., Milón, P., and Rodnina, M.V. (2015). Directional transition from initiation to elongation in bacterial translation. *Nucleic Acids Res.* *43*, 10700–10712.
- Gregory, S.T., Bayfield, M.A., O'Connor, M., Thompson, J., and Dahlberg, A.E. (2001). Probing ribosome structure and function by mutagenesis. *Cold Spring Harb. Symp. Quant. Biol.* *66*, 101–108.
- Grigorieff, N. (2016). FREALIGN: An Exploratory Tool for Single-Particle Cryo-EM. *Methods Enzymol.* *579*, 191–226.
- Grill, S., Gualerzi, C.O., Londei, P., and Bläsi, U. (2000). Selective stimulation of translation of leaderless mRNA by initiation factor 2: evolutionary implications for translation. *EMBO J.* *19*, 4101–4110.
- Grossman, T.H. (2016). Tetracycline Antibiotics and Resistance. *Cold Spring Harb. Perspect. Med.* *6*, a025387.
- Gryczan, T.J., Grandi, G., Hahn, J., Grandi, R., and Dubnau, D. (1980). Conformational alteration of mRNA structure and the posttranscriptional regulation of erythromycin-induced drug resistance. *Nucleic Acids Res.* *8*, 6081–6097.
- Gualerzi, C.O., and Pon, C.L. (2015). Initiation of mRNA translation in bacteria: structural and dynamic aspects. *Cell. Mol. Life Sci. CMLS* *72*, 4341–4367.
- Guo, Z., and Noller, H.F. (2012). Rotation of the head of the 30S ribosomal subunit during mRNA translocation. *Proc. Natl. Acad. Sci. U. S. A.* *109*, 20391–20394.
- Gupta, P., Sothiselvam, S., Vázquez-Laslop, N., and Mankin, A.S. (2013). Deregulation of translation due to post-transcriptional modification of rRNA explains why erm genes are inducible. *Nat. Commun.* *4*, 1984.
- Haas, L. (1999). Papyrus of Ebers and Smith. *J. Neurol. Neurosurg. Psychiatry* *67*, 578.
- Hansen, J.L., Schmeing, T.M., Moore, P.B., and Steitz, T.A. (2002). Structural insights into peptide bond formation. *Proc. Natl. Acad. Sci. U. S. A.* *99*, 11670–11675.
- Hardy, D.J., Guay, D.R., and Jones, R.N. (1992). Clarithromycin, a unique macrolide. A pharmacokinetic, microbiological, and clinical overview. *Diagn. Microbiol. Infect. Dis.* *15*, 39–53.
- Hartz, D., McPheeters, D.S., Traut, R., and Gold, L. (1988). Extension inhibition analysis of translation initiation complexes. *Methods Enzymol.* *164*, 419–425.
- Herrero del Valle, A., and Innis, C.A. (2020). Prospects for antimicrobial development in the cryo-EM era – a focus on the ribosome. *FEMS Microbiol. Rev.* *44*, 793–803.
- Hirashima, A., Childs, G., and Inouye, M. (1973). Differential inhibitory effects of antibiotics on the biosynthesis of envelope proteins of *Escherichia coli*. *J. Mol. Biol.* *79*, 373–389.

- Holm, M., Borg, A., Ehrenberg, M., and Sanyal, S. (2016). Molecular mechanism of viomycin inhibition of peptide elongation in bacteria. *Proc. Natl. Acad. Sci.* *113*, 978–983.
- Horinouchi, S., and Weisblum, B. (1980). Posttranscriptional modification of mRNA conformation: mechanism that regulates erythromycin-induced resistance. *Proc. Natl. Acad. Sci. U. S. A.* *77*, 7079–7083.
- Huang, C., Yang, C., Zhu, Y., Zhang, W., Yuan, C., and Zhang, C. (2018). Marine Bacterial Aromatic Polyketides From Host-Dependent Heterologous Expression and Fungal Mode of Cyclization. *Front. Chem.* *0*.
- Hughes, D., and Karlén, A. (2014). Discovery and preclinical development of new antibiotics. *Ups. J. Med. Sci.* *119*, 162–169.
- Hussein, N.H., Al-Kadmy, I.M.S., Taha, B.M., and Hussein, J.D. (2021). Mobilized colistin resistance (mcr) genes from 1 to 10: a comprehensive review. *Mol. Biol. Rep.* *48*, 2897–2907.
- Hutchings, M.I., Truman, A.W., and Wilkinson, B. (2019). Antibiotics: past, present and future. *Curr. Opin. Microbiol.* *51*, 72–80.
- Ingolia, N.T., Ghaemmighami, S., Newman, J.R.S., and Weissman, J.S. (2009). Genome-Wide Analysis in Vivo of Translation with Nucleotide Resolution Using Ribosome Profiling. *Science* *324*, 218–223.
- Ito, K., and Chiba, S. (2013). Arrest Peptides: Cis-Acting Modulators of Translation. *Annu. Rev. Biochem.* *82*, 171–202.
- Jain, A., and Dixit, P. (2008). Multidrug resistant to extensively drug resistant tuberculosis: What is next? *J. Biosci.* *33*, 605–616.
- Jenner, L., Starosta, A.L., Terry, D.S., Mikolajka, A., Filonava, L., Yusupov, M., Blanchard, S.C., Wilson, D.N., and Yusupova, G. (2013). Structural basis for potent inhibitory activity of the antibiotic tigecycline during protein synthesis. *Proc. Natl. Acad. Sci.* *110*, 3812–3816.
- Jia, Y., and Zhao, L. (2021). The antibacterial activity of fluoroquinolone derivatives: An update (2018-2021). *Eur. J. Med. Chem.* *224*, 113741.
- Johansen, S.K., Maus, C.E., Plikaytis, B.B., and Douthwaite, S. (2006). Capreomycin Binds across the Ribosomal Subunit Interface Using tlyA-Encoded 2'-O-Methylations in 16S and 23S rRNAs. *Mol. Cell* *23*, 173–182.
- Johansson, M., Jeong, K.-W., Trobro, S., Strazewski, P., Åqvist, J., Pavlov, M.Y., and Ehrenberg, M. (2011). pH-sensitivity of the ribosomal peptidyl transfer reaction dependent on the identity of the A-site aminoacyl-tRNA. *Proc. Natl. Acad. Sci. U. S. A.* *108*, 79–84.
- Kannan, K., Vázquez-Laslop, N., and Mankin, A.S. (2012). Selective Protein Synthesis by Ribosomes with a Drug-Obstructed Exit Tunnel. *Cell* *151*, 508–520.
- Kannan, K., Kanabar, P., Schryer, D., Florin, T., Oh, E., Bahroos, N., Tenson, T., Weissman, J.S., and Mankin, A.S. (2014). The general mode of translation inhibition by macrolide antibiotics. *Proc. Natl. Acad. Sci.* *111*, 15958–15963.
- Karimi, R., Pavlov, M.Y., Buckingham, R.H., and Ehrenberg, M. (1999). Novel roles for classical factors at the interface between translation termination and initiation. *Mol. Cell* *3*, 601–609.

- Katz, L., and Ashley, G.W. (2005). Translation and protein synthesis: macrolides. *Chem. Rev.* *105*, 499–528.
- Katz, L., and Baltz, R.H. (2016). Natural product discovery: past, present, and future. *J. Ind. Microbiol. Biotechnol.* *43*, 155–176.
- Kelemen, G.H., Zalacain, M., Culebras, E., Seno, E.T., and Cundliffe, E. (1994). Transcriptional attenuation control of the tylosin-resistance gene *tlrA* in *Streptomyces fradiae*. *Mol. Microbiol.* *14*, 833–842.
- Kim, D.F., and Green, R. (1999). Base-pairing between 23S rRNA and tRNA in the ribosomal A site. *Mol. Cell* *4*, 859–864.
- Klaholz, B.P. (2011). Molecular recognition and catalysis in translation termination complexes. *Trends Biochem. Sci.* *36*, 282–292.
- Klaholz, B.P., Myasnikov, A.G., and Van Heel, M. (2004). Visualization of release factor 3 on the ribosome during termination of protein synthesis. *Nature* *427*, 862–865.
- Klassen, J.L. (2014). Microbial secondary metabolites and their impacts on insect symbioses. *Curr. Opin. Insect Sci.* *4*, 15–22.
- Klugman, K.P., and Black, S. (2018). Impact of existing vaccines in reducing antibiotic resistance: Primary and secondary effects. *Proc. Natl. Acad. Sci. U. S. A.* *115*, 12896–12901.
- Kohanski, M.A., Dwyer, D.J., and Collins, J.J. (2010). How antibiotics kill bacteria: from targets to networks. *Nat. Rev. Microbiol.* *8*, 423–435.
- Konevega, A.L., Fischer, N., Semenov, Y.P., Stark, H., Wintermeyer, W., and Rodnina, M.V. (2007). Spontaneous reverse movement of mRNA-bound tRNA through the ribosome. *Nat. Struct. Mol. Biol.* *14*, 318–324.
- Korostelev, A., Asahara, H., Lancaster, L., Laurberg, M., Hirschi, A., Zhu, J., Trakhanov, S., Scott, W.G., and Noller, H.F. (2008). Crystal structure of a translation termination complex formed with release factor RF2. *Proc. Natl. Acad. Sci. U. S. A.* *105*, 19684–19689.
- Krishnan, K.M., Van Etten, W.J., and Janssen, G.R. (2010). Proximity of the start codon to a leaderless mRNA's 5' terminus is a strong positive determinant of ribosome binding and expression in *Escherichia coli*. *J. Bacteriol.* *192*, 6482–6485.
- Kühlbrandt, W. (2014). Cryo-EM enters a new era. *ELife* *3*, e03678.
- Kuhlenkoetter, S., Wintermeyer, W., and Rodnina, M.V. (2011). Different substrate-dependent transition states in the active site of the ribosome. *Nature* *476*, 351–354.
- Kwak, J.H., Choi, E.C., and Weisblum, B. (1991). Transcriptional attenuation control of *ermK*, a macrolide-lincosamide-streptogramin B resistance determinant from *Bacillus licheniformis*. *J. Bacteriol.* *173*, 4725–4735.
- Lang, K., Erlacher, M., Wilson, D.N., Micura, R., and Polacek, N. (2008). The role of 23S ribosomal RNA residue A2451 in peptide bond synthesis revealed by atomic mutagenesis. *Chem. Biol.* *15*, 485–492.
- Laurberg, M., Asahara, H., Korostelev, A., Zhu, J., Trakhanov, S., and Noller, H.F. (2008). Structural basis for translation termination on the 70S ribosome. *Nature* *454*, 852–857.

- Laursen, B.S., Sørensen, H.P., Mortensen, K.K., and Sperling-Petersen, H.U. (2005). Initiation of protein synthesis in bacteria. *Microbiol. Mol. Biol. Rev.* *MMBR* *69*, 101–123.
- Lazar, G., Zähler, H., Breiding, S., Damberg, M., and Zeeck, A. (1981). 3-Demethoxy-3-ethoxy-tetracenomycin C. *J. Antibiot. (Tokyo)* *34*, 1067–1068.
- Leclercq, R. (2002). Mechanisms of Resistance to Macrolides and Lincosamides: Nature of the Resistance Elements and Their Clinical Implications. *Clin. Infect. Dis.* *34*, 482–492.
- Ledoux, S., and Uhlenbeck, O.C. (2008). Different aa-tRNAs Are Selected Uniformly on the Ribosome. *Mol. Cell* *31*, 114–123.
- Levy, S.B., and Marshall, B. (2004). Antibacterial resistance worldwide: causes, challenges and responses. *Nat. Med.* *10*, S122–S129.
- Li, W., Atkinson, G.C., Thakor, N.S., Allas, U., Lu, C., Chan, K.-Y., Tenson, T., Schulten, K., Wilson, K.S., Hauryliuk, V., et al. (2013). Mechanism of tetracycline resistance by ribosomal protection protein Tet(O). *Nat. Commun.* *4*, 1477.
- Li, W., Ward, F.R., McClure, K.F., Chang, S.T.-L., Montabana, E., Liras, S., Dullea, R.G., and Cate, J.H.D. (2019). Structural basis for selective stalling of human ribosome nascent chain complexes by a drug-like molecule. *Nat. Struct. Mol. Biol.* *26*, 501.
- Liang, J.-H., and Han, X. (2013). Structure-activity relationships and mechanism of action of macrolides derived from erythromycin as antibacterial agents. *Curr. Top. Med. Chem.* *13*, 3131–3164.
- Lintner, N.G., McClure, K.F., Petersen, D., Londregan, A.T., Piotrowski, D.W., Wei, L., Xiao, J., Bolt, M., Loria, P.M., Maguire, B., et al. (2017). Selective stalling of human translation through small-molecule engagement of the ribosome nascent chain. *PLOS Biol.* *15*, e2001882.
- Liou, Y.-F., and Tanaka, N. (1976). Dual actions of viomycin on the ribosomal functions. *Biochem. Biophys. Res. Commun.* *71*, 477–483.
- Lipmann, F. (1969). Polypeptide chain elongation in protein biosynthesis. *Science* *164*, 1024–1031.
- Liu, B., Tan, Y., Gan, M.-L., Zhou, H.-X., Wang, Y.-G., Ping, Y.-H., Li, B., Yang, Z.-Y., and Xiao, C.-L. (2014). [Identification of tetracenomycin X from a marine-derived *Saccharothrix* sp. guided by genes sequence analysis]. *Yao Xue Xue Bao* *49*, 230–236.
- Liu, G., Luan, B., Liang, G., Xing, L., Huang, L., Wang, C., and Xu, Y. (2018). Isolation and identification of four major impurities in capreomycin sulfate. *J. Chromatogr. A* *1571*, 155–164.
- Lovmar, M., Tenson, T., and Ehrenberg, M. (2004). Kinetics of Macrolide Action: the josamycin and erythromycin cases\*. *J. Biol. Chem.* *279*, 53506–53515.
- Ly, C.T., Altuntop, M.E., and Wang, Y. (2010). Single-Molecule Study of Viomycin's Inhibition Mechanism on Ribosome Translocation. *Biochemistry* *49*, 9732–9738.
- Lyumkis, D. (2019). Challenges and opportunities in cryo-EM single-particle analysis. *J. Biol. Chem.* *294*, 5181–5197.
- Ma, Z., Ginsberg, A.M., and Spigelman, M. (2007). 7.24 - Antimycobacterium Agents. In *Comprehensive Medicinal Chemistry II*, J.B. Taylor, and D.J. Trigg, eds. (Oxford: Elsevier), pp. 699–730.

- Maden, B.E., Traut, R.R., and Monro, R.E. (1968). Ribosome-catalysed peptidyl transfer: the polyphenylalanine system. *J. Mol. Biol.* *35*, 333–345.
- Mankin, A.S. (1997). Pactamycin resistance mutations in functional sites of 16 S rRNA. *J. Mol. Biol.* *274*, 8–15.
- Maracci, C., Wohlgemuth, I., and Rodnina, M.V. (2015). Activities of the peptidyl transferase center of ribosomes lacking protein L27. *RNA N. Y. N* *21*, 2047–2052.
- Marks, J., Kannan, K., Roncase, E.J., Klepacki, D., Kefi, A., Orelle, C., Vázquez-Laslop, N., and Mankin, A.S. (2016). Context-specific inhibition of translation by ribosomal antibiotics targeting the peptidyl transferase center. *Proc. Natl. Acad. Sci. U. S. A.* *113*, 12150–12155.
- Mayer, C., Stortchevoi, A., Köhrer, C., Varshney, U., and RajBhandary, U.L. (2001). Initiator tRNA and its role in initiation of protein synthesis. *Cold Spring Harb. Symp. Quant. Biol.* *66*, 195–206.
- McGlinchy, N.J., and Ingolia, N.T. (2017). Transcriptome-wide measurement of translation by ribosome profiling. *Methods San Diego Calif* *126*, 112–129.
- McGUIRE, J.M., Bunch, R.L., Anderson, R.C., Boaz, H.E., Flynn, E.H., Powell, H.M., and Smith, J.W. (1952). Ilotycin, a new antibiotic. *Antibiot. Chemother. Northfield Ill* *2*, 281–283.
- Menninger, J.R. (1985). Functional consequences of binding macrolides to ribosomes. *J. Antimicrob. Chemother.* *16*, 23–34.
- Meydan, S., Klepacki, D., Mankin, A.S., and Vázquez-Laslop, N. (2021). Identification of Translation Start Sites in Bacterial Genomes. *Methods Mol. Biol. Clifton NJ* *2252*, 27–55.
- Miethke, M., Pieroni, M., Weber, T., Brönstrup, M., Hammann, P., Halby, L., Arimondo, P.B., Glaser, P., Aigle, B., Bode, H.B., et al. (2021). Towards the sustainable discovery and development of new antibiotics. *Nat. Rev. Chem.* 1–24.
- Milón, P., and Rodnina, M.V. (2012). Kinetic control of translation initiation in bacteria. *Crit. Rev. Biochem. Mol. Biol.* *47*, 334–348.
- Min, Y.-H., Kwon, A.-R., Yoon, J.-M., Yoon, E.-J., Shim, M.-J., and Choi, E.-C. (2008). Molecular analysis of constitutive mutations in *ermB* and *ermA* selected in vitro from inducibly MLSB-resistant enterococci. *Arch. Pharm. Res.* *31*, 377–380.
- Moazed, D., and Noller, H.F. (1989). Intermediate states in the movement of transfer RNA in the ribosome. *Nature* *342*, 142–148.
- Modolfl, J., and Vázquez, D. (1977). The Inhibition of Ribosomal Translocation by Viomycin. *Eur. J. Biochem.* *81*, 491–497.
- Moellering, R.C. (2003). Linezolid: the first oxazolidinone antimicrobial. *Ann. Intern. Med.* *138*, 135–142.
- Mohammad, F., Woolstenhulme, C.J., Green, R., and Buskirk, A.R. (2016). Clarifying the Translational Pausing Landscape in Bacteria by Ribosome Profiling. *Cell Rep.* *14*, 686–694.
- Moll, I., and Bläsi, U. (2002). Differential inhibition of 30S and 70S translation initiation complexes on leaderless mRNA by kasugamycin. *Biochem. Biophys. Res. Commun.* *297*, 1021–1026.
- Moll, I., Hirokawa, G., Kiel, M.C., Kaji, A., and Bläsi, U. (2004). Translation initiation with 70S ribosomes: an alternative pathway for leaderless mRNAs. *Nucleic Acids Res.* *32*, 3354–3363.



- Monro, R.E. (1967). Catalysis of peptide bond formation by 50 S ribosomal subunits from *Escherichia coli*. *J. Mol. Biol.* *26*, 147–151.
- Moriya, T., Saur, M., Stabrin, M., Merino, F., Voicu, H., Huang, Z., Penczek, P.A., Raunser, S., and Gatsogiannis, C. (2017). High-resolution Single Particle Analysis from Electron Cryo-microscopy Images Using SPHIRE. *J. Vis. Exp. JoVE*.
- Mulani, M.S., Kamble, E.E., Kumkar, S.N., Tawre, M.S., and Pardesi, K.R. (2019). Emerging Strategies to Combat ESKAPE Pathogens in the Era of Antimicrobial Resistance: A Review. *Front. Microbiol.* *10*, 539.
- Munro, J.B., Wasserman, M.R., Altman, R.B., Wang, L., and Blanchard, S.C. (2010). Correlated conformational events in EF-G and the ribosome regulate translocation. *Nat. Struct. Mol. Biol.* *17*, 1470–1477.
- Murata, K., and Wolf, M. (2018). Cryo-electron microscopy for structural analysis of dynamic biological macromolecules. *Biochim. Biophys. Acta BBA - Gen. Subj.* *1862*, 324–334.
- Murphy, E. (1985a). Nucleotide sequence of *ermA*, a macrolide-lincosamide-streptogramin B determinant in *Staphylococcus aureus*. *J. Bacteriol.* *162*, 633–640.
- Murphy, E. (1985b). Nucleotide sequence of *ermA*, a macrolide-lincosamide-streptogramin B determinant in *Staphylococcus aureus*. *J. Bacteriol.* *162*, 633–640.
- Muto, H., Nakatogawa, H., and Ito, K. (2006). Genetically encoded but nonpolypeptide prolyl-tRNA functions in the A site for SecM-mediated ribosomal stall. *Mol. Cell* *22*, 545–552.
- Nakahigashi, K., Takai, Y., Shiwa, Y., Wada, M., Honma, M., Yoshikawa, H., Tomita, M., Kanai, A., and Mori, H. (2014). Effect of codon adaptation on codon-level and gene-level translation efficiency in vivo. *BMC Genomics* *15*, 1115.
- Navidinia, M. (2016). The clinical importance of emerging ESKAPE pathogens in nosocomial infections. *Arch. Adv. Biosci.* *7*, 43–57.
- Nguyen, F., Starosta, A.L., Arenz, S., Sohmen, D., Dönhöfer, A., and Wilson, D.N. (2014). Tetracycline antibiotics and resistance mechanisms. *Biol. Chem.* *395*.
- Nichols, D., Cahoon, N., Trakhtenberg, E.M., Pham, L., Mehta, A., Belanger, A., Kanigan, T., Lewis, K., and Epstein, S.S. (2010). Use of ichip for high-throughput in situ cultivation of “uncultivable” microbial species. *Appl. Environ. Microbiol.* *76*, 2445–2450.
- Nissen, P., Kjeldgaard, M., Thirup, S., Polekhina, G., Reshetnikova, L., Clark, B.F., and Nyborg, J. (1995). Crystal structure of the ternary complex of Phe-tRNA<sup>Phe</sup>, EF-Tu, and a GTP analog. *Science* *270*, 1464–1472.
- Nissen, P., Hansen, J., Ban, N., Moore, P.B., and Steitz, T.A. (2000). The structural basis of ribosome activity in peptide bond synthesis. *Science* *289*, 920–930.
- Nogales, E. (2016). The development of cryo-EM into a mainstream structural biology technique. *Nat. Methods* *13*, 24–27.
- Noller, H.F. (1993). tRNA-rRNA interactions and peptidyl transferase. *FASEB J. Off. Publ. Fed. Am. Soc. Exp. Biol.* *7*, 87–89.
- Odom, O.W., Picking, W.D., Tsalkova, T., and Hardesty, B. (1991). The synthesis of polyphenylalanine on ribosomes to which erythromycin is bound. *Eur. J. Biochem.* *198*, 713–722.

- Ogle, J.M., Carter, A.P., and Ramakrishnan, V. (2003). Insights into the decoding mechanism from recent ribosome structures. *Trends Biochem. Sci.* 28, 259–266.
- Oh, E., Becker, A.H., Sandikci, A., Huber, D., Chaba, R., Gloge, F., Nichols, R.J., Typas, A., Gross, C.A., Kramer, G., et al. (2011). Selective Ribosome Profiling Reveals the Cotranslational Chaperone Action of Trigger Factor In Vivo. *Cell* 147, 1295–1308.
- Olson, M.W., Ruzin, A., Feyfant, E., Rush, T.S., O’Connell, J., and Bradford, P.A. (2006). Functional, Biophysical, and Structural Bases for Antibacterial Activity of Tigecycline. *Antimicrob. Agents Chemother.* 50, 2156–2166.
- Omura, S., Morimoto, S., Nagate, T., Adachi, T., and Kohno, Y. (1992). [Research and development of clarithromycin]. *Yakugaku Zasshi* 112, 593–614.
- Orelle, C., Carlson, S., Kaushal, B., Almutairi, M.M., Liu, H., Ochabowicz, A., Quan, S., Pham, V.C., Squires, C.L., Murphy, B.T., et al. (2013). Tools for Characterizing Bacterial Protein Synthesis Inhibitors. *Antimicrob. Agents Chemother.* 57, 5994–6004.
- Osterman, I.A., Wieland, M., Maviza, T.P., Lashkevich, K.A., Lukianov, D.A., Komarova, E.S., Zakalyukina, Y.V., Buschauer, R., Shiriaev, D.I., Leyn, S.A., et al. (2020). Tetracenomycin X inhibits translation by binding within the ribosomal exit tunnel. *Nat. Chem. Biol.* 16, 1071–1077.
- Otaka, T., and Kaji, A. (1975). Release of (oligo) peptidyl-tRNA from ribosomes by erythromycin A. *Proc. Natl. Acad. Sci.* 72, 2649–2652.
- Pan, D., Kirillov, S.V., and Cooperman, B.S. (2007). Kinetically Competent Intermediates in the Translocation Step of Protein Synthesis. *Mol. Cell* 25, 519–529.
- Pape, T., Wintermeyer, W., and Rodnina, M.V. (1998). Complete kinetic mechanism of elongation factor Tu-dependent binding of aminoacyl-tRNA to the A site of the E. coli ribosome. *EMBO J.* 17, 7490–7497.
- Parnell, K.M., Seila, A.C., and Strobel, S.A. (2002). Evidence against stabilization of the transition state oxyanion by a pKa-perturbed RNA base in the peptidyl transferase center. *Proc. Natl. Acad. Sci. U. S. A.* 99, 11658–11663.
- Pereira, D., and Fernandes, P. (2011). Synthesis and antibacterial activity of novel 4-aryl-[1,2,3]-triazole containing macrolides. *Bioorg. Med. Chem. Lett.* 21, 510–513.
- Peske, F., Savelsbergh, A., Katunin, V.I., Rodnina, M.V., and Wintermeyer, W. (2004). Conformational Changes of the Small Ribosomal Subunit During Elongation Factor G-dependent tRNA–mRNA Translocation. *J. Mol. Biol.* 343, 1183–1194.
- Peske, F., Rodnina, M.V., and Wintermeyer, W. (2005). Sequence of steps in ribosome recycling as defined by kinetic analysis. *Mol. Cell* 18, 403–412.
- Petrychenko, V., Peng, B.-Z., de A P Schwarzer, A.C., Peske, F., Rodnina, M.V., and Fischer, N. (2021). Structural mechanism of GTPase-powered ribosome-tRNA movement. *Nat. Commun.* 12, 5933.
- Pioletti, M., Schlünzen, F., Harms, J., Zarivach, R., Glühmann, M., Avila, H., Bashan, A., Bartels, H., Auerbach, T., Jacobi, C., et al. (2001). Crystal structures of complexes of the small ribosomal subunit with tetracycline, edeine and IF3. *EMBO J.* 20, 1829–1839.
- Piscitelli, S.C., Danziger, L.H., and Rodvold, K.A. (1992). Clarithromycin and azithromycin: new macrolide antibiotics. *Clin. Pharm.* 11, 137–152.

- Polacek, N., and Mankin, A.S. (2005). The ribosomal peptidyl transferase center: structure, function, evolution, inhibition. *Crit. Rev. Biochem. Mol. Biol.* *40*, 285–311.
- Polikanov, Y.S., Steitz, T.A., and Innis, C.A. (2014a). A proton wire to couple aminoacyl-tRNA accommodation and peptide-bond formation on the ribosome. *Nat. Struct. Mol. Biol.* *21*, 787–793.
- Polikanov, Y.S., Osterman, I.A., Szal, T., Tashlitsky, V.N., Serebryakova, M.V., Kusochev, P., Bulkley, D., Malanicheva, I.A., Efimenko, T.A., Efremenkova, O.V., et al. (2014b). Amicoumacin A Inhibits Translation by Stabilizing mRNA Interaction with the Ribosome. *Mol. Cell* *56*, 531–540.
- Polikanov, Y.S., Aleksashin, N.A., Beckert, B., and Wilson, D.N. (2018). The Mechanisms of Action of Ribosome-Targeting Peptide Antibiotics. *Front. Mol. Biosci.* *5*, 48.
- Punjani, A., Rubinstein, J.L., Fleet, D.J., and Brubaker, M.A. (2017). cryoSPARC: algorithms for rapid unsupervised cryo-EM structure determination. *Nat. Methods* *14*, 290–296.
- Ramrath, D.J.F., Lancaster, L., Sprink, T., Mielke, T., Loerke, J., Noller, H.F., and Spahn, C.M.T. (2013). Visualization of two transfer RNAs trapped in transit during elongation factor G-mediated translocation. *Proc. Natl. Acad. Sci.* *110*, 20964–20969.
- Ramu, H., Mankin, A., and Vazquez-Laslop, N. (2009). Programmed drug-dependent ribosome stalling. *Mol. Microbiol.* *71*, 811–824.
- Ramu, H., Vázquez-Laslop, N., Klepacki, D., Dai, Q., Piccirilli, J., Micura, R., and Mankin, A.S. (2011). Nascent Peptide in the Ribosome Exit Tunnel Affects Functional Properties of the A-Site of the Peptidyl Transferase Center. *Mol. Cell* *41*, 321–330.
- Ranjan, N., and Rodnina, M.V. (2017). Thio-Modification of tRNA at the Wobble Position as Regulator of the Kinetics of Decoding and Translocation on the Ribosome. *J. Am. Chem. Soc.* *139*, 5857–5864.
- Razi, A., Britton, R.A., and Ortega, J. (2017). The impact of recent improvements in cryo-electron microscopy technology on the understanding of bacterial ribosome assembly. *Nucleic Acids Res.* *45*, 1027–1040.
- Reyes, J., Aguilar, A.C., and Caicedo, A. (2019). Carbapenem-Resistant *Klebsiella pneumoniae*: Microbiology Key Points for Clinical Practice. *Int. J. Gen. Med.* *12*, 437–446.
- Rheinberger, H.J., Sternbach, H., and Nierhaus, K.H. (1981). Three tRNA binding sites on *Escherichia coli* ribosomes. *Proc. Natl. Acad. Sci. U. S. A.* *78*, 5310–5314.
- Rice, L.B. (2008). Federal funding for the study of antimicrobial resistance in nosocomial pathogens: no ESKAPE. *J. Infect. Dis.* *197*, 1079–1081.
- Ringquist, S., Shinedling, S., Barrick, D., Green, L., Binkley, J., Stormo, G.D., and Gold, L. (1992). Translation initiation in *Escherichia coli*: sequences within the ribosome-binding site. *Mol. Microbiol.* *6*, 1219–1229.
- Rodnina, M.V. (2018). Translation in Prokaryotes. *Cold Spring Harb. Perspect. Biol.* *10*, a032664.
- Rodvold, K.A. (1999). Clinical pharmacokinetics of clarithromycin. *Clin. Pharmacokinet.* *37*, 385–398.
- Rohr, J., and Zeeck, A. (1990). Structure-activity relationships of elloramycin and tetracenomycin C. *J. Antibiot. (Tokyo)* *43*, 1169–1178.

- de la Rosa-Trevín, J.M., Otón, J., Marabini, R., Zaldívar, A., Vargas, J., Carazo, J.M., and Sorzano, C.O.S. (2013). Xmipp 3.0: an improved software suite for image processing in electron microscopy. *J. Struct. Biol.* *184*, 321–328.
- Rubin, A.F., Gelman, H., Lucas, N., Bajjalieh, S.M., Papenfuss, A.T., Speed, T.P., and Fowler, D.M. (2017). A statistical framework for analyzing deep mutational scanning data. *Genome Biol.* *18*, 150.
- Rundlet, E.J., Holm, M., Schacherl, M., Natchiar, S.K., Altman, R.B., Spahn, C.M.T., Myasnikov, A.G., and Blanchard, S.C. (2021). Structural basis of early translocation events on the ribosome. *Nature* 1–5.
- Saito, K., Green, R., and Buskirk, A.R. (2020). Translational initiation in *E. coli* occurs at the correct sites genome-wide in the absence of mRNA-rRNA base-pairing. *ELife* *9*, e55002.
- Salsi, E., Farah, E., Dann, J., and Ermolenko, D.N. (2014). Following movement of domain IV of elongation factor G during ribosomal translocation. *Proc. Natl. Acad. Sci. U. S. A.* *111*, 15060–15065.
- Sandler, P., and Weisblum, B. (1988). Erythromycin-induced stabilization of *ermA* messenger RNA in *Staphylococcus aureus* and *Bacillus subtilis*. *J. Mol. Biol.* *203*, 905–915.
- Savelsbergh, A., Katunin, V.I., Mohr, D., Peske, F., Rodnina, M.V., and Wintermeyer, W. (2003). An elongation factor G-induced ribosome rearrangement precedes tRNA-mRNA translocation. *Mol. Cell* *11*, 1517–1523.
- Savelsbergh, A., Mohr, D., Kothe, U., Wintermeyer, W., and Rodnina, M.V. (2005). Control of phosphate release from elongation factor G by ribosomal protein L7/12. *EMBO J.* *24*, 4316–4323.
- Scharff, L.B., Childs, L., Walther, D., and Bock, R. (2011). Local absence of secondary structure permits translation of mRNAs that lack ribosome-binding sites. *PLoS Genet.* *7*, e1002155.
- Scheres, S.H.W. (2012). RELION: implementation of a Bayesian approach to cryo-EM structure determination. *J. Struct. Biol.* *180*, 519–530.
- Schlünzen, F., Zarivach, R., Harms, J., Bashan, A., Tocilj, A., Albrecht, R., Yonath, A., and Franceschi, F. (2001). Structural basis for the interaction of antibiotics with the peptidyl transferase centre in eubacteria. *Nature* *413*, 814.
- Schmeing, T.M., and Ramakrishnan, V. (2009a). What recent ribosome structures have revealed about the mechanism of translation. *Nature* *461*, 1234–1242.
- Schmeing, T.M., and Ramakrishnan, V. (2009b). What recent ribosome structures have revealed about the mechanism of translation. *Nature* *461*, 1234–1242.
- Schmeing, T.M., Seila, A.C., Hansen, J.L., Freeborn, B., Soukup, J.K., Scaringe, S.A., Strobel, S.A., Moore, P.B., and Steitz, T.A. (2002). A pre-translocational intermediate in protein synthesis observed in crystals of enzymatically active 50S subunits. *Nat. Struct. Biol.* *9*, 225–230.
- Schmeing, T.M., Moore, P.B., and Steitz, T.A. (2003). Structures of deacylated tRNA mimics bound to the E site of the large ribosomal subunit. *RNA N. Y. N* *9*, 1345–1352.
- Schmeing, T.M., Huang, K.S., Strobel, S.A., and Steitz, T.A. (2005a). An induced-fit mechanism to promote peptide bond formation and exclude hydrolysis of peptidyl-tRNA. *Nature* *438*, 520–524.
- Schmeing, T.M., Huang, K.S., Kitchen, D.E., Strobel, S.A., and Steitz, T.A. (2005b). Structural insights into the roles of water and the 2' hydroxyl of the P site tRNA in the peptidyl transferase reaction. *Mol. Cell* *20*, 437–448.

- Schmitt, E., Panvert, M., Blanquet, S., and Mechulam, Y. (1998). Crystal structure of methionyl-tRNA<sup>fMet</sup> transformylase complexed with the initiator formyl-methionyl-tRNA<sup>fMet</sup>. *EMBO J.* *17*, 6819–6826.
- Schmitz, F.-J., Petridou, J., Astfalk, N., Köhrer, K., Scheuring, S., and Schwarz, S. (2002). Molecular Analysis of Constitutively Expressed erm(C) Genes Selected In Vitro by Incubation in the Presence of the Noninducers Quinupristin, Telithromycin, or ABT-773. *Microb. Drug Resist.* *8*, 171–177.
- Schuwirth, B.S., Day, J.M., Hau, C.W., Janssen, G.R., Dahlberg, A.E., Cate, J.H.D., and Vila-Sanjurjo, A. (2006). Structural analysis of kasugamycin inhibition of translation. *Nat. Struct. Mol. Biol.* *13*, 879–886.
- Scolnick, E., Tompkins, R., Caskey, T., and Nirenberg, M. (1968). Release factors differing in specificity for terminator codons. *Proc. Natl. Acad. Sci. U. S. A.* *61*, 768–774.
- Seip, B., and Innis, C.A. (2016). How Widespread is Metabolite Sensing by Ribosome-Arresting Nascent Peptides? *J. Mol. Biol.* *428*, 2217–2227.
- Seip, B., Sacheau, G., Dupuy, D., and Innis, C.A. (2018). Ribosomal stalling landscapes revealed by high-throughput inverse toeprinting of mRNA libraries. *Life Sci. Alliance* *1*.
- Seipke, R.F., Kaltenpoth, M., and Hutchings, M.I. (2012). *Streptomyces* as symbionts: an emerging and widespread theme? *FEMS Microbiol. Rev.* *36*, 862–876.
- Seiple, I.B., Zhang, Z., Jakubec, P., Langlois-Mercier, A., Wright, P.M., Hog, D.T., Yabu, K., Allu, S.R., Fukuzaki, T., Carlsen, P.N., et al. (2016). A Platform for the Discovery of New Macrolide Antibiotics. *Nature* *533*, 338–345.
- Sherman, F., Stewart, J.W., and Tsunasawa, S. (1985). Methionine or not methionine at the beginning of a protein. *BioEssays* *3*, 27–31.
- Shimizu, Y., Inoue, A., Tomari, Y., Suzuki, T., Yokogawa, T., Nishikawa, K., and Ueda, T. (2001). Cell-free translation reconstituted with purified components. *Nat. Biotechnol.* *19*, 751–755.
- Shine, J., and Dalgarno, L. (1974). The 3'-terminal sequence of *Escherichia coli* 16S ribosomal RNA: complementarity to nonsense triplets and ribosome binding sites. *Proc. Natl. Acad. Sci. U. S. A.* *71*, 1342–1346.
- Shoji, S., Walker, S.E., and Fredrick, K. (2006). Reverse Translocation of tRNA in the Ribosome. *Mol. Cell* *24*, 931–942.
- Shortridge, V.D., Zhong, P., Cao, Z., Beyer, J.M., Almer, L.S., Ramer, N.C., Doktor, S.Z., and Flamm, R.K. (2002). Comparison of in vitro activities of ABT-773 and telithromycin against macrolide-susceptible and -resistant streptococci and staphylococci. *Antimicrob. Agents Chemother.* *46*, 783–786.
- Sievers, A., Beringer, M., Rodnina, M.V., and Wolfenden, R. (2004). The ribosome as an entropy trap. *Proc. Natl. Acad. Sci. U. S. A.* *101*, 7897–7901.
- Sigworth, F.J. (1998). A maximum-likelihood approach to single-particle image refinement. *J. Struct. Biol.* *122*, 328–339.
- Sigworth, F.J., Doerschuk, P.C., Carazo, J.-M., and Scheres, S.H.W. (2010). An introduction to maximum-likelihood methods in cryo-EM. *Methods Enzymol.* *482*, 263–294.
- Simonetti, A., Marzi, S., Billas, I.M.L., Tsai, A., Fabbretti, A., Myasnikov, A.G., Roblin, P., Vaiana, A.C., Hazemann, I., Eiler, D., et al. (2013). Involvement of protein IF2 N domain in ribosomal subunit

joining revealed from architecture and function of the full-length initiation factor. *Proc. Natl. Acad. Sci. U. S. A.* *110*, 15656–15661.

Sothiselvam, S., Liu, B., Han, W., Ramu, H., Klepacki, D., Atkinson, G.C., Brauer, A., Remm, M., Tenson, T., Schulten, K., et al. (2014). Macrolide antibiotics allosterically predispose the ribosome for translation arrest. *Proc. Natl. Acad. Sci. U. S. A.* *111*, 9804–9809.

Sothiselvam, S., Neuner, S., Rigger, L., Klepacki, D., Micura, R., Vázquez-Laslop, N., and Mankin, A.S. (2016). Binding of Macrolide Antibiotics Leads to Ribosomal Selection against Specific Substrates Based on Their Charge and Size. *Cell Rep.* *16*, 1789–1799.

Sprink, T., Ramrath, D.J.F., Yamamoto, H., Yamamoto, K., Loerke, J., Ismer, J., Hildebrand, P.W., Scheerer, P., Bürger, J., Mielke, T., et al. (2016). Structures of ribosome-bound initiation factor 2 reveal the mechanism of subunit association. *Sci. Adv.* *2*, e1501502.

Srinivas, N., Jetter, P., Ueberbacher, B.J., Werneburg, M., Zerbe, K., Steinmann, J., Van der Meijden, B., Bernardini, F., Lederer, A., Dias, R.L.A., et al. (2010). Peptidomimetic antibiotics target outer-membrane biogenesis in *Pseudomonas aeruginosa*. *Science* *327*, 1010–1013.

Stanley, R.E., Blaha, G., Grodzicki, R.L., Strickler, M.D., and Steitz, T.A. (2010). The structures of the anti-tuberculosis antibiotics viomycin and capreomycin bound to the 70S ribosome. *Nat. Struct. Mol. Biol.* *17*, 289–293.

Sutcliffe, J.A., and Leclercq, R. (2002). Mechanisms of resistance to macrolides, lincosamides, and ketolides. In *Macrolide Antibiotics*, W. Schönfeld, and H.A. Kirst, eds. (Basel: Birkhäuser Basel), pp. 281–317.

Svetlov, M.S., Vázquez-Laslop, N., and Mankin, A.S. (2017). Kinetics of drug-ribosome interactions defines the cidal activity of macrolide antibiotics. *Proc. Natl. Acad. Sci. U. S. A.* *114*, 13673–13678.

Svetlov, M.S., Koller, T.O., Meydan, S., Shankar, V., Klepacki, D., Polacek, N., Gwydosh, N.R., Vázquez-Laslop, N., Wilson, D.N., and Mankin, A.S. (2021). Context-specific action of macrolide antibiotics on the eukaryotic ribosome. *Nat. Commun.* *12*, 2803.

Syroegin, E.A., Flemmich, L., Klepacki, D., Vazquez-Laslop, N., Micura, R., and Polikanov, Y.S. (2021). Structural basis for the context-specific action of classic peptidyl transferase inhibitors.

Tacar, O., Sriamornsak, P., and Dass, C.R. (2013). Doxorubicin: an update on anticancer molecular action, toxicity and novel drug delivery systems. *J. Pharm. Pharmacol.* *65*, 157–170.

Tenson, T., Lovmar, M., and Ehrenberg, M. (2003). The Mechanism of Action of Macrolides, Lincosamides and Streptogramin B Reveals the Nascent Peptide Exit Path in the Ribosome. *J. Mol. Biol.* *330*, 1005–1014.

Thom, G., and Prescott, C.D. (1997). The selection in vivo and characterization of an RNA recognition motif for spectinomycin. *Bioorg. Med. Chem.* *5*, 1081–1086.

Thomas, M.G., Chan, Y.A., and Ozanick, S.G. (2003). Deciphering tuberactinomycin biosynthesis: isolation, sequencing, and annotation of the viomycin biosynthetic gene cluster. *Antimicrob. Agents Chemother.* *47*, 2823–2830.

Tolstrup, N., Sensen, C.W., Garrett, R.A., and Clausen, I.G. (2000). Two different and highly organized mechanisms of translation initiation in the archaeon *Sulfolobus solfataricus*. *Extrem. Life Extreme Cond.* *4*, 175–179.

Traut, R.R., and Monro, R.E. (1964). THE PUROMYCIN REACTION AND ITS RELATION TO PROTEIN SYNTHESIS. *J. Mol. Biol.* *10*, 63–72.

Travin, D.Y., Watson, Z.L., Metelev, M., Ward, F.R., Osterman, I.A., Khven, I.M., Khabibullina, N.F., Serebryakova, M., Mergaert, P., Polikanov, Y.S., et al. (2019). Structure of ribosome-bound azole-modified peptide phazolicin rationalizes its species-specific mode of bacterial translation inhibition. *Nat. Commun.* *10*, 4563.

Traxler, M.F., and Kolter, R. (2015). Natural products in soil microbe interactions and evolution. *Nat. Prod. Rep.* *32*, 956–970.

Trobro, S., and Aqvist, J. (2005). Mechanism of peptide bond synthesis on the ribosome. *Proc. Natl. Acad. Sci. U. S. A.* *102*, 12395–12400.

Tsai, K., Stojković, V., Lee, D.J., Young, I.D., Szal, T., Vazquez-Laslop, N., Mankin, A.S., Fraser, J.S., and Fujimori, D.G. (2021). Structural basis for context-specific inhibition of translation by oxazolidinone antibiotics (Biophysics).

Tsegaye, S., Dedefo, G., and Mehdi, M. (2021). Biophysical applications in structural and molecular biology. *Biol. Chem.*

Tu, D., Blaha, G., Moore, P.B., and Steitz, T.A. (2005). Structures of MLSBK Antibiotics Bound to Mutated Large Ribosomal Subunits Provide a Structural Explanation for Resistance. *Cell* *121*, 257–270.

Udagawa, T., Shimizu, Y., and Ueda, T. (2004). Evidence for the translation initiation of leaderless mRNAs by the intact 70 S ribosome without its dissociation into subunits in eubacteria. *J. Biol. Chem.* *279*, 8539–8546.

Valle, M., Sengupta, J., Swami, N.K., Grassucci, R.A., Burkhardt, N., Nierhaus, K.H., Agrawal, R.K., and Frank, J. (2002). Cryo-EM reveals an active role for aminoacyl-tRNA in the accommodation process. *EMBO J.* *21*, 3557–3567.

Valle, M., Zavialov, A., Sengupta, J., Rawat, U., Ehrenberg, M., and Frank, J. (2003). Locking and Unlocking of Ribosomal Motions. *Cell* *114*, 123–134.

Vázquez, D. (1979). Inhibitors of protein biosynthesis. *Mol. Biol. Biochem. Biophys.* *30*, i–x, 1–312.

Vázquez-Laslop, N., and Mankin, A.S. (2011). Picky nascent peptides do not talk to foreign ribosomes. *Proc. Natl. Acad. Sci. U. S. A.* *108*, 5931–5932.

Vázquez-Laslop, N., and Mankin, A.S. (2018a). How Macrolide Antibiotics Work. *Trends Biochem. Sci.* *43*, 668–684.

Vázquez-Laslop, N., and Mankin, A.S. (2018b). Context-Specific Action of Ribosomal Antibiotics. *Annu. Rev. Microbiol.* *72*, 185–207.

Vazquez-Laslop, N., Thum, C., and Mankin, A.S. (2008). Molecular Mechanism of Drug-Dependent Ribosome Stalling. *Mol. Cell* *30*, 190–202.

Vesper, O., Amitai, S., Belitsky, M., Byrgazov, K., Kaberdina, A.C., Engelberg-Kulka, H., and Moll, I. (2011). Selective translation of leaderless mRNAs by specialized ribosomes generated by MazF in *Escherichia coli*. *Cell* *147*, 147–157.

Vincent, H.A., and Deutscher, M.P. (2006). Substrate Recognition and Catalysis by the Exoribonuclease RNase R\*. *J. Biol. Chem.* *281*, 29769–29775.

- Voorhees, R.M., and Ramakrishnan, V. (2013). Structural Basis of the Translational Elongation Cycle. *Annu. Rev. Biochem.* 82, 203–236.
- Voorhees, R.M., Schmeing, T.M., Kelley, A.C., and Ramakrishnan, V. (2010). The mechanism for activation of GTP hydrolysis on the ribosome. *Science* 330, 835–838.
- Waksman, S.A., and Lechevalier, H.A. (1949). Neomycin, a New Antibiotic Active against Streptomycin-Resistant Bacteria, including Tuberculosis Organisms. *Science* 109, 305–307.
- Wallin, G., and Aqvist, J. (2010). The transition state for peptide bond formation reveals the ribosome as a water trap. *Proc. Natl. Acad. Sci. U. S. A.* 107, 1888–1893.
- Wang, J., Zhang, R., Chen, X., Sun, X., Yan, Y., Shen, X., and Yuan, Q. (2020). Biosynthesis of aromatic polyketides in microorganisms using type II polyketide synthases. *Microb. Cell Factories* 19, 110.
- Wang, L., Pulk, A., Wasserman, M.R., Feldman, M.B., Altman, R.B., Cate, J.H.D., and Blanchard, S.C. (2012). Allosteric control of the ribosome by small-molecule antibiotics. *Nat. Struct. Mol. Biol.* 19, 957–963.
- Wasserman, M.R., Alejo, J.L., Altman, R.B., and Blanchard, S.C. (2016). Multiperspective smFRET reveals rate-determining late intermediates of ribosomal translocation. *Nat. Struct. Mol. Biol.* 23, 333–341.
- Waters, M., and Tadi, P. (2021). Streptomycin. In *StatPearls*, (Treasure Island (FL): StatPearls Publishing), p.
- Weber, W., Zähler, H., Siebers, J., Schröder, K., and Zeeck, A. (1979). [Metabolic products of microorganisms. 175. Tetracenomycin C (author's transl)]. *Arch. Microbiol.* 121, 111–116.
- Weiner, J., Herrmann, R., and Browning, G.F. (2000). Transcription in *Mycoplasma pneumoniae*. *Nucleic Acids Res.* 28, 4488–4496.
- Weinger, J.S., Parnell, K.M., Dorner, S., Green, R., and Strobel, S.A. (2004). Substrate-assisted catalysis of peptide bond formation by the ribosome. *Nat. Struct. Mol. Biol.* 11, 1101–1106.
- Weisblum, B. (1995). Erythromycin resistance by ribosome modification. *Antimicrob. Agents Chemother.* 39, 577–585.
- Welch, M., Chastang, J., and Yarus, M. (1995). An inhibitor of ribosomal peptidyl transferase using transition-state analogy. *Biochemistry* 34, 385–390.
- Weston, N., Sharma, P., Ricci, V., and Piddock, L.J.V. (2018). Regulation of the AcrAB-TolC efflux pump in Enterobacteriaceae. *Res. Microbiol.* 169, 425–431.
- White, F.R. (1962). Pactamycin. *Cancer Chemother. Rep.* 24, 75–78.
- Wilson, D.N. (2014). Ribosome-targeting antibiotics and mechanisms of bacterial resistance. *Nat. Rev. Microbiol.* 12, 35–48.
- Wilson, D.N. (2016). The ABC of Ribosome-Related Antibiotic Resistance. *MBio* 7.
- Wilson, K.S., Ito, K., Noller, H.F., and Nakamura, Y. (2000). Functional sites of interaction between release factor RF1 and the ribosome. *Nat. Struct. Biol.* 7, 866–870.



- Wimberly, B.T., Brodersen, D.E., Clemons, W.M., Morgan-Warren, R.J., Carter, A.P., Vonnrhein, C., Hartsch, T., and Ramakrishnan, V. (2000). Structure of the 30S ribosomal subunit. *Nature* *407*, 327–339.
- Wise, R. (1989). The development of macrolides and related compounds. *J. Antimicrob. Chemother.* *23*, 299–300.
- Wohlgemuth, I., Brenner, S., Beringer, M., and Rodnina, M.V. (2008). Modulation of the rate of peptidyl transfer on the ribosome by the nature of substrates. *J. Biol. Chem.* *283*, 32229–32235.
- Woodcock, J., Moazed, D., Cannon, M., Davies, J., and Noller, H. f. (1991). Interaction of antibiotics with A- and P-site-specific bases in 16S ribosomal RNA. *EMBO J.* *10*, 3099–3103.
- Woolstenhulme, C.J., Guydosh, N.R., Green, R., and Buskirk, A.R. (2015). High-Precision Analysis of Translational Pausing by Ribosome Profiling in Bacteria Lacking EFP. *Cell Rep.* *11*, 13–21.
- Woosley, L.N., Castanheira, M., and Jones, R.N. (2010). CEM-101 Activity against Gram-Positive Organisms. *Antimicrob. Agents Chemother.* *54*, 2182–2187.
- Wouters, O.J., McKee, M., and Luyten, J. (2020). Estimated Research and Development Investment Needed to Bring a New Medicine to Market, 2009-2018. *JAMA* *323*, 844–853.
- Yamada, T., Teshima, T., and Shiba, T. (1981). Activity of Di-<sup>+</sup>-Lysyl-Capreomycin IIA and Palmitoyl Tuberactinamine N Against Drug-Resistant Mutants with Altered Ribosomes. *Antimicrob. Agents Chemother.* *20*, 834–836.
- Yamamoto, H., Qin, Y., Achenbach, J., Li, C., Kijek, J., Spahn, C.M.T., and Nierhaus, K.H. (2014). EF-G and EF4: translocation and back-translocation on the bacterial ribosome. *Nat. Rev. Microbiol.* *12*, 89–100.
- Youngman, E.M., Brunelle, J.L., Kochaniak, A.B., and Green, R. (2004). The active site of the ribosome is composed of two layers of conserved nucleotides with distinct roles in peptide bond formation and peptide release. *Cell* *117*, 589–599.
- Zhanel, G.G., Walters, M., Noreddin, A., Vercaigne, L.M., Wierzbowski, A., Embil, J.M., Gin, A.S., Douthwaite, S., and Hoban, D.J. (2002). The Ketolides. *Drugs* *62*, 1771–1804.
- Zhang, J., Kobert, K., Flouri, T., and Stamatakis, A. (2014). PEAR: a fast and accurate Illumina Paired-End reAd mergeR. *Bioinforma. Oxf. Engl.* *30*, 614–620.
- Zhang, L., Wang, Y.-H., Zhang, X., Lancaster, L., Zhou, J., and Noller, H.F. (2020). The structural basis for inhibition of ribosomal translocation by viomycin. *Proc. Natl. Acad. Sci.* *117*, 10271–10277.
- Zhang, Z., Pan, H.-X., and Tang, G.-L. (2017). New insights into bacterial type II polyketide biosynthesis. *F1000Research* *6*, 172.
- Zhao, Q., Xin, L., Liu, Y., Liang, C., Li, J., Jian, Y., Li, H., Shi, Z., Liu, H., and Cao, W. (2021). Current Landscape and Future Perspective of Oxazolidinone Scaffolds Containing Antibacterial Drugs. *J. Med. Chem.*

## Supplementary Data

**Supplementary Table 1 : List of oligos, section 3.3.2**

<b>T7_RBS_ATG_f</b>	CGATCGAATTCTAATACGACTCACTATAGGGCTTAAGTATAAGGAGGAAAAAATATG
<b>Stop_EcoRV_r</b>	TATATGGATCCTTTTTGATATTGATATCTCATCACACCGAGATCG
<b>T7_f</b>	CGATCGAATTCTAATACGACTCACTATAG
<b>EcoRV_r</b>	TATATGGATCCTTTTTGATATTGATA
<b>3' linker_Apol</b>	/5rAPP/GGTATCTCGGTGTGACTGACTGAAAATTTCTGTAGGCACCATCAAT/ddC
<b>Linker_r</b>	ATTGATGGTGCCTACAG
<b>cDNA_f</b>	GTATAAGGAGGAAAAAATATG
<b>Biotin_standard</b>	/5Biosg/AAAAAAAAAAAAAAAAATTAAGTCCATCTAA
<b>ermAL1_opool</b>	<p>1.CGATCGAATTCTAATACGACTCACTATAGGGCTTAAGTATAAGGAGGAAAAAATATGNNNACCAGTATCGCAGTAGTAGAAATTACTTTATCTCATTAGCGATCTCGGTGTGATGAGATATCAATATCAAAAAGGATCCATATA</p> <p>2.CGATCGAATTCTAATACGACTCACTATAGGGCTTAAGTATAAGGAGGAAAAAATATGTGCNNNAGTATCGCAGTAGTAGAAATTACTTTATCTCATTAGCGATCTCGGTGTGATGAGATATCAATATCAAAAAGGATCCATATA</p> <p>3.CGATCGAATTCTAATACGACTCACTATAGGGCTTAAGTATAAGGAGGAAAAAATATGTGCACCNNNATCGCAGTAGTAGAAATTACTTTATCTCATTAGCGATCTCGGTGTGATGAGATATCAATATCAAAAAGGATCCATATA</p> <p>4.CGATCGAATTCTAATACGACTCACTATAGGGCTTAAGTATAAGGAGGAAAAAATATGTGCACCAAGTNNNGCAGTAGTAGAAATTACTTTATCTCATTAGCGATCTCGGTGTGATGAGATATCAATATCAAAAAGGATCCATATA</p> <p>5.CGATCGAATTCTAATACGACTCACTATAGGGCTTAAGTATAAGGAGGAAAAAATATGTGCACCAAGTATCNNNGTAGTAGAAATTACTTTATCTCATTAGCGATCTCGGTGTGATGAGATATCAATATCAAAAAGGATCCATATA</p> <p>6.CGATCGAATTCTAATACGACTCACTATAGGGCTTAAGTATAAGGAGGAAAAAATATGTGCACCAAGTATCGCANNNGTAGTAGAAATTACTTTATCTCATTAGCGATCTCGGTGTGATGAGATATCAATATCAAAAAGGATCCATATA</p> <p>7.CGATCGAATTCTAATACGACTCACTATAGGGCTTAAGTATAAGGAGGAAAAAATATGTGCACCAAGTATCGCAGTANNNGAAATTACTTTATCTCATTAGCGATCTCGGTGTGATGAGATATCAATATCAAAAAGGATCCATATA</p> <p>8.CGATCGAATTCTAATACGACTCACTATAGGGCTTAAGTATAAGGAGGAAAAAATATGTGCACCAAGTATCGCAGTAGTANNNATTACTTTATCTCATTAGCGATCTCGGTGTGATGAGATATCAATATCAAAAAGGATCCATATA</p> <p>9.CGATCGAATTCTAATACGACTCACTATAGGGCTTAAGTATAAGGAGGAAAAAATATGTGCACCAAGTATCGCAGTAGTAGAANNNACTTTATCTCATTAGCGATCTCGGTGTGATGAGATATCAATATCAAAAAGGATCCATATA</p> <p>10.CGATCGAATTCTAATACGACTCACTATAGGGCTTAAGTATAAGGAGGAAAAAATATGTGCACCAAGTATCGCAGTAGTAGAAATTNNNTTATCTCATTAGCGATCTCGGTGTGATGAGATATCAATATCAAAAAGGATCCATATA</p> <p>11.CGATCGAATTCTAATACGACTCACTATAGGGCTTAAGTATAAGGAGGAAAAAATATGTGCACCAAGTATCGCAGTAGTAGAAATTACTNNNTCTCATTAGCGATCTCGGTGTGATGAGATATCAATATCAAAAAGGATCCATATA</p> <p>12.CGATCGAATTCTAATACGACTCACTATAGGGCTTAAGTATAAGGAGGAAAAAATATGTGCACCAAGTATCGCAGTAGTAGAAATTACTTTANNNCATTAGCGATCTCGGTGTGATGAGATATCAATATCAAAAAGGATCCATATA</p> <p>13.CGATCGAATTCTAATACGACTCACTATAGGGCTTAAGTATAAGGAGGAAAAAATATGTGCACCAAGTATCGCAGTAGTAGAAATTACTTTATCTNNNTCAGCGATCTCGGTGTGATGAGATATCAATATCAAAAAGGATCCATATA</p>

	<p>14.CGATCGAATTCTAATACGACTCACTATAGGGCTTAAGTATAAGGAGGAAAAAAT ATGTGCACCAGTATCGCAGTAGTAGAAATTACTTTATCTCATNNNGCGATCTCGGT GTGATGAGATATCAATATCAAAAAGGATCCATATA</p> <p>15.CGATCGAATTCTAATACGACTCACTATAGGGCTTAAGTATAAGGAGGAAAAAAT ATGTGCACCAGTATCNNNGTAGTANNNATTACTTTATCTCATTAGCGATCTCGGT GTGATGAGATATCAATATCAAAAAGGATCCATATA</p>
ermCL_opool	<p>1.CGATCGAATTCTAATACGACTCACTATAGGGCTTAAGTATAAGGAGGAAAAAAT ATGNNNATTTTTAGTATTTTTGTAATCAGCACAGTTCATTATCAACCAAACAAAA AAGCGATCTCGGTGTGATGAGATATCAATATCAAAAAGGATCCATATA</p> <p>2.CGATCGAATTCTAATACGACTCACTATAGGGCTTAAGTATAAGGAGGAAAAAAT ATGGGCNNNTTTAGTATTTTTGTAATCAGCACAGTTCATTATCAACCAAACAAAA AAGCGATCTCGGTGTGATGAGATATCAATATCAAAAAGGATCCATATA</p> <p>3.CGATCGAATTCTAATACGACTCACTATAGGGCTTAAGTATAAGGAGGAAAAAAT ATGGGCATTNNNAGTATTTTTGTAATCAGCACAGTTCATTATCAACCAAACAAAA AAGCGATCTCGGTGTGATGAGATATCAATATCAAAAAGGATCCATATA</p> <p>4.CGATCGAATTCTAATACGACTCACTATAGGGCTTAAGTATAAGGAGGAAAAAAT ATGGGCATTTTTNNNATTTTTGTAATCAGCACAGTTCATTATCAACCAAACAAAA AAGCGATCTCGGTGTGATGAGATATCAATATCAAAAAGGATCCATATA</p> <p>5.CGATCGAATTCTAATACGACTCACTATAGGGCTTAAGTATAAGGAGGAAAAAAT ATGGGCATTTTTAGTNNNTTTGTAATCAGCACAGTTCATTATCAACCAAACAAAA AAGCGATCTCGGTGTGATGAGATATCAATATCAAAAAGGATCCATATA</p> <p>6.CGATCGAATTCTAATACGACTCACTATAGGGCTTAAGTATAAGGAGGAAAAAAT ATGGGCATTTTTAGTATTNNNGTAATCAGCACAGTTCATTATCAACCAAACAAAA AAGCGATCTCGGTGTGATGAGATATCAATATCAAAAAGGATCCATATA</p> <p>7.CGATCGAATTCTAATACGACTCACTATAGGGCTTAAGTATAAGGAGGAAAAAAT ATGGGCATTTTTAGTATTTTTNNNATCAGCACAGTTCATTATCAACCAAACAAAA AAGCGATCTCGGTGTGATGAGATATCAATATCAAAAAGGATCCATATA</p> <p>8.CGATCGAATTCTAATACGACTCACTATAGGGCTTAAGTATAAGGAGGAAAAAAT ATGGGCATTTTTAGTATTTTTGTANNNAGCACAGTTCATTATCAACCAAACAAAA AAGCGATCTCGGTGTGATGAGATATCAATATCAAAAAGGATCCATATA</p> <p>9.CGATCGAATTCTAATACGACTCACTATAGGGCTTAAGTATAAGGAGGAAAAAAT ATGGGCATTTTTAGTATTTTTGTAATCNNNACAGTTCATTATCAACCAAACAAAA AAGCGATCTCGGTGTGATGAGATATCAATATCAAAAAGGATCCATATA</p> <p>10.CGATCGAATTCTAATACGACTCACTATAGGGCTTAAGTATAAGGAGGAAAAAAT ATGGGCATTTTTAGTATTTTTGTAATCAGCNNNGTTCATTATCAACCAAACAAAA AAGCGATCTCGGTGTGATGAGATATCAATATCAAAAAGGATCCATATA</p> <p>11.CGATCGAATTCTAATACGACTCACTATAGGGCTTAAGTATAAGGAGGAAAAAAT ATGGGCATTTTTAGTATTTTTGTAATCAGCACANNNCATTATCAACCAAACAAAA AAGCGATCTCGGTGTGATGAGATATCAATATCAAAAAGGATCCATATA</p> <p>12.CGATCGAATTCTAATACGACTCACTATAGGGCTTAAGTATAAGGAGGAAAAAAT ATGGGCATTTTTAGTATTTTTGTAATCAGCACAGTTNNNTATCAACCAAACAAAA AAGCGATCTCGGTGTGATGAGATATCAATATCAAAAAGGATCCATATA</p> <p>13.CGATCGAATTCTAATACGACTCACTATAGGGCTTAAGTATAAGGAGGAAAAAAT ATGGGCATTTTTAGTATTTTTGTAATCAGCACAGTTCATNNNCAACCAAACAAAA AAGCGATCTCGGTGTGATGAGATATCAATATCAAAAAGGATCCATATA</p> <p>14.CGATCGAATTCTAATACGACTCACTATAGGGCTTAAGTATAAGGAGGAAAAAAT ATGGGCATTTTTAGTATTTTTGTAATCAGCACAGTTCATTATNNNCCAAACAAAA AAGCGATCTCGGTGTGATGAGATATCAATATCAAAAAGGATCCATATA</p> <p>15.CGATCGAATTCTAATACGACTCACTATAGGGCTTAAGTATAAGGAGGAAAAAAT ATGGGCATTTTTAGTATTTTTGTAATCAGCACAGTTCATTATCAANNNAACAAAA AAGCGATCTCGGTGTGATGAGATATCAATATCAAAAAGGATCCATATA</p>
NGS_f	AATGATACGGCGACCACCG

NGS_r	CAAGCAGAAGACGGCATAACGAG
NGS_adapter_f	AATGATACGGCGACCACCGAGATCTACACTCTTTCCCTACACGACGCTCTTCCG ATCTGTATAAGGAGGAAAAAATATG
NGS_adapter_index1 (ermAL1_NoAB1)	CAAGCAGAAGACGGCATAACGAGAT <b>CGTGAT</b> GTGACTGGAGTTCAGACGTGTGCT CTTCCGATCGATTGATGGTGCCTACAG
NGS_adapter_index2 (ermAL1_NoAB2)	CAAGCAGAAGACGGCATAACGAGAT <b>ACATCG</b> GTGACTGGAGTTCAGACGTGTGCT CTTCCGATCGATTGATGGTGCCTACAG
NGS_adapter_index3 (ermAL1_Ery1)	CAAGCAGAAGACGGCATAACGAGAT <b>GCCTAAG</b> TGACTGGAGTTCAGACGTGTGCT CTTCCGATCGATTGATGGTGCCTACAG
NGS_adapter_index4 (ermAL1_Ery2)	CAAGCAGAAGACGGCATAACGAGAT <b>TGGTCAG</b> TGACTGGAGTTCAGACGTGTGCT CTTCCGATCGATTGATGGTGCCTACAG
NGS_adapter_index5 (ermAL1_NoAB3)	CAAGCAGAAGACGGCATAACGAGAT <b>CACTGT</b> GTGACTGGAGTTCAGACGTGTGCT CTTCCGATCGATTGATGGTGCCTACAG
NGS_adapter_index6 (ermAL1_NoAB4)	CAAGCAGAAGACGGCATAACGAGAT <b>ATTGGC</b> GTGACTGGAGTTCAGACGTGTGCT CTTCCGATCGATTGATGGTGCCTACAG
NGS_adapter_index7 (ermAL1_Ery3)	CAAGCAGAAGACGGCATAACGAGAT <b>GATCTG</b> GTGACTGGAGTTCAGACGTGTGCT CTTCCGATCGATTGATGGTGCCTACAG
NGS_adapter_index8 (ermAL1_Ery4)	CAAGCAGAAGACGGCATAACGAGAT <b>TCAAGT</b> GTGACTGGAGTTCAGACGTGTGCT CTTCCGATCGATTGATGGTGCCTACAG
NGS_adapter_index9 (ermAL1_NoAB5)	CAAGCAGAAGACGGCATAACGAGAT <b>CTGATC</b> GTGACTGGAGTTCAGACGTGTGCT CTTCCGATCGATTGATGGTGCCTACAG
NGS_adapter_index10 (ermAL1_NoAB6)	CAAGCAGAAGACGGCATAACGAGAT <b>AAGCTA</b> GTGACTGGAGTTCAGACGTGTGCT CTTCCGATCGATTGATGGTGCCTACAG
NGS_adapter_index11 (ermAL1_Ery5)	CAAGCAGAAGACGGCATAACGAGAT <b>GTAGCC</b> GTGACTGGAGTTCAGACGTGTGCT CTTCCGATCGATTGATGGTGCCTACAG
NGS_adapter_index12 (ermAL1_Ery6)	CAAGCAGAAGACGGCATAACGAGAT <b>TACAAG</b> GTGACTGGAGTTCAGACGTGTGCT CTTCCGATCGATTGATGGTGCCTACAG
NGS_adapter_index13 (ermCL_NoAB1)	CAAGCAGAAGACGGCATAACGAGATTG <b>TTGACT</b> GTGACTGGAGTTCAGACGTGTG CTCTTCCGATCGATTGATGGTGCCTACAG
NGS_adapter_index14 (ermCL_NoAB2)	CAAGCAGAAGACGGCATAACGAGATAC <b>GGAAC</b> TGTGACTGGAGTTCAGACGTGTG CTCTTCCGATCGATTGATGGTGCCTACAG
NGS_adapter_index18 (ermCL_Ery1)	CAAGCAGAAGACGGCATAACGAGAGTGC <b>GGACCT</b> GTGACTGGAGTTCAGACGTG TGCTCTT CCGATCGATTGATGGTGCCTACAG
NGS_adapter_index19 (ermCL_Ery2)	CAAGCAGAAGACGGCATAACGAGAAAGG <b>CCACCT</b> GTGACTGGAGTTCAGACGTG TGCTCTTCCGATCGATTGATGGTGCCTACAG
NGS_adapter_index21 (ermCL_NoAB3)	CAAGCAGAAGACGGCATAACGAGATTCCG <b>AAACCT</b> GTGACTGGAGTTCAGACGTG TGCTCT TCCGATCGATTGATGGTGCCTACAG
NGS_adapter_index22 (ermCL_NoAB4)	CAAGCAGAAGACGGCATAACGAGATTACG <b>TACGCT</b> GTGACTGGAGTTCAGACGTG TGCTCTTCCGATCGATTGATGGTGCCTACAG
NGS_adapter_index23 (ermCL_Ery3)	CAAGCAGAAGACGGCATAACGAGATATCC <b>ACTCCT</b> GTGACTGGAGTTCAGACGTG TGCTCTTCCGATCGATTGATGGTGCCTACAG
NGS_adapter_index25 (ermCL_Ery4)	CAAGCAGAAGACGGCATAACGAGATATAT <b>CAGTCT</b> GTGACTGGAGTTCAGACGTG TGCTCTTCCGATCGATTGATGGTGCCTACAG
NGS_adapter_index27 (ermCL_NoAB5)	CAAGCAGAAGACGGCATAACGAGATAAAG <b>GAATCT</b> GTGACTGGAGTTCAGACGTG TGCTCTTCCGATCGATTGATGGTGCCTACAG
NGS_adapter_index28 (ermCL_NoAB6)	CAAGCAGAAGACGGCATAACGAGAT <b>CTTTTG</b> GTGACTGGAGTTCAGACGTGTGCT CTTCCGATCGATTGATGGTGCCTACAG
NGS_adapter_index29 (ermCL_Ery5)	CAAGCAGAAGACGGCATAACGAGAT <b>TAGTTG</b> GTGACTGGAGTTCAGACGTGTGCT CTTCCGATCGATTGATGGTGCCTACAG
NGS_adapter_index30 (ermCL_Ery6)	CAAGCAGAAGACGGCATAACGAGAT <b>CCGGTG</b> GTGACTGGAGTTCAGACGTGTGCT TCTTCCGATCGATTGATGGTGCCTACAG

**Supplementary Table 2 : List of oligos, section 4.2.4**

<b>T7_RBS_ATG_f</b>	CGATCGAATTCTAATACGACTCACTATAGGGCTTAAGTATAAGGAGGAAAAAAT ATG
<b>Stop_EcoRV_r</b>	TATATGGATCCTTTTTGATATTGATATCTCATCACACCGAGATCG
<b>T7_f</b>	CGATCGAATTCTAATACGACTCACTATAG
<b>EcoRV_r</b>	TATATGGATCCTTTTTGATATTGATA
<b>3' linker_Apol</b>	/5rAPP/GGTATCTCGGTGTGACTGACTGAAAAATTTCTGTAGGCACCATCAAT/ddC
<b>Linker_r</b>	ATTGATGGTGCCTACAG
<b>cDNA_f</b>	GTATAAGGAGGAAAAAATATG
<b>Biotin_standard</b>	/5Biosg/AAAAAAAAAAAAAAAAATTAACCTCATCTAA
<b>NGS_f</b>	AATGATACGGCGACCACCG
<b>NGS_r</b>	CAAGCAGAAGACGGCATACGAG
<b>NGS_adapter_f</b>	AATGATACGGCGACCACCGAGATCTACACTCTTCCCTACACGACGCTCTTCC GATCTGTATAAGGAGGAAAAAATATG
<b>NGS_adapter_index31 (NNN15_NoAB1)</b>	CAAGCAGAAGACGGCATACGAGATATCGTGGTGACTGGAGTTCAGACGTGTG CTCTTCCGATCGATTGATGGTGCCTACAG
<b>NGS_adapter_index41 (NNN15_Pac1)</b>	CAAGCAGAAGACGGCATACGAGATGTCGTGGTGACTGGAGTTCAGACGTGTG CTCTTCCGATCGATTGATGGTGCCTACAG GATGGTGCCTACAG
<b>NGS_adapter_index44 (NNN15_NoAB2)</b>	CAAGCAGAAGACGGCATACGAGATATTATAGTGACTGGAGTTCAGACGTGTGC TCTTCCGATCGATTGATGGTGCCTACAG
<b>NGS_adapter_index3+2 (NNN15_Pac2)</b>	CAAGCAGAAGACGGCATACGAGATGCCTAAGTGACTGGAGTTCAGACGTGTG CTCTTCCGATCTCGATTGATGGTGCCTACAG
<b>NGS_adapter_index7+2 (NNN15_NoAB3)</b>	CAAGCAGAAGACGGCATACGAGATGATCTGGTGACTGGAGTTCAGACGTGTG CTCTTCCGATCTCGATTGATGGTGCCTACAG
<b>NGS_adapter_index19+ 3 (NNN15_Pac3)</b>	CAAGCAGAAGACGGCATACGAGATTTTCACGTGACTGGAGTTCAGACGTGTGC TCTTCCGATCTCTCGATTGATGGTGCCTACAG
<b>Fwd_short</b>	CGATCGAATTCTAATACGACTCACTATAG
<b>Fragment1_fwd</b>	CGATCGAATTCTAATACGACTCACTATAGGGCTTAAGTATAAGGAGGAAAAAAT ATG
<b>TP_frag2_rev</b>	CTTGCTGCGCACGAAGAGTACGGATGTTGTTTCAGAGTCAGTTATTATTCGCT
<b>TP_frag2_NV_rev</b>	GGTTATAATGAATTTTGCTTATTAACCTTGCTGCGCACG
<b>TP_rev_short</b>	GGTTATAATGAATTTTGCTT
<b>TP_rev_YakimaYellow</b>	/5YakYel/GGTTATAATGAATTTTGCTTATTAAC
<b>TP_Pac_MCAPV*_fwd</b>	GTATAAGGAGGAAAAAATATGTGTGCACCGGTGTGAAGCGAATAATAACTGAC TCTG

## **Mécanismes d'inhibition de la traduction contexte-dépendants par des antibiotiques ciblant le ribosome bactérien**

Les bactéries sont présentes partout dans notre environnement et sont indispensables à notre bon fonctionnement. Malheureusement, certaines d'entre elles provoquent également des maladies infectieuses, que nous traitons avec des antibiotiques. Dans certains cas, les bactéries pathogènes sont capables de survivre à l'exposition à ces antibiotiques, grâce à une série de phénomènes connus collectivement sous le nom de résistance aux antibiotiques. L'utilisation excessive des antibiotiques a accéléré ce processus, qui est aujourd'hui l'une des menaces les plus graves pour la santé publique. Mon travail de thèse porte sur les antibiotiques qui ciblent le ribosome, la grande usine moléculaire responsable de la production de protéines dans tous les organismes vivants. Plus précisément, j'ai cherché (i) à comprendre le mécanisme par lequel les bactéries deviennent résistantes aux antibiotiques largement utilisés comme l'érythromycine, et (ii) à déterminer le mode d'action moléculaire de plusieurs antibiotiques, dont les antituberculeux de seconde ligne capréomycine et viomycine, et l'antibiotique tétracénomycine X, plus récent mais très prometteur. Une meilleure compréhension de ces processus pourrait à terme apporter des solutions pour ralentir la propagation de la résistance aux antibiotiques.

**Ribosome, Antibiotiques, Traduction, Antibio-résistance, Bactéries pathogènes**

---

## **Mechanisms of context-dependent translation inhibition by ribosome-targeting antibiotics**

Bacteria are present everywhere in our environment and are essential for our proper functioning. Unfortunately, some of them also cause infectious diseases, which we treat with antibiotics. In some cases, pathogenic bacteria are able to survive exposure to these antibiotics, through a series of phenomena collectively known as antibiotic resistance. The misuse of antibiotics has accelerated this process, which is now one of the most serious threats to global health. My thesis work focuses on antibiotics that target the ribosome, the large molecular factory responsible for producing proteins in all living organisms. Specifically, I have sought (i) to understand the mechanism by which bacteria become resistant to widely used antibiotics like erythromycin, and (ii) to determine the molecular mode of action of several antibiotics, including the second line antituberculosis drugs capreomycin and viomycin, and the more recent but very promising antibiotic tetracenomycin X. A better understanding of these processes could ultimately provide solutions to slow the spread of antibiotic resistance.

**Ribosome, Antibiotics, Translation, Antibiotic Resistance, Bacterial pathogens**

**ARNA INSERM U1212, CNRS UMR 5320**

146 rue Léo Saignat, 33076 Bordeaux